AD-774 590

NOSETIP COOLING TECHNOLOGY (NCT) PROGRAM: INVESTIGATION OF DISCRETE INJECTION COOLING

N. A. Jaffe, et al

Acurex Corporation

Prepared for:

Air Force Systems Command

October 1973

DISTRIBUTED BY:

NTIS

National Technical Information Service
U. S. DEPARTMENT OF COMMERCE
5285 Port Royal Road, Springfield Va. 22151

UNCLASSIFIED
Security Classification

DOCUMENT CONTROL DATA - R & D

(Security classification of title, body of abstract and indexing annotation must be entered when the overall report is classified)

1 ORIGINATING ACTIVITY (Corporate author) AEROTHERM DIVISION/ACUREX CORPORATION 485 Clyde Ave., Mountain View, California 94042	2a. REPORT SECURITY CLASSIFICATION UNCLASSIFIED 2b. GROUP

3 REPORT TITLE

Final Technical Report of the Nosetip Cooling Technology (NCT) Program: Investigation of Discrete Injection Cooling

4 DESCRIPTIVE NOTES (Type of report and inclusive dates)

Final Report - October 1973

5 AUTHOR(S) (First name, middle initial, last name)

N. A. Jaffe L. W. Anderson
K. J. Clark
C. T. Nardo

6 REPORT DATE	7a. TOTAL NO. OF PAGES	7b. NO. OF REFS
October 1973		

8a CONTRACT OR GRANT NO	9a. ORIGINATOR'S REPORT NUMBER(S)
F04701-71-C-0087 b. PROJECT NO	Aerotherm Final Report 73-84
c. d.	9b. OTHER REPORT NO(S) (Any other numbers that may be assigned this report) SAMSO-TR-73-380

10 DISTRIBUTION STATEMENT

Approved for public release, distribution unlimited.

11 SUPPLEMENTARY NOTES	12. SPONSORING MILITARY ACTIVITY

13 ABSTRACT

The objective of the Nosetip Cooling Program (NCT) has been to develop engineering methods for designing discrete injection hardware based on a fundamental understanding of the complex mechanisms associated with heat and mass transfer over and within slotted surfaces. As a result, a series of experimental programs have been performed to identify the critical aerothermodynamic parameters associated with discrete injection transpiration cooling systems.

The major finding of the NCT Program has been the identification and quantification of the effective surface roughness due to slotted surfaces. This roughness gives rise to augmented heating levels, both locally and downstream, for injection flow rates of interest.

Correlations based on the experimental data and supporting analyses have been incorporated into a prediction technique which is utilized in the computation of discrete injection cooling requirements for arbitrary surface geometries and heating environments.

COLOR ILLUSTRATIONS REPRODUCED IN BLACK AND WHITE

ia

DD FORM 1 NOV 68 1473 REPLACES DD FORM 1473, 1 JAN 68, WHICH IS OBSOLETE FOR ARMY USE.

UNCLASSIFIED
Security Classification

14 KEY WORDS	LINK A		LINK B		LINK C	
	ROLE	WT	ROLE	WT	ROLE	WT
Transpiration						
Reentry						
Discrete injection						
Active cooling						
Aero-heating						
Film cooling						
Roughness-Augmented heating						

ib.

SAMSO-TR-73-380

FINAL TECHNICAL REPORT
NOSETIP COOLING TECHNOLOGY (NCT) PROGRAM
INVESTIGATION OF DISCRETE INJECTION COOLING

N. A. Jaffe
K. J. Clark
C. T. Nardo
L. W. Anderson

Approved for public release, distribution unlimited.

FOREWORD

The technical information reported herein has been developed by the Aerotherm Division of the Acurex Corporation, Mountain View, California in accordance with Contract F04701-71-C-0087.

This work has been sponsored by the Space and Missile Systems Organization, Air Force Systems Command, Los Angeles, California. The Air Force Project Officer was Captain M. Anderson. Messrs. C. Melfi and W. Portnier were the Aerospace Project Officers and Mr. P. Crowell served as the principle technical monitor.

The authors are indebted to Drs. L. Alpinieri and W. Frost and Messrs. J. Ferrell, E. Bartlett, W. Lapson, O. Mehner and D. Knirck in addition to the Aerotherm supporting staff for their efforts and contributions to the accomplishments of the overall program objectives.

This report has been reviewed and approved by

Kenneth L. Gilbert, Lt. Col., USAF
Chief, Aero & Materials Division
Directorate of Systems Engineering
Deputy for Reentry Systems

Space and Missile System Organization, AFSC
Reentry Systems Division
Los Angeles, California 90009

ABSTRACT

The objective of the Nosetip Cooling Program (NCT) has been to develop engineering methods for designing discrete injection hardware based on a fundamental understanding of the complex mechanisms associated with heat and mass transfer over and within slotted surfaces. As a result, a series of experimental programs have been performed to identify the critical aerothermodynamic parameters associated with discrete injection transpiration cooling systems.

The major finding of the NCT Program has been the identification and quantification of the effective surface roughness due to slotted surfaces. This roughness gives rise to augmented heating levels, both locally and downstream, for injection flow rates of interest.

Correlations based on the experimental data and supporting analyses have been incorporated into a prediction technique which is utilized in the computation of discrete injection cooling requirements for arbitrary surface geometries and heating environments.

TABLE OF CONTENTS

Section	Title	Page
1	INTRODUCTION	1-1
2	PROBLEM REVIEW AND EXPERIMENT RECOMMENDATIONS	2-1
	2.1 Problem Review	2-2
	2.1.1 Questions Addressed in the Sensitivity Study	2-2
	2.1.2 Results of the Sensitivity Study	2-3
	2.1.3 Establishment of Technological Priorities	2-17
	2.2 Experiment Objectives and Requirements	2-17
	2.2.1 Internal Cooling Experiment	2-19
	2.2.2 External Cooling Experiments	2-19
	2.2.3 Combined Cooling Experiment	2-22
	2.2.4 Additional Remarks	2-22
	2.3 Assessment of NCT Program With Respect to the Original Problem Review and Experiment Recommendations	2-23
3	INTERNAL COOLING EXPERIMENT	3-1
	3.1 Experimental Apparatus	3-1
	3.2 Instrumentation	3-7
	3.3 Test Matrix	3-12
	3.4 Test Results	3-12
	3.5 Discussion of Results	3-24
	3.5.1 Single Phase Flow	3-24
	3.5.2 Two Phase Flow	3-24
	3.5.3 Concluding Statements	3-28
4	EXTERNAL COOLING EXPERIMENT	4-1
	4.1 Test Facility	4-1
	4.1.1 Scaling Considerations	4-1
	4.1.2 AEDC, Tunnel B, Test Facility	4-9
	4.2 Model and Test Hardware	4-11
	4.2.1 Models	4-11
	4.2.2 Support Assembly	4-19
	4.2.3 Flow Distribution System	4-19
	4.3 Instrumentation	4-25
	4.3.1 Heat Flux Instrumentation	4-25
	4.3.2 Pressure Taps	4-37
	4.3.3 Boundary Layer Probes	4-37
	4.3.4 Optical Instrumentation	4-43
	4.3.5 Operational Instrumentation	4-43
	4.4 Test Matrix	4-44
	4.5 Results	4-44
	4.6 Conclusions	4-78
5	COMBINED COOLING EXPERIMENT	5-1
	5.1 Facility	5-2
	5.1.1 Scaling	5-2
	5.1.2 Facility Selection	5-7
	5.1.3 Facility Specifications	5-9

Preceding page blank

TABLE OF CONTENTS

(Continued)

Section	Title	Page
	5.2 Models	5-11
	5.2.1 Design Guidelines	5-11
	5.2.2 Model Hardware Specifications	5-18
	5.3 Instrumentation	5-22
	5.3.1 Pyrometer: Average Surface Temperature at Injection Module	5-24
	5.3.2 Color Photography: State of Coolant Exiting Slots	5-25
	5.3.3 Infrared Photography: Injection Module Surface Temperature Distribution	5-26
	5.3.4 Vacuum-Deposited and Wire Thermocouples: Slot In-Depth Temperature Distribution	5-28
	5.3.5 Rotameters: Total Coolant Flowrate to Injection Module	5-29
	5.3.6 Metering Plates: Individual Slot Coolant Flowrate	5-29
	5.3.7 Gardon Gages: Downstream Heat Flux Distribution	5-31
	5.3.8 Opposite Wall Gardon Gages and Pressure Tops: Cold-Wall, No-Injection Heat Flux and Pressure Distributions	5-32
	5.3.9 Miscellaneous Instrumentation	5-32
	5.4 Test Matrix	5-33
	5.4.1 Overview	5-33
	5.4.2 Procedures	5-35
	5.5 Results	5-38
	5.5.1 Arc Heater Operating Conditions	5-38
	5.5.2 Test Section Cold-Wall Heat Flux and Static Pressure	5-40
	5.5.3 Thermodynamic and Fluid Mechanic Parameters at the Test Section	5-40
	5.5.4 Pyrometer and Slot Indepth Thermocouples	5-48
	5.5.5 Downstream Gardon Gages	5-64
	5.5.6 Photography	5-64
	5.5.7 Teflon Models	5-77
	5.5.8 Correlations and Comparison with Flight Data	5-77
	5.6 Summary and Conclusions	5-85
6	ANALYSIS PROCEDURE	6-1
	6.1 General Description	6-1
	6.1.1 Correlation Analysis	6-1
	6.1.2 Internal Cooling Analysis	6-14
	6.2 Data Comparison	6-18
	6.2.1 External Cooling Data Correlation Comparison	6-18
	6.2.2 Combined Cooling Data Correlation Comparison	6-18
7	APPLICATION STUDY	7-1
	7.1 Introduction	7-1
	7.2 Geometry and Environment Definition	7-2
	7.2.1 Nosetip Definition	7-2

7.2.2 Environment Definition 7-2
7.2.3 Wall Boundary Condition 7-2
7.2.4 Edge Conditions 7-3
7.3 Results 7-6
7.3.1 Previous and Current Technique 7-6
7.3.2 Results of Current Prediction Technique 7-11
7.4 Concluding Remarks and Recommendations 7-14

REFERENCES R-1

LIST OF FIGURES

Figure		Page
1-1	Schematic of Discrete Injection Concept	1-2
1-2	Discrete Injection Transpiration Cooled Nosetip Sections	1-3
2-1	Sonic Point Heat Transfer For Trajectory C Including Rough Wall Effects	2-1
2-2	Increase in Flow Rate Requirements Due to Roughness Augmented Turbulent Heating for Trajectory C	2-2
2-3	Stable Liquid Layer Thickness Over Sphere Cone For Continuous Injection as Calculated by BLIMPL	2-12
3-3	Schematic of Flow Loop	3-1
3-2	Mounting of Test Package in Pressure Vessel	3-2
3-3	Photograph of Finned Heat Exchanger and Cooling Jacket	3-3
3-4	Plenum Chamber and Manifold	
3-5	Fabrication of Slotted Plate	3-8
3-6	Junction Box in Test Package	3-9
3-7	Thermocouple at Exit Plane	3-11
3-8	Single Phase Data, Set 10 -- Runs 1 and 2	3-15
3-9	Temperature Distribution, Test 9 -- Runs 14-20	3-16
3-10	Temperature Distribution, Test 11 --Runs 12, 15, and 16	3-17
3-11	Consecutive Temperature Profiles During Oscillating Flow	3-19
3-12	Temperature at Station 1 Versus Time for Oscillating Flow	3-20
3-13	Single-phase Flow	3-21
3-14	Two-phased Dispersed Flow	3-22
3-15	Two-phased Globule Flow	3-23
3-16	Correlation of Heat Transfer Coefficient for Liquid Water	3-25
3-17	Comparison of Single Phase Pressure Drop With Aerojet Design Correlation	3-26
3-18	Comparison of The University of Tennessee Space Institute Computer Code Solutions With Data From Test 15, Run 1	3-29
4-1	Tunnel B Window Layout	4-3

LIST OF FIGURES
(CONTINUED)

Figure		Page
4-2	Apparent Roughness Due to Slots	4-4
4-3a	2.0/2.0 Model Without Filler Block	4-7
4-3b	2.0/2.0 Model With Filler Block in Place	4-8
4-4	Slot Model, Machining, 2.0 Slot/2.0 Land	4-12
4-5	Photo of Model Flow Surface as Cast	4-13
4-6	Photo of Model Backside as Cast	4-14
4-7	Slot Model Assy., 2.0 Slot/2.0 Land	4-16
4-8	2.0/2.0 Model in Preparation (Flow Surface)	4-17
4-9	2.0/2.0 Model Backside in Preparation	4-18
4-10	Support Ring	4-20
4-11	Schematic Of Flow Distribution Network	4-21
4-12	Flow Distribution Box Assembly	4-23
4-13	Leak Path Detail	4-24
4-14a	Heat Flux Recovery 2.0/2.0 Configuration Land 1 Maximum Flow Rate	4-26
4-14b	Heat Flux Recovery 2.0/2.0 Configuration Land 2 Maximum Flow Rate	4-27
4-14c	Heat Flux Recovery 2.0/2.0 Configuration Downstream Section Maximum Flow Rate	4-28
4-14d	Heat Flux Recovery 2.0/2.0 Configuration For Downstream Section - Maximum Flow Rate	4-29
4-15	Slot Model, Machining, 2.0 Slot/ .8 Land	4-31
4-16	Slot Model, Machining, 2.0 Slot/2.0 Land	4-32
4-17	Slot Model, Machining, 2.0 Slot/10.0 Land	4-33
4-18	Slot Model, Machining, 5.0 Slot/4.0 Land	4-34
4-19	Off Centerline Gardon Gage Mounting	4-36
4-20	Boundary Layer Probe Assembly	4-39
4-21	Detail of Boundary Liner Probe Mounting	4-40
4-22	Boundary Layer Probe Relative Locations	4-41
4-23	Comparison of Various Total Pressure Measurement Techniques	4-42
4-24	Wind Tunnel Interior With 2.0/10.0 Model Installed	4-47
4-25	External View of 2.0/10.0 Model During Test	4-48

LIST OF FIGURES
(CONTINUED)

Figure		Page
4-26	2.0/10.0 Model	4-55
4-27	5.0/5.0 Model	4-58
4-28	2.0/0.8 Model	4-61
4-29	2.0/2.0 Model	4-64
4-30	2.0/2.0 Model With Filler	4-67
4-31	Comparison of Heat Flux For Duplicate Test Conditions	4-70
4-31	Comparison of Heat Flux For Duplicate Test Conditions	4-71
4-32	Schematic of Transverse Gardon Gage Location	4-72
4-32	Transverse Arrays Without Blowing	4-73
4-33	Schematic of Transverse Gardon Gage Location	4-74
4-34	Configuration For Sensors In Slot	4-76
4-35a	Investigation of the Boundary Layer Behavior on the First Land of the 2.0/10.0 Model with no Blowing	4-79
4-35b	Investigation of the Boundary Layer on the Second Land (Downstream Section) of the 2.0/10.0 Model with No Blowing	4-82
4-35c	Investigation of the Behavior of the Boundary Layer Behavior at Two Points For Three Flow Rates.	4-85
4-36	Survey of Boundary Layer Behavior on First Land of the 5.0/5.0 Model Without Blowing	4-88
4-37	Detailed Profile on Initial Downstream Segment After Four Slots on 2.0/0.8 Model Without Blowing	4-91
4-38	Detailed Survey of Second Land on the 2.0/2.0 Model to Attempt to Trace Profile Development on a Fine Scale With No Blowing	4-94
4-39a	Baseline Transverse Profiles Without Blowing for the 2.0/2.0 Configuration With The Filler Block Mounted	4-97
4-39b	Transverse Survey Downstream of the Filler Block with Full Mass Injection.	4-100
4-40	Heat Transfer Distribution For 2.0/10.0 Case	4-103
4-41	Heat Transfer Distribution For 5.0/5.0 Case	4-104
4-42	Heat Transfer Distribution for 2.0/0.8 Case	4-105
4-43	Heat Transfer Distribution for 2.0/2.0 Case	4-106
5-1	Heat Transfer Simulation for Internal Cooling	5-4
5-2	Scaling of Land Surface Temperature	5-5
5-3	Scaling of Vaporization Depth	5-6

LIST OF FIGURES

(CONTINUED)

Figure		Page
5-4	Schematic of the Arc-Heated Turbulent Duct Facility at NASA Ames, with Aerotherm Model and Instrumentation in Position	5-10
5-5	Schematic of Combined Cooling Model Assembly	5-12
5-6	Combined Cooling-Flight and Ground Test Injection Surfaces	5-14
5-7	Combined Cooling Ground Test Hardware	5-19
5-8	Duct Wall Static Pressure Distributions	5-41
5-9	Duct Cold-Wall Heat Flux Distributions	5-43
5-10	Turbulent Flow Heat Blockage for a Flat Plate	5-47
5-11	Surface and Indepth Temperatures vs Total Injection Flowrate	5-49
5-12	Surface Temperature Vs. Margin Factor	5-62
5-13	Slot Indepth Temperatures vs. Depth Below Surface and Margin Factor	5-63
5-14	Downstream Heat Flux Distribution vs. Margin Factor	5-65
5-15	Normalized Downstream Heat Flux Distributions at $\tilde{M} = 4.5$	5-72
5-16	Normalized Downstream Heat Flux Distributions at $\tilde{M} = 1.0$	5-73
5-17	Combined Cooling-Color Slide Photography	5-74
5-18	Combined Cooling Infrared Photography	5-75
5-19	Land Temperature Distributions (from Infrared Photography)	5-78
5-20	Combined Cooling Comparison of Discrete and Porous Injection	5-82
5-21	Margin at T_D = 300°F Equivalent Sand Grain Roughness	5-83
5-22	Margin at Downstream Threshold Vs. Equivalent Sand Grain Roughness	5-84
5-23	Comparison of Combined Cooling Slot In-Depth Temperatures With Those From Flight Test	5-86
6-1	Schematic of Correlation Procedure	6-2
6-2	Downstream Cooling Effectiveness Correlation	6-10
6-3	Discrete Injection Blockage Factor Based on Slot Area	6-12
6-4	Discrete Injection Blockage Factor Based on Total Area	6-13
6-5	Internal Cooling Analysis Schematic	6-15
6-6	Internal Nodal Network Schematic	6-16
6-7	Downstream Cooling Effectiveness of External Cooling Experiment, 2.0/10.0	6-19

LIST OF FIGURES

(CONCLUDED)

Figure		Page
6-8	Downstream Cooling Effectiveness of External Cooling Experiment, 5.0/5.0	6-20
6-9	Downstream Cooling Effectiveness of External Cooling Experiment, 2.0/0.8	6-21
6-10	Downstream Cooling Effectiveness of External Cooling Experiment, 2.0/2.0	6-22
7-1	Coldwall Heat Flux Distribution	7-4
7-2	SAANT Predictions for Application Study	7-5
7-3	Aerospace/GE Q* Correlation	7-7
7-4	Coldwall Heat Transfer Distribution Over Aerojet Nosetip Used In Application Study	7-8
7-5	Mass Flow Distribution for Aerospace/GE Q* Correlation	7-9
7-6	Effects of Overcooling in Cap Region of Aerotip	7-10
7-7	ADICT Solution of Application Study	7-13
7-8	ADICT Solution of Application Study	7-15

LIST OF TABLES

Table		Page
2-1	Summary of Key Problem Areas and Priorities	2-18
2-2	Key Problem Areas Being Addressed In Each Experimental Series	2-20
2-3	Key Problem Areas Addressed In Each Final Experiment	2-25
3-1	Test Matrix	3-13
4-3	Coolant Flow Ranges	4-10
4-6	Heat Flux Sensor Location Summary	4-35
4-7	Run Schedule	4-44
4-8	Injectant Conditions	4-45
4-9	Test Summary, 2.0 in. Slot, 10.0 in. Land Configuration	4-50
4-10	Test Summary, 5.0 in. Slot, 5.0 in. Land Configuration	4-51
4-11	Test Summary, 2.0 in. Slot, 0.8 in. Land Configuration	4-52
4-12	Test Summary, 2.0 in. Slot, 2.0 in. Land Configuration	4-53
4-13	Test Summary, 2.0 in. Slot, 2.0 in. Land (Staggered Slot) Configuration	4-54
5-1	Slot/Land Configurations	5-15
5-2	Thermophysical Properties of Quartz	5-17
5-3	Summary of Measurements and Instrumentation for the Combined Cooling Experiment	5-23
5-4	Summary of Test Runs	5-34
5-5	Arc Heater Operating Conditions	5-39
5-6	Test Section Static Conditions and Recovery Enthalpy	5-45
5-7	Ideal Injection Flowrate	5-46
6-1	Test Program-Primary Objectives and Impact on Correlation Study	6-3
6-2	Experiment-Data Taken-And Impact	6-5
7-1	Summary of ADICT Predictions	7-12
7-2	Comparison of ADICT Total Coolant Flow Rate Prediction to Aerospace/GE Q* Correlation	7-12

LIST OF SYMBOLS

A	Area
B'	Blowing rate parameter
C_H, S_T	Stanton number
D	Diameter
E	Voltage
F	$\rho_w u_w / \rho_e u_e$
g	Gravitational constant
h	Heat transfer coefficient
H_T	Stagnation enthalpy
I	Current
k	Roughness height
K_r	$\dot{q}''_{w,r} / \dot{q}''_{o,r}$
ℓ	Film thickness
L	Land length
$\dot{m}''$	Mass flow rate ($lbm/ft^2/sec$)
M	Margin factor
N_u	Nusselt number

P_c	Chamber pressure
P_m	Manifold pressure
P_n	Nozzle pressure
p	Pressure
P_{t_2}	Body stagnation pressure
P_e	Peclet number
P_r	Prantl number
$\dot{q}''$	Heat transfer rate ($Btu/ft^2/sec$)
R_N	Nose radius
R_e	Reynolds number
s	Running length
S	Slot opening
W_e	Weber number
δ	Boundary layer thickness
Λ	Wave length
θ	Momentum thickness
θ_c	Cone angle
ρ	Density
η	Quality factor

Subscripts

e	Edge conditions
f	Fluid
g	Gas
l	Liquid
lg	Two phase
s	Stagnation conditions
∞	Upstream conditions
o	Cold wall conditions
r	With roughness

SECTION 1

INTRODUCTION

Transpiration cooled nosetips currently provide the only means of avoiding ablation-induced shape change of the nose region during reentry. Such nosetips provide protection by a) the injected coolant distorting the boundary-layer, causing a decrease in heat transfer to the surface and by b) absorption of heat through an enthalpy rise of the injected coolant. The former mechanism is termed blocking and exists due to thickening and boundary layer profile modifications induced by surface mass transfer. The injected coolant can be delivered to the surface through a porous matrix or discrete injection slots. It is pointed out that for the case of discrete injection, the blocking effect can be offset by roughness augmented heating, due to the surface configuration. This report documents the results of an investigation of the discrete injection concept.

Design and operation of discrete injection hardware is inherently more complex than that of porous hardware. The demonstrated desirable characteristic of operating at temperatures above saturation (References 1 and 2) and the lack of an understanding of the fundamental operating principles of discrete injectors were the primary motivating factor for this investigation.

Interest in the discrete injection (DI) transpiration cooled nosetip (TCNT) centers around the Aerotip, Reference 1, which nominally utilizes water as a coolant. Liquid coolants have the desirable advantage of low storage volumes, in comparison to gaseous coolants. An important feature of the DI concept is the manner in which the coolant is delivered to the surface. The flow metering is accomplished by a subsurface system consisting of manifolded channels that deliver the coolant to pods that are open to the surface. A schematic of this system is illustrated in Figure 1-1. Figure 1-2 contains photogarphs of flight hardware at various surface locations. Since the flow is metered in passages upstream of the pods, pod temperatures may exceed in saturation temperature, resulting in internal vaporization without disrupting the coolant flow. Therefore, in order to design DI nosetips the complex mechanisms associated with heat and mass transfer over slotted surfaces and internal heat transfer accompanied by phase change in narrow passages must be understood. In addition to the above problem

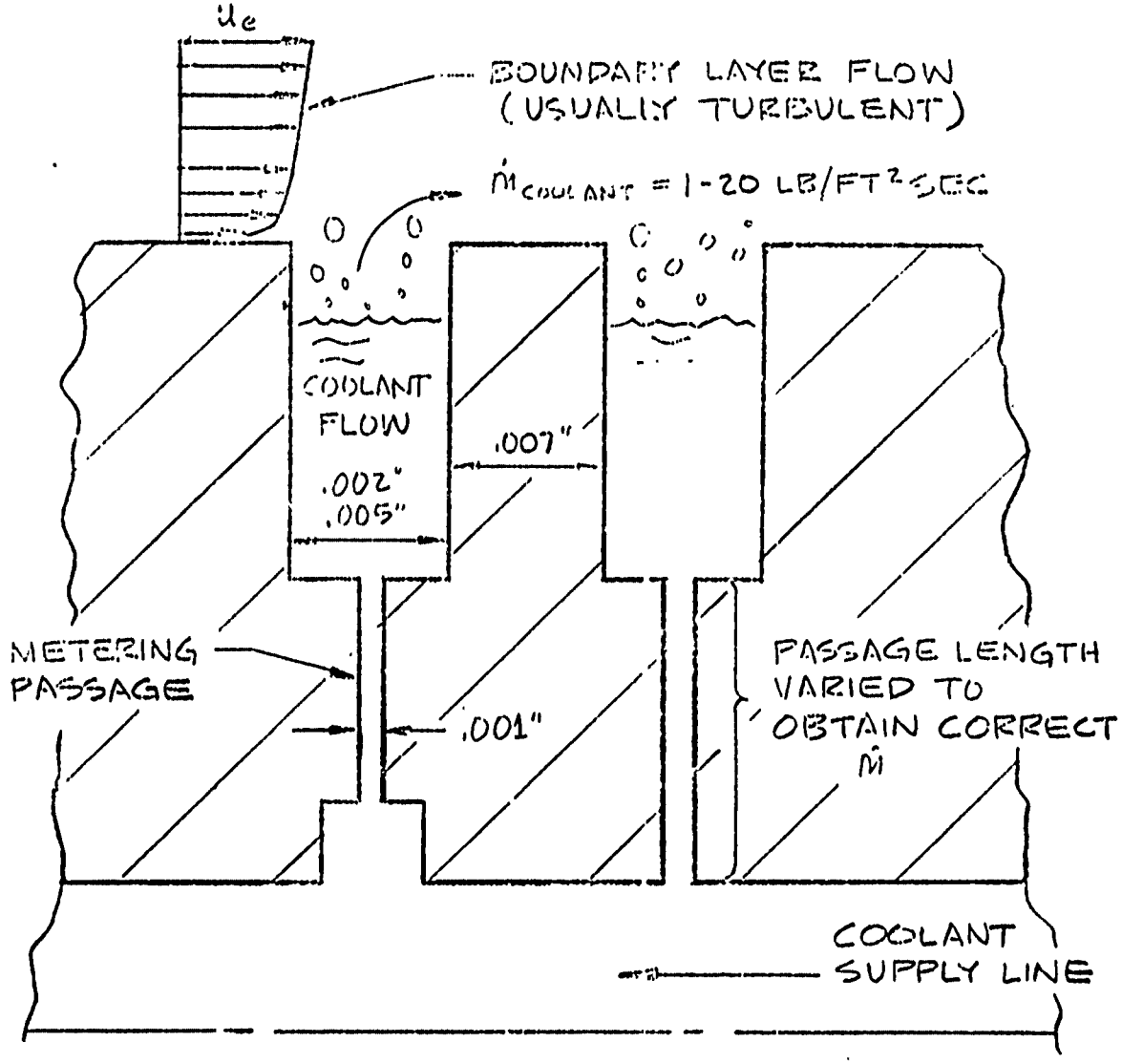

Figure 1-1. Schematic of Discrete Injection Concept

A-5326

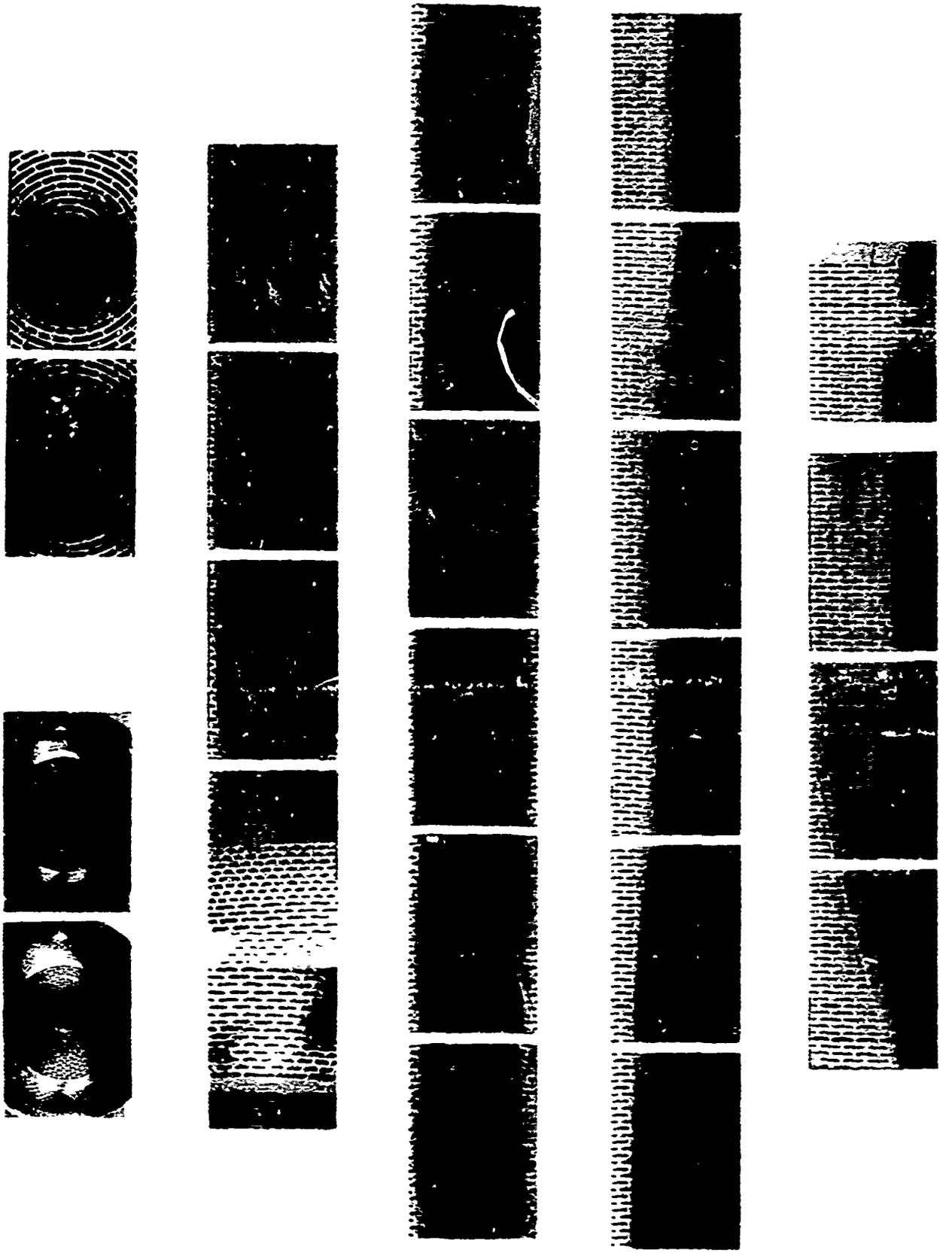

Figure 1-2. Discrete Injection Transpiration Cooled Nosetip Sections

areas uncertainties in the mode of operation of discrete injectors necessitates assessment of the potential for formation of protective surface liquid films and their stability in high shear and heat transfer environments.

The objective of this investigation has been to develop engineering methods for designing DI hardware based on a fundamental understanding of the aforementioned technology problem areas. The approach has consisted of analytic and experimental investigations required to provide the following information applicable to DI flight type water cooled nosetips:

a) Adequate engineering predictions of internal flow phenomena

b) Adequate engineering predictions of external, local and downstream flow performance

c) Adequate engineering prediction of combined internal and external fluid flow and heating phenomena.

In regard to items (b) and (c) the requirements included developing prediction techniques for the case of injection slot width to boundary-layer thickness ratios that range from values significantly less than to significantly greater than unity. It is noted that, excluded from the scope of this investigation were the following areas: i) the selection of coolants alternate to water; ii) the effects of downstream chemical reactions of the coolant with ablative heat shields; iii) coolant flow control, storage and expulsion systems for reentry vehicles; and iv) improved or novel TCNT concepts.

In order to maximize the output of the program relative to available resources an extensive problem review was carried out, resulting in a set of recommended experiments. The review considered all pertinent problem areas. Environmental effects including angle of attack were considered. Specific recommendations in regard to the need for the generation of analyses and data related to the pertinent problem areas were made and assigned priorities. The results of this study are documented in Reference 3. The priorities assigned to various items recommended for investigation were based on the state of knowledge at the onset of this program. As a result of new information generated during the program it became apparent that modifications were required in regard to the assigned priorities on certain items. The impact of new information on determining the relative importance of various technology areas is discussed in Section 2 of this report.

A theoretical study of liquid film formation, stability, and entrainment was conducted as part of this program and documented in Reference 4. Due to the complexities associated with this problem area, theoretical modelling cannot be applied to actual hardware. That is, at present the modelling is only

applicable to flow over very smooth surfaces under conditions of relatively low shear and low heat transfer rates. Hence, the treatment given in Reference 4 represents only a small step towards developing a model applicable to DI flight hardware. It is pointed out that the design surface temperature for existing hardware is above saturation values, that is, at temperatures above which liquids would be expected to exist. Furthermore, observations made during the combined cooling experiment, conducted during this program, indicate that liquid films are not present even at coolant flow rates substantially higher than design values.

The problem review resulted in the recommendation of five experiments, Reference 3, three of these were conducted, consisting of an internal cooling experiment, an external cooling experiment, and a combined cooling experiment.

The primary objective of the internal cooling experiment was to determine heat transfer coefficients in narrow passages for single and two phase flow. The approach was to provide a heat flux at the exit (downstream) location of rectangular channels and to measure temperatures as a function of mass flow rate for a fixed power input to the system. The environmental test plan containing a detailed description of the apparatus and test conditions for this experiment is documented in Reference 5 and experimental results are presented in Reference 6. The results of this study indicate that existing correlation techniques provide adequate predictions of heat transfer coefficients for flow in narrow passages. Photographic coverage revealed regimes of film boiling and nucleate boiling. Tests were conducted under conditions causing all liquid flow, mist flow, and liquid slug flow to exist at the slot exit. It is pointed out that during the combined cooling tests mist and slug flow were not observed under conditions at which these flow regimes existed during the internal cooling experiment. As was mentioned during the internal cooling experiment, heat was supplied only to the exit portion of the channel; however, during the combined cooling experiment, as would be the case in flight, heat is transferred to the area through which the coolant exists as well as to the channel bounding the exit area. Thus it can be inferred that these differences in boundary conditions apparently have significant effects on the heat paths, especially near the surface. Consequently, to simulate internal cooling phenomena it is necessary to have heat transfer across the slot exit area as well as to the channel.

The primary objective of the external cooling experiment was to obtain heat transfer data over slotted surfaces with mass transfer. Models having ratios of slot to land (distance between slots) and slot to boundary layer thickness varying from less than to greater than unity were employed. The tests were conducted in a hypersonic wind tunnel, under conditions yielding extremely thick

turbulent boundary-layers. Thus large slot and land distances were employed permitting the acquisition of detailed heat transfer distributions over lands. The models were water cooled and instrumentation included several gardon heat transfer gauges placed along the surface of lands. The environmental test plan, containing a detailed description of the test facility, models, instrumentation and test conditions is documented in Reference 7. Reference 8 presents the test results. The primary finding of this experiment was that slotted surfaces present effective roughness elements that significanlty augment heating rates in the vicinity of the leading edge of lands. These results strongly impact the analytic model developed to predict coolant requirements.

The combined cooling experiment was conducted in order to obtain data on a system in which external and internal heat transfer are operating simultaneously in a coupled mode. In this experiment discrete injection models were mounted in the duct wall of an arc. Slot and land values varied over an order of magnitude, beginning at values corresponding to those of existing flight hardware. In order to duplicate surface and in-depth temperatures, for the purpose of simulating internal heat transfer a low, relative to flight, conductivity material was employed, since test values of heat flux are significantly lower than reentry values. Stainless steel is currently used to fabricate flight hardware whereas quartz models were employed in the present experiments. Diagnostics consisted of in-depth thermocouples, downstream gardon gauges, a surface pyrometer, and infrared and color photography of the surface. The environmental test plan, which gives a detailed description of models, test facility, instrumentation and test conditions is documented in Reference 9. The results of the combined cooling experiments are contained in Reference 10. These results verified the roughness effect observed during the external cooling experiment and measured surface temperatures were predictable using standard channel heat transfer correlations for internal heat transfer.

The experimental data from the previously described experiments were factored into the development of an analytical model. Within the framework of this model internal heating are coupled. The model can be employed to predict the effects of material properties and geometric configuration. That is, in principle the model can be applied to predicting performance of DI hardware fabricated of arbitrary materials and having arbitrary slot and land dimensions. The model predicts surface temperature as a function of coolant flow rate for a specified environment. The resulting model was applied to predicting coolant requirements for a nosetip in environment producible by the Edwards RPL rocket facility. The results were then compared to those using previously existing design techniques given in Reference 1. Differences in predicted coolant requirements were not large. However, it is pointed out that the nosetip used

in this study is precisely that for which the methods described in Reference 1 were developed. That is, the previously existing design procedure was applicable only to specific hardware. The technique was based on an effective heat of ablation, Q^*. This approach does not model the essential fluid mechanics and heat transfer mechanisms and is thus strongly suspect when applied to predicting performance at conditions other than those for which the data upon which Q^* is based. The present model is considerably more general and hence can be employed in optimization studies as well as for predicting coolant requirements for a specific piece of hardware.

The remainder of this report summarizes the significant findings of this investigation. Detailed descriptions of various aspects of the program can be found in References 4 through 10.

SECTION 2

PROBLEM REVIEW AND EXPERIMENT RECOMMENDATIONS

The purpose of this section is to summarize the findings documented in Reference 3. The study of Reference 3 was carried out in the first phase of the NCT program in order to identify discrete injection phenomena which were not well understood at that time. Having defined the technologically weak areas of interest, a series of NCT experiments was then recommended which would provide the data required to improve the state-of-the-art of discrete injection technology.

It was determined that the two most important areas of uncertainty were the following:

1. Internal cooling capabilities -
   To what extent does subsurface vaporization of the coolant occur, since this determines the phase of the coolant as it exits the slots which, in turn, has a large influence on external cooling capabilities?
2. External heating environment-
   To what extent does roughness-augmented heating occur for gas, liquid, and two-phase injection?

To answer these questions, a series of five experiments was proposed.

1. An internal cooling experiment, to study heat transfer phenomena to liquid coolant in small slots.
2. Three external cooling experiments:
   a. Sphere/cone model in a wind tunnel with gas injection, to study gas film cooling effectiveness with discrete injection.
   b. Large slot model in a wind tunnel with liquid, gas, and two-phase injection to obtain fundamental data on roughness heating phenomena.
   c. Sphere/cone model in a rocket exhaust with liquid injection, to study liquid layer phenomena.

3. A combined cooling experiment, to study the interaction and net efficiency of internal and external cooling phenomena.

In the remainder of this section, the Problem Review and Experimental Recommendations are discussed in greater detail. In addition, the original review and recommendations, as presented in Reference 3, is compared with NCT program which actually evolved.

2.1 PROBLEM REVIEW

The problem review consisted of two major parts:

- A sensitivity study, performed with existing analytical tools, to identify the critical parameters associated with discrete injection transpiration-cooled nosetips (DI-TCNT) and to determine the sensitivity of coolant flowrate requirements to uncertainties in these parameters.
- Establishment of technological priorities, based upon the results of the sensitivity study, which could be used to design relevant experiments.

2.1.1 Questions Addressed in the Sensitivity Study

The critical design of DI-TCNT under severe reentry conditions requires that a number of phenomenological questions be answered. A synthesis of a large number of considerations resulted in the formulation of the following six key questions:

1. What effects does the DI-TCNT hardware and liquid or gas injection have on boundary layer transition?
2. Under what conditions can vaporization in-depth be tolerated?
3. Why are multiples of ideal injection rates required in ground tests and what multiples are needed in flight?
4. If the fluid is injected as a liquid, under what conditions can a liquid layer be depended upon for protection?
5. What degree of downstream cooling is provided by the DI-TCNT?
6. What are the consequences of operating at angle of attack?

In order to obtain answers to these questions, a variety of calculations was performed. These analyses and their results are summarized briefly here. Detailed solutions are contained in References 4, 11 and 12.

The primary types of analyses which were performed included:

1. Solutions for environmental parameters and local boundary layer edge conditions for three trajectories using the modified COCAN computer code (Reference 13).
2. Laminar/turbulent boundary layer solutions for continuous injection and for discontinuous slot/land/slot/land flows using the BLIMP computer code (Reference 14).
3. Liquid layer solutions for continuous injection and for slot/land slot/land flows using the BLIMPL computer code (Reference 15).
4. Two-dimensional and simple one-dimensional in-depth conduction solutions of the lands.
5. Solutions for the effects of rough walls on boundary layer transition and turbulent heat transfer rates using correlations developed under PANT (References 16 and 17).
6. Downstream heat shield ablation solutions using the COCAN computer code.

Further details of these solutions will become evident as they are discussed below in relation to the above questions. In addition to these analyses, extensive literature reviews were performed in the areas of internal flow phenomena (Reference 4), the liquid layer phenomena (Reference 12), boundary layer separation and reattachment in flow over cavities, and transpiration and film cooling studies.

2.1.2 Results of the Sensitivity Study

2.1.2.1 Boundary Layer Transition

The smooth and rough wall transition criteria* developed to date under PANT (Reference 16) were applied to Trajectory C** for assumed roughness heights of 0.1, 1.0, and 5.0 mils. The first value is representative of roughness which might be associated with a liquid layer surface (see Section 2.1.2.4); the second with a 5 mil slot with separation and reattachment on the lip of the land.

Transition for a smooth wall was predicted to progress up the TCNT skirt towards the nose as the altitude decreased from 28 to 5 kilofeet. Roughness causes transition to occur first in the nose cap region, but allows a potential

---

* Rough wall augmented heating is discussed in Section 2.1.2.3.B.

** The trajectories referenced in the Statement of Work for the NCT program are referred to in this document as Trajectories A, B, and C, respectively.

for reliminarization on the skirt. The transition altitude in the stagnation region is 76 kft for the 1 mil roughness. Discrete mass injection would tend to destabilize the boundary layer even further. Since peak heating tends to occur at substantially lower altitudes, it was deemed not excessively conservative to design for all-turbulent flow. Therefore, transition tests under the NCT program were assigned a low priority.

2.1.2.2 Indepth Vaporization and Limiting Heat Flux to the Land

In order to answer the question of in-depth vaporization, a series of two-dimensional conduction solutions was generated (Reference 12) to determine limiting heat fluxes under various internal flow conditions considering a steel land 7 mils wide and assuming an upper temperature limit for steel of 1800°F. Resulting values of limiting heat fluxes for various film coefficients are tabulated below

h Btu/hr ft^2 °F	$\dot{q}_w$ Btu/sec ft^2
10	400
100	1,300
1,000	4,000
10,000	11,000
100,000	25,000

Values of steady state laminar flow* heat transfer coefficients for 5 mil slots are about 3700 for liquid water and 270 for steam (Reference 12) corresponding to limiting heat fluxes of 7,500 and 2,000 Btu/sec ft^2, repsectively. Typical nucleate boiling heat transfer coefficients can be as high as 300,000 Btu/ft ft^2 °F. If such values were realized, a heat flux of 30,000 Btu/sec ft^2 could be accomodated. However, classical nucleate boiling was not anticipated in thin slots since this involves the growth and collapse of bubbles and typical bubble sizes are much larger than the available space in a 5 mil slot. Tests in resistance heated capillary tubes (Reference 18) suggest that a distinct liquid-gas interface forms resulting in a high (but not as high as nucleate pool boiling) h over a very small region with considerably reduced h on both sides, corresponding to liquid and gas flow, repsectively. However, with heating of the surface of the land (rather than volume heating) this interface may oscillate.

Thus, in order to accomodate heat fluxes above 7500 Btu/sec ft^2, it is necessary to achieve in-depth vaporization, but little is known of the nature of

* The Reynolds numbers in the channel are sufficiently low that laminar flow would be expected.

two-phase flow and resulting film coefficients for the minute channels of interest. Operation with vaporization in depth also requires better information on nonequilibrium evaporation and the nature of the liquid entrained in the fluid which could be a fine mist or could represent relatively large droplets "pumped" out of the tube by two-phase flow instabilities. These phenomena are also discussed further in Reference 12.

Based upon the preceding discussion, important goals of the NCT program included measurement of film coefficients for minute passages including two-phase effects, determination of flow instabilities due to channel blockage by bubbles, measurement of two-phase nonequilibrium in the flow passages, and determination of the sensitivity of the "nucleate boiling regime" to flow conditions.

2.1.2.3 Margin Factor Requirements

There are a number of possible causes for the requirements for multiples of ideal flow rates* to protect a DI-TCNT. The major causes for the need for excess coolant which were identified were entrainment, rough wall effects, and the effects of discontinuous injection.

A. Entrainment

In the ideal case of liquid injection, sufficient liquid is injected from a slot to protect the land immediately downstream of the slot. The local flow rate out of the slot is, of course, higher than the ideal flow rate based on continuous injection since the fraction of open area is less than unity. The excess fluid would ideally flow over the land and be depleted by vaporization at the end of the land. If a continuous liquid layer were desired with finite thickness everywhere, higher liquid injection rates would be required since fluid is carried downstream by aerodynamic shear. This would be necessary if liquid downstream cooling were desired. Furthermore, higher flow rates are required if any liquid is entrained in the gas boundary layer. This very likely event is discussed in Section 2.1.2.4.

B. Wall Roughness Effects

When a boundary layer flows over a rough surface, the heat transfer rate is augmented relative to that for a smooth wall. From a global point of view this means that a rough wall has a higher efficiency for transmitting available energy in the freestream to the wall. Locally, the increased heating is the result of boundary layer separation and reattachment. In the case of DI-TCNT substantially increased heating rates would be expected on the "forward facing step" of the land and on the surface of the land. This separation/reattachment

* In general, the ideal flow rate is that amount of coolant necessary to maintain a specified wall temperature assuming a smooth wall and continuous injection. Later in this report, for comparison purposes, the wall temperature assumed in this definition is the water saturation temperature at local pressure.

phenomena is affected by gas addition from the slots, there being an optimum flow rate which effectively elliminate boundary layer separation. Based on the gas injection results of Nicoll (Reference 19) the optimum flow rate is substantially higher than injection rates for DI-TCNT except when the percent open area becomes very small. For still higher injection rates, the injection jets would themselves act as roughness elements. Liquid injection, on the other hand, would be expected to "smooth out" the mechanical roughness elements and decrease the rough-wall heating effect somewhat.

In order to develop a quantitative global assessment of rough-wall heating augmentation, the correlation developed by Powars under PANT (Reference 17) was applied to the three reference trajecgories. The augmented sonic point turbulent heating rates for Trajectory C are presented in Figure 2-1 for several assumed roughness heights and are compared to laminar heating rates and to heating rates for a totally rough wall ($K_r = \dot{q}''_{w_{rough}} / \dot{q}''_{w_{smooth}} \approx 3$). The increased heating rates are related directly to increased flow rate requirements. The corresponding margin requirements attributable to roughness are presented in Figure 2-2. A second rough-wall heating correlation due to Welsh (Reference 20) is also shown in Figure 2-2. The margin approaches values of 3 with the Welsh correlation and values of 1.5 with the Powars correlation for one mil roughness. The effect of a 0.1 mil roughness element is seen to be negligible with both correlations. This is significant since roughness associated with liquid layers would be expected to be of this order (see Section 2.1.2.4).

In summary, rough wall effects were considered to be important. Furthermore, it was felt that a quantitative assessment of the effective roughness of injection geometries with mass injection must be determined by experiment. Acquisition of two types of data was recommended: global data for heat transfer to a DI-TCNT sphere cone model with and without gas injection, and local data for heat transfer to slots sufficiently large to obtain heating distribution data, again with and without mass transfer. In both cases, flight values of K/θ were recommended (where, for instance, K can be taken as 20 percent of the slot width, consistent with boundary layer separation data). The former data would be directly useful in flight design codes, whereas the latter would provide a better fundamental understanding of rough wall effects wtih discontinuous gas injection and improve the reliability of extrapolating to flight.

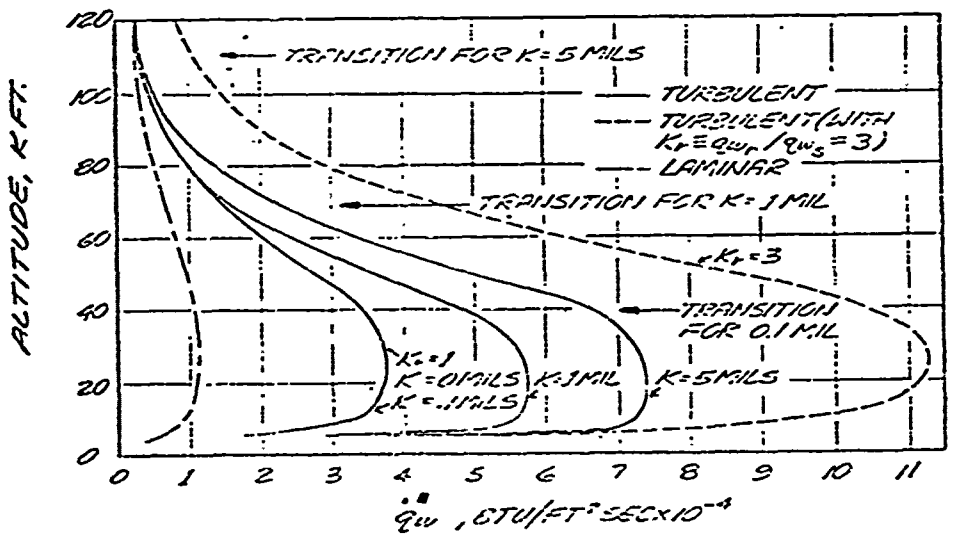

Figure 2-1. Sonic Point Heat Transfer for Trajectory C Including Rough Wall Effects.

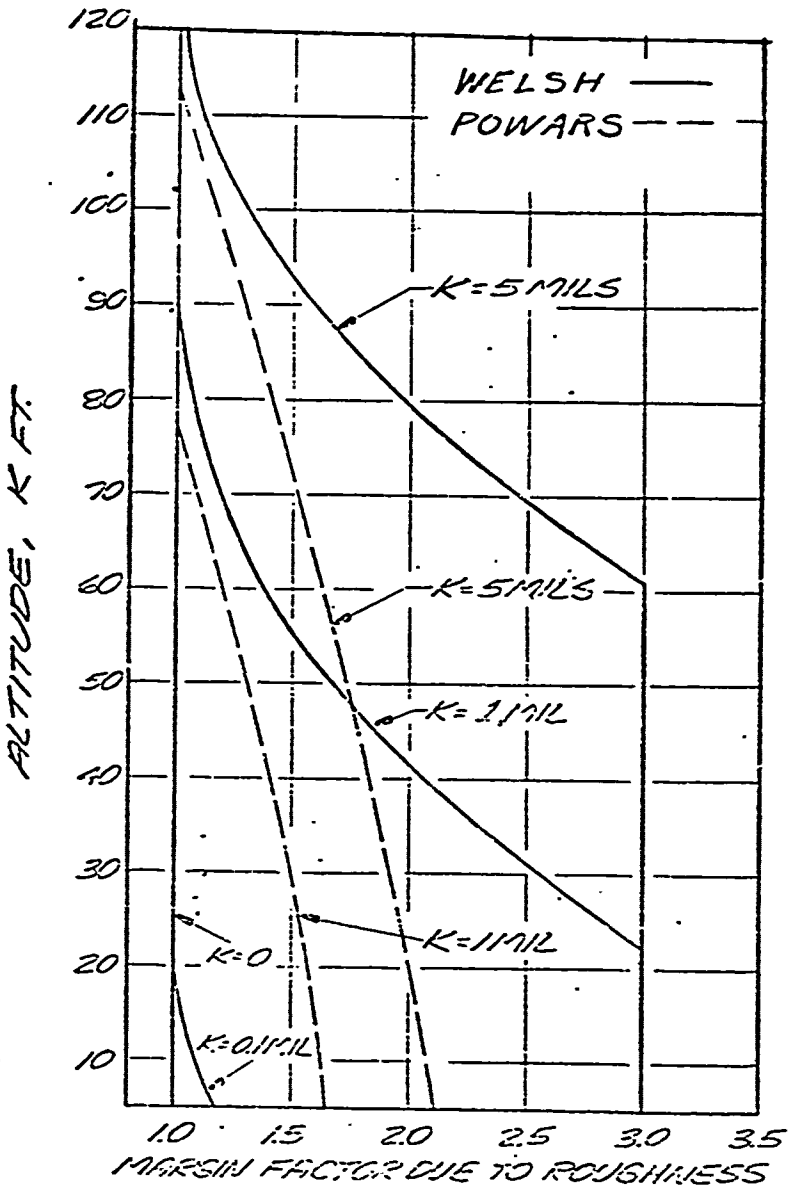

Figure 2-2. Increase in Flow Rate Requirements Due to Roughness Augmented Turbulent Heating for Trajectory C.

C. Discontinuous Injection Effects

In the problem review it was reasoned that the DI-TCNT approach would most likely require a margin factor in the case of gas injection if external cooling were to be relied upon because of the basic inefficiency of discontinuous injection. Because the percent of open area is less than 100, overcooling must always exist in the near vicinity of the slot. The excess coolant cannot be transferred with 100 percent efficiency to the downstream land because coolant injected far into the boundary layer does not have a chance to fully contribute to cooling the land. This phenomena was studied through a series of discrete injection boundary layer solutions generated with the BLIMP code (Reference 14). Solutions were generated for the stagnation region for several flight conditions and for several positions around the body for a single "peak heating" flight condition (20,000 ft/sec at 30 kft altitude corresponding to P_{t_2} = 163 atm, H_T = 8,000 Btu/lb). Solutions were also generated for typical wind tunnel conditions for water vapor injection, air injection, and CCL_4 injection. A detailed discussion of these solutions, including graphical presentation of predictions, is available in Reference 1.

The principal results of the BLIMP calculations of discontinuous injection effects are summarized as follows:

1. Margin factors of 4 to 10 are required to maintain the steel surface below its melting point for an adiabatic land (no internal cooling) immediately downstream of a 5 mil slot.

2. Large margin factors are required if little heat flux can be accommodated internally, but M $\doteq$ 1 - 2 would be possible of operation with evaporation on the slot walls were possible, since considerable energy is accommodated internally and the blockage requirement is reduced to the level where film cooling is adequate.

3. Isothermal heat flux and adiabatic temperature recoveries are basically the same for different flight conditions relative to the zero-injection heat flux and adiabatic wall temperature, respectively. However, the fraction of energy which can be accommodated internally is increased for less severe flight (or ground test) conditions and actual margin requirements due to discontinuous injection are reduced accordingly. This was significant in considering the merits of alternative test facilities for the Combined Cooling tests. In particular, a high pressure rocket facility was judged to be superior to low pressure rocket or arc facilities, since heat transfer rates in the former are greater than the limiting heat flux while they they tend to be lower in the latter such that an inordinate (and therefore misleading) amount of internal cooling can be realized without melting

the lands. (However, as described in Section 5, this problem can be alleviated by using a model with lower thermal conductivity than the flight value in a low-heat-flux ground test).

4. Blowing rates due to natural vaporization of water in a wind tunnel are very low with the consequence that gas injection rates 20 to 40 times greater than ideal are needed to match downstream cooling effects encountered in flight. Simulation can be achieved by injecting a gas (e.g., air) while matching the blowing rates of flight. It can also be obtained by natural vaporization by injection a liquid such as CCl_4 with appropriately low heat of vaporization. BLIMP calculations for discrete injection in a wind tunnel were made for water, air, and CCl_4 to quantify these conclusions.

5. At positions around the body S/L is no longer important from a downstream cooling point of view. Instead, the important parameter is the total integrated mass flux upstream of the land normalized by the land length, $\int_0 \dot{m}\, dx/L$. The S/L ratio is important from the standpoint of internal energy accommodation, however. The choice of optimum S and L must consider not only downstream cooling and internal energy accommodation, however, but rough wall and liquid layer formation and entrainment effects. Tradeoffs between discontinuous injection, internal cooling and rough wall heating were performed and are presented in Reference 11.

6. Margin requirements at the sonic point (turbulent flow) considering downstream cooling of the land and internal cooling are similar to those at the stagnation point since the benefit of a long running length of injection is offset by the increased heating rates.

7. At positions on the skirt downstream of the tangent point, the situation improves considerably (at least at zero angle of attack) because the running length of injection is increased and the heating rates are reduced. Thus, the possibility of operating with vaporization in-depth is greatly enhanced at positions on the skirt and operation with margin factors approaching unity may in fact be realizable without reliance on a liquid layer or significant gas film cooling.

D. Margin Factor Requirements - Summary

This portion of the problem reviews revelaed several phenomena which can combined to produce margin factor requirements. Basically, extra coolant is required when heating rates are increased dur to rough walls, when heat fluxes are sufficiently high that substantial internal cooling is not possible without burnout, and because of inefficiencies in downstream gas film cooling or in laying down a continuous liquid film.

2.1.2.4 Liquid Layer Phenomena

In the event that a continuous liquid layer forms in flight, it will be extremely thin. To demonstrate this result for a stable (no entrainment) liquid layer about a sphere cone (R_N = 1/2", θ_c = 7°), Figure 2-3 is presented for the same "peak heating" condition described previously for multiples of ideal flow rates of 1.1, 2, and 4. These solutions were generated with the BLIMPL computer code (Reference 15) which treats the liquid layer differential equations in detail and considers equilibrium vaporization at the outer surface. The liquid layer thickness at the end of each land is zero for ideal injection (margin of 1.0). A margin of 2 is seen to yield a thickness of 0.1 mil in the stagnation region which increases to 0.4 mils at an S/R_N of 5. A solution is also shown in Figure 2-3 for M = 2 for downstream liquid layer thickness with liquid injection terminated at an S/R_N of 2.4. The thickness is seen to hold nearly constant at 0.3 mils even though the surface is vaporizing and the liquid is expanding over a cone. Thus these thinning mechanisms are balanced by the thickening mechanism of decreasing shear and thus decreasing interfacial velocity.

An investigation of liquid layer formation and entrainment mechanisms as related to the proposed NCT experiments (Reference 12) yielded the following major conclusions:

1. Present analyses of liquid layer formation and stability have serious shortcomings which obviate their direct use in support of experiment definition. However, they do suggest scaling parameters as will be discussed below.

2. Experiments related to wetting, droplet formation and entrainment have primarily been conducted at low speeds and are not directly relevant to the NCT application. Those few high speed experiments which have been conducted have serious shortcomings which defeat their utility as well.

3. Wetting is typically a serious problem in liquid film experiments extreme caution being needed to ensure a liquid film. The dominant mechanisms governing liquid layer formation and surface wetting suggest the important parameters to scale are Reynolds number and Weber number based on liquid film thickness, ℓ, surface contact angle (this requires the same liquid, surface material and contamination), and thickness ratios ℓ/S and ℓ/L where S and L are the slot and land widths, respectively.

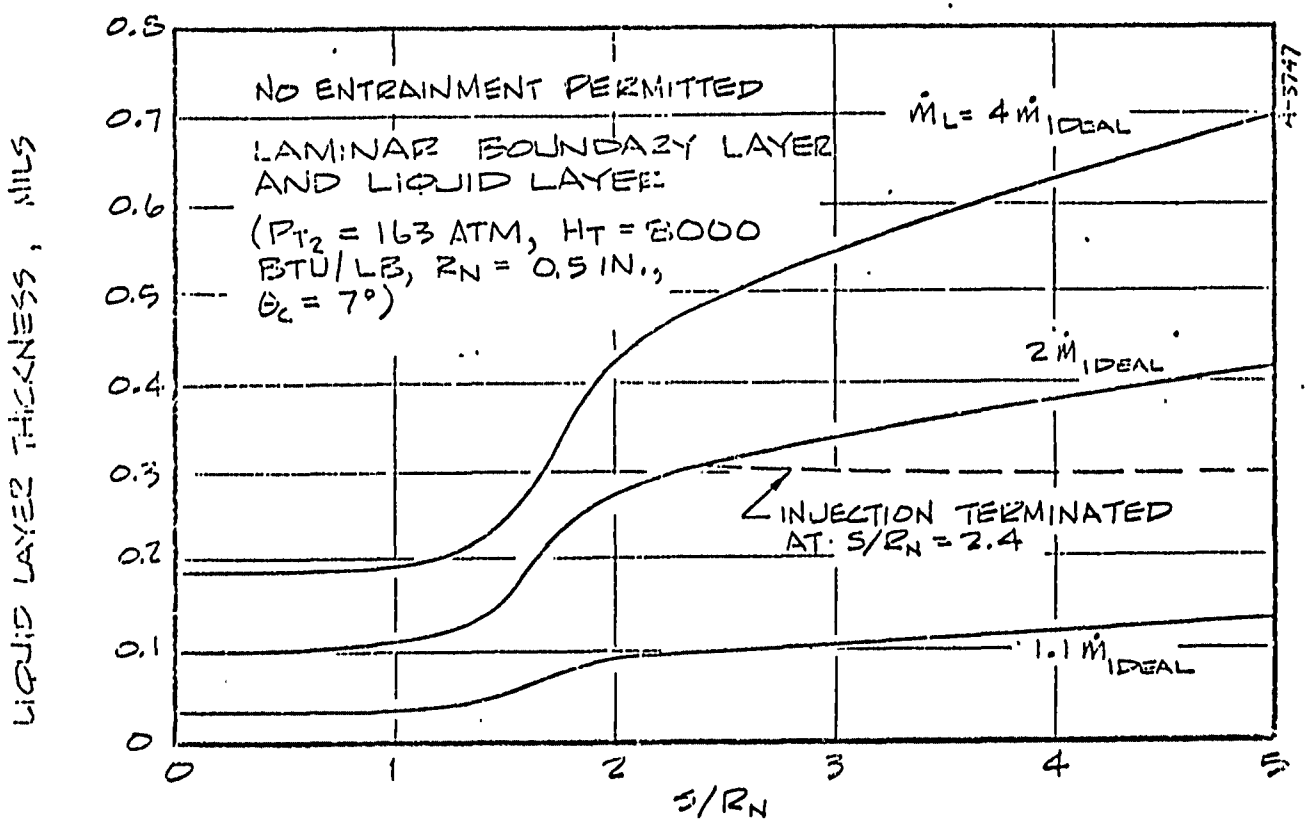

Figure 2-3. Stable Liquid Layer Thickness Over Sphere Cone for Continuous Injection as Calculated by BLIMPL.

4. Entrainment would be expected to be proportional to the liquid Weber number where the proportionality constant depends only on external aerodynamic properties such as Mach number. The correlation of Gater (Reference 21) is dimensional and there is no valid way of applying it to the TCNT problem. High speed experiments are needed where entrainment is accurately measured and related to aerodynamic properties to determine the proportionality factor in the above expression. Perhaps the most enlightening experiments on entrainment are those of Cresci and Starkenberg (Reference 22) who tested sphere cones with water injection through a porous wall at Mach 8. They obtained large entrianment yet the liquid surface appeared to be smooth! This suggests that the bulk of the entrainment occurred during the formation of the layer. This is consistent with the supersonic sphere cone results of Gold, et al., (Reference 23) who carefully layed down a layer and then observed little or no entrainment, and the results of Hermann, et al., (Reference 24) who injected normally through a slot and needed very large multiples of ideal to establish a liquid film.

5. Based on available experimental data, wave amplitude can be taken as $\ell/2$ where ℓ is the film thickness, and wave length can be estimated as $\Lambda = 2\ell\ Re/We$ where Re and We are liquid Reynolds number and Weber number based on ℓ.

6. Because of the high heating rates to the liquid surface, thermal instability of a dry patch which may form may be a potential problem.

7. No films appear to have even been observed in ground tests which approach the thinness of liquid films predicted in flight. However, the situation is complicated as the layer thickness can be the same order as scratches on the surface of the lands.

8. In the event liquid enters the boundary layer as a mist in the near vicinity of the slot (or is entrained downstream) there is a potential for enhanced film cooling of the land (or of the downstream region) due to droplet vaporization. This problem was studied analytically in Reference 25. Some beneficial effect was noted but the results are inconclusive. In the event that a liquid layer is not possible, and that gas film cooling indeed requires very large margins, mist flow with subsequent droplet evaporation could prove to be the basic cooling mechanism in the vicinity of the land. Hence, it should be studied experimentally under the NCT program.

In conclusion, the current state of technology was found to be incapable of determining if, how, or when a liquid film will form over a flight vehicle. The available high speed data does not simulate all of the correct parameters nor are there adequate procedures for extrapolation to flight. However, experience gained in ground facilities usually has shown that it is very difficult to lay down a liquid film. While this difficulty would probably he enhanced in the flight environment due to the presence of very thin layers and surface irregularities, it may be reduced by the presence of high shears. There appears to be no entrainment correlation applicable to flight if a liquid layer does lay down. Also, little information is available on the injection of a mist into a boundary layer. Thus, it was felt that well planned experiments which a addressed the liquid layer formation and entrainment problems while simulating the proper parameters (identified above and in more detail in Reference 12) were urgently needed.

2.1.2.5 Downstream Cooling

In the critical design of a DI-TCNT, it is necessary to know to what extent the tip will provide film cooling to the downstream heat shield since this influences the DI skirt length requirements. Small decreases in heat shield ablation due to downstream cooling can permit use of substantially shorter DI skirt.

To assess this effect a series of calculations was performed for gas film cooling using the BLIMP code. Also, ideal liquid film characteristics (i.e., with vaporization but not entrainment) were calculated with the BLIMPL code. As discussed in Section 2.1.3.4, the present state-of-the-art in liquid entrainment analyses on sphere cones under flight conditions is not adequate to permit realistic calculation of non-ideal liquid layer characteristics.

All calculations for an adiabatic wall downstream of injection on a sphere cone resulted in a very rapid rise in temperature, followed by a very gradual decay to the zero-injection adiabatic wall temperature. Also, in all cases a substantial cooling effect was seen for several inches downstream. Heat flux recovery to an iosthermal downstream wall was also calculated. The predicted heat flux was substantially reduced (compared to local values with no upstream injection), especially for a margin factor of 2. Reference 3 presents a detailed discussion of these calculations.

Ideal liquid layer lengths (i.e., vaporization but no entrainment) were also calculated for several combinations of DI-TCNT skirt lengths and margin factors. Entrainment could increase flow rate requirements substantially. Heat flux recovery downstream of the liquid was also calculated. It was

predicted that appreciable additional gas film cooling is provided by the water vapor which enters into the gas-phase boundary layer by vaporization of the upstream liquid surface.

As a final downstream cooling consideration, heat shield ablation calculations were made with the PANT version of the COCAN computer code (Reference 13) to determine DI-TCNT skirt lengths required in flight for the 3 reference trajectories including their respective angle-of-attack histories. Calculations were performed at a 7° cone with 1/2 and 1 inch nose radii for carbon phenolic and silica phenolic. The total ablated depth plus final insulation requirement to maintain an 360°R back wall temperature (including a 30 percent safety factor) was calculated. It was found that the TCNT skirt can terminate at an S/R_N of 1 to 2 except for silica phenolic with a 1/2 inch nose radius where S/R_N of 2 to 6 are required. These data indicated the span of DI lengths of interest for experimental evaluation. In particular, it was recommended that downstream cooling data should be obtained for a skirt which extends to an S/R_N of about 4 and for a skirt which terminates in the vicinity of the sonic point, where the downstream cooling phenomena may be fundamentally different due to the severe pressure gradients.

2.1.2.6 Angle-of-Attack Effects

The effects of angle of attack fall into three major categories:

1. Local effects in the nose cap region
2. Local effects on a DI-TCNT skirt
3. Effects downstream of the DI region.

Angle of attack introduces no new fundamental phenomena in the nose cap region with the exception that the critical stagnation point is moved to different positions on the nose and the slots are oriented differently to the flow. The major consequence of this latter consideration is that a circumferential pressure differential exists along a single slot when flying at angle of attack. Calculations were performed which show that a differential of 1 atm can exist along a slot with the current Aerotip design.

With regard to a DI-TCNT skirt or nose cap, it is of course necessary to meter the coolant circumferentially around the tip to avoid extensive overcooling on the leeward side. Also, it is necessary to calculate the local flow conditions and heating rates to determine the ideal flow rate and margin requirements. The major effect of angle of attack on a DI skirt is that the heating rates on the windward side of the skirt remain sufficiently high that the prospect of internal cooling is unlikely. For sample, at 20° angle of attack, data of

Widhopf (Reference 26) suggest that windward side turbulent heat transfer rates continue to increase with distance down the skirt at S/R_N up to 5 and above. Thus, it may be necessary to provide high margins on the windward side to obtain a liquid film on the surface or adequate downstream film cooling on the lands to block the major fraction of the cold wall heat flux. This implied that sphere cone tests at angle of attack in a high heat flux environment such as a high pressure rocket would be essential in order to critically design a DI-TCNT for angle of attack with confidence.

The primary effect of angle of attack on downstream cooling is, again, not a change in the fundamental phenomena associated with gas film cooling and liquid layer vaporization and entrainment, but alternation of the basic gas and liquid boundary layers. In other words, given the ability to calculate three-dimensional boundary layers, the correlations for gas film cooling effectiveness, entrainment, etc., could be applied directly with reasonable confidence. However, such codes are not available. The state-of-the-art in calculating three dimensional boundary layers neglects cross flow within the boundary layer and treats streamline spreading using the axsymmetric analogy or (usually) the effective cone approach. These approaches work quite well for angles of attack up to the body half angle but are less accurate thereafter. These limitations implied the need to obtain downstream liquid and gas film cooling data on sphere cones at angles of attack in order to validate state-of the-art analysis techniques and to provide data for use in flight design.

2.1.3 Establishment of Technological Priorities

The results of the problem review are summarized in Table 2-1, which addresses those technology items judged, at the beginning of the NCT program, to be potentially critical to the successful design of discrete injection TCNT Each individual technology item is identified, the importance of the item is presented, the current state of technology and curret design techniques are reviewed, the need for experiments is identified, and the priorities for performing these experiments under the NCT program are established. "Current State of Technology" represents the capabilities current at the beginning of the NCT program. "Current Design Techniques" are the approaches which would have been used at that time to design DI-TCNT flight hardware. A major objective of the NCT program was to incorporate available technology, with additional data to be generated under the program, into an improved engineering design procedure The specific types of experiments which were recommended and their objectives and requirements are presented in Section 2.2 below. In Section 2.3, an assessment is made of the degree to which the completed NCT program has addressed each of the key problem areas designated in Table 2-1.

2.2 EXPERIMENT OBJECTIVES AND REQUIREMENTS

The problem Review identified several key problem areas where the current information base was inadequate to critically design DI-TCNT with confidence. The technology base for these problem areas was determined, and the priorities for performing experiments and analyses established.

It was confirmed that NCT program objectives could best be met by performing three basic types of experiments: internal cooling, external cooling, and combined cooling. In summary, the following test series were recommended.

1. Internal Cooling -
   Experiments with no external flow where heating is provided to the surface with water used as the coolant
2. External Cooling -
   a) Experiments with a sphere cone at zero and non zero angle of attack in a wind tunnel with gas injection.
   b) Experiments with simple large slot models in a wind tunnel with gas, liquid, and two-phase injection.
   c) Experiments with a sphere cone in a high pressure rocket exhaust with water injection.
3. Combined Cooling -
   Experiments with wedge models in a high pressure rocket exhaust with water and two-phase injection.

TABLE 2-1
SUMMARY OF KEY PROBLEM AREAS AND PRIORITIES

Technology Item	Importance of Item	State of Technology	Design Techniques	Experiments Required Under RCT	Original Priority	Final Priority	Addressed in Final Experiment
Internal Cooling Phenomena							
Internal thermal analysis	Basic requirement	Excellent	Inadequate	No - 2D conduction codes are well validated	---	---	No
Limiting heat flux	Critical for design	Can only be estimated	Inadequate	Yes - to establish limiting heat flux under various conditions	High	---	No
Film coefficients in narrow passages	Basic requirement	Not well known	Inadequate	Yes - to provide data for liquid flow and nucleate boiling	High	High	Yes
Two-phase flow phenomena (including nonequilibrium, flow instabilities, and state of fluid at exit plane)	Important for operation with two-phase flow	Not known for small channels	Inadequate	Yes - to establish regimes where film coefficient data for different types of flow apply	High for two-phase flow	High	Yes
External and Combined Cooling Phenomena (In DI-TCNT Region)							
Smooth wall heating for continuous injection	Basic requirement	Adequate	Adequate	No - present technology base is adequate	---	---	Yes
Discontinuous gas injection over land	Important for local gas film cooling	Data lacking to validate predictions	Not considered	Yes - since this can be a major cause for margin requirements for gas injection	High for gas injection	High	Yes
Liquid layer formation	Important for local liquid film cooling	No data applicable to flight	Not considered	Yes - if liquid layers are to be counted upon for thermal protection	High for liquid injection	---	No
Two-phase injection	Important for liquid injection	No data applicable to flight	Not considered	Yes - since downstream droplet vaporization may be mechanism which makes DI-TCNT viable	High for liquid injection	High	Yes
Mechanical roughness augmented heating with mass transfer	Important	Data base inadequate	Not considered	Yes - to provide data for range of S/L with and without mass transfer	High	High	Yes
Liquid layer roughness augmented heating	Not important	Adequate to estimate magnitude of effect	Not considered	No - roughness small compared to mechanical roughness	---	---	No
Mechanical roughness effect on transition	Not important	Adequate to estimate magnitude of effect	Adequate since design for all turbulent	No - design for all turbulent flow not overly conservative	---	---	No
Effect of injection on transition	"	"	"	"	---	---	No
Effect of liquid layer waves on transition	"	"	"	"	---	---	No
Local angle of attack effects	Important	Inadequate data base	Inadequate	Yes - to validate application of zero incidence correlations to incidence	Medium	---	No
Mutually interacting phenomena	Important	Inadequate	Inadequate	Yes - to confirm correlations derived from above experiments	High	High	Yes
External Cooling Phenomena (Downstream of DI-TCNT)							
Stable liquid film characteristics	Basic requirement for liquid film cooling	Adequate	Not considered	No - present technology base is adequate	---	---	No
Entrainment	Important for liquid layers	Inadequate	Inadequate	Yes - since this could be a major source of liquid film ineffectiveness	High for liquid injection	Medium	Yes
Gas film cooling with upstream gas injection	Important for gas injection	Need data to validate predictions	Probably adequate	Yes - to validate analysis	Medium for gas injection	High	Yes
Gas film cooling with upstream liquid injection	Could be important for liquid injection	Not well understood	Inadequate	Yes - to determine possible beneficial effects of droplet vaporization	High for liquid injection	Medium	Yes
Angle of attack effects on gas film cooling	Important for gas injection	Can be estimates for $\alpha < \alpha_c$	Inadequate	Yes - need data to confirm analyses for $\alpha < \alpha_c$ and to develop correlations for $\alpha > \alpha_c$	High for gas injection	Medium	No
Angle of attack effects on liquid layer	Important for liquid injection	Not well established	Inadequate	Yes - need data to confirm analyses	High for liquid injection	---	No

The basic data identified in Section 2.1 as needed for the critical design of DI-TCNT and the specific experiments which would provide these data are presented in Table 2-2. Each data source is identified as primary or secondary or as a validation experiment. It was felt that all test series would be needed to meet all primary data requirements. The specific experiment objectives and requirements are presented in the following sections.

2.2.1 Internal Cooling Experiment

1. Primary Objectives

   a) To determine film coefficients in minute slots with liquid and two-phase flow and to characterize nature of two-phase flow (nonequilibrium, flow instabilities, state at exit plane)

   b) To establish internal heat paths and values of limiting heat fluxes that can be accommodated internally.

2. Experiment Requirements

   a) Tests with water coolant and at conditions for which phase change will and will not occur within the slot.

   b) Slot widths must be varied about nominal flight design values.

   c) Heating must be applied at the surface.

   d) No external flow.

   e) Surface heat fluxes to 7000 Btu/sec ft^2 required.

2.2.2 External Cooling Experiments

2.2.2.1 Gas Film Cooling Experiments - Sphere Cone in Wind Tunnel

1. Primary Objectives

   a) To determine local and downstream gas film cooling effectiveness for sphere cones at zero and non-zero angle of attack.

   b) To obtain global heating data on lands from combined effects of roughness and discontinuous gas injection.

2. Experiment Requirements

   a) Sphere cone model with gas injection and cooled skirt lengths spanning range of interest.

   b) Simulate s/δ and B' of flight with water injection.

   c) Tests under turbulent flow conditions.

   d) Tests at angle of attack.

   e) Measurements to enable determination of average $\dot{q}''_w$ and/or T_w on lands and local $\dot{q}''_w$ and T_w downstream of cooled section.

TABLE 2-2

KEY PROBLEM AREAS BEING ADDRESSED IN EACH EXPERIMENTAL SERIES

Test Series / Data Requirement	Internal Cooling Experiments	External Cooling Experiments			Combined Cooling Experiments
		Sphere Cone in Wind Tunnel	Large Slot Model in Wind Tunnel	Sphere Cone in Rocket Exhaust	
Internal Cooling Phenomena					
Limiting Heat Flux	Primary*				Validation*
Film Coefficients in Narrow Passages	Primary*				Validation*
Two-Phase Flow Effects in Narrow Passages	Primary*				Validation*
External & Combined Cooling Phenomena (in DI-TCNT Region)					
Discontinuous Gas Injection over Lands		Primary (Global)	Primary* (Local)		Validation*
Liquid Layer Formation			Primary*	Primary	Validation*
Two-Phase Injection			Primary*		Validation*
Roughness Augmented Heating with Mass Transfer		Primary (Global)	Primary* (Local)		Validation*
Local Angle-of-Attack Effects		Primary (gas)	Primary (ΔP on Slot)	Primary (Liquid)	
Mutually Interacting Phenomena					Primary*
External Cooling Phenomena (Downstream of DI-TCNT Region)					
Entrainment			Secondary	Primary	Validation
Gas Film Cooling with Upstream Gas Injection		Primary	Primary (Near TCNT)		Validation
Gas Film Cooling with Upstream Liquid Injection			Secondary	Primary	Validation
Angle-of-Attack Effects on Gas Film Cooling		Primary			
Angle-of-Attack Effects on Liquid Layer				Primary	

*Investigates Slot/Land Ratio

2.2.2.2 Large Scale Experiments - Large Slot Model in Wind Tunnel

1. Primary Objectives

   a) to obtain fundamental data on liquid layer formation and two-phase injection.

   b) To obtain fundamental data on boundary layer separation and reattachment with discontinuous gas injection.

   c) To determine the effect of pressure gradient on local coolant effectiveness.

   d) To provide nearby downstream cooling data for liquid, gas, and two-phase injection.

2. Experiment Requirements

   a) Tests with large slots to permit resolution of T_w and/or $\dot{q}_w''$ distributions on lands.

   b) Scale liquid layer formation parameters in liquid injection tests.

   c) Scale roughness to boundary layer thickness parameters.

   d) Simulate flight B' in gas and two-phase injection experiments (this necessitates use of a liquid which simulates vaporization thermodynamics in two-phase flow experiments).

   e) Tests under turbulent flow conditions.

   f) Perform some tests with canted slots to simulate effects of pressure gradient across a single slot at angle of attack.

2.2.2.3 Liquid Film Cooling Experiments - Sphere Cone in Rocket Exhaust

1. Primary Objectives

   To determine liquid layer formation characteristics, entrainment and downstream cooling effectiveness on sphere cone models at zero and non-zero angle of attack with liquid injection for range of cooled section lengths.

2. Experiment Requirements

   a) Sphere cone models with water injection and skirt lengths that span range of interest.

   b) Simulate liquid layer flow parameters (this requires a high pressure, high enthalpy flow).

   c) Tests at angle of attack.

d) Tests under turbulent flow conditions.

e) Use conventional skirt heat shield materials in order to survive severe environment and to provide the type of data directly applicable to flight.

f) Measurements of liquid layer lengths sufficient to determine degree of entrainment.

2.2.3 Combined Cooling Experiment

1. Primary Objectives

   a) To obtain necessary data for validation of computational procedures (based on correlations developed under previous test series) while internal and external phenomena are mutually interacting.

   b) To determine burnout modes.

   c) To determine the effects of slot/land ratios on margin requirements.

   d) To determine the effects of realistic two phase injection on margin requirements.

2. Experiment Requirements

   a) Tests with simple model/flow geometry in turbulent flow and with stagnation flow.

   b) Tests in high pressure, high enthalpy environment to simulate liquid layer characteristics and to provide high heat fluxes.

   c) Tests with water, over a range of flow rates to produce liquid two phase and vapor.

   d) Vary slot size and slot/land width ratio.

   e) Measure T_w and/or $\dot{q}''_w$ locally (on lands) and downstream (aft of cooled sections)

   f) Perform some tests to failure.

2.2.4 Additional Remarks

Two phenomena which were initially expected to be important were not addressed in the proposed experiments. Their exclusion was based on the following:

1. Effect of vapor or liquid injection on transition - Calculations demonstrated that transition would be expected at sufficiently high altitude that for all practical purposes the TCNT must be designed for all turbulent flow (Section 2.1.2.1).

2. Effect of rough liquid layers on heat flux -
Calculations demonstrated that the roughness associated with liquid layers is insignificant, especially compared to the scale of mechanical roughness (Section 2.1.1.2.3.B).

2.3 ASSESSMENT OF NCT PROGRAM WITH RESPECT TO THE ORIGINAL PROBLEM REVIEW AND EXPERIMENT RECOMMENDATIONS

In the course of carrying out the NCT program, the importance of several of the originally designated key problem areas diminished considerably, due both to the acqusition of new data as the program proceeded and to an improved understanding of the problem. The final two columns of Table 2-1 indicate, first, the final priority assigned to each of the various technology items identified in the problem review and, second, whether or not the item was addressed in the experiments actually carried out.

The concept of the limiting heat flux decreased in importance when it became apparent that heating directly from the external flowfield to the slot affected the state of the coolant below the surface as much as or more than heating from the slot walls to the coolant. This finding is discussed further in Sections 3.5 and 3.6.

The importance of studying liquid layer formation diminished when calculations revealed that, for thermodynamically adequate injection flowrates, the liquid layer on a flight nosetip would be thinner than surface imperfections. This indicated that design of a DI-TCNT should not rely upon a liquid layer for cooling. Consideration of this parameter was further discouraged when it was found that proper scaling of the most appropriate liquid layer parameters was impossible under all but flight conditions.

The priority for studying entrainment from liquid layers was reduced when it became evident that the liquid layer should not be considered as a practical cooling mechanism.

The priority for studying gas film cooling with upstream gas injection was increased when it became evident that, for injection flowrates of interest, the coolant was vaporized at or below the slot exit. Correspondingly, the study of gas film cooling with upstream liquid injection was deemphasized.

The study of angle-of-attack effects on gas film cooling was not possible within the constraints of resources and program schedule.

Finally, angle-of-attack effects on liquid layer formation were lowered in priority when it was found that the formation of well-defined liquid layers would be unlikely under the conditions of interest at zero angle-of-attack.

As indicated in the final two columns of Table 2-1, all technology items with a high final priority designation were addressed in the experiments carried out during the NCT program.

As summarized in Section 2.2, a total of five experiments was recommended in Reference 1. Due to time and economical constraints, three experiments were in fact performed. These Internal Cooling, External Cooling and Combined Cooling experiments are described in detail in Sections 3, 4, and 5, respectively. The Internal Cooling experimrent was that outlined in Section 2.2.1, and the External Cooling experiment was the large scale experiment outlined in Section 2.2.2.2, except that only gas injection was considered. The Combined Cooling experiment differed considerably from that described in Section 2.2.3. The experiment was characterized by liquid, two-phase, and gas injection into a hot boundary layer. However, a high enthalpy, high pressure test facility was not used. Instead, it was found that a much more economical and technically feasible facility with relatively low enthalpy and pressure could be used, and the proper scaling of important physical phenomena could be obtained, by simply utilizing injection models with an appropriately-selected thermal conductivity.

Table 2-3 is a revised version of Table 2-2 updating the key problem areas treated by each of the three experiments. The most significant difference, compared to Table 2-3, is that the Combined Cooling experiment provided more "primary" data and less "validation" data than originally intended.

TABLE 2-3

KEY PROBLEM AREAS ADDRESSED IN EACH FINAL EXPERIMENT

Test Series / Data Requirement	Internal Cooling Experiments	External Cooling Experiments	Combined Cooling Experiments
Internal Cooling Phenomena			
Film Coefficients in Narrow Passages	Primary		Validation
Two-Phase Flow Effects in Narrow Passages	Primary		Validation
External & Combined Cooling Phenomena (in DI-TCNT Region)			
Discontinuous Gas Injection over Lands		Primary (Global)	Primary (Local)
Liquid Layer Formation			Primary
Two-Phase Injection			Primary
Roughness Augmented Heating with Mass Transfer		Primary (Global)	Primary (Local)
Mutually Interacting Phenomena			Primary
External Cooling Phenomena (Downstream of DI-TCNT Region)			
Entrainment			Primary
Gas Film Cooling with Upstream Gas Injection		Primary (Near TCNT)	Primary
Gas Film Cooling with Upstream Liquid Injection			Primary

SECTION 3

INTERNAL COOLING EXPERIMENT

The material presented in this section is a condensation of the results documented in Reference 6. The primary objective of this experiment was to determine heat transfer coefficients for single and two phase flow through narrow passages. Knowledge of the local surface heat flux distribution to a channel was obtained from the external cooling study. The internal cooling study is thus directed at providing methods for predicting the following:

a) Flow conditions through the slot and at the slot exit, the exit conditions being necessary to establish boundary conditions for external flow analysis.

b) Land surface and in-depth temperatures.

3.1 EXPERIMENTAL APPARATUS

The apparatus used was assembled at the University of Tennessee Space Institute and the experiments conducted by UTSI personnel under the direction of Dr. W. Frost.

The apparatus was designed to provide close simulation of flight hardware internal cooling phenomena. In so doing, attempts were made to simulate the following parameters:

a) Heat flux
b) Mass flux
c) Heat paths
d) External pressure
e) Flow channel geometry.

The major components of the test apparatus are a flow loop designed to provide steady high pressure flow (0 - 500 psig) at very low and accurately measured flow rates (0 - 2 lbm/minute), a pressure vessel in which the high pressure reentry environment is simulated, and a test package which models the discrete injection slots and the heating on the exit surface as experienced in flight.

A schematic of the flow loop is shown in Figure 3-1. Initially water is degassed by heating it to 220°F with the use of an electrical heating element submerged in a stainless steel degassing and storage tank. The temperature of the water in the storage tank is controlled with an adjustable thermostat having a temperature sensing element submerged in the water. A nitrogen bottle and 3000 psi regulator are used to pressurize the storage tank to 30 psi providing sufficient suction head for the downstream pump. The tank is designed to hold pressures up to 300 psi and has a safety valve to prevent over-pressurization. A diaphragm piston feed pump delivers the water.

A 5000 psi rotameter measures the flow rate of water into the pressure vessel. An accuracy of one percent full scale is obtained with this rotameter. A 0 to 5000 psi pressure gauge upstream from the rotameter is used to monitor the approximate inlet feed line pressure.

A digital needle valve is located downstream from the rotameter to act as a shut-off and control valve for the water flowing into the vessel. Its main function is to act as a shut-off valve to allow the pressure vessel to be evacuated and pressurized without interfering with the flow loop. A bypass valve and the diaphragm stroke control on the pump are the primary flow control devices. The bypass valve is simply a digital needle valve which bleeds off mass flow from the pump exit and returns it to the degassing and storage tank.

A stainless steel pressure vessel 18.5 x 15 inches O.D. with two one inch diameter windows directly opposite to one another for direct viewing and photographic purposes contains the test package and instrumentation. The test package is directly attached to the pressure vessel cover as shown in Figure 3-2. A copper cooling jacket surrounds the inner walls of the vessel and a finned heat exchanger is positioned on the bottom as shown in Figure 3-3. The purpose of the heat exchanger and cooling jacket are to condense the steam flowing from the slotted test section, thus eliminating condensate on the observation windows, and to maintain the pressure vessel at a safe operating temperature for structural integrity during high pressure and high heat flux operations.

The vessel is pressurized using 6000 psig bottled nitrogen. A regulator and needle shut-off valve control the flow of nitrogen to the vessel. A safety relief valve set at a pressure of 3200 psi prevents over-pressurization of the vessel.

A manifold arrangement delivered coolant to the individual channels. The manifold effect is achieved by inserting the slotted plate into the plenum chamber hence the fluid does not flow directly at any single slot but enters the plenum in an axial direction and flows up and over to the slot inelt assuring uniform flow distribution. Figure 3-4 shows the plenum chamber and manifold arrangement.

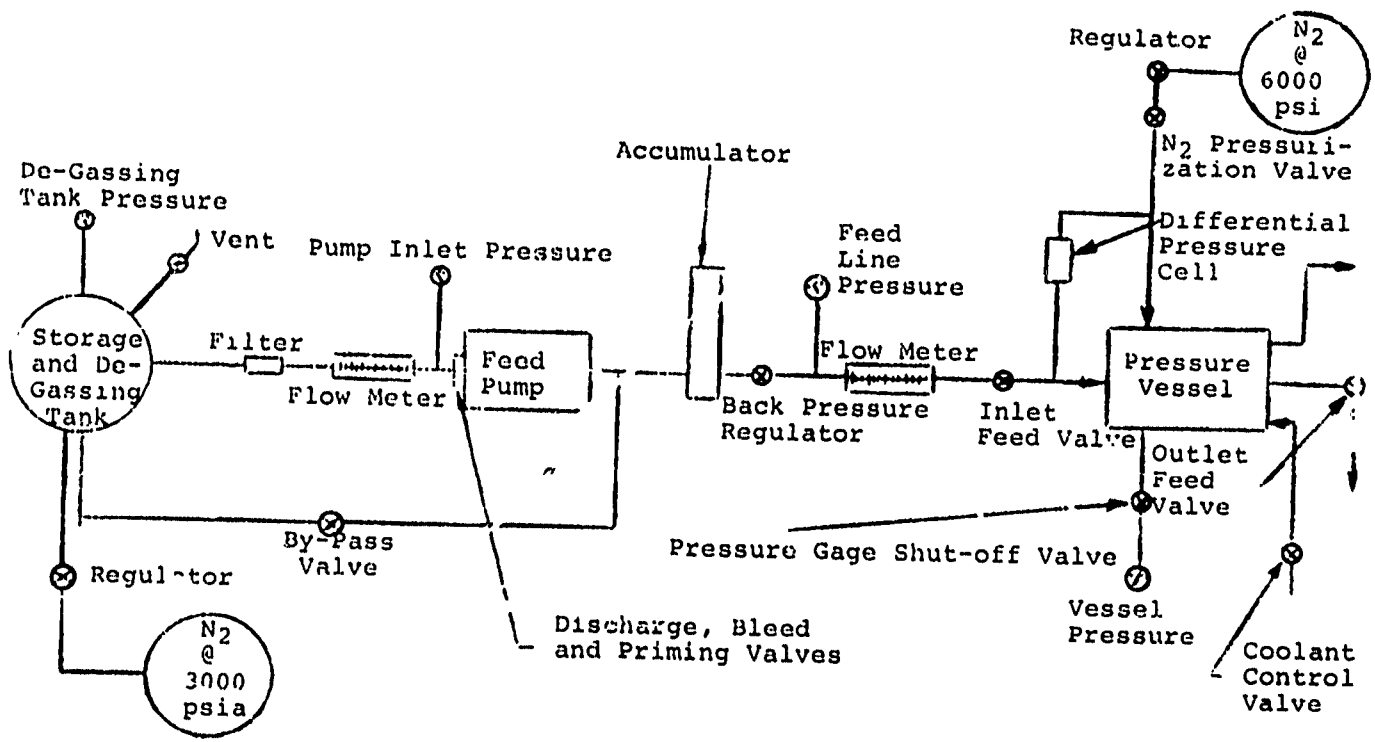

Figure 3-1. Schematic of Flow Loop

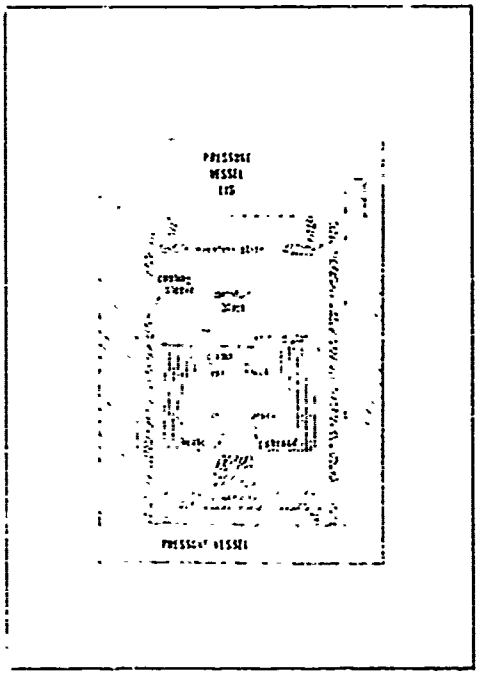

Figure 3-2. Mounting of Test Package in Pressure Vessel

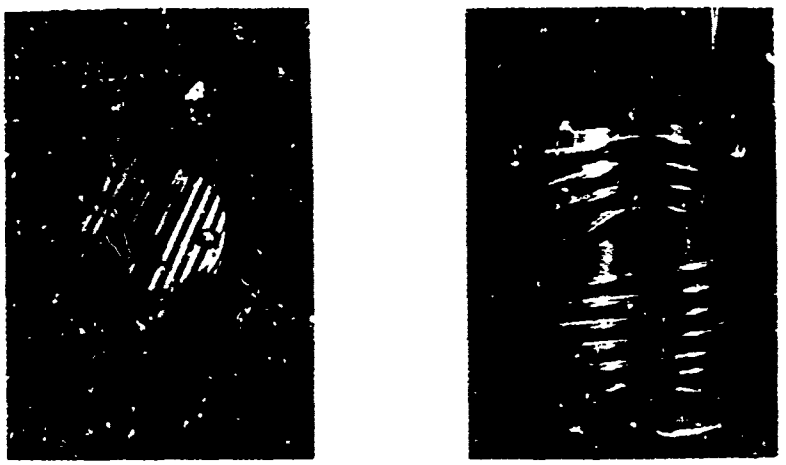

Figure 3-3. Photograph of Finned Heat Exchanger and Cooling Jacket

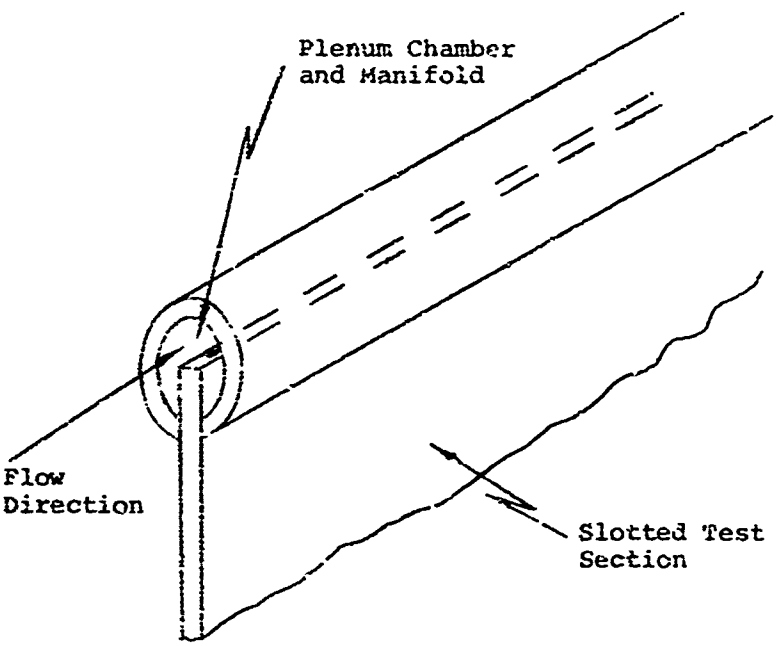

Figure 3-4. Plenum Chamber and Manifold

The slotted test section consists of 15 rectangular channels, 0.005 x 0.02 inches, machined in a central stainless steel plate which is sandwiched between two 0.035 inch flat stainless steel plates and the complete unit fusion bonded. The size of the slots are typical of those of a transpiration cooled nosetip. The outer plates are bent 90 degrees at one end to form a lip which contacts the copper heater upon installation in the test package (Figure 3-5).

The heat flux to the slotted test section is supplied by a triangular shaped copper wedge which focuses the energy of eight 200 watt electrical cartridge heaters embedded inside the wedge of the lip of the slotted test section. The maximum block temperature is dictated by the melting temperature of the block approximately 1200°F. A significant amount of energy is lost from the exposed areas of the heater by convection. Strong convection currents were actually visible through the observation window. The heat flux steadily increases as the energy flow area decreases until it reaches a maximum value at the tip of the wedge. Design analysis indicated that heat fluxes to the surface of the lands on the order of 2000 Btu/ft^{2}sec were possible with the copper block heater; however, heat fluxes on the order of only 200 Btu/ft^{2}sec were intially achieved. The reason for this is the high contact resistance between the tip of the copper wedge and flange on the test section. Severe corrosion on the flange resulted at high temperatures and pressures despite the 99 percent nitrogen atmosphere. This corrosion greatly increases the contact resistance. The ceramic clamping blocks lost considerable strength after heating and hence did not allow high clamping pressures between the glange and wedge tip. This further increased the contact resistance. For later runs stainless steel support blocks were machined and replaced the ceramic blocks. Higher heat fluxes were finally achieved but the 2000 Btu/ft^{2}sec value was still not approached.

3.2 INSTRUMENTATION

The entire flow loop and test package is instrumented to measure the necessary transpiration cooled nosetip design parameters and monitor the test equipment during operation. One of the more critical measurements is the temperature gradient along the beginning of the channels wall since this wall will provide a measurement of the heat flux.

Five chromel-alumel thermocouples are spot welded about .01 inch apart along one side of the center slot to measure the temperature gradient at the exit of the slot. Two additional chromel-alumel thermocouples are spot welded at positions of 0.25 inches and 0.5 inches upstream of the exit. Originally one mil wire was used for the thermocouples. The wires were run along one side of the slotted test section to a junction box in the test section, Figure 3-6. At the junction box sheathed thermocouple wire was soldered to the one mil wires.

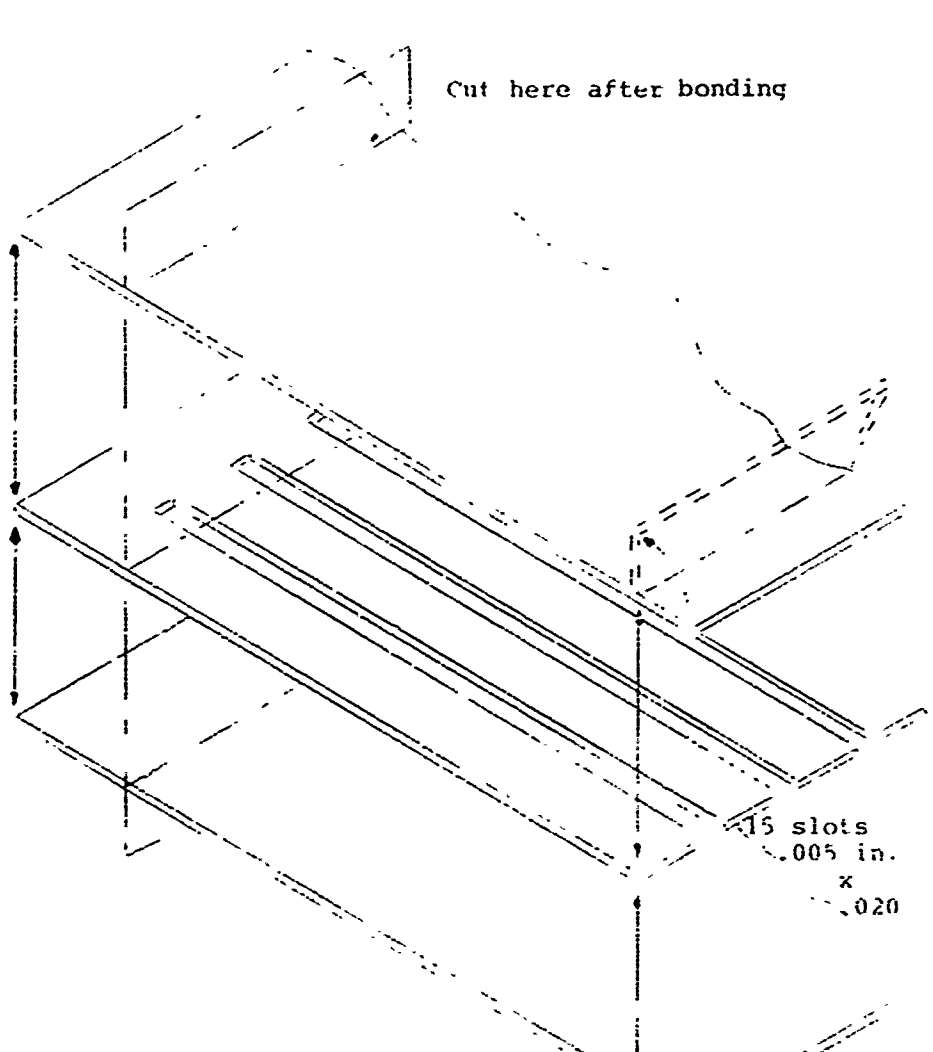

Figure 3-5. Fabrication of Slotted Plate

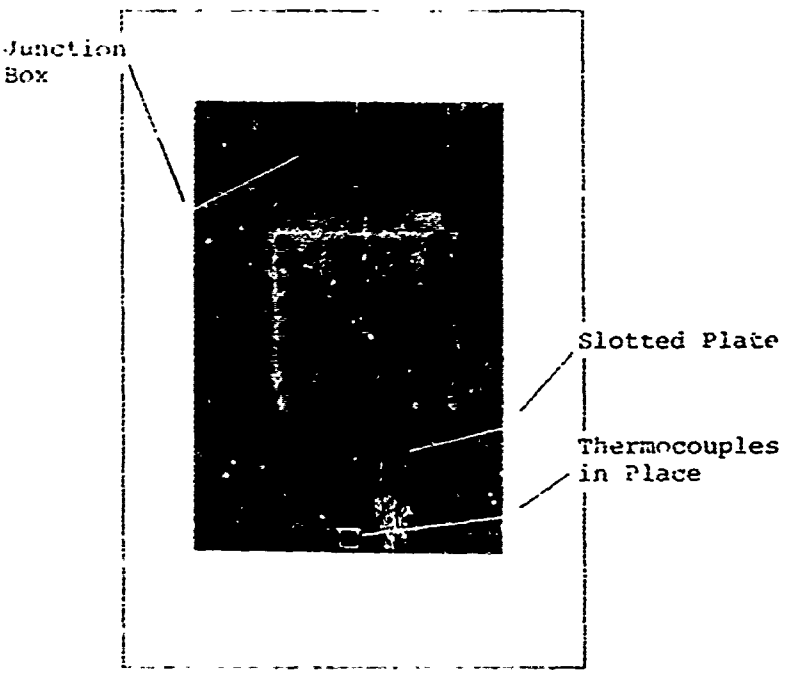

Figure 3-6. Junction Box in Test Package

The sheathed wires were fed out of the vessel through a fitting. Several of the one mil wires broke by mechanical failure during the first test possibly due to thermal-expansion of the assembly. The junction box was eliminated and three mil wires were used to replace the one mil wires. With this change, failure during repeated testing and thermal cycling did not occur.

The temperature of the liquid exhausting from the slots is measured with a thermocouples at the exit plane of the slotted test section as shown in Figure 3-7. The thermocouple wire runs along one wide of the copper wedge and up to the top of the test package where a sheathed thermocouple wire is soldered to it. Since the wire is against the surface of the wedge at 1200°F, the thermocoupled temperature must be corrected for conduction from the block.

A chromel-alumel thermocouple is located in the plenum chamber to measure water inlet temperatures. Two additional thermocouples are mounted on each side of the copper wedge to determine the symmetry of the heat flux applied to the test section and to monitor the block temperature to avoid exceeding the melting temperature.

Thermocouples are also located on the window, cooling jacket, and finned heat exchanger plus the inlets and outlets of the cooling jacket and finned heat exchanger.

A Differential Pressure Transducer is used to measure the pressure difference between the vessel and inlet line which is essentially the pressure drop over the length of the slot. The transducer can measure differential pressures up to 18 psi with an accuracy of 0.25 percent full scale.

Tubing, 0.25 inch in diameter, connects the pressure vessel chamber to a pressure gauge measuring the pressure in the vessel. A shut-off valve is located between the pressure gauge and vessel to protect the gage during evacuation of the vessel and allow changing of the pressure gauge without depressurizing the vessel. Three different pressure gauges are used to cover the ranges of 0 - 100, 0 - 400, and 0 - 5000 psi. The accuracy of the gauges is 0.25 percent full scale for 0 - 100, 0 - 400 psi and 0.5 percent full scale for the 0 - 5000 psi range.

A 5000 psi rated rotameter measures the flow rate of the test fluid. Flow ranges between 0.1 - 1.0, 0.5 - 4.96, and 2.0 - 28.2 cc/minute can be measured. All three flow ranges are calibrated by the manufacturer to an accuracy of one percent full scale and obatined by interchanging guide tubes and floats. A high pressure gauge upstream from the rotameter ranging from 0 - 5000 psi is used to monitor the feed line pressure.

Photographic coverage of the test section is provided by a 16 mm high speed motion picture camera. The camera can photograph the exit plane at 500 frames/second during selected runs. This is sufficient to measure exit velocities of

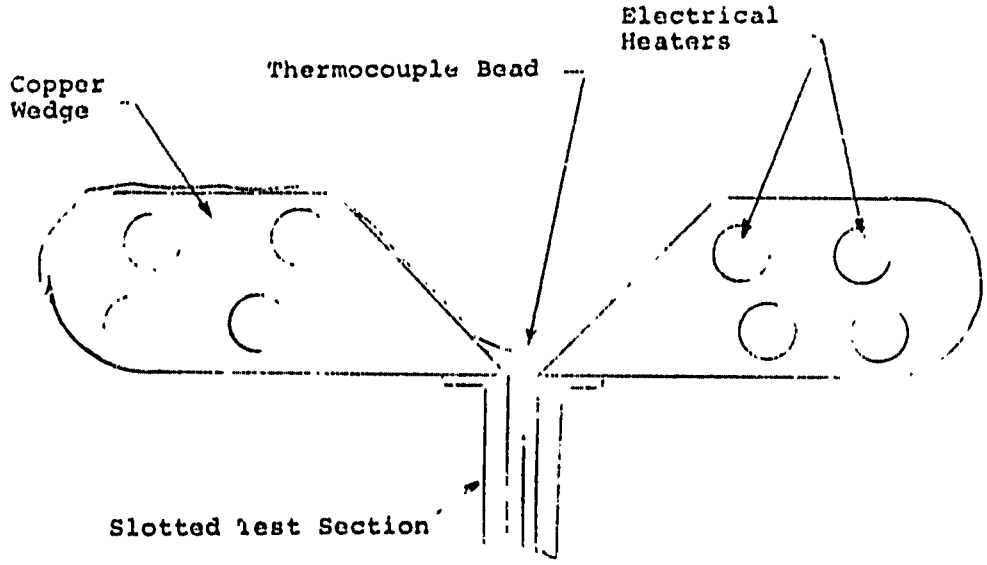

Figure 3-7. Thermocouple at Exit Plane

liquid droplets on the order of 50 ft/second over a one inch field of view. Lighting is diffuse backlighting through the opposite window. Droplet size, speed, and bubble size can be determined from the photographs, and growth rate or the bubbles can be measured from the sequence of photographs.

3.3 TEST MATRIX

Nine runs at pressure levels of 0, 200, 500, 1000, and 2000 psig were carried out. Table 3-1 lists the steady state settings during each run. The measured flow rate and heater block temperature are indicated; the latter is a measure of the heat flux level. All measured data for each steady state setting are tabulated in Reference 6. Runs 9 through 11 were made with the test section suspended in the atmosphere. Runs 12 through 17 were made inside the pressure vessel without removing the test section between runs. Although visual inspection showed water was flowing during these runs it is now apparent that the slots were becoming progressively plugged with each run. Finally, during run 17 the plenum chamber plug blew out requiring an equipment overhaul. Run 18 was made after cleaning the system and replacing the ceramic heater clamping blocks with stainless steel blocks which provided greater clamping pressures and thus reduced heater contact resistance. Additional runs after number 18 were attempted at 3000 and 1000 psig. Plugging occurred within 15 to 20 minutes in all cases. The plugging is attributed to the formation of an oxide scale on the blocks and around the slots.

3.4 TEST RESULTS

The total coolant flow delivered to the manifolded channels was measured; however due to plugging, which varied from channel to channel, the mass flux through individual channels was not accurately known. Thus, the term measured mass flux, refers to values obtained by averaging the measured flow rate over the total channel area, and will not necessarily correspond to the actual flux through any given channel. The most reliable experimental data is the temperature distribution along the channel wall. The data for single phase flow (i.e., liquid exit conditions was used to compute mass fluxes analytically, employing a one-dimensional model accounting for conduction along the land (channel) and convection from channel wall to coolant (see Reference 6). The analysis requires an iteration on mass flux and heat transfer coefficient until predicted temperatures are matched to measured values. Figure 3-8 illustrates the results of this treatment. Values of G (measured)/G (calculated) were continuously monitored using data from single phase flow tests, since plugging became progressively worse during the tests. Typical temperature profiles for the two phase flow data are shown in Figures 3-9 and 3-10. Data for the case of liquid-vapor mixture at the exit and of superheated vapor at the exit can be distinguished. The data for which the liquid-vapor

TABLE 3-1

TEST MATRIX

0 psig T_{sat} = 212 °F		200 psig T_{sat} = 381 °F		500 psig T_{sat} = 467 °F		1000 psig T_{sat} = 544 °F		2000 psig T_{sat} = 635 °F	
Flow Rate cc/min	Block Temp. °F	Flow Rate cc/min	Block Temp. °F	Flow Rate cc/min	Block Temp. °F	Flow Rate cc/min	Block Temp. °F	Flow Rate cc/min	Block Temp. °F
0.4	786	0.5	924	0.1	909	0.37	1046	0.4	679
0.4	841	0.5	937	0.1	917	0.5	1042	0.5	682
0.4	713	0.6	928	0.21	926	1.0	1040	1.0	672
0.4	610	0.7	947	0.4	936	1.5	1042	1.5	693
0.4	521	0.82	946	0.5	930	2.0	1035	2.0	690
0.4	494	0.9	947	0.6	930	2.5	1040	2.5	675
0.4	828	0.8	937	0.7	926	3.0	1010	3.5	663
0.44	912			0.8	922	3.5	1042	3.5	699
0.44	957			0.8	922	4.0	1034		
0.44	780*			0.9	922	4.5	854		
0.44	710*			1.0	930	4.5	701		
0.44	690			1.0	934	0	931		
0.44	552			1.0	937	0.5	930		
0.44	860			0.24	926	2.0	936		
0.44	780*			0.2	926	3.0	923*		
0.44	379			2.0	496*	3.7	923*		
0.44	344			2.0	550*	4.0	905*		
0.44	296*			2.0	886				
0.44	255*			2.0	885				
2.0	255*			2.0	902				
2.0	964*								
2.0	1040*								
2.0	1040*								

TABLE 3-1 (continued)

0 psig T_{sat} = 212 °F		200 psig T_{sat} = 381 °F		500 psig T_{sat} = 467 °F		1000 psig T_{sat} = 544 °F		2000 psig T_{sat} = 635 °F	
Flow Rate cc/min	Block Temp. °F	Flow Rate cc/min	Block Temp. °F	Flow Rate cc/min	Block Temp. °F	Flow Rate cc/min	Block Temp. °F	Flow Rate cc/min	Block Temp. °F
2.0	684*								
2.0	477*								
3.0	361*								
3.0	306*								
4.0	295*								
2.0	296*								
2.0	884*								
2.0	1052*								
2.0	133*								
2.0	924*								
0	846								
0	675								

*Single phase flow conditions.

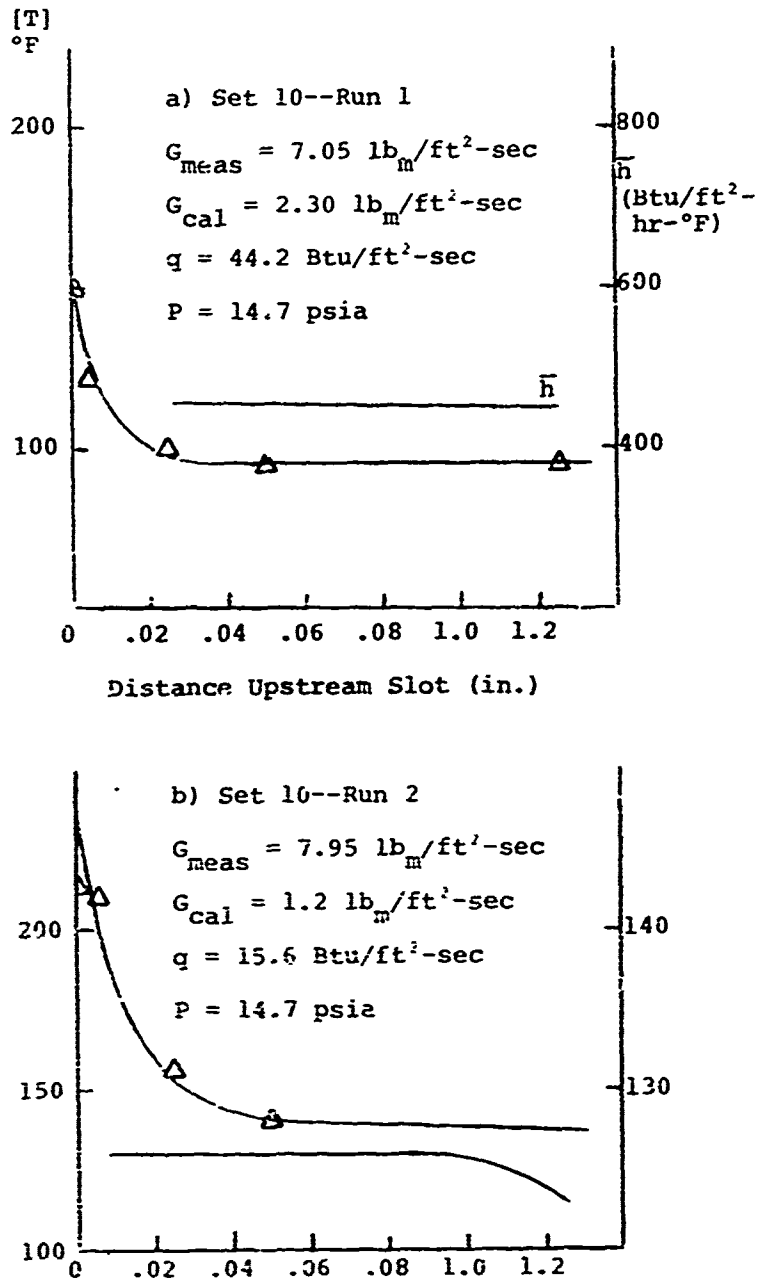

Figure 3-8. Single phase data, set 10 -- runs 1 and 2.

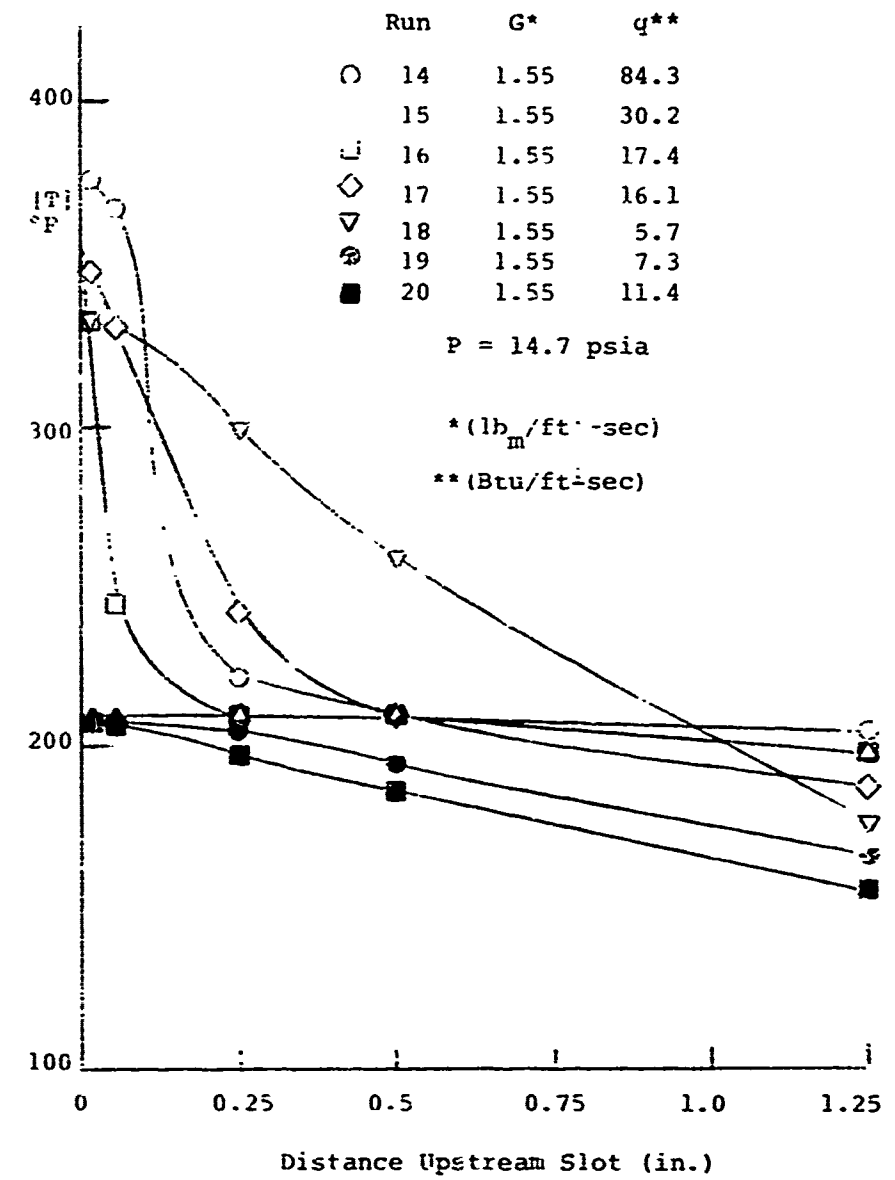

Figure 3-9. Temperature Distribution, Test 9 -- Runs 14-20

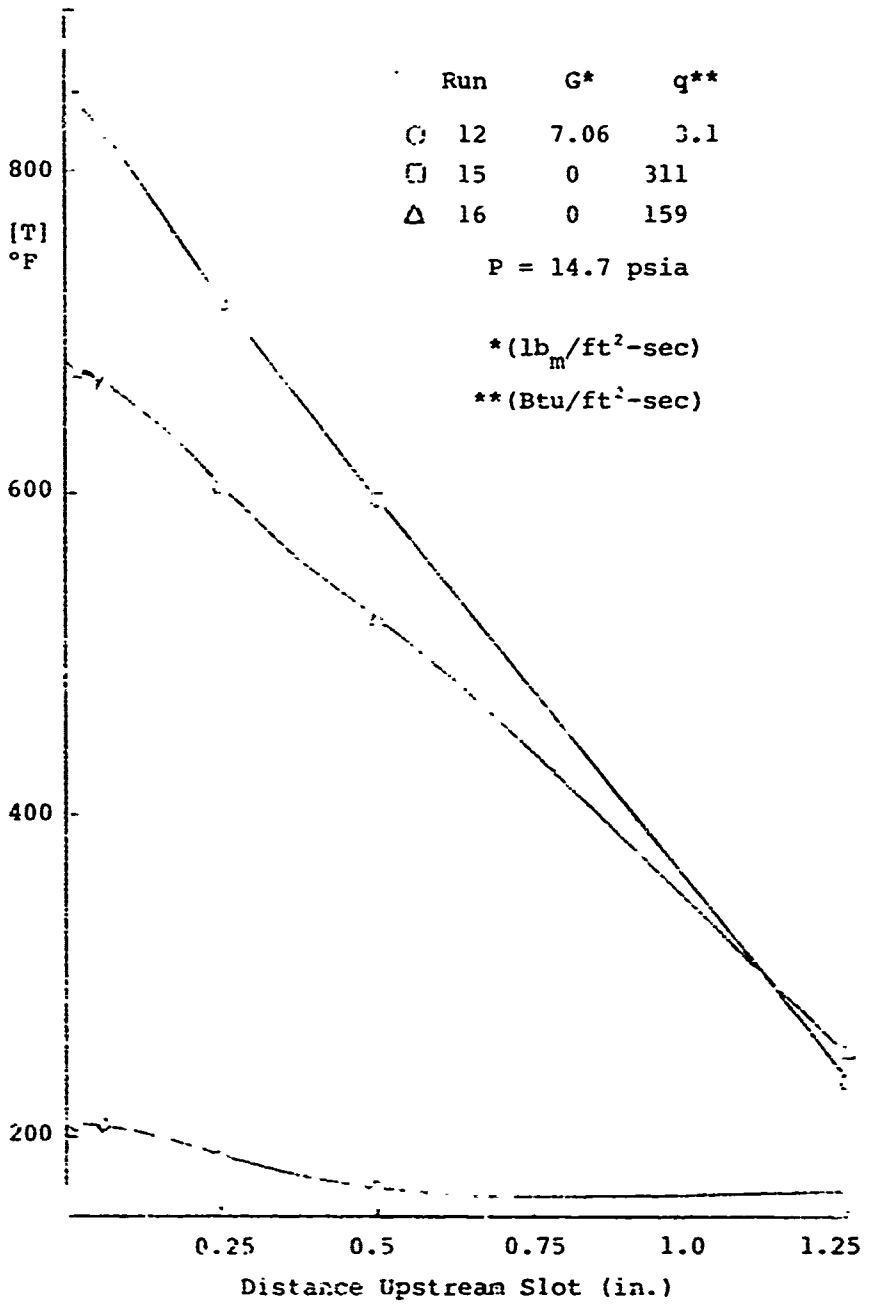

Figure 3-10. Temperature Distribution, Test 11 -- Runs 12, 15, and 16.

mixture occur at the exit have essentially a constant temperature (approximately saturation temperature) along the surface. The constant temperature results from the high heat transfer coefficient in the two-phase regime coupled with a heat leak from the copper block through the ceramic insulator behind the upper 1/8 inch of the plate. The land very near the surface thus behaves as a constant heated duct which in two-phase flow generally takes on a temperature near the saturated temperature of the fluid.

For super-heated vapor flow at the exit the temperature profiles are essentially linear from the surface to approximately saturation temperature then become uniform at the saturation value over a short length, dropping finally to the inlet temperature.

Under certain conditions of two-phase flow a steady-state setting was not possible due to oscillations of the flow. This was primarily encountered for the zero psig runs when the fluid inlet temperature was close to the saturation value. Figure 3-11 shows temperature profiles obtained from consecutive recorder print-outs during oscillating flow. Continuous monitoring of the temperature was not possible, but a plot of the temperature measured by the surface thermocouple as a function of time based on the period of recorder printout cycle is shown in Figure 3-12. Sudden excursions in the temperature profiles were also observed. This type of temperature excursion is believed to be associated with a change from film boiling to nucleate boiling, commonly encountered in two phase flow heat transfer.

Further evidence of different two phase flow patterns occurring in the slots is given by photographs taken of the slot exit during various flow conditions (Figures 3-13, 3-14 and 3-15). In Figure 3-13 liquid water is emerging from the slots (only four slots are unplugged in these photographs). During photographing of these pictures the test apparatus was positioned on its side and the water is exiting horizontally. The water formed a free surface tension with ripples directly over the open slots and extending down over a fraction of the lower block where it evaporates. The temperature of the plate is below the saturation value. In Figure 3-14 the flow rate has been reduced and two phase flow occurs directly at the exit. The fluid is ejected in a highly dispersed pattern, which will be referred to as mist flow, and the land temperature is approximately equal to the saturation value. It is evident from this picture that complete evaporation does not occur and the latent heat of evaporation is not available for cooling the plate. In Figure 3-15 a further reduction in flow has resulted in a globule flow pattern where the water is ejected in globules. The temperature of the plate is very high (on the order of 800 - 900°F). This flow regime is similar to the film boiling phenomenon in pools where the water is separated from the heated surface by a film of vapor.

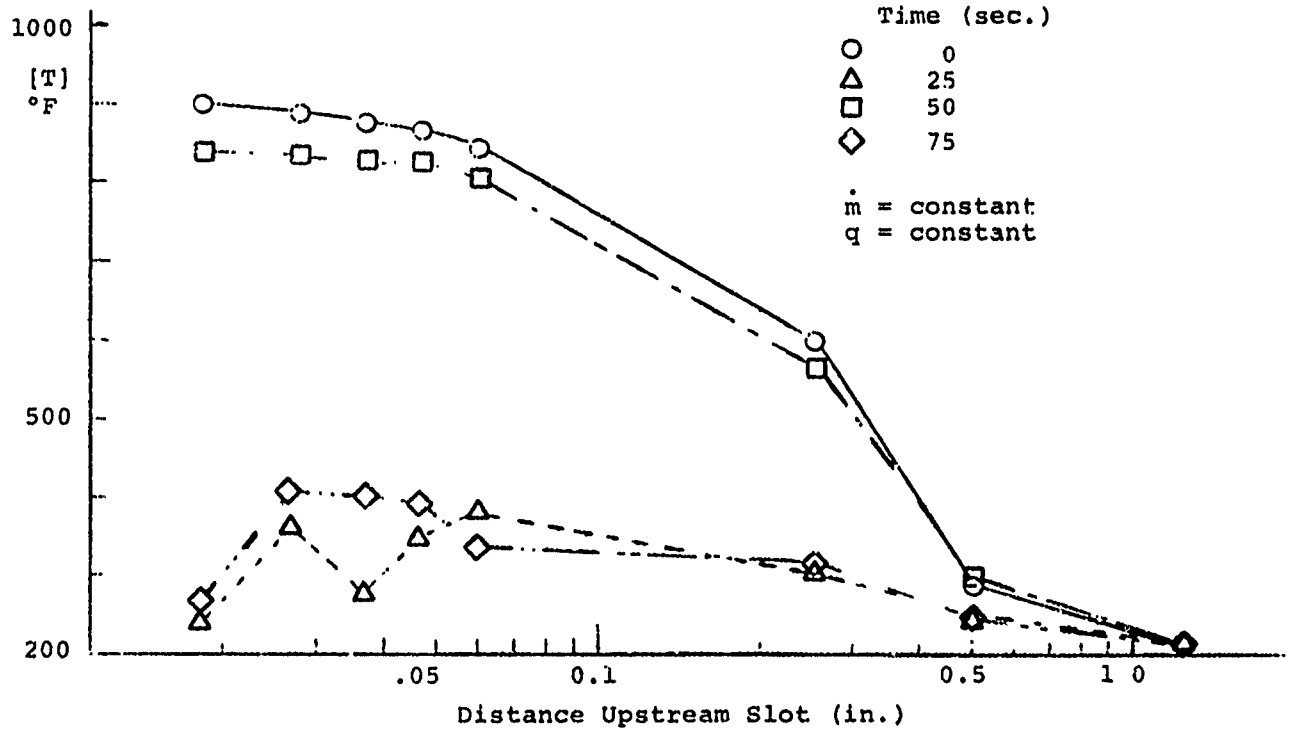

Figure 3-11. Consecutive Temperature Profiles During Oscillating Flow.

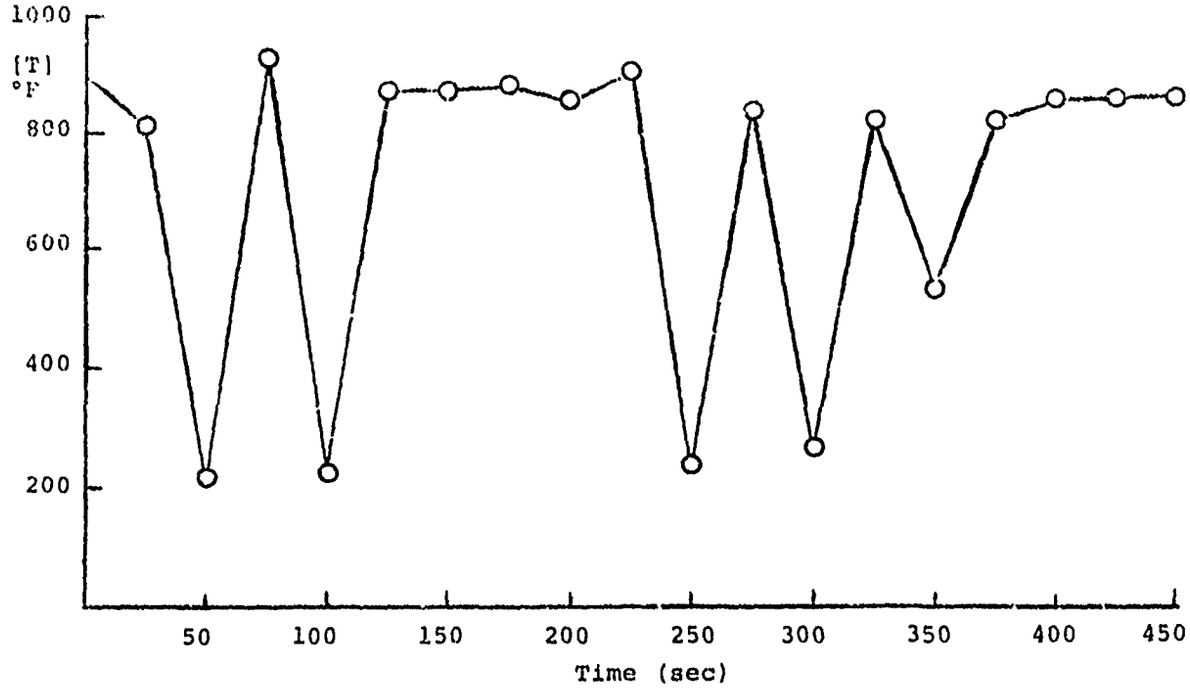

Figure 3-12. Temperature at Station 1 Versus Time for Oscillating Flow.

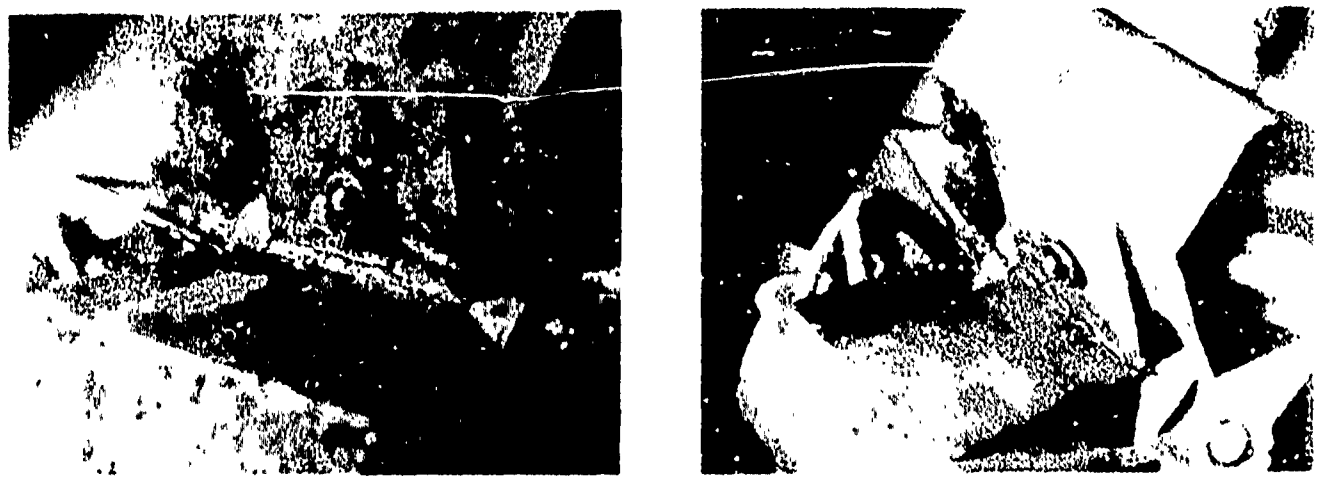

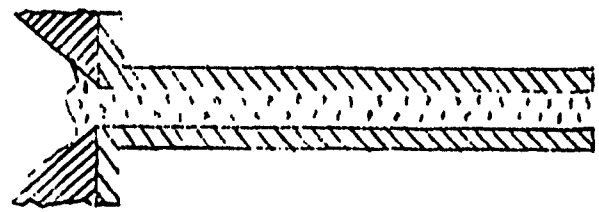

Figure 3-13. Single-phase Flow

Figure 3-14. Two-phase Dispersed Flow.

Reproduced from best available copy.

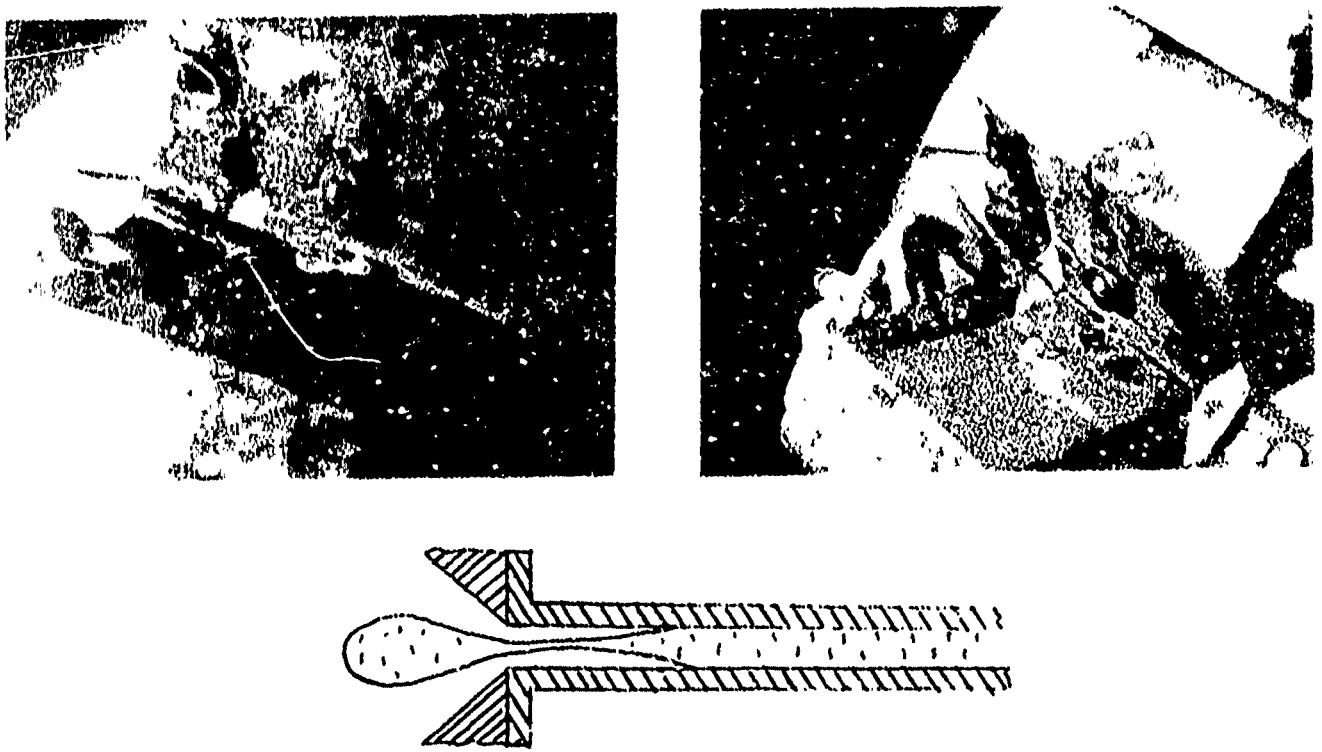

Figure 3-15. Two-phase Globule Flow.

A thorough compilation of all test data is given in Reference 6, hence only representative results have been quoted here.

3.5 DISCUSSION OF RESULTS

3.5.1 Single Phase Flow

The temperature distribution in the land correaltes very well with the model presented in Reference 6. Values of Nu based on data, correlates with the Peclet number, RePr, as shown in Figure 3-16. This value of the heat transfer coefficient, designated h, does not necessarily represent the actual value of h in the slot flow passage, but rather the value of h above which any larger value of h would not contribute to the heat transfer process. Expressed differently, this implies that the thermal energy capacity of the mass is so small that its temperature adjusts almost instantaneously to that of the solid. The heat transfer coefficient controls the rate at which energy flows from the wall to the mass. Hence, the correlation given in Figure 3-16, i.e., Nu = $0.00454\ Pe^{1.946}$, predicts the limiting value of h.

The pressure drop in the single phase region is compared with the Aerojet design correlation in Figure 3-17.

$$\dot{m} = A\left[\left(\frac{2g}{144}\ \rho\Delta p\right)/K_c + k_e + f\frac{L}{D}\right]^{1/2}$$

where

K_c = Contraction coefficient

K_e = Expansion coefficient

f = Friction factor.

Curves for 0 to 90 precent reduction in channel area are plotted to assess the effect of plugging. All measured pressure drops are considerably higher than the theoretical values. No explanation of these discrepancies is presently available.

3.5.2 Two Phase Flow

Correlation of the two phase flow data has been carried out at the University of Tennessee Space Institute computer code (1). The two phase flow region was analyzed using the governing equations:

$$\frac{d^2T_s}{dx^2} = \frac{h\ P(T_s - T_f)}{K_s A_c}$$

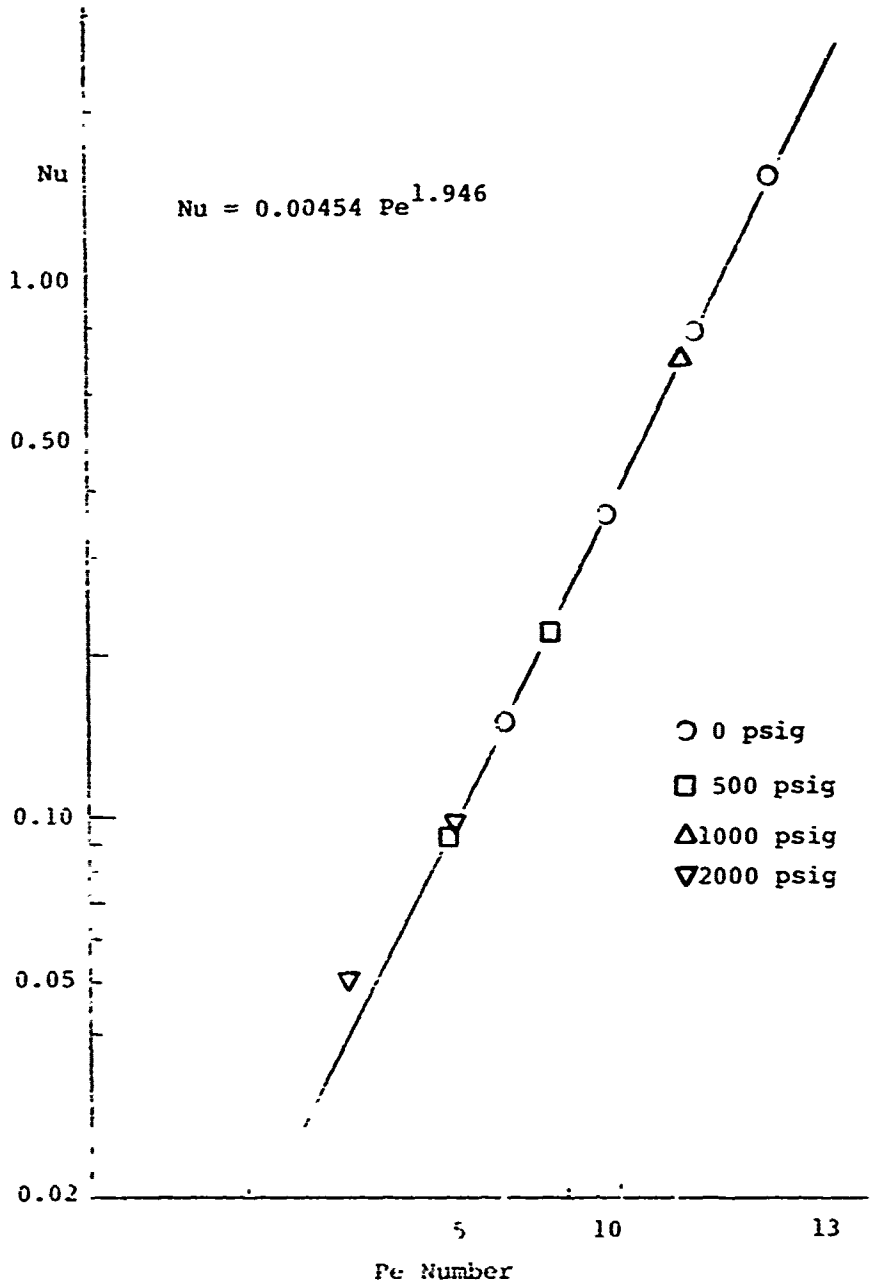

Figure 3-16. Correlation of Heat Transfer Coefficient for Liquid Water.

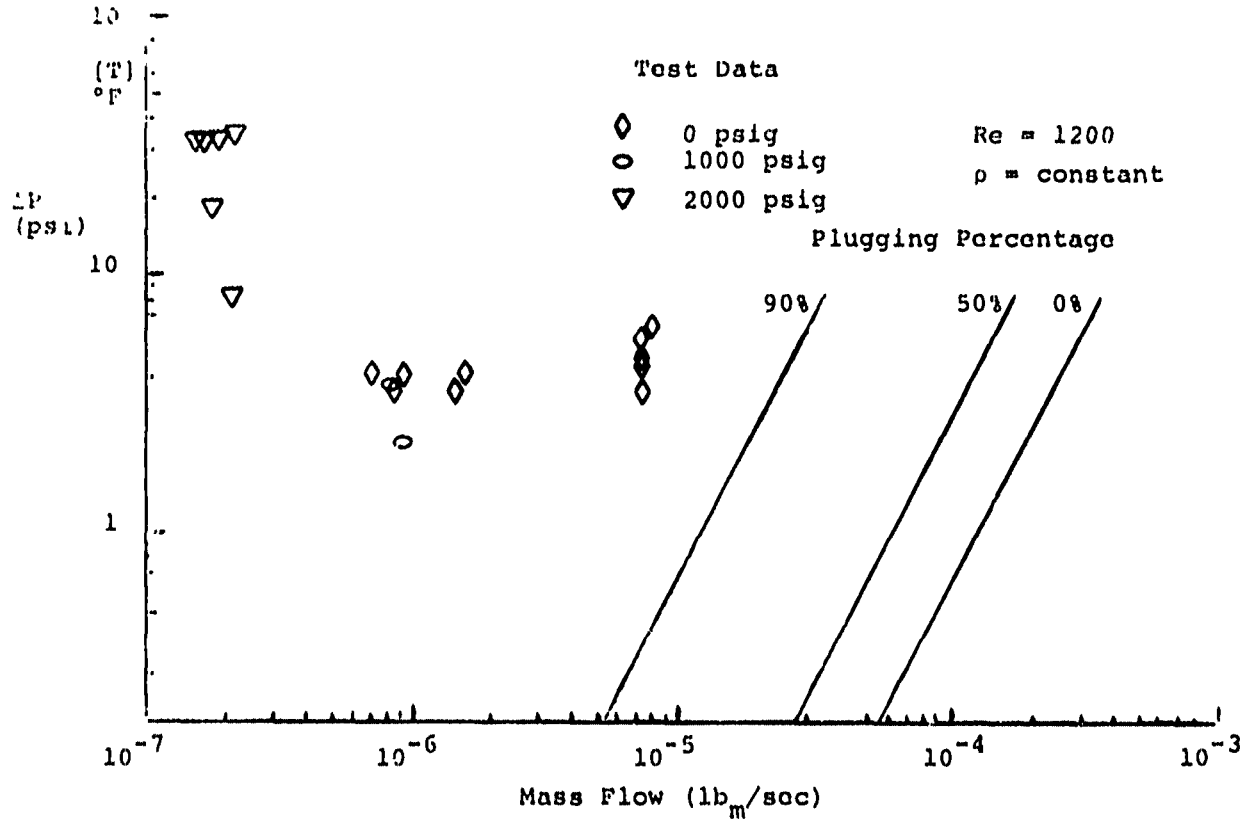

Figure 3-17. Comparison of Single Phase Pressure Drop With Aerojet Design Correlation.

$$\frac{dH_T}{dx} = \frac{h\,P(T_s - T_f)}{\dot{m}}$$

where

P = Periphery of slot

A_c = Cross-sectional area of solid

$\dot{m}$ = Mass flow rate of fluid per unit area of plate (lbm/ft^{2}sec)

In two phase regions, the quality ($\bar{x}$) is introduced and an additional equation is required. An energy balance equation on a volume fluid element can be written in terms of a variable, η. η is defined as the fraction of the total amount of thermal energy used for evaporation in an element of mixture of thickness dx. Thus the equation is:

$$\frac{d\bar{x}}{dx} = \eta \frac{P}{\dot{m}} \frac{h(T_s - T_f)}{h_{\ell g}}$$

η is a parameter which accounts for the departure from thermodynamic equilibrium. The limiting case, $\eta = 1.0$, means all the energy transferred to an element of mixture causes evaporation of the liquid and not superheating of the vapor; a constant vapor temperature also results. If $\eta = 0$, the quality would be constant and all heat transferred to the mixture would be used to superheat the vapor.

One parameter which is input to the analysis is the heat transfer coefficient. Precise relations for the coefficient are not available. For the forced convection region the heat transfer coefficient used is that for laminar fully developed flow in circular tubes:

$$h_c = Ek\frac{\alpha}{\beta}$$

where

k = Fluid thermal conductivity

α = Viscous resistance coefficient

β = Inertial resistance coefficient.

An average value for the constant E in the relation for the Nusselt number for constant heat flux and constant wall temperature was used.

The forced convection nucleate boiling heat transfer coefficient is estimated by superposition of forced convection and nucleate pool boiling coefficients.

$$h = h_{\text{forced convection}} + h_{\text{pool boiling}}$$

$$h = \frac{Nu\, k_\ell}{D_H} + \frac{k_\ell^3}{B^3 \mu_\ell^2 H_{\ell g}^2}\left[\frac{1}{\sigma}\left[\frac{1}{V_\ell} - \frac{1}{V_g}\right]\right]^{1/2} \frac{(T_s - T_\ell)^3}{T_s - T_f}$$

where B is a function of evaporating liquid and surface material. For water and stainless steel liquid-solid surface interaction B equals 0.013. σ is the surface tension and the subscript ℓ denotes values at saturated conditions. V is the specific volume.

A criterion for the value $(T_s - T_\ell)$ above which the transition to film boiling occurs is given by:

$$(T_s - T_\ell)^3_{crit} = \frac{0.397\, B^2 H_{\ell g}}{V_g F_\ell}\left[\frac{V_g}{V_\ell} - 1\right]^{0.6}$$

$$F_\ell = \frac{k_\ell^3}{\mu_\ell^2 H_{\ell g}^2}\left[\frac{1}{\sigma_\ell}\left[\frac{1}{V_\ell} - \frac{1}{V_g}\right]\right]^{1/2}$$

Where $H_{\ell g}$ is the latent heat of vaporization.

Figure 3-18 shows a comparison of the data for Test 15 - Run 1 with the computerd curve for a number of combinations of the parameters, h. η, G. For mass fluxes on the order of measured values, conventional boiling heat transfer coefficient and $\eta = 1$ (i.e., thermodynamic equilibrium) the correlation immediately departs from the two-phase flow data. By assuming a constant heat transfer coefficient and reducing its magnitude, the theoretical curves approach experimental values only for ridiculously low values of h. Finally, the theoretical curve can be matched to the measured data for reduced values of η.

3.5.3 Concluding Statements

It is pointed out that large uncertainties are contained in the correlations previously presented due to uncertainties associated with the value of mass flux as a result of plugging and heat flux due to leaks. Moreover, significant differences in qualitative, photographic, observations existed between the coolant state exiting the slot in these experiments and the coolant state exiting the slot in the combined cooling experiment. The major difference being that

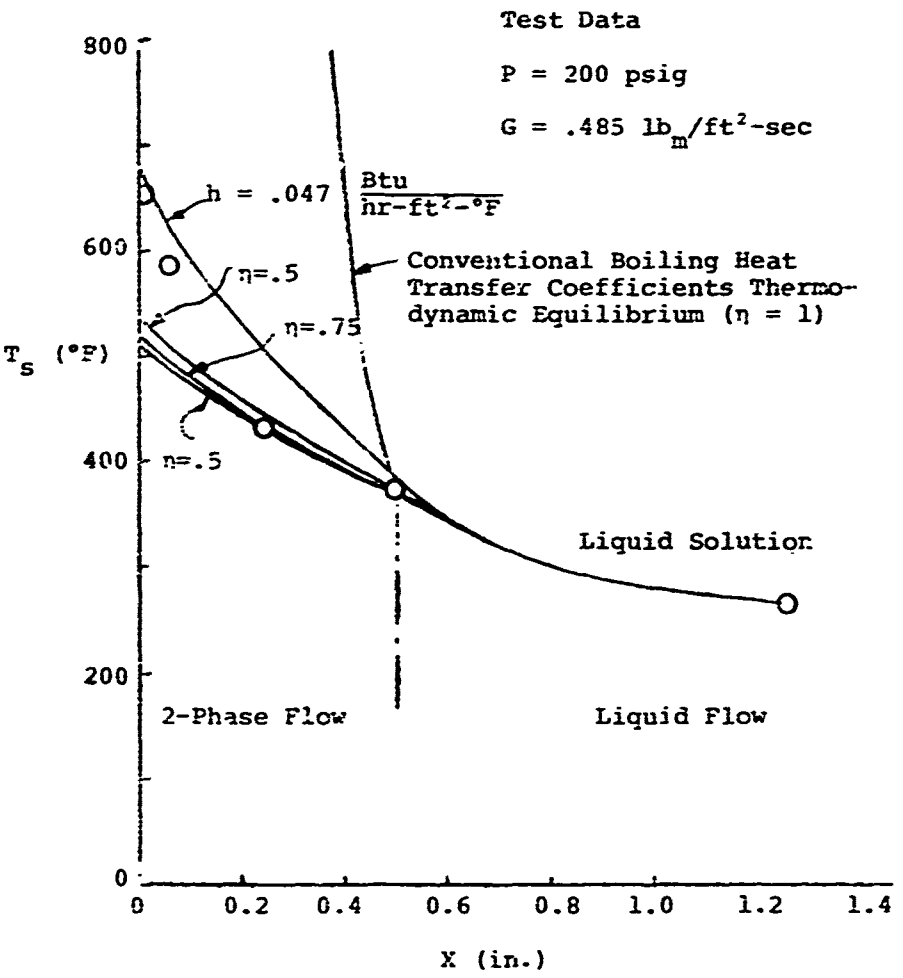

Figure 3-18. Comparison of The University of Tennessee Space Institute Computer Code Solutions With Data From Test 15, Run 1.

mass fluxes up to an order of magnitude larger were observed to produce two phase (mist) flow exiting the slots in the combined cooling experiment than in the internal cooling experiment. That is, at mass fluxes well within design values, only single phase (100 percent quality steam) exited the slots during the combined cooling experiment whereas under similar conditions two phase flow and liquid flow are observed in the internal cooling experiment. Moreover, at low mass fluxes liquid slugs were observed exiting the slot in the internal cooling experiment; however slug flow was never observed during the combined cooling experiment. This is attributed to the fact that heat was transferred to the slot exit as well as to the land (as is the case during reentry) in the combined cooling experiment. Thus it is concluded that the internal cooling experiment did not adequately simulate actual hardware heat paths in the vicinity of the slot exit. However, the results indicate that by employing reasonable assumptions, the single phase liquid data can be used to obtain a correlation between Nusselt number and Peclet number. Such correlations havebeen well established in the past and can be found in standard heat transfer texts (i.e., Reference 28). The two phase retuls can also be explained utilizing reasonable assumptions and employing standard correlation procedures, Reference 29. Hence, the approach to modelling internal cooling has been to rely on standard correlations given in References 28 and 29, adjusted so as to yield accurate predictions of the combined cooling results.

SECTION 4

EXTERNAL COOLING EXPERIMENT

The intent of the Nosetip Cooling Technology Program is to provide critical aerothermodynamic ground test data and supporting analyses for the design of discrete injected cooled nosetips. The purpose of the external cooling large slot experiment is to provide information pertaining to the detailed flow behavior of a supersonic turbulent boundary layer flowing over a series of rectangular openings (slots) through which a gaseous coolant may or may not be issuing. In particular, the large slot tests are to provide a description of the heat flux recovery over slot-land configurations for a wide range of injection rates. Such a description will be used as a baseline in establishing a correlation procedure which then may be used as an engineering design tool. Specifically, the large slot tests are to provide.

- A fluid mechanic description of the supersonic turbulent boundary layer over a slot-land discrete injection configuration.
- An aerothermodynamic description of the above phenomena.
- A data base for a correlation procedure to describe the aerothermodynamic behavior.
- A data point in the analysis of viscous - inviscid (separation) phenomena including in-depth slot aeromechanics.

In Section 4.1, the test facility description will be given in addition to the scaling procedures utilized in the rationalization of what combination of tunnel facility and model designs most closely reproduced the flight configuration and environment. Section 4.2 describes the models and Section 4.3 describes the model and tunnel instrumentation. In Section 4.4, the test matrix is described. Finally, Sections 4.5 and 4.6 present the results and conclusions of the large slot experiments respectively.

4.1 TEST FACILITY

4.1.1 Scaling Considerations

The wind tunnel used in this program was Tunnel B at AEDC, as described in Reference 30. Within this facility two modes of boundary layer testing are possible. The test may be conducted either on a model sting in the test stream

or testing can be done using the tunnel wall boundary layer. Testing in the wall boundary layer has the advantage of a sufficiently large boundary layer thickness to allow large slots and still maintain a slot size to boundary layer thickness ratio representative of flight. The test conditions, chosen to maximize wall heat flux for this experiment, was a free stream Mach number of 8 and the maximum Reynolds number attainable. Due to a twenty-three foot run between the nozzle throat and the test section, the boundary layer was fully turbulent. The wall boundary layer thickness at these conditions has been measured to be approximately 7 inches by Matthews and Trimmer in Reference 31. They also calculated the momentum thickness for this boundary layer to be approximately 0.25 inch. AEDC reported the nominal cold wall heat flux for this set of test conditions to be 0.58 Btu/ft^{2}sec, Reference 32*. An opening for windows for the schlieren system provided a convenient location in the test section wall to mount the model to be tested, as illustrated in Figure 4-1.

With the flow characteristics as defined, the design of the model was selected to obtain close scaling of flight conditions. The pertinent parameters for scaling the flight environment has been identified in the NCT proposal (Reference 33) and the experiment recommendation document (Reference 34). In these documents the rationale for the large slot tests was developed. The two principal slot-boundary layer interaction phenomena to be examined in this test series were slot augmented turbulent heating and heat flux recovery over the land between slots with blowing. Augmentation of the heating by the effective roughness of the slot-land configuration occurs as shown in Figure 4-2. One critical parameter for scaling this phenomenon is the ratio of the slot width to boundary layer momentum thickness (chosen as the boundary layer thickness parameter most relevant to augmented heating). In flight, the slot width to boundary layer momentum thickness (S/θ) ratio varies from 0.5 to 30.0. Since the lower end of this regime corresponds to low perceived roughness and thus little increase over smooth wall heating, this end of the range is of less interest. The nominal model slot width range corresponding to flight S/θ values is 0.125 inches to 7.5 inches. Unfortunately 7.5 inch slots could not be accommodated in the test area and five slots were selected as the maximum convenient size at the S/θ ratio of 20. Economics of model construction permitted only additional smaller slot size. Maintaining the bias towards the upper end of the S/θ range, a two inch slot (S/θ = 8.0) was selected as the additional model to be tested.

*These design values corresponded reasonably well to measurements during the actual testing where momentum thickness was calculated to be ~ 0.22 inch and the heat flux was about 0.48 Btu/ft^{2}sec. No major effect on the model scaling resulted from these variations.

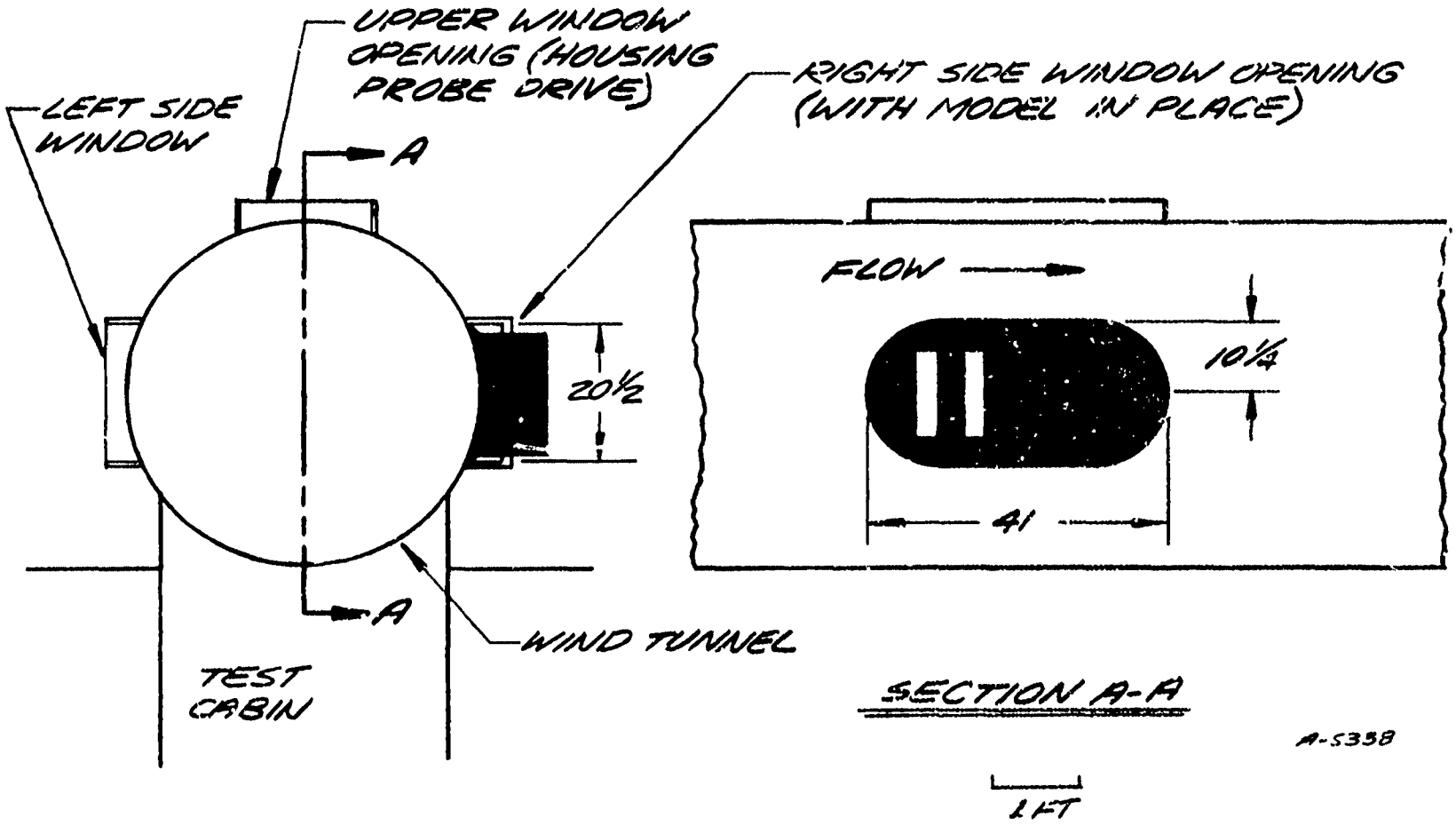

Figure 4-1. Tunnel B Window Layout

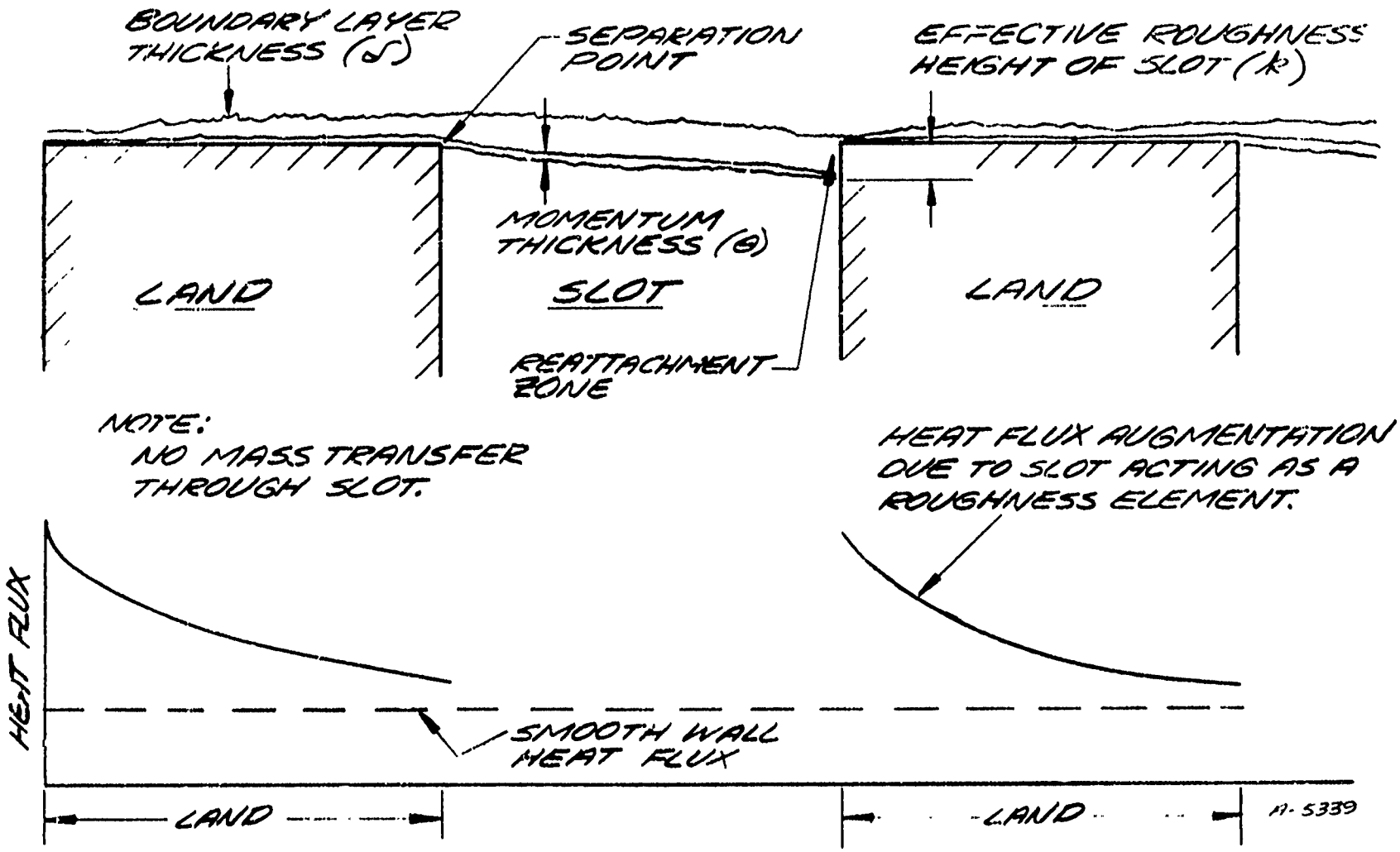

Figure 4-2. Apparent Roughness Due to Slots

The principal geometric factors of importance are the slot to land (S/L) ratio and the number of slots. The set of four configurations chosen (shown in Table 4-1) allow varying slot size while holding S/L ratio constant and also variation of S/L ratio at a constant slot size.

TABLE 4-1

MODEL CONFIGURATIONS

Slot Size (in)	Slot/Land Ratio	Land Size (in)
2.0	0.2	10.0
2.0	1.0	2.0
2.0	2.5	0.8
5.0	1.0	5.0

Having decided the slot and land sizes, the number of slots was determined next. Prime physical constraints in choosing the number of slots to test were as follows:

- The flight hardware has many slots, therefore multiple slot effects are of interest.
- Depending on the locations on the flight hardware, cooling is dominated either by the slot immediately upstream or by the integrated effect of numerous upstream slots (Reference 34). The model must allow enough slots to obtain data on integrated effects.
- Space is rather limited, with only 41 inches available in the flow direction for the entire experimental package.
- The total cooled length of plate should be kept as constant as possible from one test to another so that no major coolant supply system changes are needed.
- A significant amount of room downstream of the last slot is needed for the heat transfer to recover to its unblown value. Measurement of this entire recovery process is desirable.

An analysis of the heat transfer recovery rate downstream of multiple slots was made using the method of Chin et al., (Reference 34) extended to compressible flow. The results were relatively insensitive to the various configurations, depending mainly on the total cooled length. Thus a nominal cooled length of 10 inches was selected as reasonable for the 41 inch total length available

resulting in the numbers of slots as shown in Table 4-2. The 2.0/10.0 and 5.0/5.0 configurations required somewhat longer cooled lengths to maintain the minimum experimental configuration.

TABLE 4-2

NUMBER OF SLOTS

Slot (in)	Land (in)	Number of Slots	Total Included Cooled Length (in)
2.0	10.0	2	14.0
2.0	2.0	3	10.0
2.0	0.8	4	10.4
5.0	5.0	2	15.0

Two additional geometric considerations required definition before completely resolving the model configurations: 1) slot overlap, and 2) slot aspect ratio. The flight hardware has an overlapping slot pattern to prevent formation of long uncooled regions between the ends of the slots. This staggering induces a corner effect which was modeled for the 2.0 inch slot, 2.0 inch land case. The second of the three slots was partially blocked by a solid insert of half slot width (Figures 4-3) and the test matrix repeated to produce a variation in upstream boundary conditions to the third slot corresponding to the flight case. Additional instrumentation was placed around the corner to observe any flow perturbations.

Aspect ratio simulation is realistic, varying from 3.2 to 20 as the S/θ ratio increases. The flight values for the Aerotip vary in the same general range with aspect ratios from about 3 to 15. Aspect ratio increases as the boundary layer grows in moving toward the rear of the tip.

The remaining parameter to scale to flight after the gemoetry has been determined is the coolant flow rate. For the present series of tests, only one gaseous coolant, N_2, was injected. The tests attempted to cover the entire range of the flight vehicle dimensionless blowing parameter B',

$$B' = \frac{\dot{m}_{coolant}}{\rho_e u_e C_H}$$

Figure 4-3a. ?.0/2.0 Model Without Filler Block

Figure 4-3b. 2.0/2.0 Model With Filler Block In Place

In flight, B' varies between 0.5 and 2.0 with overcooling above these values by a factor of 3 on some regions of the nosetip. For a nominal tunnel wall heat transfer rate of 0.6 Btu/ft^2-sec, the cooling rates of interest are 0.0012 - 0.0113 lb/ft^2-sec, over the entire vehicle surface. To determine the mass flow rates for each slot a cooled area must be associated with each slot. From flight design procedures, it appears that each slot is primarily responsible for protecting an area consisting of itself and the land region immediately downstream. The flow rates from the slots of the external cooling model were adjusted accordingly to protect an area consisting a length equal to the slot and one land and a width equal to the width of the slot in the transverse direction. The blowing rates from the slots which correspond to the maximum and minimum mass transfer rates are shown in Table 4-3. Also listed are the ratios of slot blowing rate to the freestream specific mass flow rate, λ,

$$\lambda = \frac{\dot{m}''}{\rho_e U_e}$$

The nominal values of λ for the total cooled area range from 1.34×10^{-3} for the maximum blowing down to 1.425×10^{-4} for the minimum case.

In addition to the standard series of tests at margin factors (over-cooling ratios) of 3 or less, one test was run under massive blowing conditions for the 2.0/2.0 model. This test was conducted at the maximum flow rate the coolant system could provide. The average λ over the cooled surface resulting from this test was 4.03×10^{-3}.

4.1.2 AEDC, Tunnel B, Test Facility

All testing was performed in Tunnel B of the Von Karman Gas Dynamics Facility at AEDC. The tunnel is an axisymmetric continuous flow facility with a Mach 8 nozzle. A natural gas air preheater is required to prevent condensation of the air in the tunnel. The operating conditions for the large slot tests are listed in Table 4-4. These are nominal conditions for operation in the closed circuit mode and were maintained constant through the tests.

TABLE 4-4

WIND TUNNEL OPERATING CONDITIONS

Stagnation Pressure	850 psia
Stagnation Temperature	1350°R
Mach Number	8
Freestream Reynolds Number	3.6×10^5/ft

TABLE 4-3

COOLANT FLOW RANGES

Configuration	Coolant Flow Rate Over Surface lbm/ft^2sec	Coolant Flow Rate/Slot $lbm/sec/ft^2$ of slot area	λ_{slot}
Normal Testing			
2.0/0.8	0.0012	0.0017	2.02×10^{-4}
	0.0113	0.0158	1.88×10^{-3}
2.0/2.0	0.0012	0.0024	2.85×10^{-4}
	0.0113	0.0226	2.69×10^{-3}
2.0/10.0	0.0012	0.0072	8.56×10^{-4}
	0.0113	0.0678	8.06×10^{-3}
5.0/5.0	0.0012	0.0024	2.85×10^{-4}
	0.0113	0.02..	2.69×10^{-3}
Massive Blowing			
2.0/2.0	0.0339	0.0678	8.06×10^{-3}

The test section for Tunnel B is nominally fifty inches in diameter with a slight expansion in the downstream direction to allow for boundary layer growth. There are three observation ports in the test section, one on top and one on each side. The observation (or Schlieren) port opening (Figure 4-1) is approximately oval, measuring 41 inches in length by 21 inches in width, with the long axis aligned with the flow. The model was placed in the right side port when looking upstream. The model surface thus could be examined through the observation port on the control room side of the tunnel.

4.2 MODEL AND TEST HARDWARE

The general assembly of one configuration for the experiment is shown in Figure 4-4. The three major components of the test apparatus are the model, the support assembly, and the flow distribution system. The model is the heart of the experiment providing the test surface, slots for injection, and housing for the instrumentation. The support apparatus mated the model to the tunnel opening and provided a means of adjusting the model position to best fit the tunnel contour. The flow distribution system provided the air for injection and the water for cooling the model.

4.2.1 Models

The model was cast from aluminum to the approximate shape required. The results are shown in Figures 4-5 and 4-6. In general, the models were solid with little evidence of porosity. Some minor filling was required on the machined surface and three pressure taps were found to be leaking due to internal leakage. These taps were not at critical locations and were sealed at the flow surface to prevent leakage through the model which might perturb the experimental results. In order to fit the internal contour of the tunnel, the surface of the model is conical with a 0° 45' taper from front to rear. This contour was machined to a 63 microinch finish. Machining drawings of the model (Figure 4-4) are included for a typical configuration (2.0 inch slot, 2.0 inch land) to indicate the complexity of the machining performed. The other configurations are essentially identical with the exception of the slot/land ratios. The 5.0 inch slot model was also increased in height from approximately 7.5 inches to approximately 11.5 inches. The increased height of the 5.0 inch slot model was incorporated to retain a deep slot, i.e., slot length to height ratio less than 0.5. The machined results are shown in Figure 4-5 for the flow surface and Figure 4-6 for the back side. To provide the simulation of overlapping slots, a half slot filler block was fabricated to fit the second slot in the 2.0/2.0 model. The filler block was machined in place at the same time the model was contour machined, thus there was no discernable change in surface finish and no step

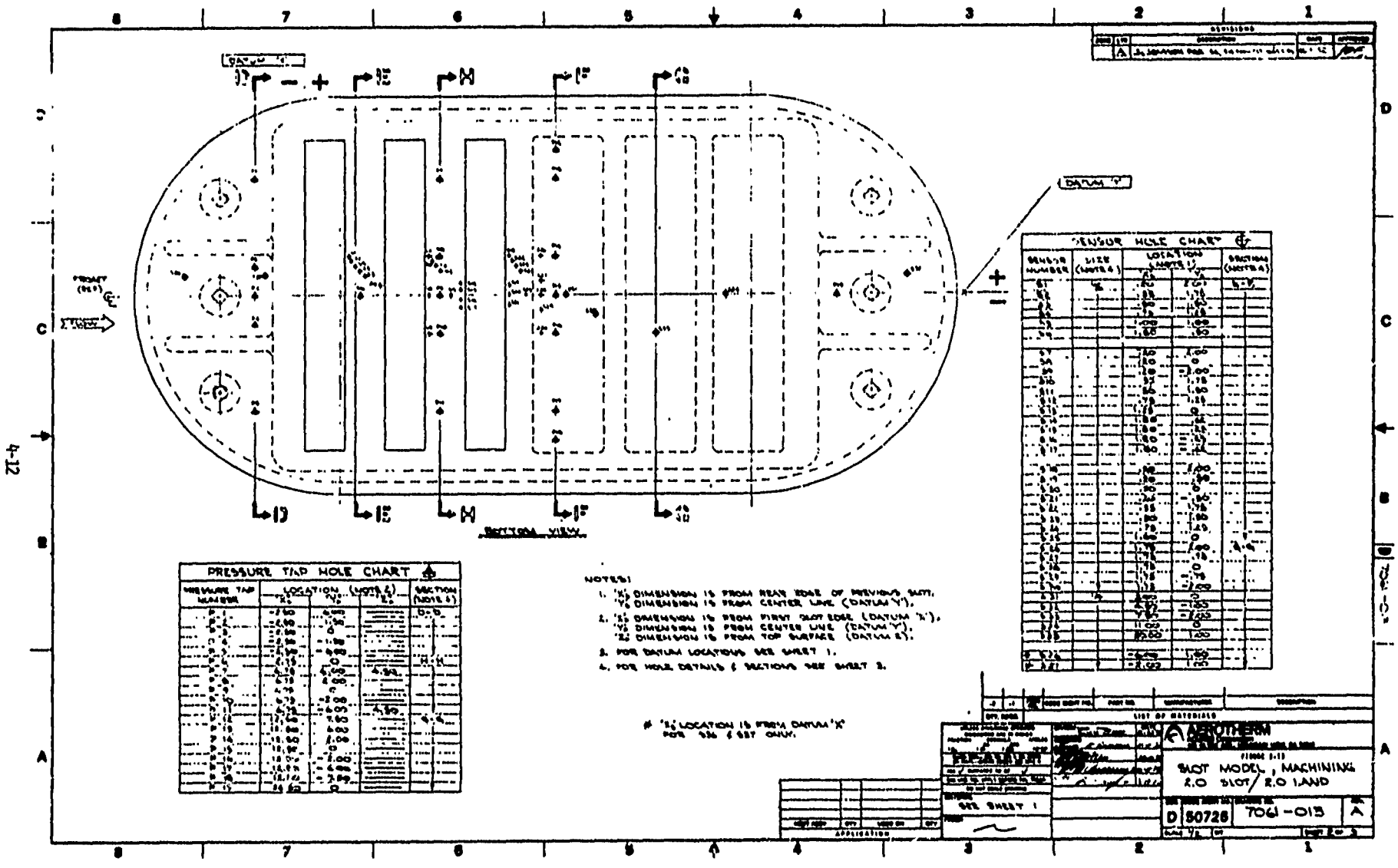
SECTION VIEW
PRESSURE TAP HOLE CHART
SENSOR HOLE CHART
NOTES:
1. 'X' DIMENSION IS FROM REAR EDGE OF PREVIOUS SLOT.
'Y' DIMENSION IS FROM CENTER LINE (DATUM 'Y').
2. 'X' DIMENSION IS FROM FIRST SLOT EDGE (DATUM 'X').
'Y' DIMENSION IS FROM CENTER LINE (DATUM 'Y').
'Z' DIMENSION IS FROM TOP SURFACE (DATUM 'Z').
3. FOR DATUM LOCATIONS SEE SHEET 1.
4. FOR HOLE DETAILS & SECTIONS SEE SHEET 3.
'X' LOCATION IS FROM DATUM 'X' FOR 936 & 937 ONLY.
SEE SHEET 1
AEROTHERM
SLOT MODEL, MACHINING
2.0 SLOT/2.0 LAND
D 50726
7061-015

Figure 4-4.

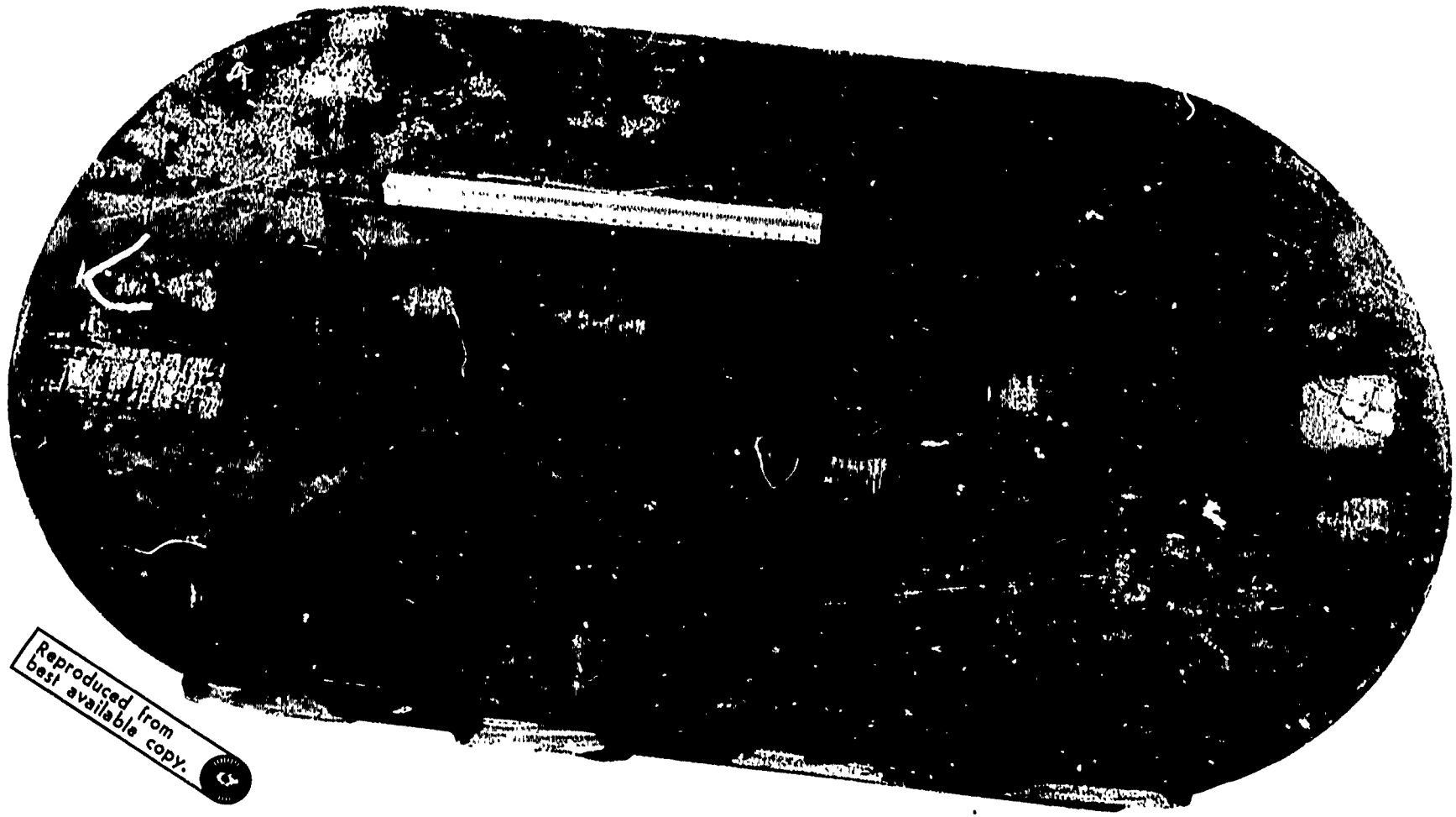

Reproduced from best available copy.

Figure 4-6. Photo Of Model Backside As Cast

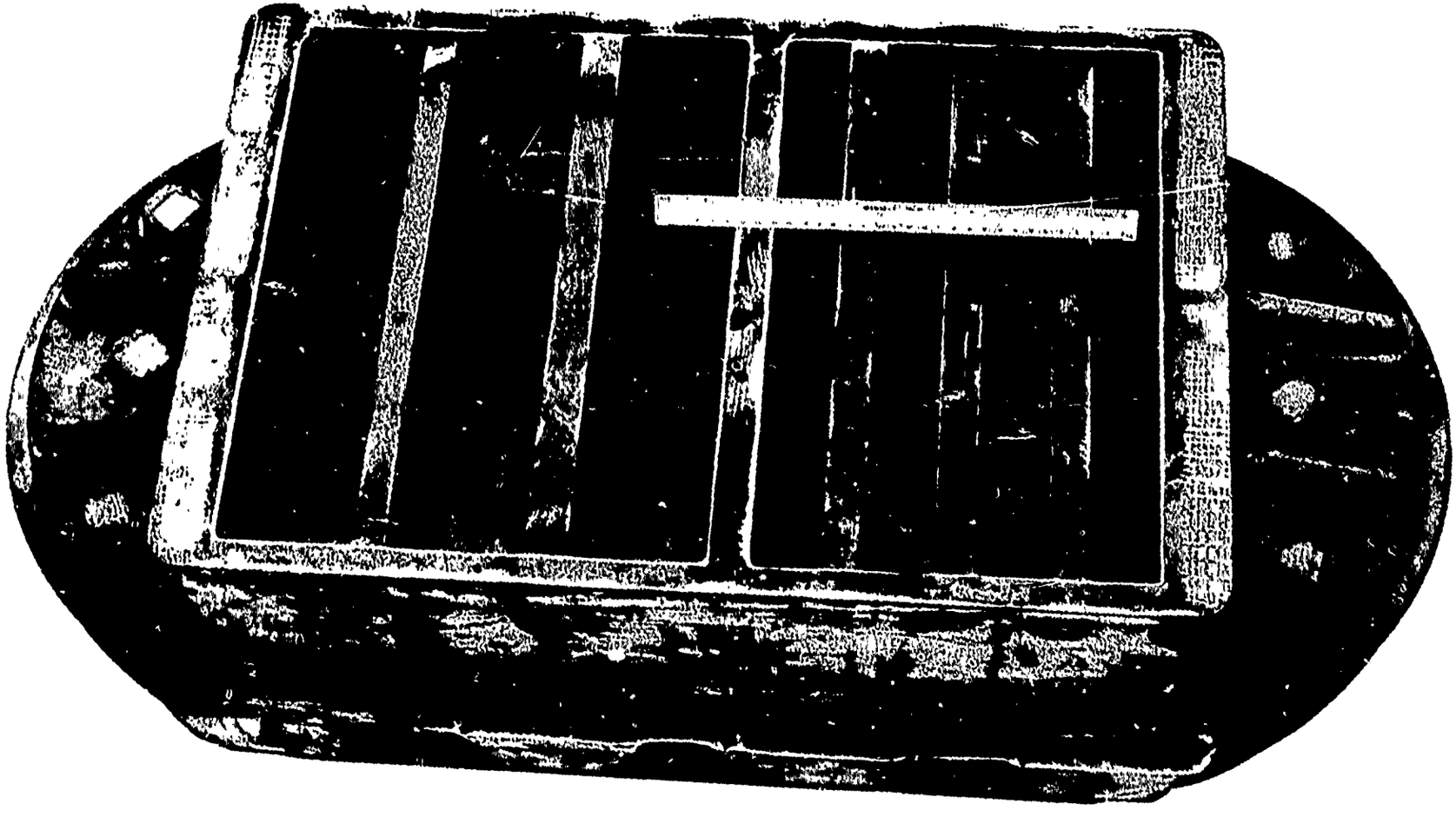

Figure 4-5. Photo of Model Flow Surface As Cast

between the model and filler block. Figure 4-3b shows the filler block as it appeared when installed and also demonstrates the array of sensor locations used to indicate the effects of the overlapping slot on the heat transfer distribution.

Since the wind tunnel flow is continuous, provision was made for cooling the model to prevent overheating. The tunnel walls are water cooled and thus to avoid a step in wall temperature which could drastically affect the boundary layer profiles, cooling was designed to maintain the model at approximately the tunnel wall temperature. Two principal forms of water cooling were used. Cooling passages were drilled through the ribs of the casting with bypass loops utilized to avoid conflict with instrumentation holes. Cooling loops were also placed on the front and rear lips of the casting. These additional cooling loops were added just before testing as a precaution to eliminate any overheating of the front and rear extremities of the plate due to the distance to the closest cooling passage in the model. Operation of these systems gave a uniform model wall temperature of approximately 80°F, quite comparable to the tunnel wall temperatures.

The tunnel static pressure is about 0.1 psia, requiring some form of sealing to prevent room air leakage into the tunnel. To maintain access to the instrumentation on the back side of the model, the seal was made between the wall of the window opening and the perimeter of the model. A Presray inflatable rubber seal mounted in a notch on the edge of the model as shown in Figure 4-7. To prevent possible overheating of the rubber inflatable seal which was in an especially vulnerable position, the seal was pressurized (inflated) with circulating water. Inflated, the seal appeared to conform adequately to the interior surface of the window well. Since the window walls were relatively rough, painted surfaces leakage was anticipated. To minimize the influence of any leaks, the gap between the tunnel surface and the model was filled with RTV silicone rubber except for the rear semicircular area which was left open as a vent. Any leaks should then be exhausted downstream without effect on the experiment. Zyglo dye penetrant was sprayed around the accessible seal area and the window well was examined with a black light for evidence of leakage. No Zyglo was found, indicating acceptable sealing was achieved. The seal was equipped with an inlet and outlet about three inches apart with a flow restrictor between them allowing pressurization with approximately 35 psig water, resulting in a flow rate of about 0.5 gal/min through the seal (Figures 4-8 and 4-9).

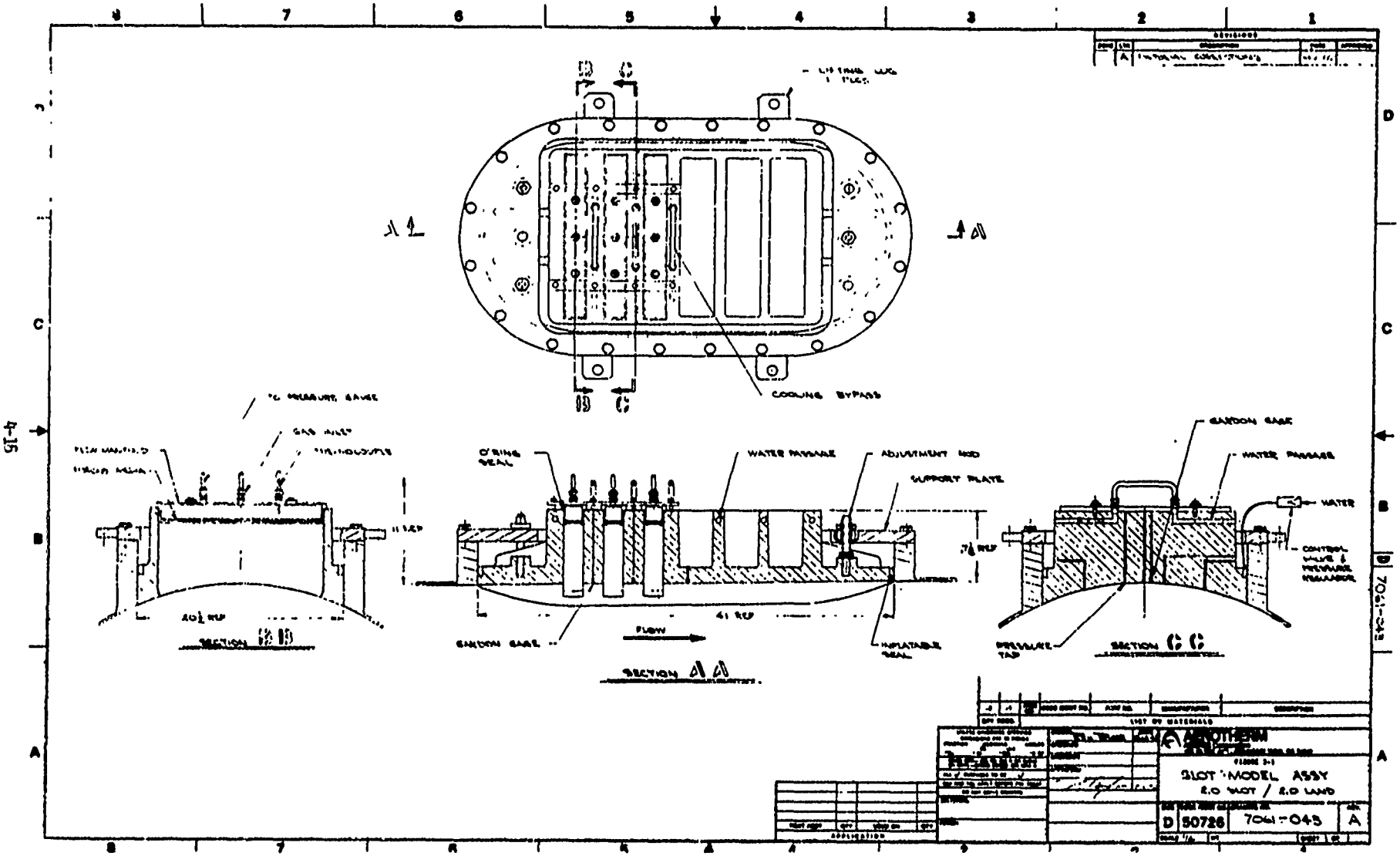
COOLING BYPASS
SECTION B B
SECTION A A
SECTION C C
FLOW
O'RING SEAL
WATER PASSAGE
ADJUSTMENT ROD
SUPPORT PLATE
GAUGE
INFLATABLE SEAL
PRESSURE TAP
WATER
SLOT MODEL ASSY
2.0 SLOT / 2.0 LAND
D 50726
7041-045
A

FIGURE 4-7

Figure 4-8. 2.0/2.0 Model In Preparation (Flow Surface)

Figure 4-9. 2.0/2.0 Model Backside In Preparation

4.2.2 Support Assembly

The support ring shown in Figure 4-10 was used to mount the model in the opening. The model was connected to the support ring by three adjustment rods which allowed some freedom to fit the tunnel contour. The support ring then bolted to the mounting circle used by the schlieren window fixture. The adjustment rods proved quite useful in obtaining the proper match of the model to the tunnel contour. The adjustments were predicated on fitting the forward end of the model flush at the centerline, then attempting to match the rest of the front to the wall and finally making whatever adjustments were possible to bring the tail of the model into position. The resulting fit in general was very good. Typically, with the forward centerline flush, there was a rearward facing step of about 0.010 in. at the upper and lower forward corners of the model and the tail of the model extended about 0.060 in. into the flow.

It would have been desirable to have had some means of adjusting the model in the window opening to ease alignment of the model centerline with the tunnel centerline. With the present arrangement, the only adjustment is through the play in the holes on the bolt circle resulting in a sometimes tedious alignment process. In general this was not a major concern, only on the half slot model was there a problem. On that model the tunnel centerline was 80 mils above the end of the filler block. Since the boundary layer surveys were referenced to the tunnel centerline, there were some discrepancies in attempting to survey matching points above and below the filler block.

4.2.3 Flow Distribution System

The flow distribution system for the large slot tests was comprised of three diverse subsystems. Most crucial of the three subsystems was the injectant supply to the slots which was basic to the experiment and also represented the major source of problems in the course of the tests. The two coolant water systems feeding the model and the seal operated routinely.

The major components of the N_2 supply system are shown in Figure 4-11. The sole means of adjustment of the flow was the adjustable control valve (1) upstream of the AEDC-supplied sonic orifice (2) the flow was then stagnated in a plenum (3) and from there a set of matched orifices (4) delivered equal amounts of flow to each flow distribution box (5) and thus to each slot. Although the general system concept was valid and ultimately worked well, there were three problem areas which arose. The first problem was the uniformity of mass injection to the slot. While little attempt was made to affect the flow pattern in the slot from the time the flow left the box, it did appear desirable to avoid inducing any major nonuniformities in the injection pattern at the

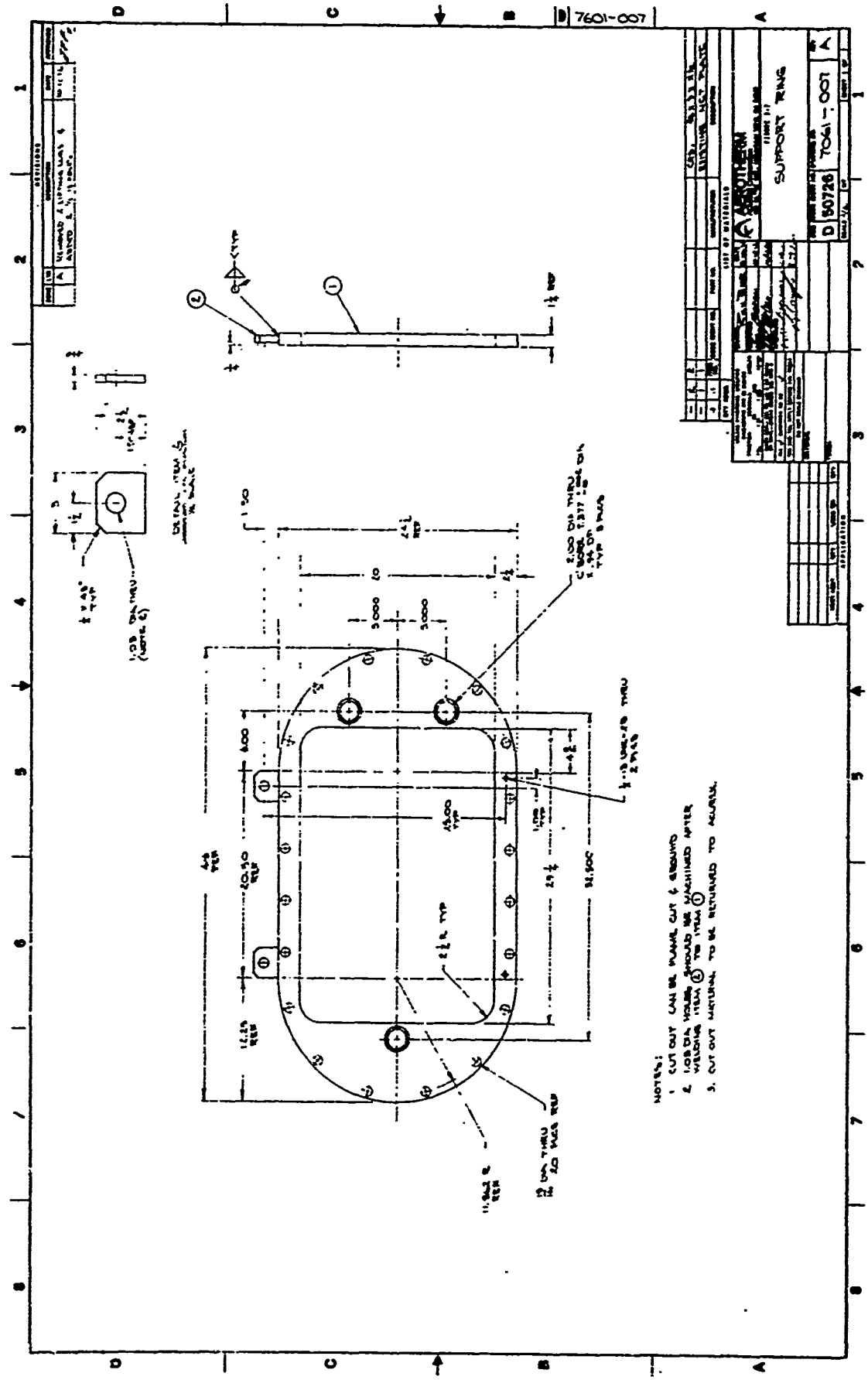
7601-007
SUPPORT RING
D 80726 7061 - 007
NOTES:
1. CUT OUT CAN BE FLAME CUT & GROUND
2. 1.05 DIA HOLES SHOULD BE MACHINED AFTER WELDING ITEM ② TO ITEM ①
3. CUT OUT MATERIAL TO BE RETURNED TO ACUREX.

FIGURE 4-10

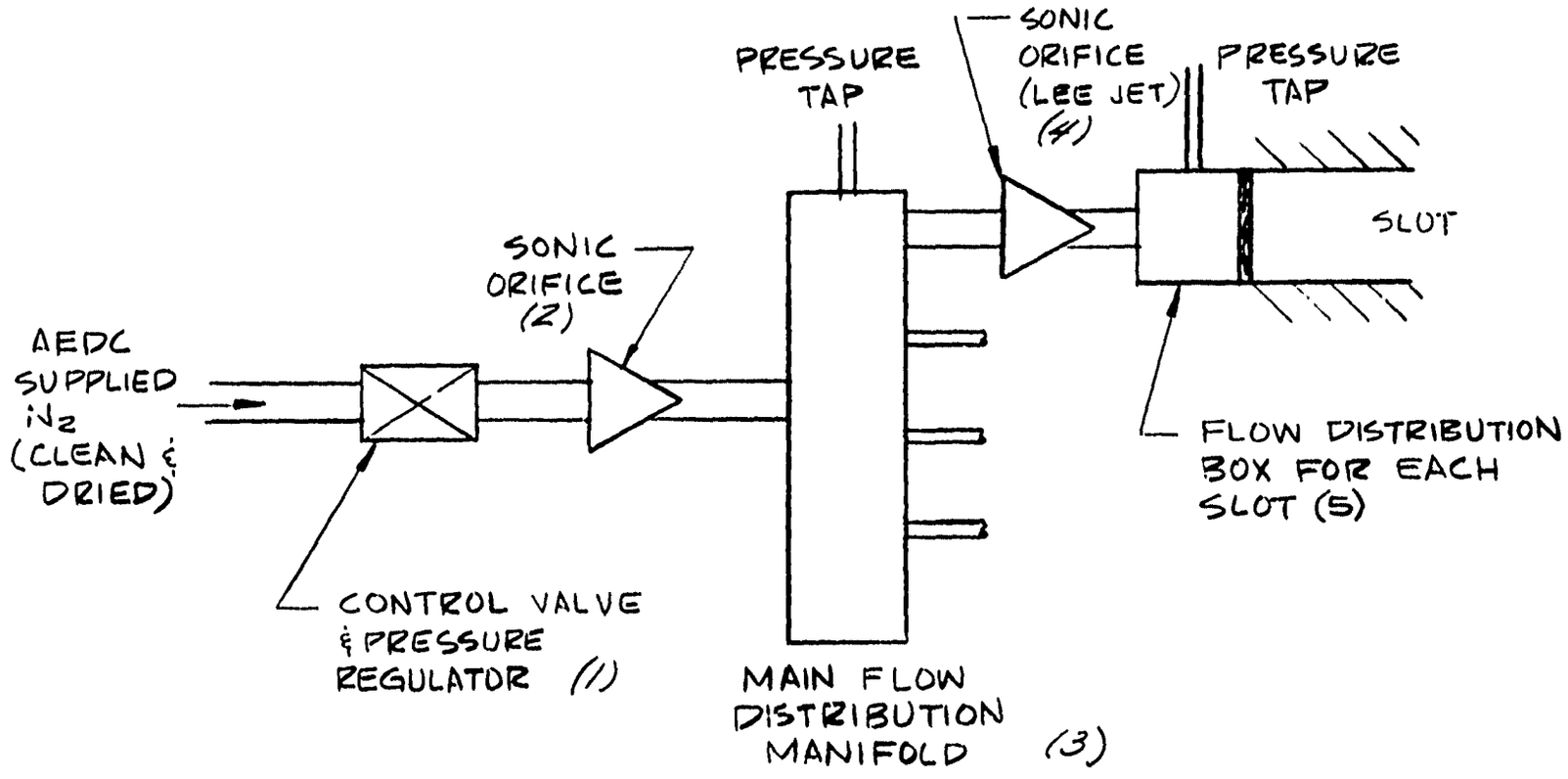

Figure 4-11. Schematic of Flow Distribution Network

A-5213

bottom of the slot. After fabrication and testing of alternative approaches, the most feasible method of maintaining uniformity appeared to be the concept shown in Figure 4-12. The flow uniformity of the box arrangement as shown was tested to be on the order of ± 10 percent at the porous media, which was judged to be acceptable.

Obviously the success of the experiment was dependent on knowing the actual mass flux from the slot and therefore any leakage from the atmosphere through the boxes was intolerable. The first testing performed at AEDC indicated that there definitely was leakage into the slot. Subsequent tests confirmed that the first day's results had been gravely affected by the extra mass addition. Leakage was occuring at the bond line between the box proper and the side rails. The side rails retained the O-ring which sealed the box to the top of the slot (Figure 4-13). When the tunnel was evacuated, the Scotchweld bond proved incapable of withstanding the shear forces and cracked. The solution chosen was to clamp the siderails tightly to the box to minimize the size of the cracks and then apply heavy vacuum grease liberally over the entire box surface and the joints between the box and the model. This arrangement appeared to work satisfactorily. The entire assembly was saturated with Zyglo and the slot surface checked both during testing and at the conclusion. For all tests there appeared to be no weeping of the Zyglo through the vacuum grease to the slot and thus a leakproof seal was assumed.

The other major problem found in the flow distribution system was the nitrogen supply system used by AEDC. The flow apparently was being contaminated by dirt from an undetermined source. Despite the high initial quality of the input nitrogen and the presence of a filter in the line, sufficient amounts of particulate matter were flowing through the control valve to foul the valve seat and, on one occasion, to clog the AEDC orifice. For the first two models (2.0/10.0 and 5.0/5.0) this contamination problem resulted in major delays in the testing. Modifications made after the completion of testing for the second configuration eliminated the problems and from that point on, the flow distribution systems appeared to have worked quite reliably. When the AEDC orifice was clogged, the data was not lost and could still be salvaged if the resulting partial flow rates were of interest. The model orifices which actually fed the slots were equipped with screens and showed no signs of clogging. The flow rates, while not set with the model orifices, were measured with those orifices and then are correct.

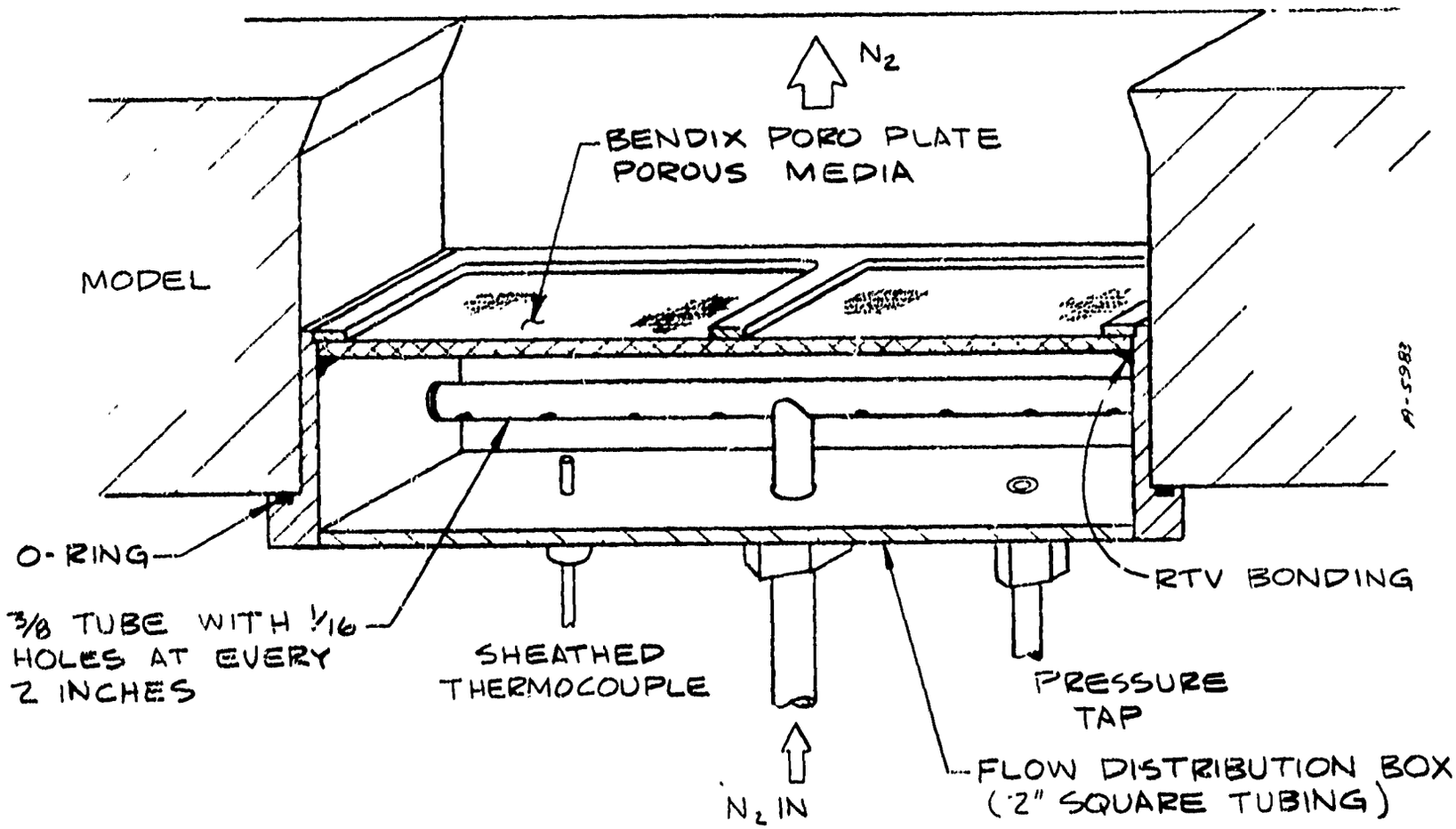

Figure 4-12. Flow Distribution Box Assembly

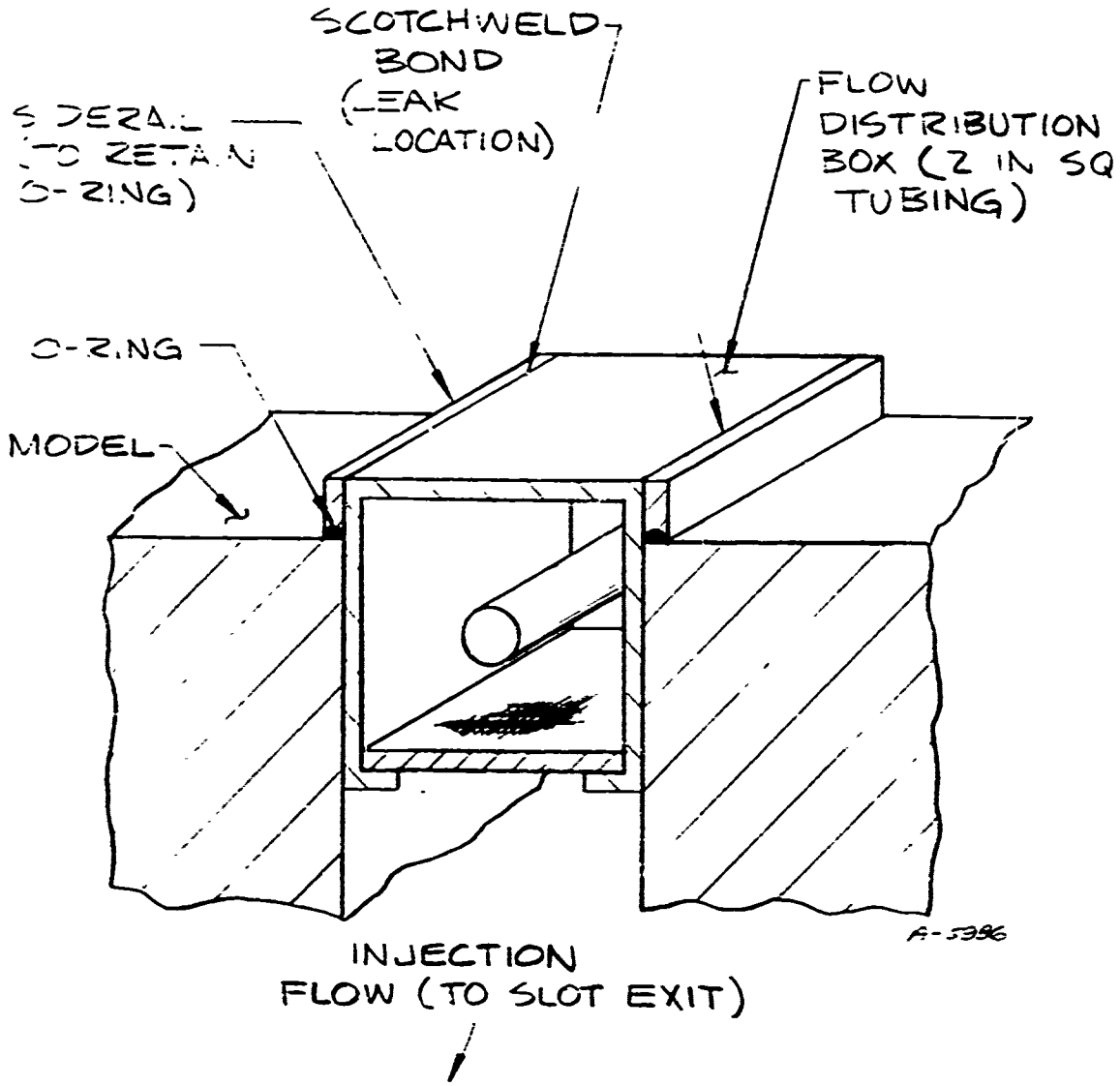

Figure 4-13. Leak Path Detail

4.3 INSTRUMENTATION

4.3.1 Heat Flux Instrumentation

The critical instruments for this test program were the heat flux sensors. The problems associated with selection of heat flux sensors were magnified by the low heat flux level (~ 0.5 Btu/ft^{2}sec) and the requirement for steady state instrumentation. The only feasible sensor for this application appeared to be a thermopile Gardon gage. The thermopile gage uses vapor-deposited layers of antimony and bismuth to form a thermopile on the back of the sensing foil and thus amplify the signal corresponding to the foil center temperature. The result is an order of magnitude increase in sensitivity over conventional Gardon gages as shown in Table 4-5 from Reference 7. The sensitivity shown is the level at which gage errors exceed ± 5 percent of the input heat flux.

TABLE 4-5

GARDON GAGE SENSITIVITY

Diameter (in)	Response Time (sec)	Conventional Gage Sensitivity (Btu/ft^{2}sec)	Thermopile Gage Sensitivity (Btu/ft^{2}sec)
0.125	0.2	1.0 - 20	0.2 - 20
0.187	0.5	0.4 - 18	0.04 - 18
0.250	1.0	0.2 - 15	0.01 - 15

Considering the nominal heat flux range, it is apparent that the thermopile gage was the only choice. By proper amplification the response from a conventional Gardon gage can be increased but only at greatly increased expense.

The 0.25 inch diameter gages represent a more desirable sensor for a variety of reasons. They are more sensitive, they are easier to fabricate, and they are more rugged and reliable. Unfortunately even in the largest slot case, large changes in the heat flux level, particularly at low coolant flow rates, occur in a region short enough to require use of the 0.125 inch gages. The conflict between gage size and sensitivity is a definite problem in resolving the initial heat flux recovery. Figures 4-14 define the predicted heat flux recovery for a typical maximum flow rate case from the Chin correlation (Reference 34). The results from the Chin correlation were used only as guides to possible heat flux behavior and not as definitive predictions of the gage behavior. The correlation did not account for the magnitude of roughness augmented heating actually seen and thus the spacing might have been less than optimum except

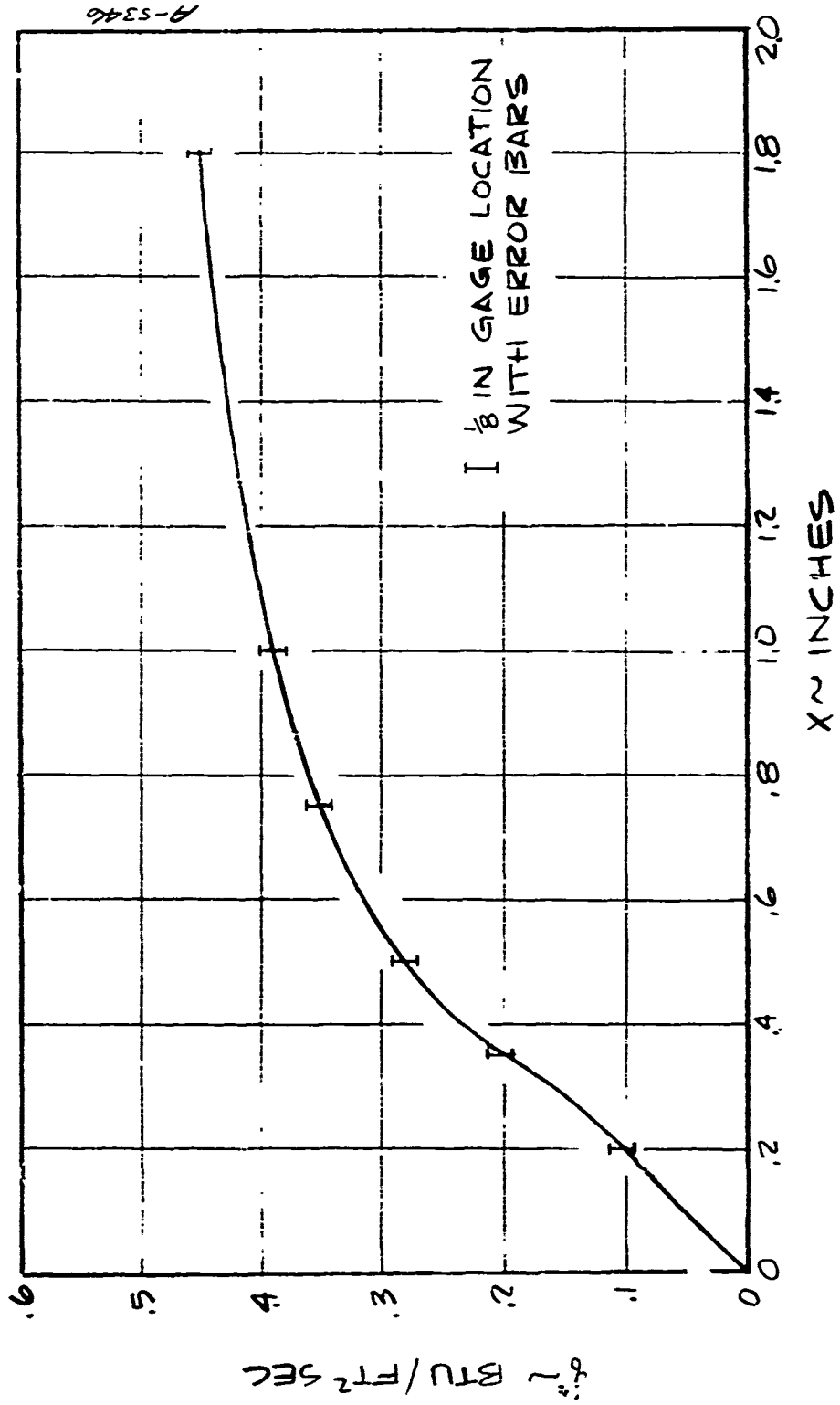

Figure 4-14a. Heat Flux Recovery 2.0/2.0 Configuration Land 1 - Maximum Flow Rate

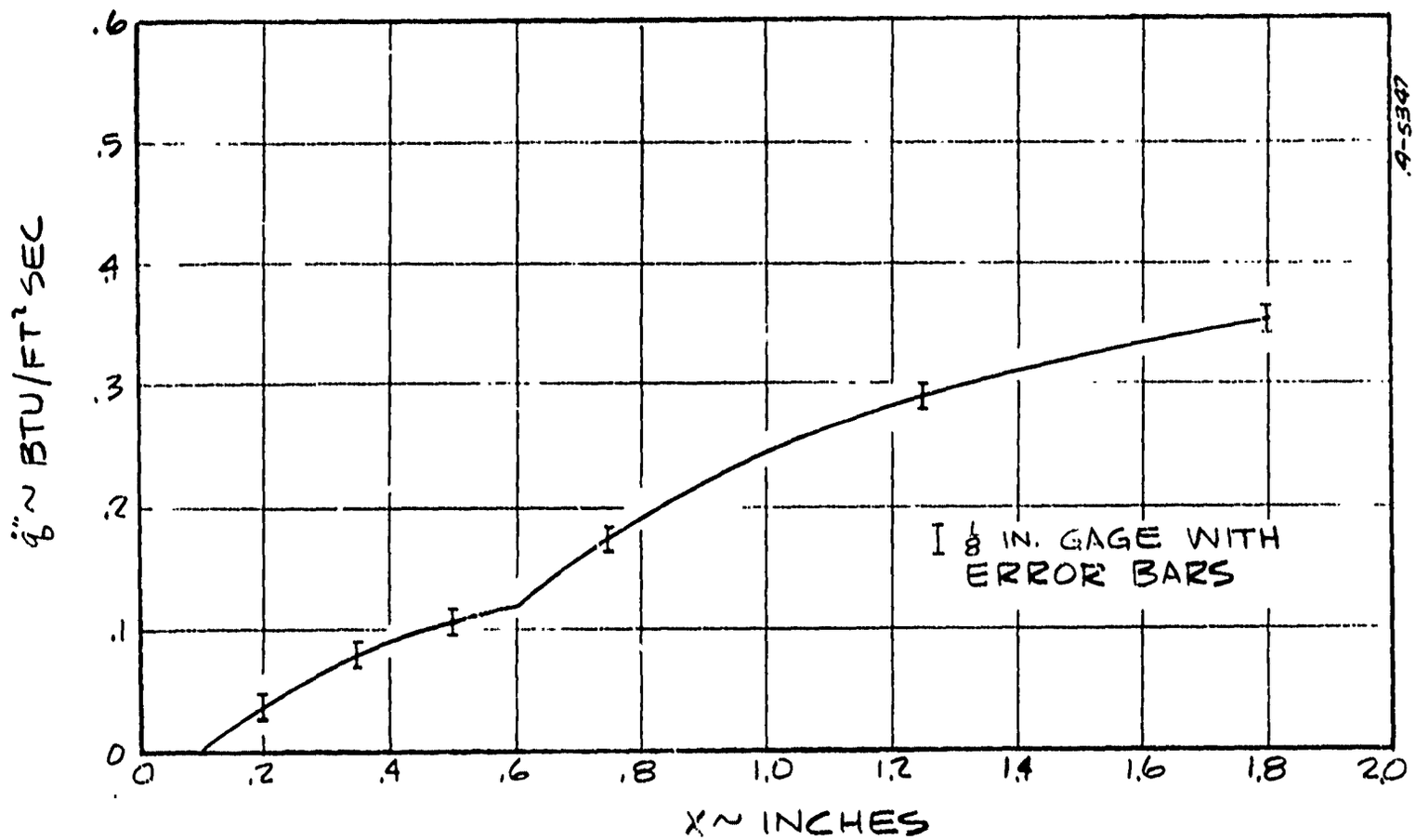

Figure 4-14b. Heat Flux Recovery 2.0/2.0 Configuration Land 2 Maximum Flow Rate

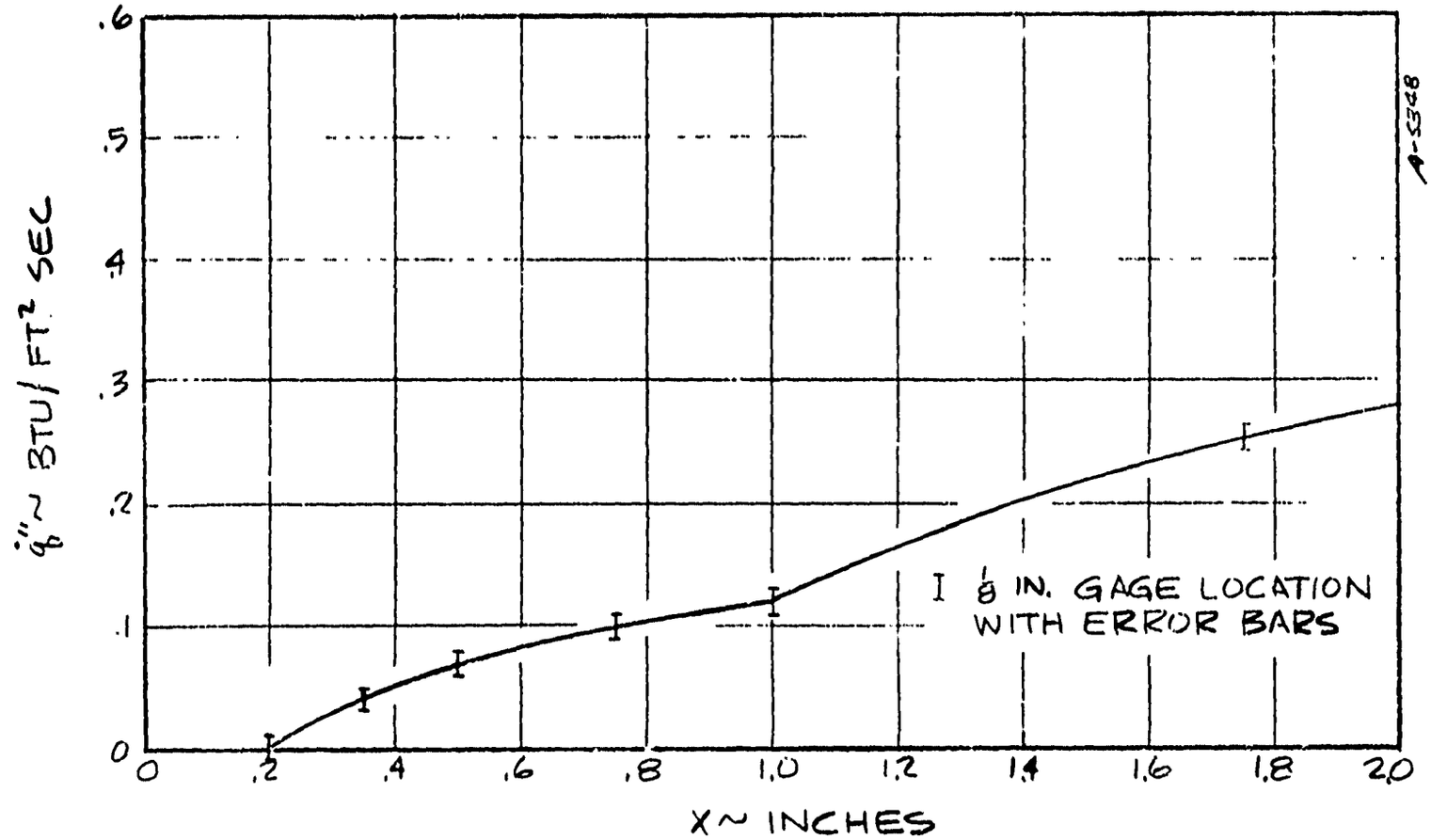

Figure 4-14c. Heat Flux Recovery 2.0/2.0 Configuration Downstream Section Maximum Flow Rate

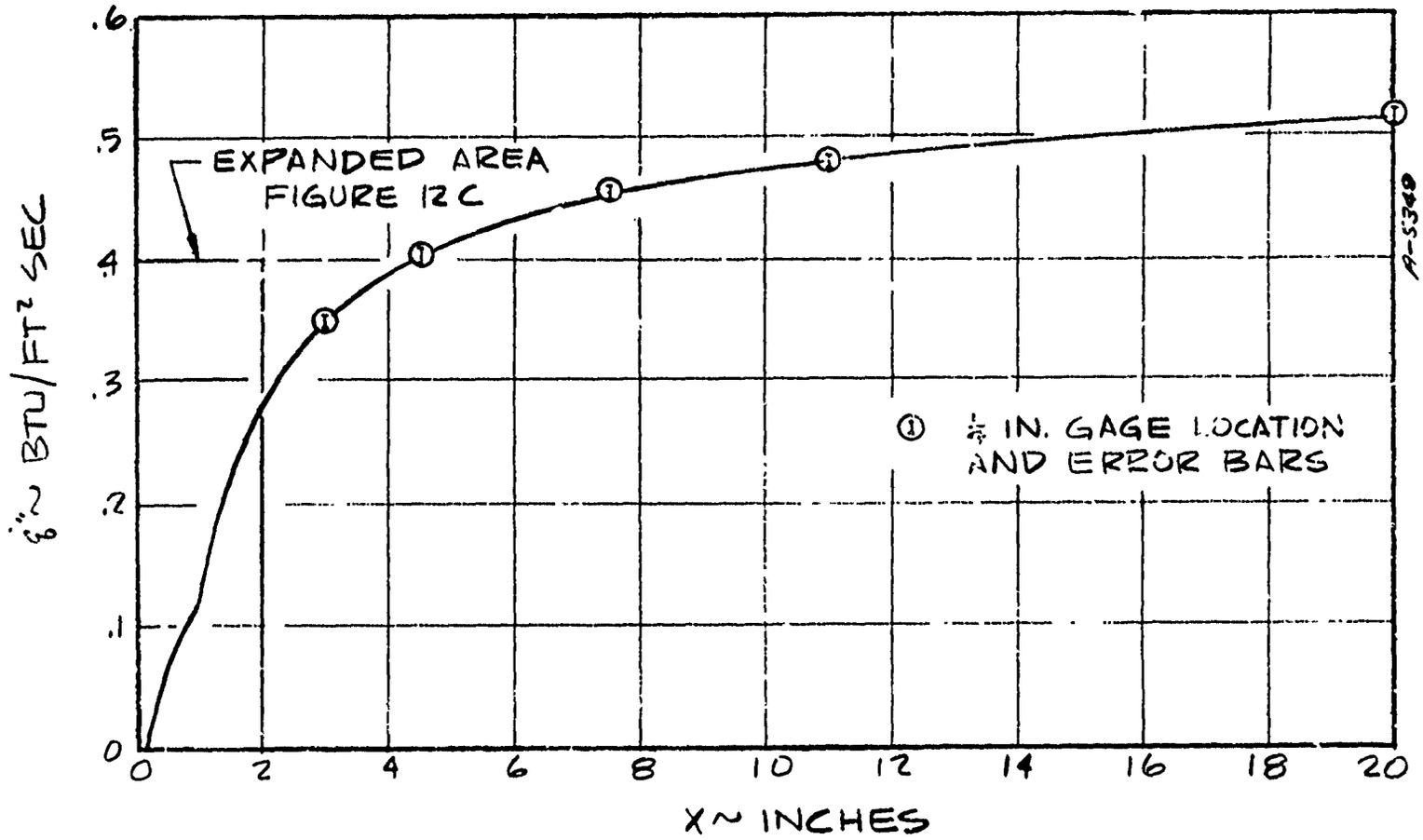

Figure 4-14d. Heat Flux Recovery 2.0/2.0 Configuration Far Downstream Section - Maximum Flow Rate

that in critical areas the spacing was dominated by geometric constraints. The sensor locations and the gage error bars are also shown. As can be seen, the sensitivity in the low heat flux regime is less of a problem than maintaining spatial resolution. The decision to use 0.125 gages was further confirmed by the lower flow rate cases where the heat flux recovers much more quickly.

The gage locations illustrated in Figures 4-14 represent the principal data sources for the heat flux recovery. These were in addition to a variety of gages utilized for auxiliary purposes. Figures 4-15 through 4-18 list all the gages actually installed in the model and their locations. The two gages upstream of the first slot were used to monitor the undisturbed heat flux. By comparison with the reference sensor mounted in the tunnel wall, they ensure that the model installation was not affecting the undisturbed heat flux. Since the slot sizes are now reasonably sized, it is feasible to measure heat fluxes to the forward facing slot wall. This done for second slot on the 5.0/5.0 model. Five 0.25 inch gages were placed in the slot wall at distances from the exit plane to the gage center of 0.25 inch, 1.25 inch, 2.5 inch, 5.0 inch and 10.0 inches. Gages were also placed in four transverse arrays on the 2.0/2.0 model to examine the effects of the half-slot filler block and to indicate the uniformity of the heat flux across the model for the unfilled configuration. All of these variations are indicated on Figures 4-15 through 4-18 and summarized in Table 4-6. Also to be noted on these figures is the offset used to prevent disturbances from one gage propagating downstream to other nearby gages.

Due to the problems associated with drilling holes perpendicular to the contoured surface of the model, all mounting holes for the Gardon gages were drilled straight down, i.e., perpendicular to the model surface at the centerline. Thus the gage holes which were off the centerline presented a slight discontinuity to the flow. The worst situation tolerated is portrayed in Figure 4-19a for a 0.25 gage located 1 inch off the centerline resulting in a 0.005 inch discontinuity. Those cases resulting in worse discontinuities were redrilled perpendicular to the local model surface. Analysis indicated that the 0.005 inch discontinuity was not going to affect the measurements and to ensure that this was the case, the gages were mounted as in Figure 4-19c rather than Figure 4-19b which might result in roughness augmentation of the local heat transfer. Examination of the Gardon gages on the 2.0/2.0 model which were mounted in transverse arrays, differing only by distance off centerline, showed no discernable heating trends with distance off the centerline.

In addition there were some problems with installation on the 2.0/2.0 model where gage 18 protruded slightly resulting in consistently high readings and gage 23 was recessed so that it consistently read low. In general the behavior of the AEDC-supplied Gardon gages was excellent. The gages appeared to be consistently reliable and repeatable causing no operational problems.

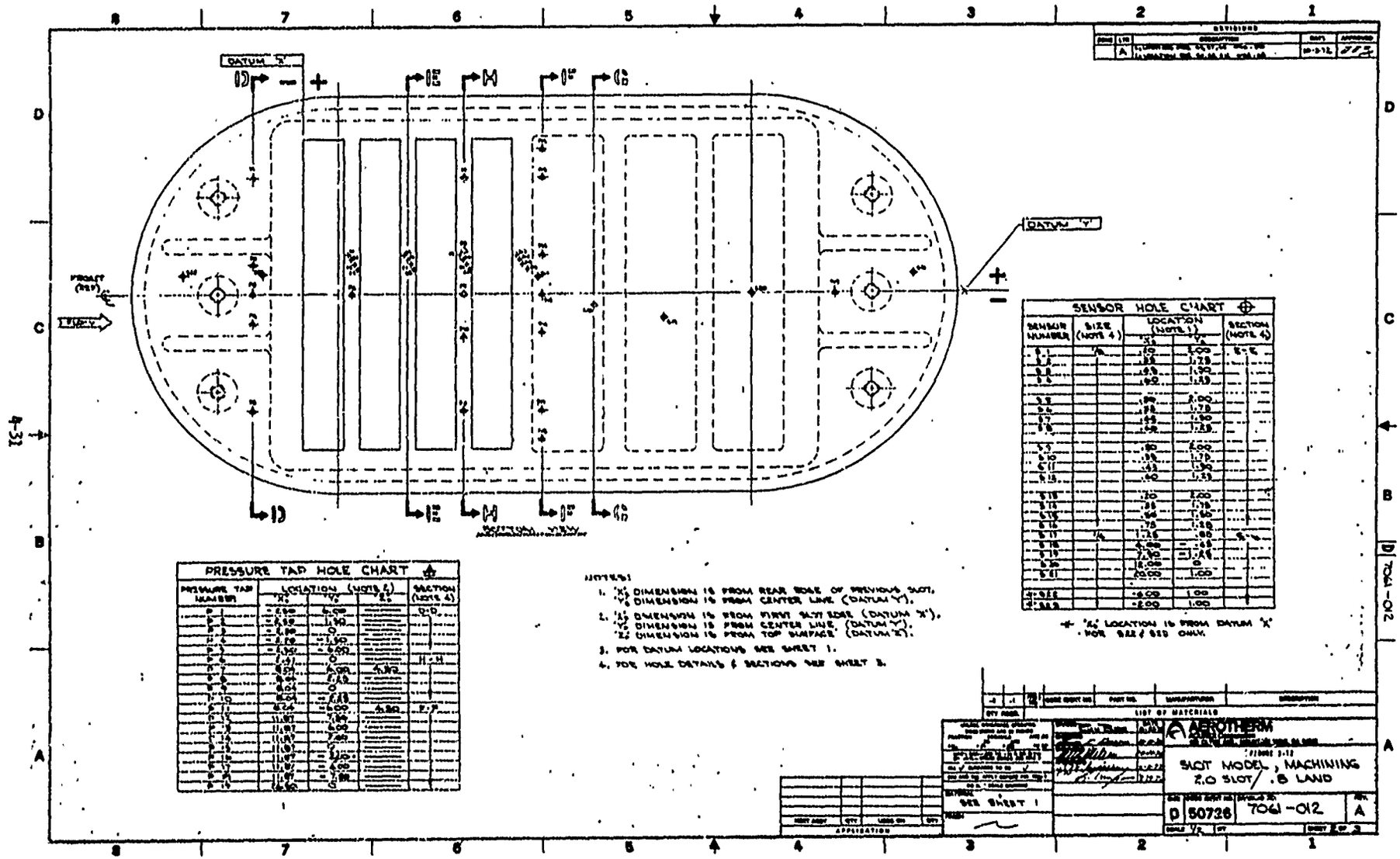
DATUM 'X'
DATUM 'Y'
FLOW
SENSOR HOLE CHART
PRESSURE TAP HOLE CHART
NOTES:
1. 'X' DIMENSION IS FROM REAR EDGE OF PREVIOUS SLOT, 'Y' DIMENSION IS FROM CENTER LINE (DATUM 'Y').
2. 'X' DIMENSION IS FROM FIRST SLOT EDGE (DATUM 'X'). 'Y' DIMENSION IS FROM CENTER LINE (DATUM 'Y'). 'Z' DIMENSION IS FROM TOP SURFACE (DATUM 'Z').
3. FOR DATUM LOCATIONS SEE SHEET 1.
4. FOR HOLE DETAILS & SECTIONS SEE SHEET 3.
AEROTHERM
SLOT MODEL, MACHINING
2.0 SLOT/.8 LAND
P 50726
7061-012
A

FIGURE 4-15

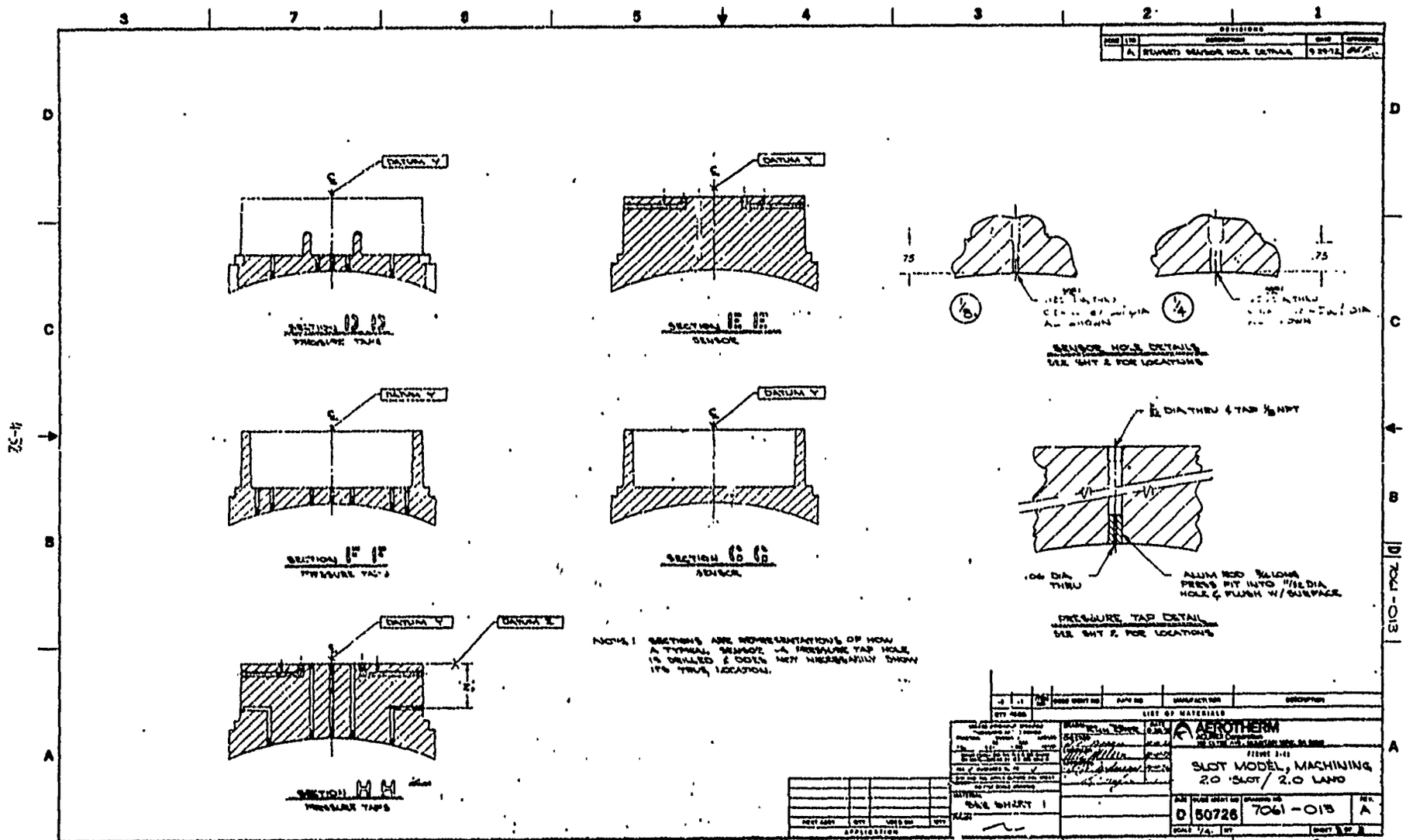
DATUM Y
DATUM X
SECTION J-J
PRESSURE TAPS
SECTION K-K
SENSOR
SECTION L-L
PRESSURE TAPS
SECTION M-M
PRESSURE TAPS
SENSOR HOLE DETAILS
SEE SHT 2 FOR LOCATIONS
PRESSURE TAP DETAIL
SEE SHT 2 FOR LOCATIONS
NOTE: 1 SECTIONS ARE REPRESENTATIONS OF HOW A TYPICAL SENSOR OR PRESSURE TAP HOLE IS DRILLED & DOES NOT NECESSARILY SHOW ITS TRUE LOCATION.
AEROTHERM
SLOT MODEL, MACHINING
2.0 SLOT / 2.0 LAND
D 50726
7061-013
A
SHEET 1

FIGURE 4-16

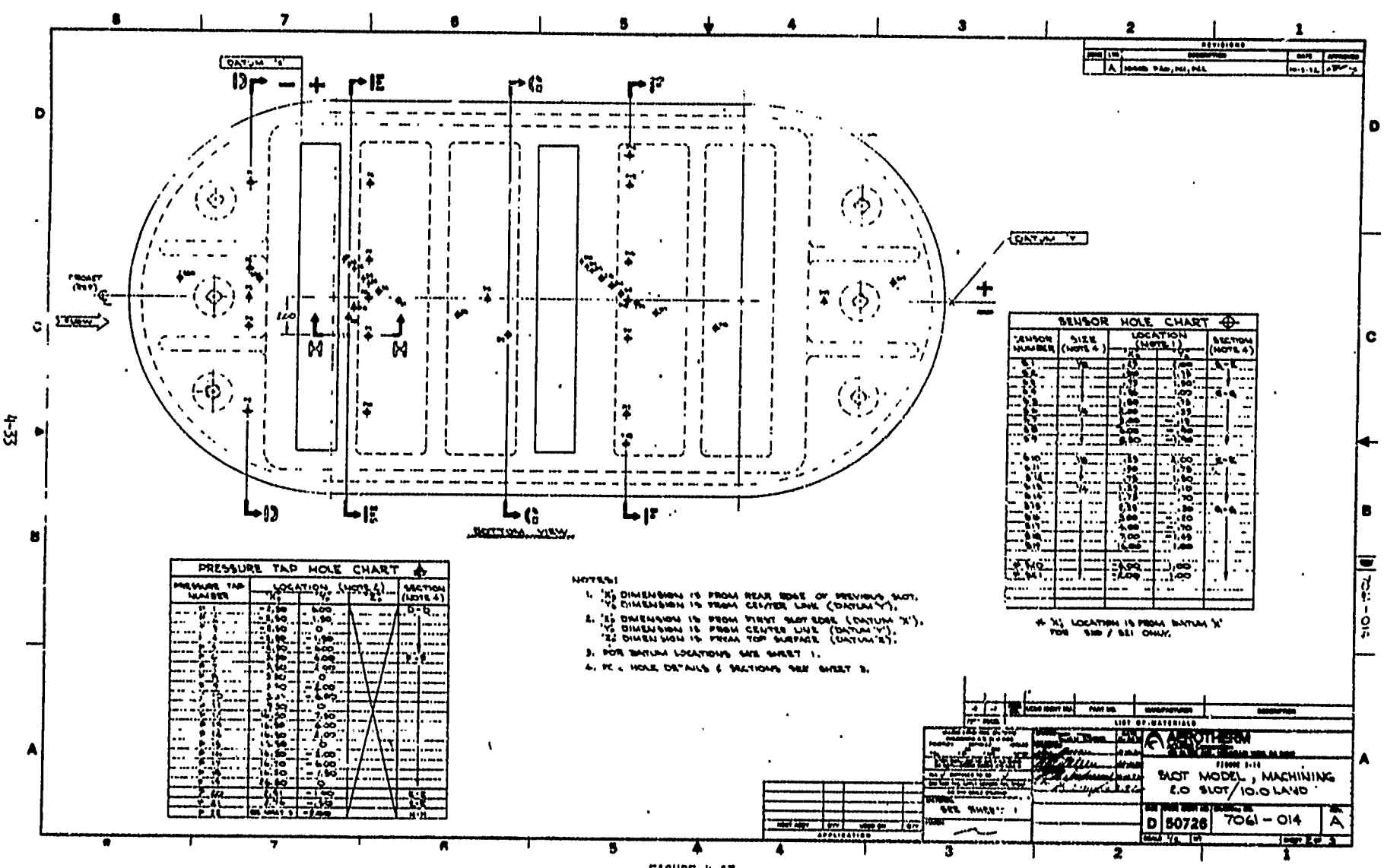
SENSOR HOLE CHART
PRESSURE TAP HOLE CHART
NOTES:
1. 'X' DIMENSION IS FROM REAR EDGE OF PREVIOUS SLOT.
'Y' DIMENSION IS FROM CENTER LINE (DATUM 'Y').
2. 'X' DIMENSION IS FROM FIRST SLOT EDGE (DATUM 'X').
'Y' DIMENSION IS FROM CENTER LINE (DATUM 'Y').
'Z' DIMENSION IS FROM TOP SURFACE (DATUM 'Z').
3. FOR DATUM LOCATIONS SEE SHEET 1.
4. FOR HOLE DETAILS & SECTIONS SEE SHEET 3.
SLOT MODEL, MACHINING
2.0 SLOT/10.0 LAND
D 50726
7061 - 014
A

FIGURE 4-17

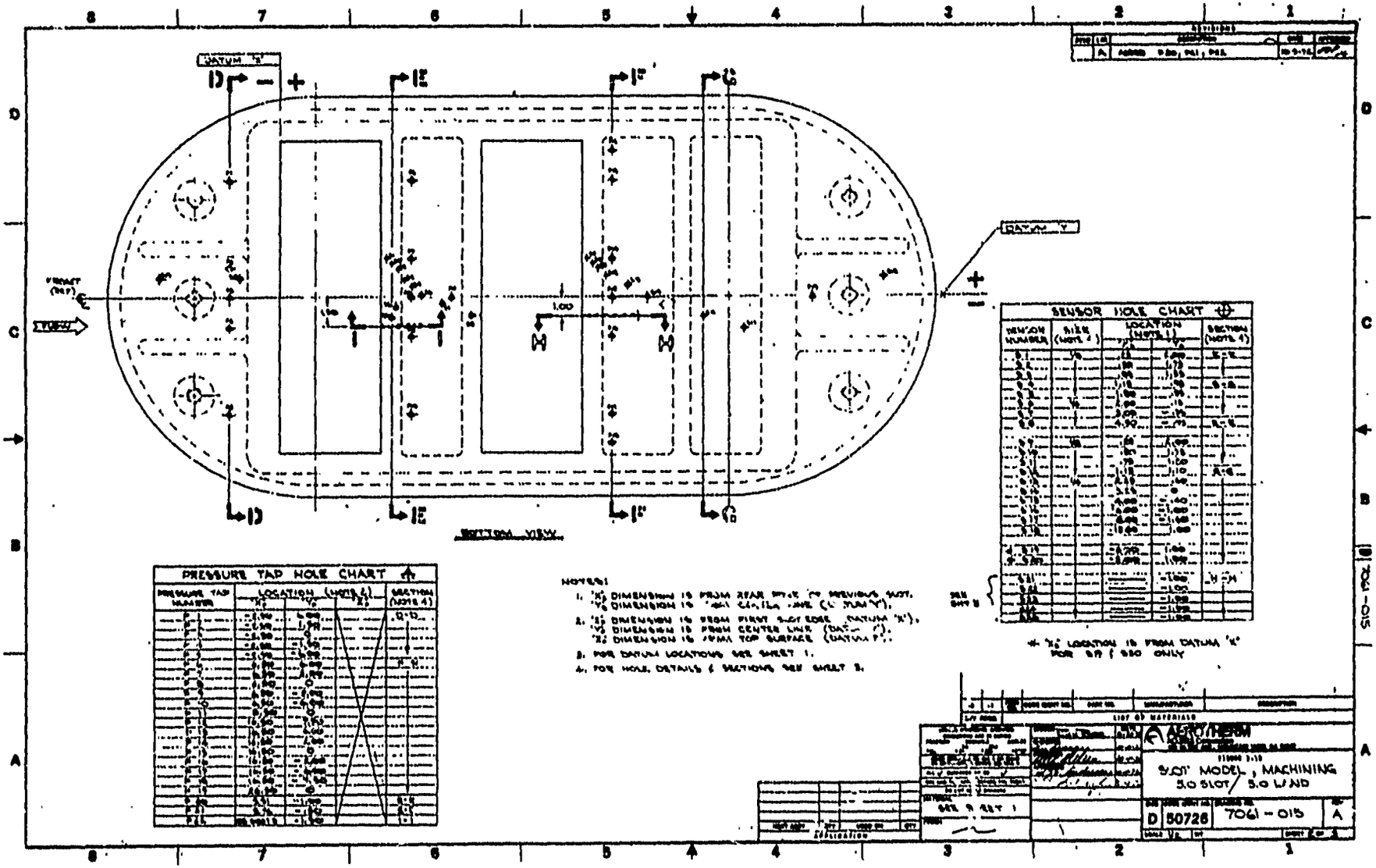
DATUM 'X'
DATUM 'Y'
SECTION VIEW
SENSOR HOLE CHART
PRESSURE TAP HOLE CHART
NOTES:
1. 'X' DIMENSION IS FROM REAR EDGE OF MODEL (DATUM 'X').
'Y' DIMENSION IS FROM CENTER LINE (DATUM 'Y').
'Z' DIMENSION IS FROM TOP SURFACE (DATUM 'Z').
3. FOR DATUM LOCATIONS SEE SHEET 1.
4. FOR HOLE DETAILS & SECTIONS SEE SHEET 3.
* 'X' LOCATION IS FROM DATUM 'K' FOR SN 1 050 ONLY
LIST OF MATERIALS
9.0% MODEL, MACHINING
5.0 SLOT / 5.0 LAND
D 50726
7061 - 015

FIGURE 4-18

TABLE 4-6

HEAT FLUX SENSOR LOCATION SUMMARY

Model Configuration	Number of Sensors			Locations				
	0.25	0.125	Total	Upstream	Per Land	Downstream	In Slot	Staggered Slot
2.0/ 0.8	7	16	23	2	4	9		
2.0/ 2.0	7	30	37	2	6	11		12
2.0/10.0	8	13	21	2	9	10		
5.0/ 5.0	16	9	25	2	8	10	5	
Total	38	68	106	8	41	40	5	12

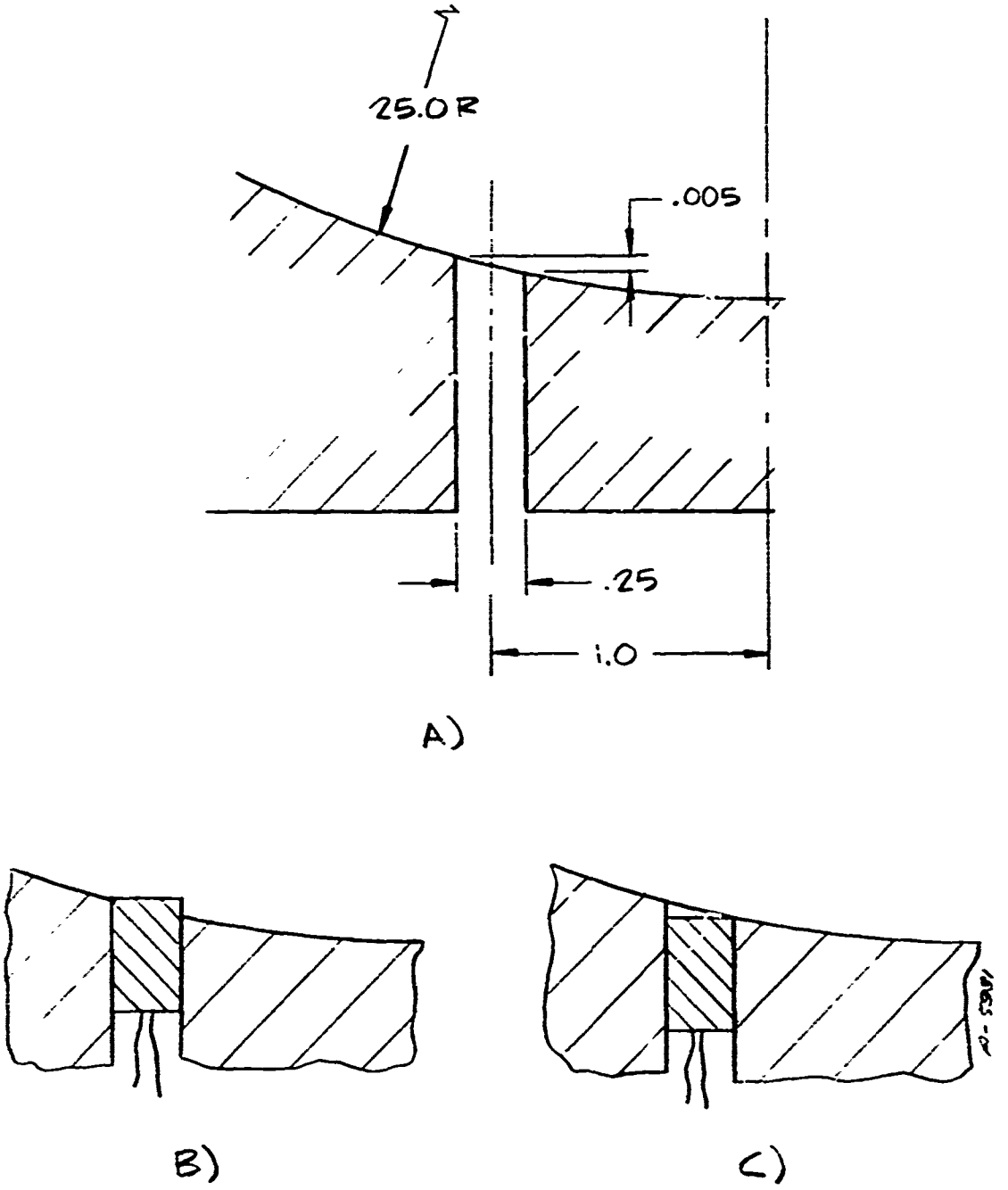

Figure 4-19. Off Centerline Gardon Gage Mounting

4.3.2 Pressure Taps

The pressure taps located over the model surface were primarily to provide increased confidence in the quality of the flow over the model. Secondarily it was hoped that some information could be gained on the behavior of the pressure field in the vicinity of a slot with mass injection. Due to the complexity of mounting pressure taps in the desired locations and the potential for interference with the Gardon gages, the second objective was not strongly stressed. The pressure tap locations are included in Figures 4-15 thru 4-18. In addition to the locations depicted, two pressure taps were installed one inch from the exit plane on the forward facing wall of the front slots for the 2.0/10.0 and 5.0/5.0 models.

The installation of the pressure taps in the model is shown in Figure 4-8b. The holes in the model were connected to 0.125 inch O.D. tubing which ran from the model to the transducer bank located in the test cabin under the wind tunnel. The standard tunnel B transducer systems were used with 1.0 psid transducers.

As mentioned previously, leakage was detected in some of the pressure taps on the 2.0/0.8 and 2.0/2.0 models. Since the data from the previous configurations had indicated little fluctuation in the pressures, the pressure tap data was not considered crucial to the experiment and thus the number 7 and 11 pressure taps on the 2.0/0.8 model and the number 7 pressure tap on the 2.0/2.0 model were sealed. These three pressure taps were all located near the ends of the slot, a relatively uninteresting area, and thus sealing them resulted in no impact on the experiment. Since the half slot filler block might result in noticeable perturbations of the pressure field in the vicinity of the centerline of the 2.0/2.0 model, the number 8, 9, and 10 pressure taps which were located just downstream of the filler-open slot interface were salvaged although leaking. For these three taps, 0.125 inch tubing was run from the rear through the pressure tap holes until flush with the model front surface. These lines were then connected to the standard pressure tap tubing and the area around the tubes sealed at the back surface.

4.3.3 Boundary Layer Probes

While the surface heat transfer data was the crux of the experiment, the detailed data on flow behavior to be gained by probing the boundary layers can be expected to provide the basic information required to explain the surface data. Because Tunnel B is a continuous flow tunnel and there was no chance to switch or alter the model appreciably, the bulk of the tunnel operating shift could be devoted to boundary layer probing after the heat transfer data were taken. Due to the large thickness of the boundary layer (~ 8 inches) and the probe drive speed of about 2 inches per minute, each boundary layer survey took 12 to 15 minutes to perform. The result was about 15 surveys per configuration.

The general probe configuration used for the experiment is shown in Figure 4-20 which illustrates the layout of the probe in the tunnel. The standard probe drive mechanism in the top of the tunnel was used necessitating the hammerhead assembly to equalize aerodynamic loads and prevent unacceptably high rotational moments on the drive mechanism. Figure 4-21 shows the probes in close up. The standard probe configuration consisted of the total temperature and two total pressure probes. The disk static pressure probe was an ancillary experiment to provide data on static pressure variations through the boundary layer. The pitot probe arrangement for these tests was selected to (1) provide measurements as close to the model surface as possible, even at the expense of larger lag time in the measurements and (2) provide rapid data acquisition once the near-surface measurements had been obtained. Therefore, a small, flattened probe with a total height of 0.022 inch was utilized near the surface and a larger, 0.093-inch diameter probe was positioned approximately 0.6 inch above the smaller probe. Exact dimensions are shown in Figure 4-22. The larger probe was installed to reduce the lag time, which would increase the speed at which the larger portion (~ 80 percent) of the boundary layer survey could be obtained; in fact, the probe was driven continously at a speed of approximately 2 inches per minute. The region of principal interest was the first inch or so and in this region detailed data were obtained in 0.020 inch increments, stopping at each position to allow the small pitot probe time to stabilize. During the testing, however, a repeat survey was obtained where all data points were allowed sufficient time to stabilize to check for possible error in the continuous drive data. These results are presented as Figure 4-23 showing that no appreciable pressure lag was experienced with the continuous drive data, even on the small pitot probe.

The total temperature probe was a standard AEDC design utilizing a shielded Chromel/Alumel thermocouple. The calibration of the probe for variation in mass flux was accomplished as the tunnel was being shut down by moving the probe to the tunnel freestream and then gradually reducing the tunnel total pressure. The results of these calibrations is given in Apperdix B. The disk static probe which was also mounted suffered a variety of problems and no usable data was obtained. This had no impact on the experiment.

The probe arm was electrically insulated from the shaft so that contact between the lower pitot probe and the model would result in completion of an electrical circuit, turning on a light in the control room. The zero position for the probes was considered to be the position where this foul light was just flickering. The insulation between the probe arm and shaft failed on occasion resulting in constant appearance of the light. Correction of the foul light troubles typically required about two hours of down time. This problem was a major factor in the relatively few surveys completed in the first three days of testing. Subsequent measures allowed completion of full 8 hours shifts without foul light problems.

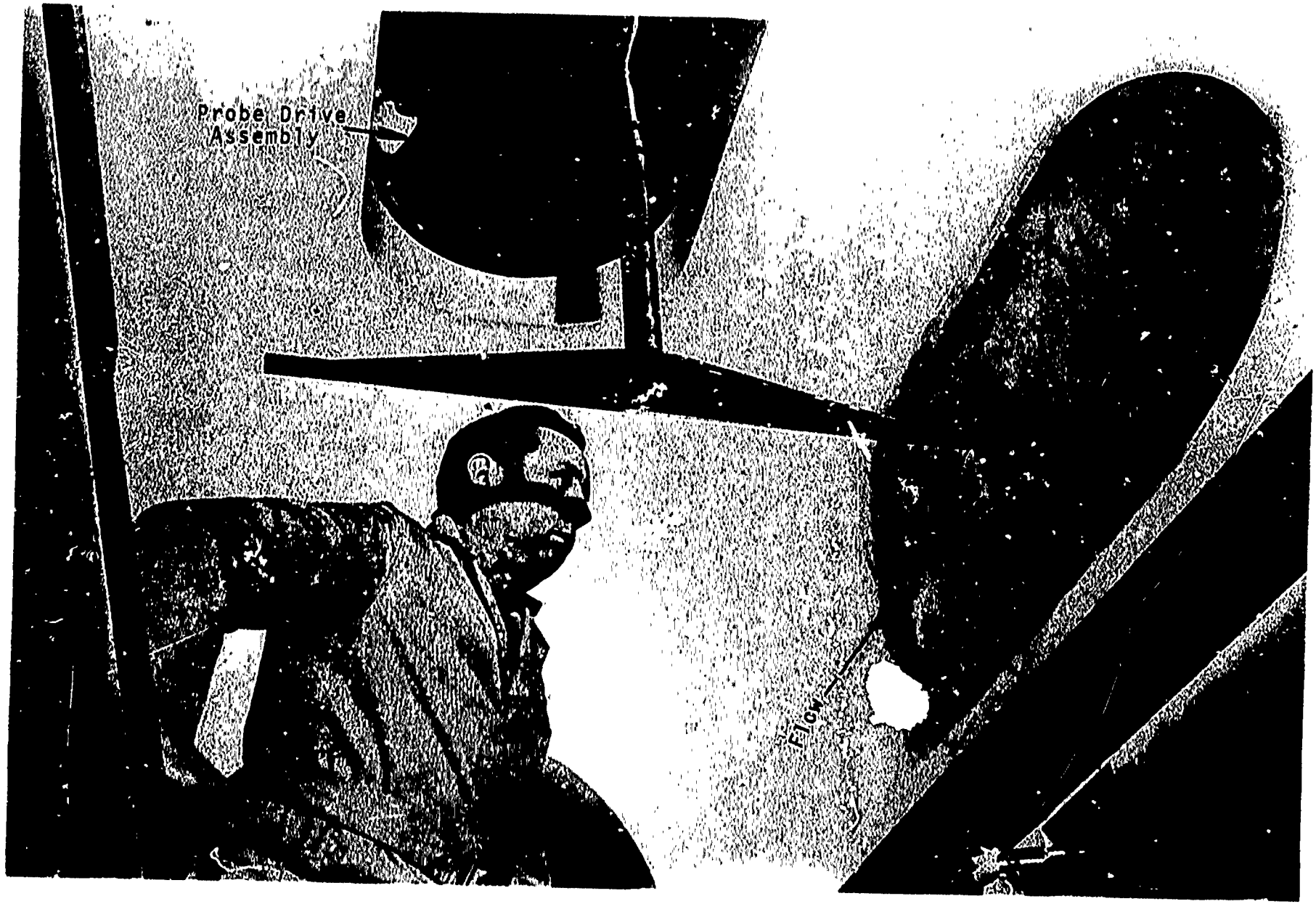

Figure 4-20. Boundary Layer Probe Assembly

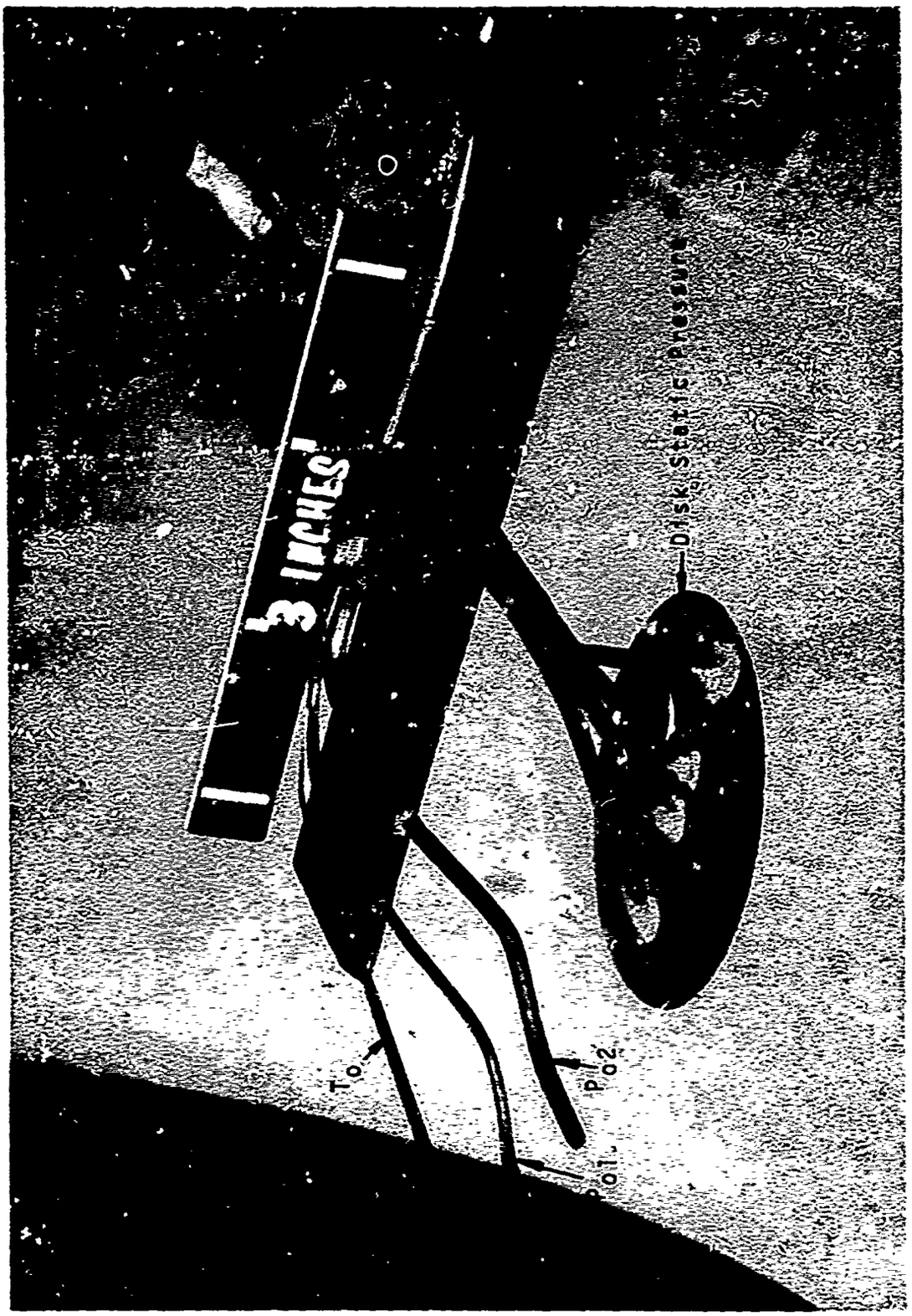

Figure 4-21. Detail Of Boundary Liner Probe Mounting

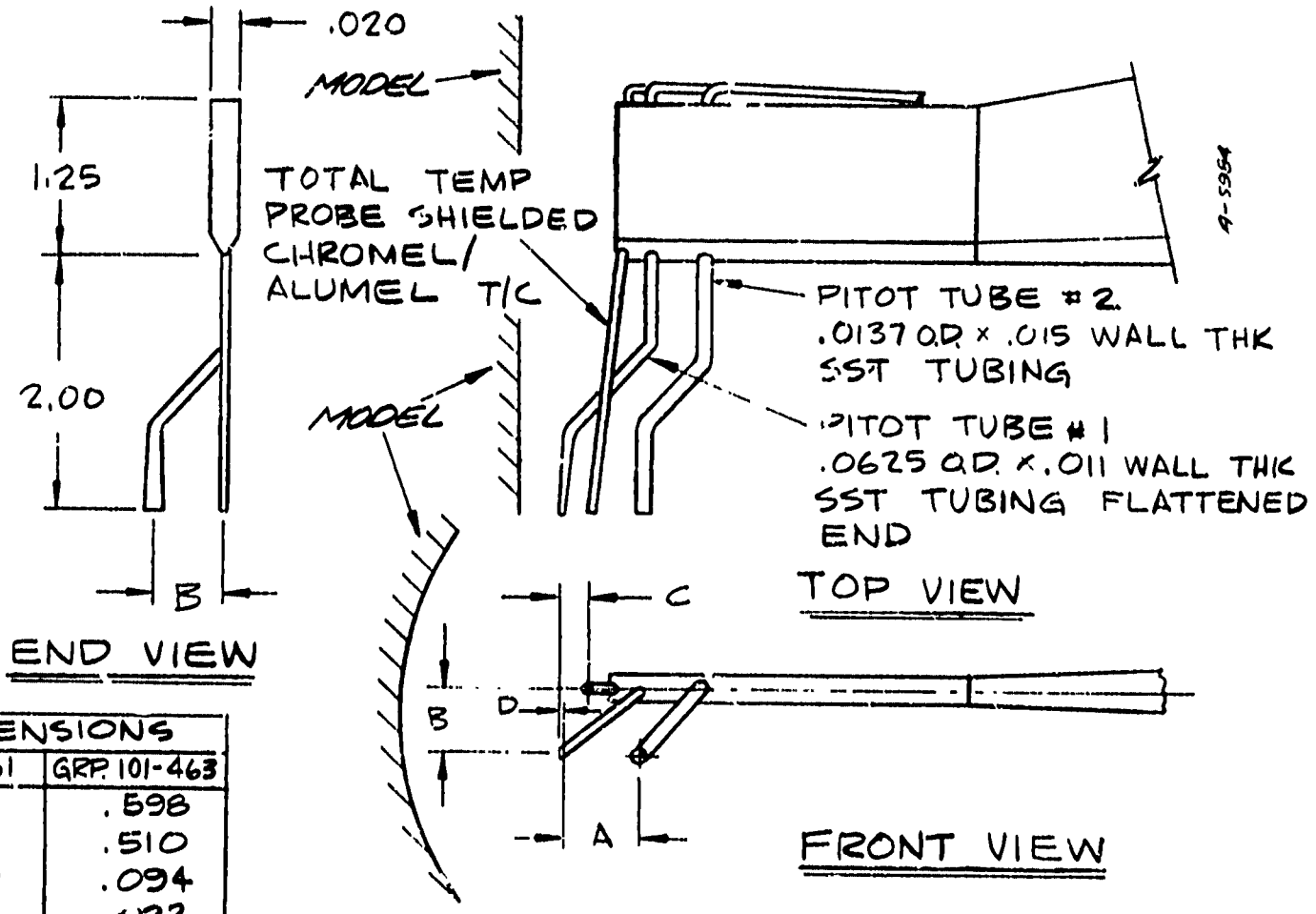

PROBE DIMENSIONS		
DIM	GRP. 1-61	GRP. 101-463
A	.584	.598
B	.518	.510
C	.059	.094
D	.022	.022

Figure 4-22. Boundary Layer Probe Relative Locations.

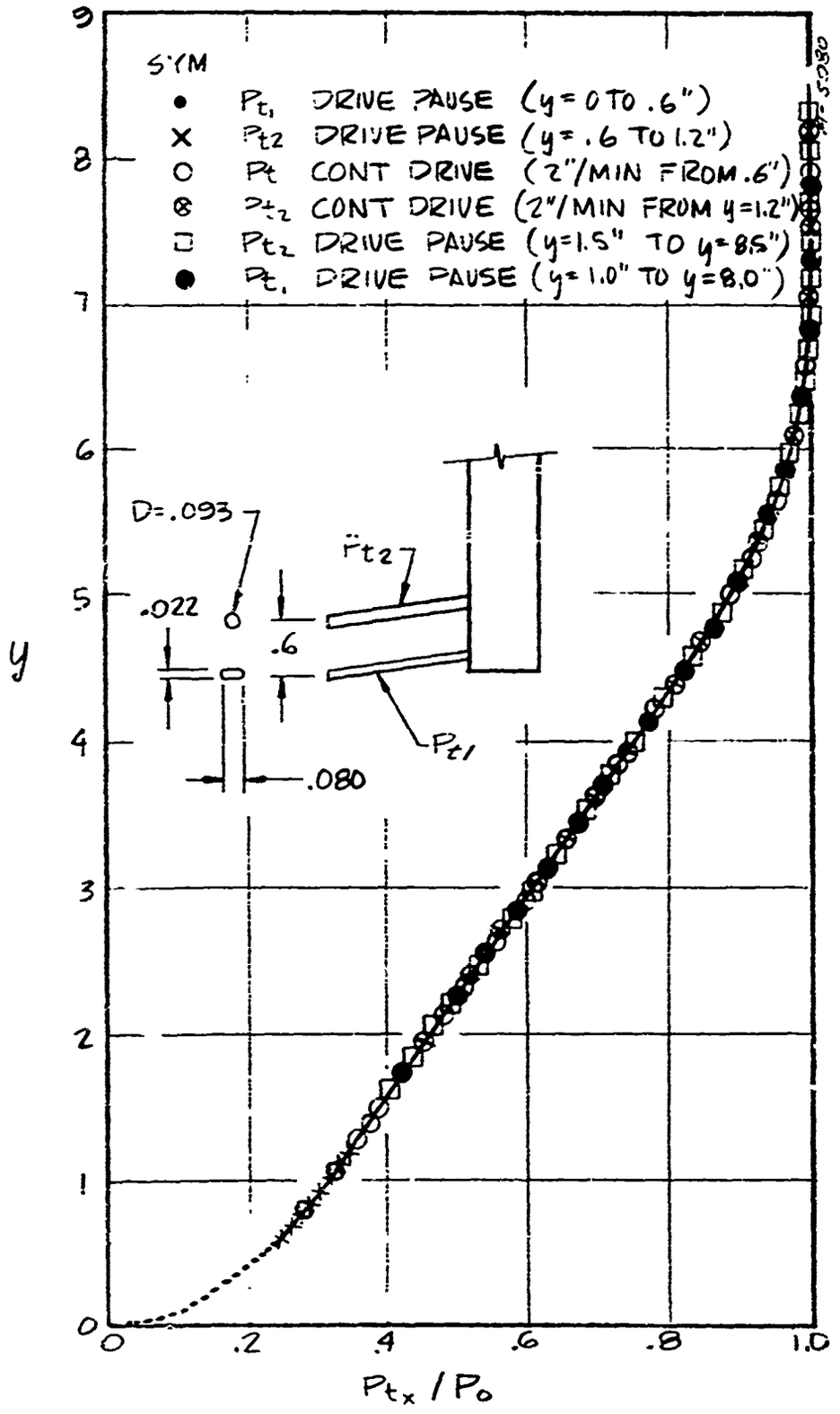

Figure 4-23. Comparison of Various Total Pressure Measurement Techniques. X=-2.0", Z=0

4.3.4 Optical Instrumentation

While quantitative data from optical sources is relatively rare, the flow visualization obtained can be invaluable in understanding the flow patterns involved. It was unfortunate for this experiment that the model configuration precluded use of traditional schlieren or shadowgraph systems. Since the model was sitting in one of the windows typically used for the schlieren system, an alternative cross-axis viewing arrangement would have been required to use a schlieren or shadowgraph system. The location of the model made the construction of such a viewing system impractical. As a substitute, vapor screen photography was attempted. The tunnel was operated without preheaters resulting in air condensation in the test stream. All areas of increased static temperature, such as the injection region, vaporize the mist of condensate. For some configurations the result can be quite impressive delineation of the viscous regions. For the large slot experiment the wall boundary layer resulted in vaporization of the mist out about 4 - 5 inches and any impact of injection or any other fine structure associated with the experiment was totally obscured.

4.3.5 Operational Instrumentation

In addition to the instrumentation designed to provide data on the physical phenomena, diagnostic instrumentation was provided to monitor the operation of the experiment. Two types of operational instrumentation were employed: thermocouples to measure model heating and pressure taps to monitor the flow through the injection systems. Thermocouples were mounted at four locations on the model, in each of the flow distribution boxes, in the flow distribution manifold, and in the cooling water manifolds. The thermocouples in the flow distribution system indicated the injectant temperature for mass flow calculations. The other thermocouples plus the thermocouples on the Gardon gage bodies indicated that the model was quite uniform in temperature and that the possibility of hot spots was negligible.

The primary pressure measurement of interest was the upstream pressure ahead of the AEDC control valve, however the other pressure readings confirmed that the mass flows were as expected. This redundancy proved quite useful in the one instance when the AEDC orifice partially clogged. This was discovered only when the downstream pressures indicated that the resulting mass flows were substantially less then the upstream pressure indicated.

4.4 TEST MATRIX

Testing of the models was performed between December 8 and December 19, 1972 at AEDC. Table 4-7 lists the test dates for each configuration. The first day of testing for the 2.0/10.0 model amounted to a shakedown test for the experiment. Leakage problems, foul light failures, and inability to set the proper injectant mass flow rates resulted in the data from the first day (Groups 1-20) being discarded. Vapor screen photography also consumed approximately one hour a day for the first two days.

TABLE 4-7

RUN SCHEDULE

Date	Configuration	Data Groups
8 Dec.	2.0/10.0	1 - 20*
11 Dec.	2.0/10.0	21 - 61
14 Dec.	5.0/ 5.0	101 - 150
15 Dec.	2.0/ 0.8	201 - 248
18 Dec.	2.0/ 2.0	301 - 354
19 Dec.	2.0/ 2.0	401 - 463

*All data discarded.

Table 4-8 lists the flowrates of nitrogen injectant required for each model. Surface data was taken for all flow rates, but boundary layer profiles were concentrated on the maximum and zero flow conditions with some attention to a medium blowing case at approximately half the maximum flow rate. Note that the flow rate number 0 for the 2.0/2.0 model with and without the filler block represents the massive blowing case run at the operating limit of the system (~ 1500 psia). Unfortunately unanticipated shutdown eliminated a similar massive blowing case for the 2.0/0.8 model. Figures 4-24 and 4-25 are photographs of the model as installed in the tunnel. In general the experiment appears to have performed substantially as designed. All critical data were obtained and seem to be of high quality.

4.5 RESULTS

The data taken in the course of the experiment was automatically collected, digitized, and stored on magnetic tape. These tapes were subsequently utilized with a data reduction computer code at AEDC to produce the final tabulated and plotted output. The procedures used to reduce the data are documented as

TABLE 4-8

INJECTANT CONDITIONS

Model		Cooled Area $\dot{m}$ lbm/ft²sec	Cooled Area B'_o	Slot $\dot{m}$ lbm/ft²sec	Slot B'_o	Slot $\dot{m}$ lbm/sec	Slot $\dot{m}$ ft³/sec	Total Injectant Flow lbm/sec	Total Injectant Flow ft³/sec	AEDC Supply Pressure (psia)	Manifold Pressure (psia)
Series 10											
2.0/10.0	1	.11125	4.5090	.06750	27.0541	.015000	.001108	.030000	.002217	1522.19	628.67
2.0/10.0	2	.09975	3.9078	.05850	24.4469	.013000	.000961	.026000	.001921	1325.66	544.84
2.0/10.0	3	.08825	3.3066	.04950	19.8397	.011000	.000813	.022000	.001626	1124.42	461.02
2.0/10.0	4	.06675	2.7054	.04050	16.2325	.009000	.000665	.018000	.001330	924.31	377.20
2.0/10.0	5	.05525	2.1042	.03150	12.6253	.007000	.000517	.014000	.001035	723.16	293.38
2.0/10.0	6	.04375	1.5030	.02250	9.0180	.005000	.000369	.010000	.000739	520.63	209.56
2.0/10.0	7	.03225	1.0822	.01620	6.4930	.003600	.000266	.007200	.000532	377.75	150.88
2.0/10.0	8	.02183	.7214	.01080	4.3287	.002400	.000177	.004800	.000355	254.24	100.59
2.0/10.0	9	.01213	.4810	.00720	2.8858	.001600	.000118	.003200	.000236	171.11	67.06
2.0/10.0	10	.00000	.0000	.00000	.0000	.000000	.000000	.000000	.000000	.00	.00
Series 100											
5.0/5.0	1	.11125	4.5090	.02250	9.0180	.012500	.000924	.025000	.001847	1273.92	523.89
5.0/5.0	2	.09975	3.9078	.01950	7.8156	.010833	.000801	.021667	.001601	1107.78	454.04
5.0/5.0	3	.08825	3.3066	.01650	6.6132	.009167	.000677	.018333	.001355	941.03	384.19
5.0/5.0	4	.06675	2.7054	.01350	5.4108	.007500	.000554	.015000	.001108	773.56	314.33
5.0/5.0	5	.05525	2.1042	.01050	4.2084	.005833	.000431	.011667	.000862	605.21	244.48
5.0/5.0	6	.04375	1.5030	.00750	3.0060	.004167	.000308	.008333	.000616	435.72	174.63
5.0/5.0	7	.03225	1.0822	.00540	2.1641	.003000	.000222	.006000	.000443	310.14	125.73
5.0/5.0	8	.02183	.7214	.00360	1.4429	.002000	.000148	.004000	.000296	212.77	83.82
5.0/5.0	9	.01213	.4810	.00240	.9619	.001333	.000099	.002667	.000197	143.20	55.88
5.0/5.0	10	.00000	.0000	.00000	.0000	.000000	.000000	.000000	.000000	.00	.00
Series 200											
2.0/0.8	1	.11125	4.5090	.01575	6.3126	.003500	.000259	.014000	.001035	723.16	146.69
2.0/0.8	2	.09975	3.9078	.01365	5.4709	.003033	.000224	.012133	.000897	628.84	127.13
2.0/0.8	3	.08825	3.3066	.01155	4.6293	.002567	.000190	.010267	.000759	534.19	107.57
2.0/0.8	4	.06675	2.7054	.00945	3.7876	.002100	.000155	.008400	.000621	439.12	88.01
2.0/0.8	5	.05525	2.1042	.00735	2.9459	.001633	.000121	.006533	.000483	343.56	68.45
2.0/0.8	6	.04375	1.5030	.00525	2.1042	.001167	.000086	.004667	.000345	247.34	48.90
2.0/0.8	7	.03270	1.0822	.00378	1.5150	.000840	.000062	.003360	.000248	179.06	35.21
2.0/0.8	8	.02180	.7214	.00252	1.0100	.000560	.000041	.002240	.000166	120.78	23.47
2.0/0.8	9	.01120	.4810	.00158	.6733	.000373	.000028	.001493	.000110	81.29	15.65
2.0/0.8	10	.00000	.0000	.00000	.0000	.000000	.000000	.000000	.000000	.00	.00

Cooled Area Parameters are Taken Over an Area of Slot and Land Length by Slot Width

$B'_o = \dot{m}/r_e u_e C_{H_o}$

Reproduced from best available copy.

TABLE A-8 (Concluded)

INJECTANT CONDITIONS

Model		Cooled Area $\dot{m}$ lbm/ft²sec	Cooled Area B'_o	Slot $\dot{m}$ lbm/ft²sec	Slot B'_o	Slot $\dot{m}$ lbm/sec	Slot $\dot{m}$ ft³/sec	Total Injectant Flow lbm/sec	Total Injectant Flow ft³/sec	AEDC Supply Pressure (psia)	Manifold Pressure (psia)
Series 300											
2.0/2.0	0	.12211	4.8814	.34452	17.7655	.039849	.010728	.029547	.002183	1499.72	412.78
2.0/2.0	1	.01125	1.5090	.12250	9.018	.005090	.000569	.015000	.001198	775.56	209.56
2.0/2.0	2	.01075	1.4078	.01050	7.8150	.004555	.000520	.013000	.000961	672.67	181.61
2.0/2.0	3	.00825	1.1366	.01050	6.6152	.003667	.000271	.011000	.000813	571.42	153.67
2.0/2.0	4	.00675	2.7054	.01450	5.4130	.003000	.000222	.009000	.000665	469.73	125.73
2.0/2.0	5	.00525	2.1342	.01050	4.2091	.002333	.000172	.007000	.000517	367.50	97.79
2.0/2.0	6	.00375	1.5630	.00750	3.0060	.001667	.000123	.005000	.000369	264.58	69.85
2.0/2.0	7	.00270	1.0822	.00540	2.1645	.001200	.000089	.003600	.000266	191.97	50.29
2.0/2.0	8	.00180	.7214	.00360	1.4429	.000800	.000059	.002400	.000177	129.20	33.55
2.0/2.0	9	.00120	.4810	.01240	.9613	.000533	.000039	.001600	.000118	86.96	22.35
2.0/2.0	10	.00000	.0000	.00000	.0000	.000000	.000000	.000000	.000000	.00	.00
Series 400											
2.0/HALF	0	.12211	4.8814	.34452	17.7655	.039849	.010728	.028622	.001820	1255.12	412.78
2.0/HALF	1	.01125	1.5090	.12250	9.018	.005090	.000569	.012500	.000924	647.39	209.56
2.0/HALF	2	.01075	1.4078	.01050	7.8150	.004555	.000520	.010833	.000801	562.96	181.61
2.0/HALF	3	.00825	1.1366	.01050	6.6152	.003667	.000271	.009167	.000677	478.22	153.67
2.0/HALF	4	.00675	2.7054	.01450	5.4130	.003000	.000222	.007500	.000554	393.12	125.73
2.0/HALF	5	.00525	2.1342	.01050	4.2091	.002333	.000172	.005833	.000431	307.56	97.79
2.0/HALF	6	.00375	1.5630	.00750	3.0060	.001667	.000123	.004167	.000308	221.43	69.85
2.0/HALF	7	.00270	1.0822	.00540	2.1645	.001200	.000089	.003000	.000222	160.66	50.29
2.0/HALF	8	.00180	.7214	.00360	1.4429	.000800	.000059	.002000	.000148	108.13	33.53
2.0/HALF	9	.00120	.4810	.00240	.9613	.000533	.000039	.001333	.000099	72.77	22.35
2.0/HALF	10	.00000	.0000	.00000	.0000	.000000	.000000	.000000	.000000	.00	.00

Reproduced from best available copy.

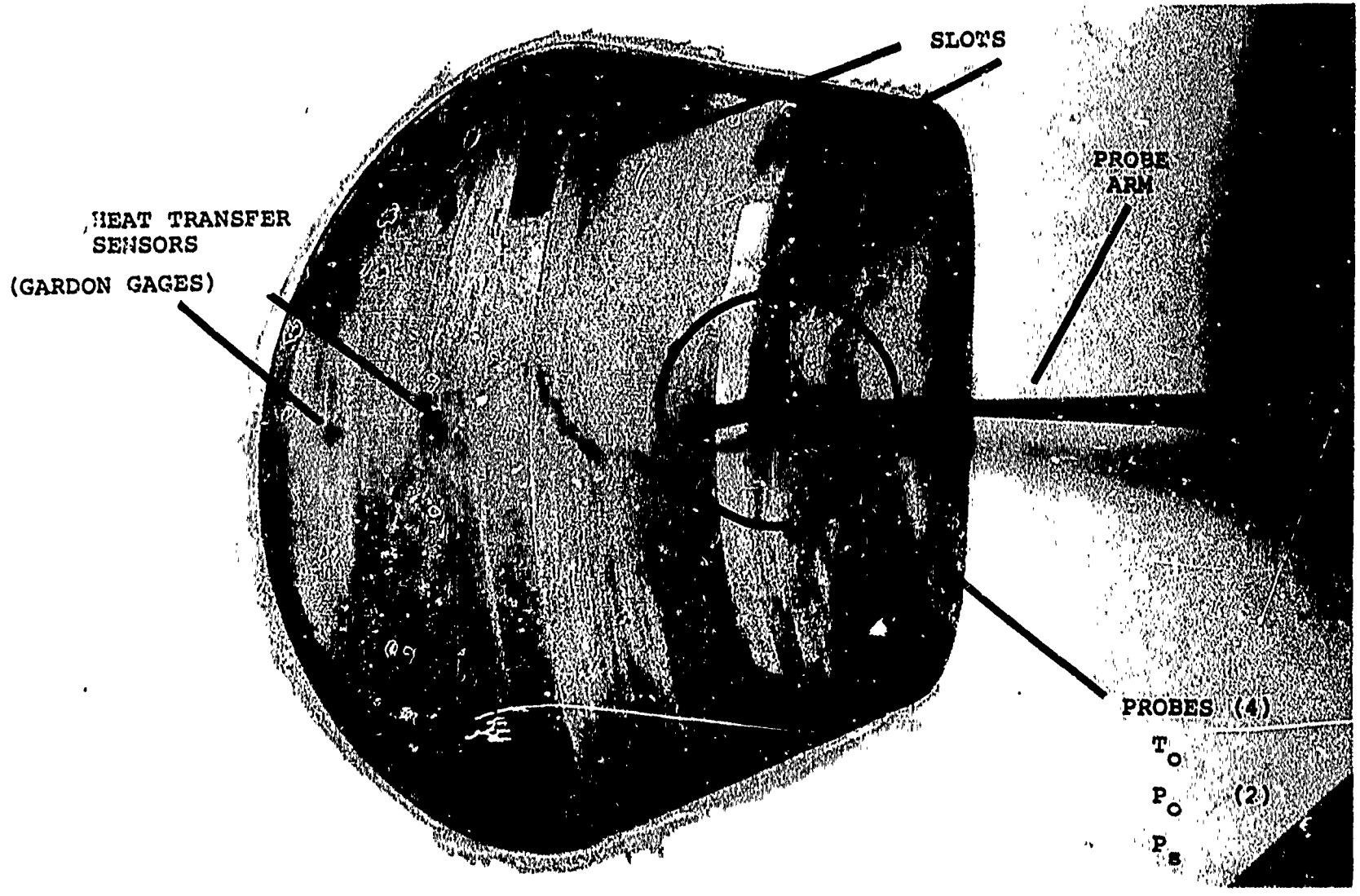

Figure 4-24. Wind Tunnel Interior With 2.0/10.0 Model Installed

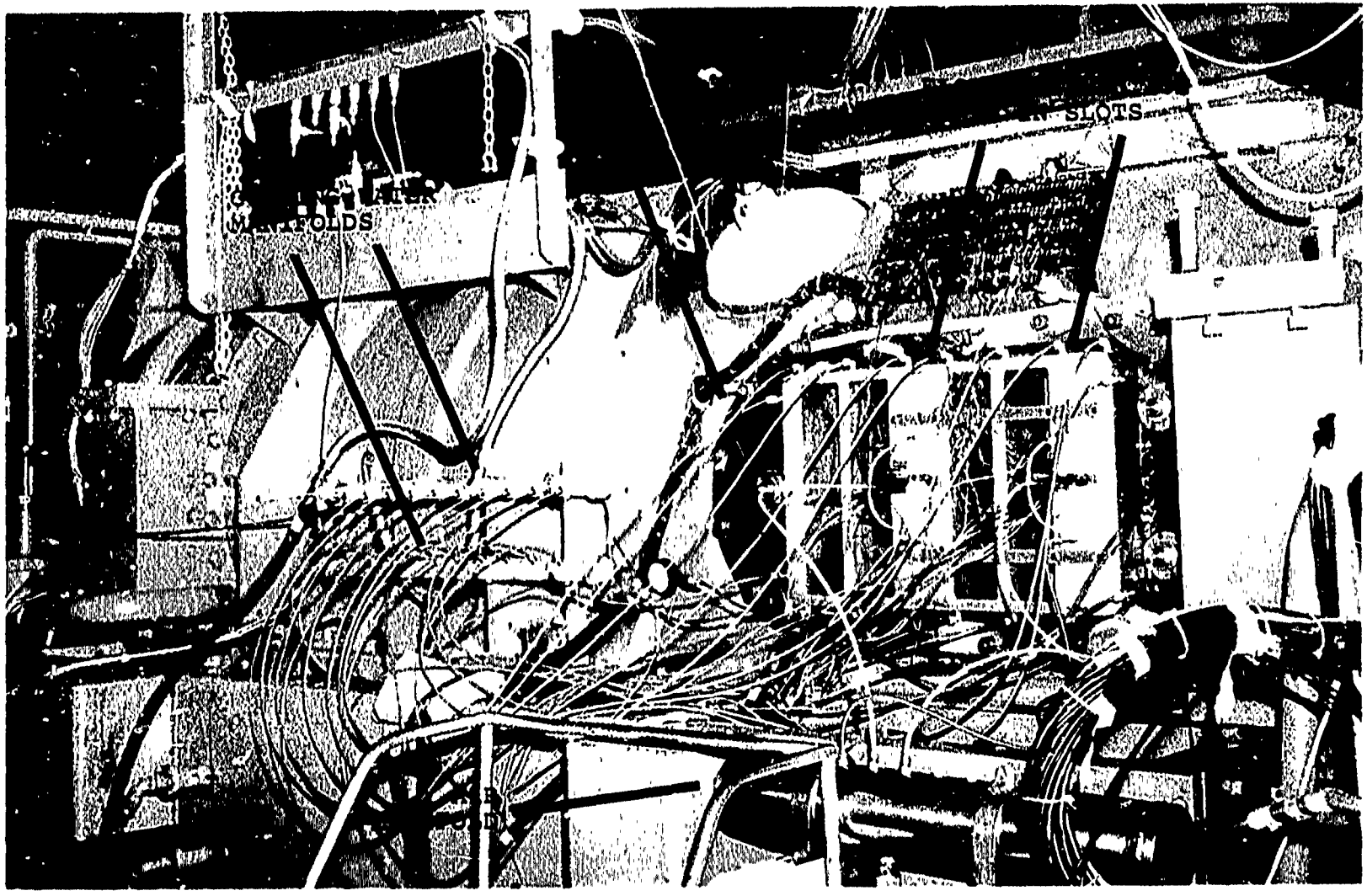

Figure 4-25. External View of 2.0/10.0 Model During Test

Reference 4-8. The raw data tapes, data reduction code, and documentation for use are stored at AEDC and will remain available for five years. Tables 4-9 through 4-13 list the data sets which have survived the checking process at AEDC.

The tables list $\dot{m}_T$ which is the total mass flow rate from all the slots (lbm/sec), Z which is the transverse dimension measured in inches and positive upwards, and X which is the distance downstream of the leading edge of the first slot measured in inches.

Due to the large quantity of data taken and to avoid duplication of results presented elsewhere, only an example of each type of data is presented herein. For a complete set of data, the reader is refered to Reference 8.

In addition to the surface data sets labelled as such, all of the surface instrumentation was also recorded at each point in the boundary layer survey. While this data is stored on tape, no attempt has been made to examine it.

The surface data results for the standard set of mass flow rates as measured on each model are shown in Figures 4-26 through 4-30 as plotted by AEDC. The table appended to each figure shows the flow rate parameters actually measured for each of the surface data measurements. The variables plotted are surface heat transfer rate ratio to the undisturbed heat transfer rate and surface pressure ratioed to freestream pressure. The X and Z definitions remain as explained above. The results shown in the plots indicate that the effects of roughness augmentation on the land heat transfer are more appreciable than anticipated and that this effect is not masked significantly by the blowing from the slot.

Figures 4-31 - 4-34 indicate some special results of the heat transfer measurements. Figure 4-31 compares, for selected cases, the results for the same flow conditions to indicate the repeatibility of the measurements. No substantial differences are seen in data for the same test conditions taken at different times. Figures 4-32 and 4-33 plot the transferse Gardon gage arrays for the 2.0/2.0 model. Figure 4-32 plotting the case for the unfilled center slot, indicates that the heat flux distributions for the standard case appeared to be relatively uniform without any noticeable persistent trends favoring one portion of the slot over any other. The runs made with the filler block are shown in Figure 4-33. As seen from these results, the effect of the filler block was relatively insignificant, impacting only the immediate downstream section of the second land. Due to the severity of the roughness augmentation, the result is a behavior exactly opposite to that expected, namely the filled side of the land generally remained cooler than the unfilled. Figure 4-34 illustrates the dramatic decay of heat flux as one enters the cavity. Blowing

TABLE 4-9

TEST SUMMARY

2.0 in. Slot, 10.0 in. Land Configuration

MODEL SURFACE DATA									
$\dot{m}_T$ lbm/sec (1)									
0	.00292	.00459	.00689	.00928	.0138	.0175	.0213	.0253	0.030
21[2]	22	23	24	25	26	27	28	29	30[4]
32					53				57[4]
35					55				59[4]
37									61[4]
39									
41									
43									
45									
47									
49									
51									

BOUNDARY LAYER SURVEYS								
$\dot{m}_T$ = 0			$\dot{m}_T$ = 0.0138			$\dot{m}_T$ = 0.030		
Z	X	Gp	Z	X	Gp	Z	X	Gp
0	-2.00[3]	31,33	0	2.27	52	0	2.29	58[4]
|	2.27	34	0	3.56	54	0	3.54	56[4]
|	2.82	36				3.00	2.29	60[4]
|	3.27	38						
|	4.07	40						
|	10.52	42						
|	14.32	44						
|	14.78	46						
|	16.26	48						
|	17.00	50						

(1) Total mass flux to model (see Table 4-2).

(2) Listed groups represent those without known major defects.

(3) Both manual and automatic probe drive.

(4) $\dot{m}_T$ not correct, orifice partially plugged, use

Gp	$\dot{m}_1 + \dot{m}_2$
56-57	0.0244
58-61	0.0238

TABLE 4-10

TEST SUMMARY

5.0 in. Slot, 5.0 in. Land Configuration

MODEL SURFACE DATA									
$\dot{m}_T$ lbm/sec (1)									
0.0	.0028	.0040	.0060	.0083	.0114	.0145	.0178	.0213	.0245
116[2]	106	107	108	109	110	131	132	133	134
118					142				146
120					144				148
122									150
124									
126									
128									
130									
136									
138									
140									

BOUNDARY LAYER SURVEYS								
$\dot{m}_T$ = 0			$\dot{m}_T$ = .0114			$\dot{m}_T$ = .0246		
Z	X	Gp	Z	X	Gp	Z	X	Gp
0	5.24	117	0	15.25	143	0	15.23	145
|	5.70	119	0	15.68	141	|	15.68	147
|	6.44	121				|	13.92	149
|	6.94	123						
|	9.44	125						
|	15.21	127						
|	15.67	129						
|	16.44	135						
|	17.46	137						
|	21.98	139						

(1) Total mass flux to model (see Table 4-2).

(2) Listed groups represent those without known major defects.

TABLE 4-11

TEST SUMMARY

2.0 in. Slot, 0.8 in. Land Configuration

MODEL SURFACE DATA									
$\dot{m}_T$ lbm/sec (1)									
0	.00147	.00214	.00338	.00472	.00654	.00836	.00994	.0118	.0138
210[2]	209	208	207	206	205	204	203	202	201
212									218
214									220
216									222
224									238
226									240
228									242
230									244
232									246
234									248
236									

BOUNDARY LAYER SURVEYS					
$\dot{m}_T$ = 0			$\dot{m}_T$ = .0138		
Z	X	Gp	Z	X	Gp
0	-2.00	211	0.03	10.11	217
|	5.20	213	|	5.18	219
|	10.16	215		2.31	221
3.00	-2.03	223	3.00	8.42	237
|	2.35	225	|	8.01	239
|	5.18	227	|	7.81	241
|	7.69	229	|	7.74	243
|	7.81	231	|	2.08	245
|	8.00	233	|	2.14	247
|	8.41	235	|		

(1) Total mass flux to model (see Table 4-2).

(2) Listed groups represent those without known major defects.

TABLE 4-12

TEST SUMMARY

2.0 in. Slot, 2.0 in. Land Configuration

MODEL SURFACE DATA										
$\dot{m}_T$ lbm/sec (1)										
0	.0016	.0024	.0036	.0050	.0070	.009	.0109	.013	.0149	.0292
311[2]	310	309	308	307	306	305	304	303	302	301
313									324	
316									326	
318									328	
320									330	
322									332	
346									334	
348									336	
350									338	
352									340	
354									342	
									344	

BOUNDARY LAYER SURVEYS					
$\dot{m}_T$ = 0			$\dot{m}_T$ = .0149		
Z	X	Gp	Z	X	Gp
3.00	6.07	312	3.00	7.79	323
	6.22	315		6.68	325
	6.31	317		6.35	327
	6.71	319		6.19	329
	7.79	321		6.07	331
	14.52	345		10.08	333
	11.78	347		10.30	335
	10.32	349		10.32	337
	10.12	351		10.71	339
	10.22	353		11.74	341
				14.46	343

(1) Total mass flux to model (see Table 4-2).

(2) Listed groups represent those without known major defects..

TABLE 4-13

TEST SUMMARY

2.0 in. Slot, 2.0 in. Land (Staggered Slot) Configuration

MODEL SURFACE DATA										
$\dot{m}_T$ lbm/sec (1)										
0	.00132	.00200	.00297	.00414	.0058	.0074	476	.0107	.0135	.0245
411[2]	410	409	408	407	406	405	404	403	402[3]	401
413					459				417	
415					461				419	
441					463				421	
443									423	
445									425	
447									427	
449									429	
									431	
									433	
									435	
									437	
									439	
									451	
									453	
									455	
									457	

BOUNDARY LAYER SURVEYS								
$\dot{m}_T$ = 0			$\dot{m}_T$ = .0058			$\dot{m}_T$ = .0135		
Z	X	Gp	Z	X	Gp	Z	X	Gp
3.00	2.02	412	0.35	6.20	458	3.00	3.27	416
3.00	3.81	414	0.20	6.16	460		2.00	418
-0.50	6.20	440	0.20	7.81	462		6.16	420
-0.20	6.19	442				0.50	6.17	422
0.20	6.18	444				0.20	6.19	424
0.50	6.20	446				0.20	6.31	426
0	-2.30	448				0.20	7.78	428[4]
						-0.20	6.14	430[4]
						-0.20	6.31	432[4]
						-0.20	7.80	434[4]
						-0.50	6.19	436
						-3.00	6.16	438
						0.70	10.19	450
						-0.70	10.23	452
						-0.35	6.22	454
						0.36	6.15	456

(1) Total mass flux to model (see Table 4-2).

(2) Listed groups represent those without known major defects.

(3) $\dot{m}_T$ = 0.0124

(4) $\dot{m}_T$ varied more than normal on these Gps.

Group	$B'_{o\ avg}$ *	$B'_{o\ slot}$	λ_{avg}	λ_{slot}	$\dot{m}_{slot}$ (lbm/sec)
30	5.00	29.98	.00143	.00858	.01611
29	4.19	25.13	.00120	.00719	.0135
28	3.66	21.98	.00105	.00629	.01181
27	2.88	17.25	.000823	.00494	.00927
26	2.28	13.68	.000652	.00391	.00735
25	1.55	9.29	.000443	.00266	.00499
24	1.18	7.11	.000339	.00203	.00382
23	0.779	4.67	.000223	.00134	.00251
22	0.509	3.05	.000146	.000873	.00164
21	0	0	0	0	0

* $B'_{o\ avg} = \dot{m}_{slot}/(A_{tot} \cdot \rho_e u_e C_H)$ where A_{tot} = (slot + land) x width

$B'_{o\ slot} = \dot{m}_{slot}/(A_{slot} \cdot \rho_e u_e C_H)$ where A_{slot} = (slot x width)

$\lambda'_{avg} = \dot{m}_{slot}/(A_{tot} \cdot \rho_e u_e)$

$\lambda'_{slot} = \dot{m}_{slot}/(A_{slot} \cdot \rho_e u_e)$

Figure 4-26 2.0/10.0 Model

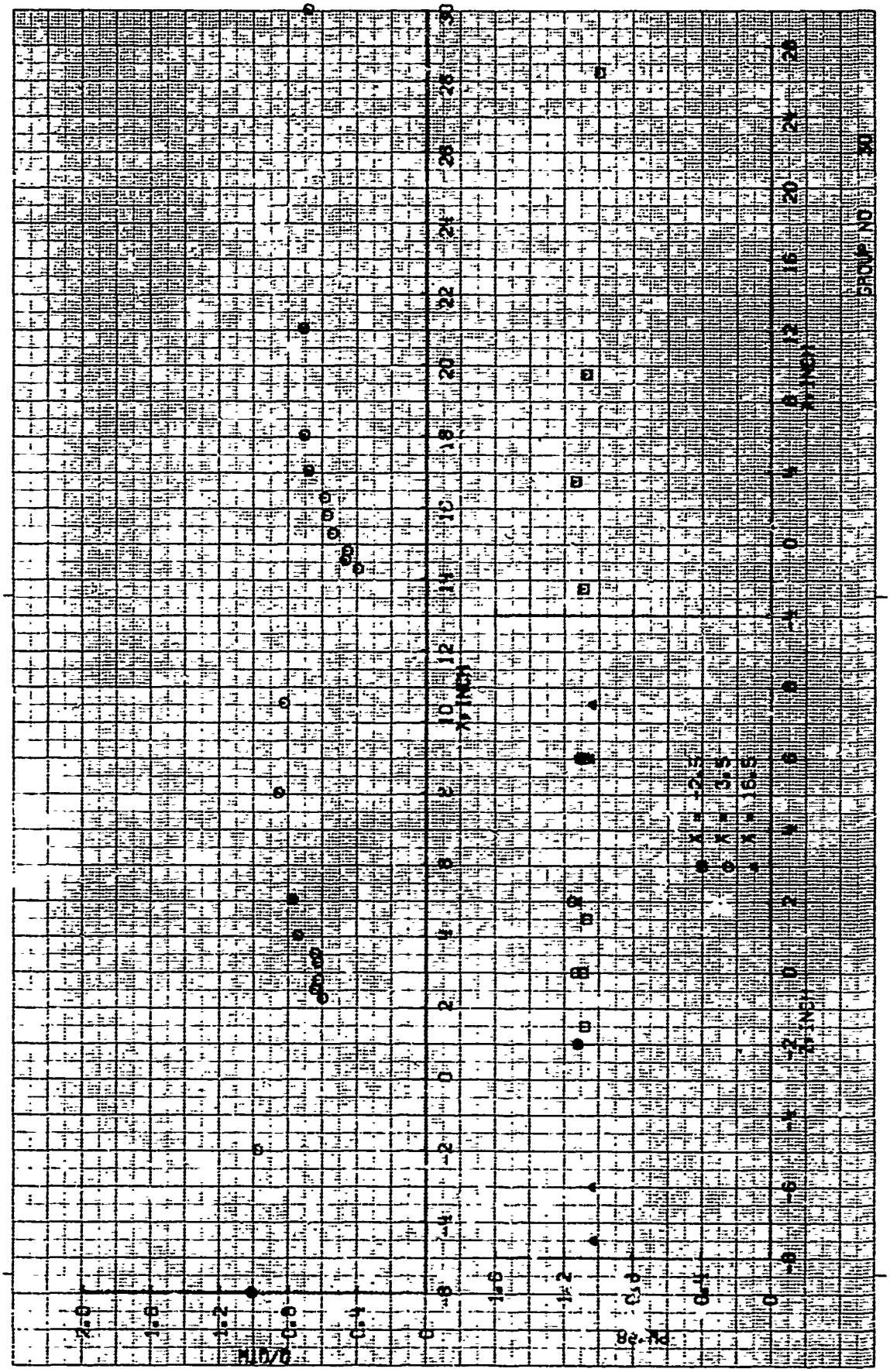
GROUP NO.
X1 (INCH)
X2 (INCH)
H1D/D
PK-PK

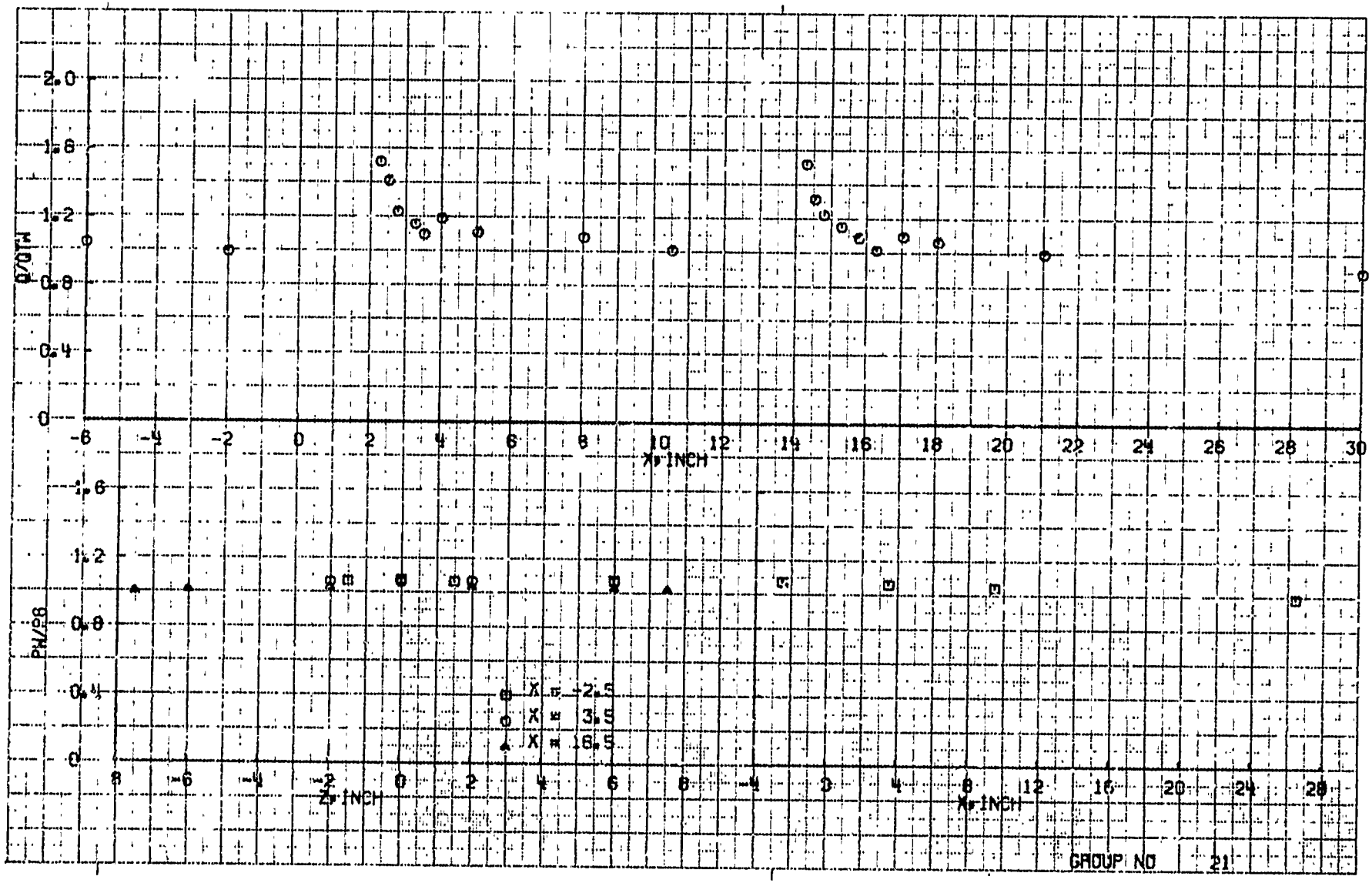
2.0
1.6
1.2
0.8
0.4
0
MW/CM
-6
-4
-2
0
2
4
6
8
10
12
14
16
18
20
22
24
26
28
30
X, INCH
1.6
1.2
0.8
0.4
0
PW/CM
X = -2.5
X = 3.5
X = 16.5
-8
-6
-4
-2
0
2
4
6
8
-4
0
4
8
12
16
20
24
28
Z, INCH
X, INCH
GROUP NO 21

Group	$B'_{o\ avg}$*	$B'_{o\ slot}$	λ_{avg}	λ_{slot}	$\dot{m}_{slot}$ (lbm/sec)
116	0	0	0	0	0
106	.566	1.132	.000162	.000324	.00152
107	.838	1.675	.000240	.000480	.00225
108	1.247	2.494	.000357	.000714	.00335
109	1.709	3.418	.000489	.000978	.00459
110	2.390	4.780	.000684	.00137	.00642
131	2.952	5.905	.000844	.00169	.00793
132	3.619	7.238	.00104	.00207	.00972
133	4.246	8.451	.00121	.00242	.01135
134	5.071	10.141	.00145	.00290	.01362

*

$B'_{o\ avg} = \dot{m}_{slot}/(A_{tot} \cdot \rho_e u_e C_H)$ where A_{tot} = (slot + land) x width

$B'_{o\ slot} = \dot{m}_{slot}/(A_{slot} \cdot \rho_e u_e C_H)$ where A_{slot} = (slot x width)

$\lambda'_{avg} = \dot{m}_{slot}/(A_{tot} \cdot \rho_e u_e)$

$\lambda'_{slot} = \dot{m}_{slot}/(A_{slot} \cdot \rho_e u_e)$

Figure 4-27 5.0/5.0 Model

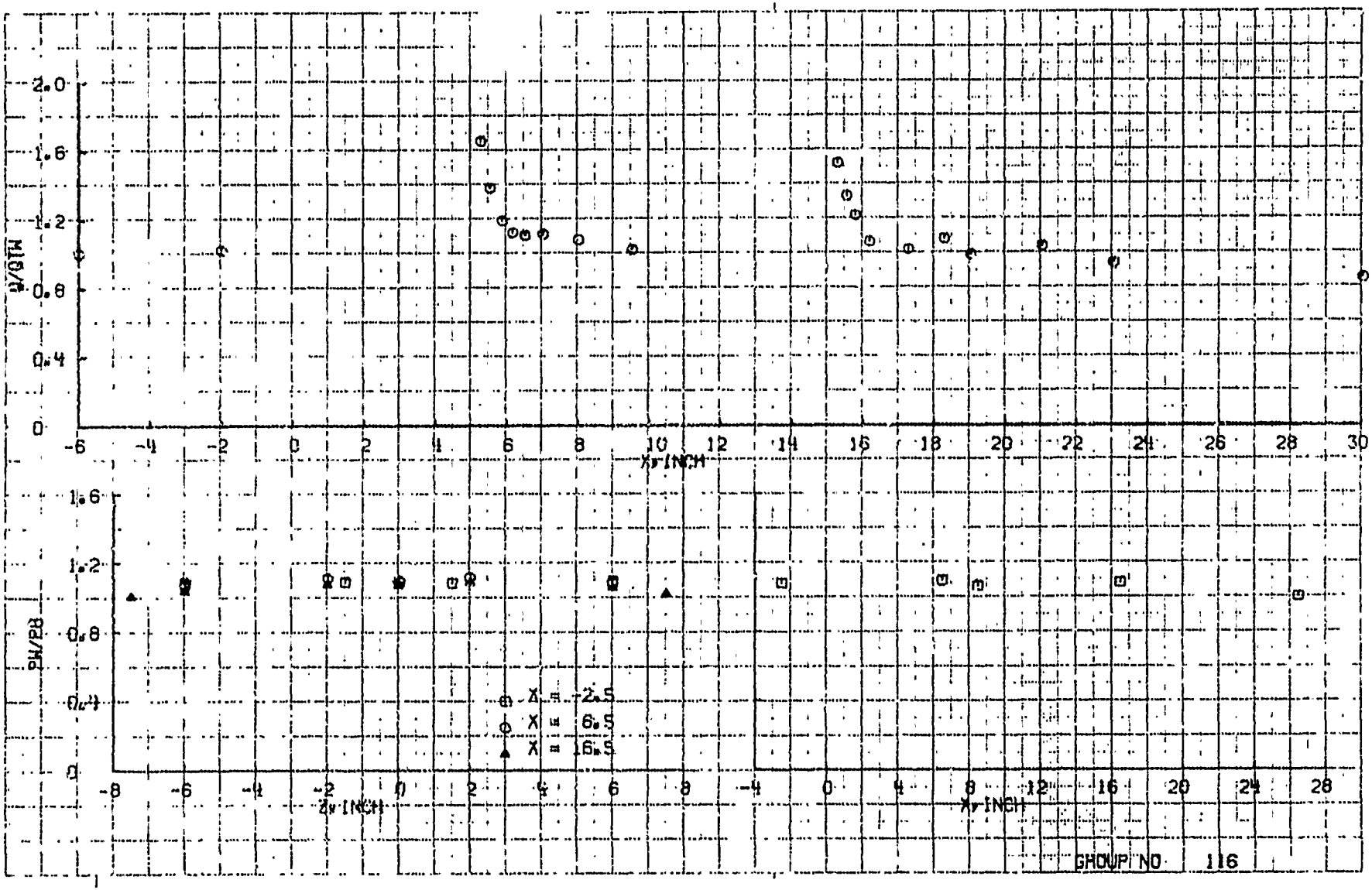
2.0
1.6
1.2
0.8
0.4
0
H1/H1
-6 -4 -2 0 2 4 6 8 10 12 14 16 18 20 22 24 26 28 30
Xy INCH
1.6
1.2
0.8
0.4
0
H2/H2
X = -2.5
X = 6.5
X = 16.5
-8 -6 -4 -2 0 2 4 6 8
Zy INCH
-4 0 4 8 12 16 20 24 28
Xy INCH
GROUP NO 116

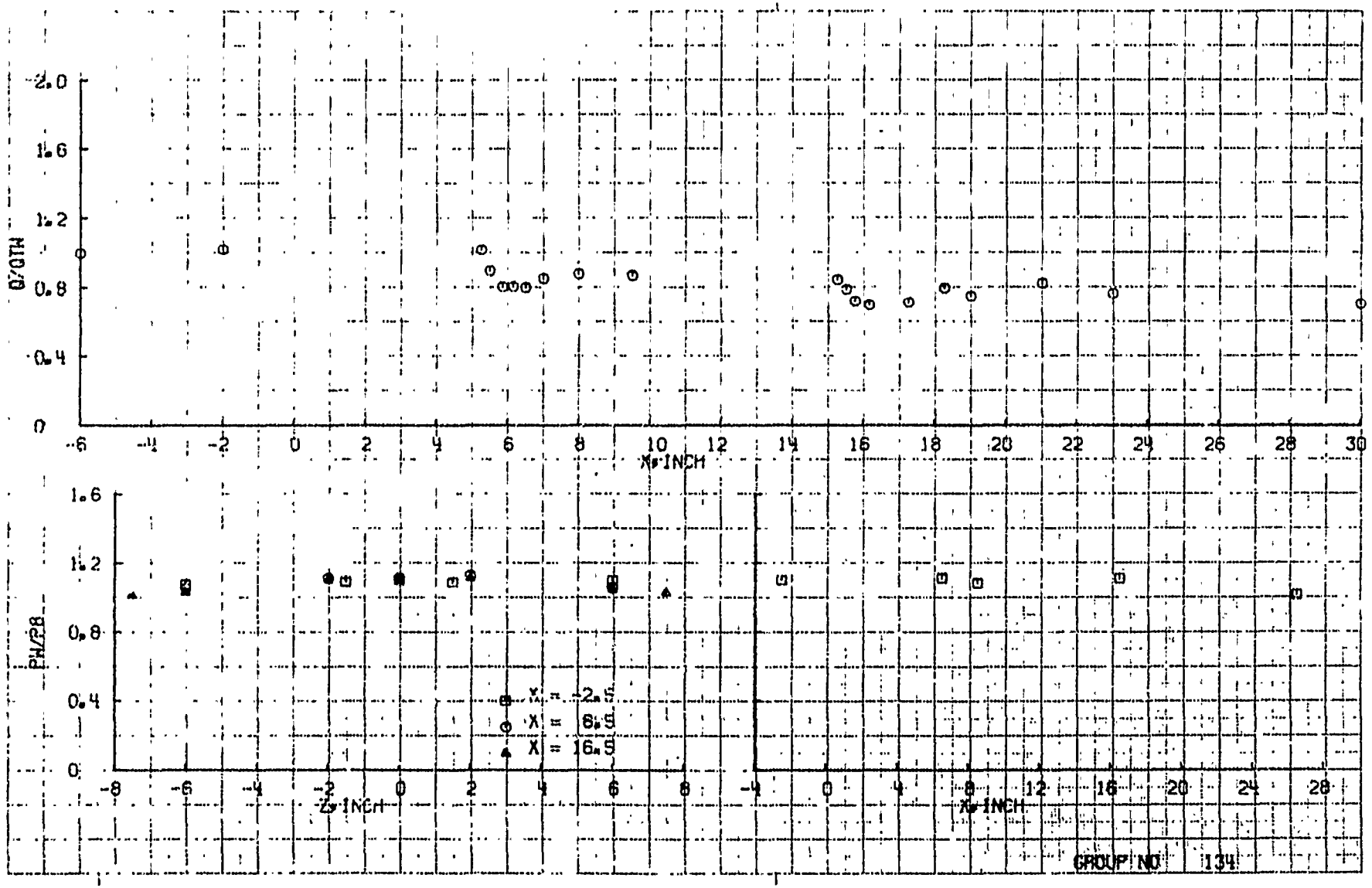
M10/0
2.0
1.6
1.2
0.8
0.4
0
-6 -4 -2 0 2 4 6 8 10 12 14 16 18 20 22 24 26 28 30
X, INCH
P4/28
1.6
1.2
0.8
0.4
0
X = -2.5
X = 8.5
X = 16.5
-8 -6 -4 -2 0 2 4 6 8
Z, INCH
-4 0 4 8 12 16 20 24 28
X, INCH
GROUP NO 134

Group	$B'_{o\ avg}$*	$B'_{o\ slot}$	λ_{avg}	λ_{slot}	$\dot{m}_{slot}$ (lbm/sec)
210	0	0	0	0	0
209	0.571	0.800	.000163	.000229	.00043
208	0.811	1.135	.000232	.000325	.00061
207	1.26	1.768	.000361	.000506	.00095
206	1.74	2.438	.000498	.000698	.00131
205	2.38	3.33	.000680	.000953	.00179
204	3.00	4.21	.000859	.00120	.00226
203	3.63	5.08	.00104	.00145	.00273
202	4.29	6.01	.00123	.00172	.00323
201	4.86	6.81	.00139	.00195	.00366

* $B'_{o\ avg} = \dot{m}_{slot}/(A_{tot} \cdot \rho_e u_e C_H)$ where A_{tot} = (slot + land) x width

$B'_{o\ slot} = \dot{m}_{slot}/(A_{slot} \cdot \rho_e u_e C_H)$ where A_{slot} = (slot x width)

$\lambda'_{avg} = \dot{m}_{slot}/(A_{tot} \cdot \rho_e u_e)$

$\lambda'_{slot} = \dot{m}_{slot}/(A_{slot} \cdot \rho_e u_e)$

Figure 4-28 2.0/0.8 Model

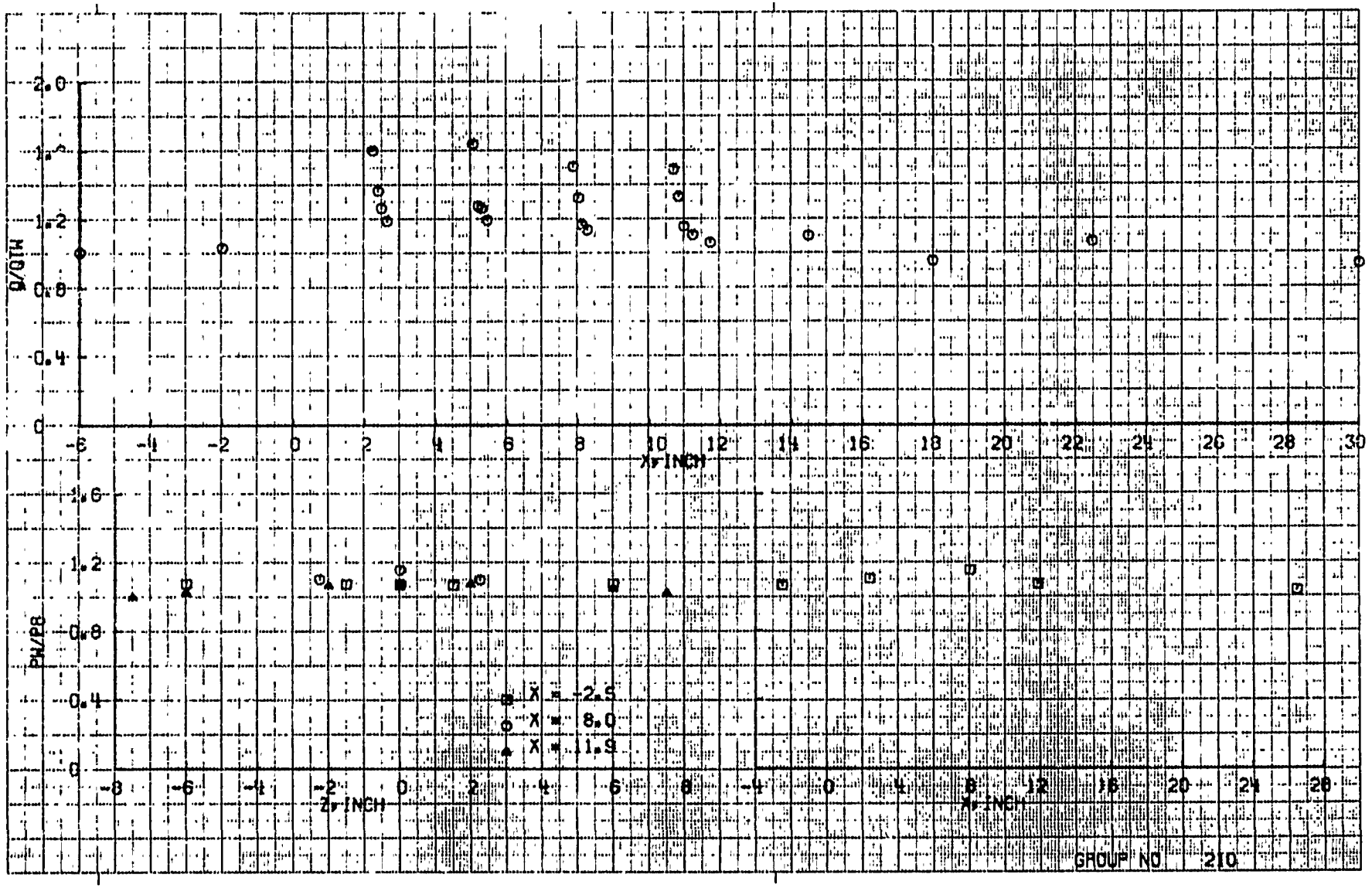
Q/QTH
PH/PB
Z, INCH
X, INCH
X, INCH
X = -2.5
X = 8.0
X = 11.5
GROUP NO 210

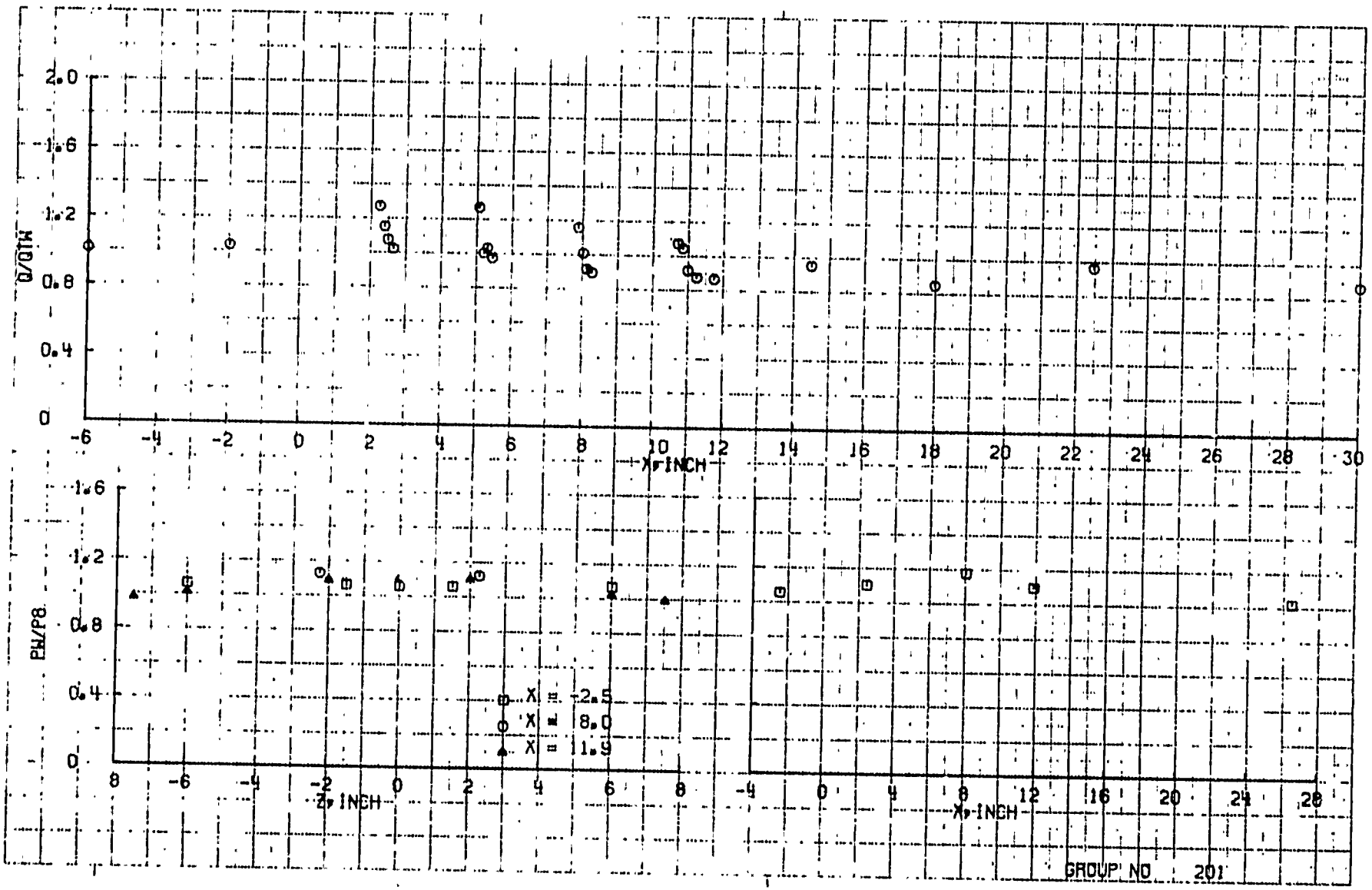
PH/P0
2.0
1.6
1.2
0.8
0.4
0
-6
-4
-2
0
2
4
6
8
10
12
14
16
18
20
22
24
26
28
30
X, INCH
PH/P0
1.6
1.2
0.8
0.4
0
X = -2.5
X = 8.0
X = 11.9
8
-6
-4
-2
0
2
4
6
8
-4
0
4
8
12
16
20
24
28
Z, INCH
X, INCH
GROUP NO 201

Group	$B'_{o\ avg}$*	$B'_{o\ slot}$	λ_{avg}	λ_{slot}	$\dot{m}_{slot}$ (lbm/sec)
311	0	0	0	0	0
310	0.558	1.117	.000160	.000319	.00060
309	0.819	1.638	.000234	.000469	.00088
308	1.256	2.513	.000359	.000719	.00135
307	1.684	3.369	.000482	.000964	.00181
306	2.345	4.690	.000671	.00134	.00252
305	3.052	6.10	.000873	.00175	.00328
304	3.76	7.52	.00108	.00215	.00404
303	4.28	8.56	.00122	.00245	.00460
302	4.95	9.90	.00142	.00283	.00532
301	9.44	18.89	.00270	.0054	.01015

* $B'_{o\ avg} = \dot{m}_{slot}/(A_{tot} \cdot \rho_e u_e C_H)$ where A_{tot} = (slot + land) x width

$B'_{o\ slot} = \dot{m}_{slot}/(A_{slot} \cdot \rho_e u_e C_H)$ where A_{slot} = (slot x width)

$\lambda'_{avg} = \dot{m}_{slot}/(A_{tot} \cdot \rho_e u_e)$

$\lambda'_{slot} = \dot{m}_{slot}/(A_{slot} \cdot \rho_e u_e)$

Figure 4-29 2.0/2.0 Model

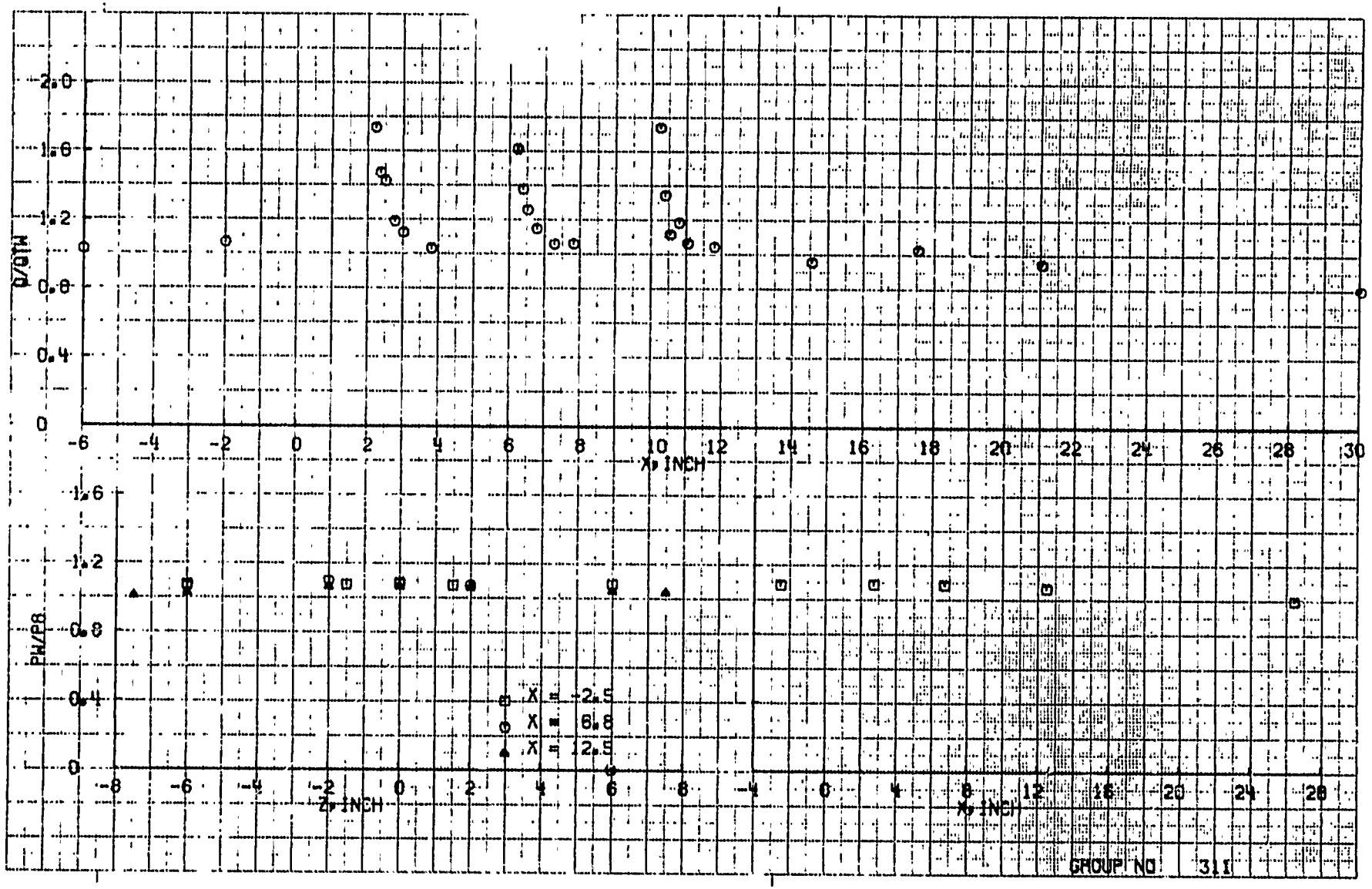
PM/P0
2.0
1.6
1.2
0.8
0.4
0
-6
-4
-2
0
2
4
6
8
10
12
14
16
18
20
22
24
26
28
30
X, INCH
PM/P0
1.6
1.2
0.8
0.4
0
X = -2.5
X = 6.8
X = 12.5
-8
-6
-4
-2
0
2
4
6
8
-4
0
4
8
12
16
20
24
28
Z, INCH
X, INCH
GROUP NO 311

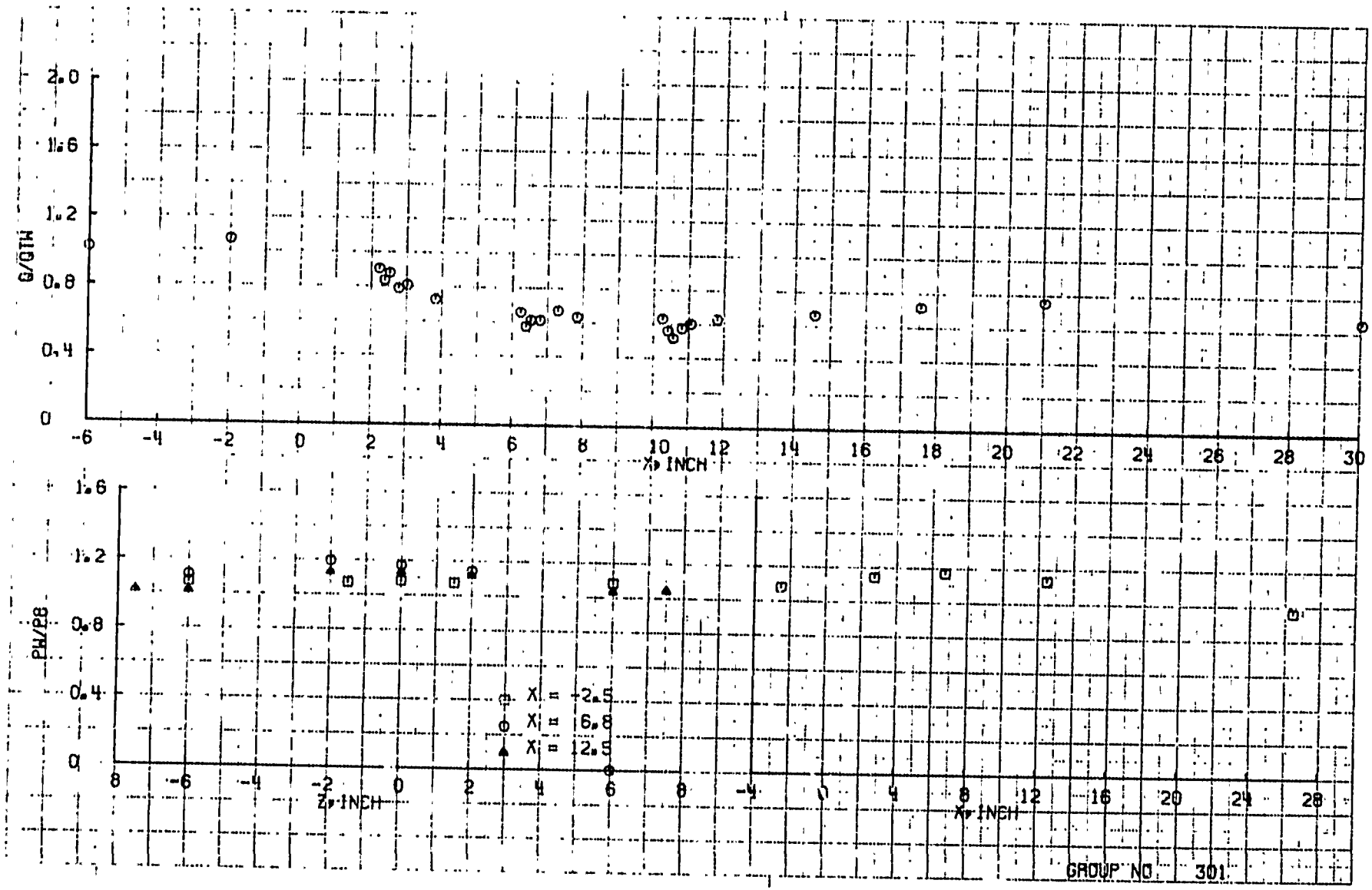
G/GTW
2.0
1.6
1.2
0.8
0.4
0
-6
-4
-2
0
2
4
6
8
10
12
14
16
18
20
22
24
26
28
30
X, INCH
PW/PB
1.6
1.2
0.8
0.4
0
X = -2.5
X = 6.8
X = 12.5
8
-6
-4
-2
0
2
4
6
8
-4
0
4
8
12
16
20
24
28
Z, INCH
X, INCH
GROUP NO 301

Group	$B'_{o\ avg}$ *	$B'_{o\ slot}$	λ_{avg}	λ_{slot}	$\dot{m}_{slot}$ (lbm/sec)
411	0	0	0	0	0
410	0.549	1.098	.000157	.000314	.00059
409	0.838	1.675	.000240	.000479	.00090
408	1.210	2.420	.000346	.000692	.00130
407	1.647	3.294	.000471	.000942	.00177
406	2.299	4.597	.000658	.00132	.00247
405	2.95	5.90	.000844	.00169	.00317
404	3.57	7.15	.00102	.00204	.00384
403	4.28	8.56	.00122	.00245	.0046
417	5.24	10.48	.00150	.00300	.00563
401	9.306	18.61	.00266	.00532	.010

*

$$B'_{o\ avg} = \dot{m}_{slot}/(A_{tot} \cdot \rho_e u_e C_H) \quad \text{where} \quad A_{tot} = (\text{slot} + \text{land}) \times \text{width}$$

$$B'_{o\ slot} = \dot{m}_{slot}/(A_{slot} \cdot \rho_e u_e C_H) \quad \text{where} \quad A_{slot} = (\text{slot} \times \text{width})$$

$$\lambda'_{avg} = \dot{m}_{slot}/(A_{tot} \cdot \rho_e u_e)$$

$$\lambda'_{slot} = \dot{m}_{slot}/(A_{slot} \cdot \rho_e u_e)$$

Figure 4-30 2.0/2.0 Model with Filler

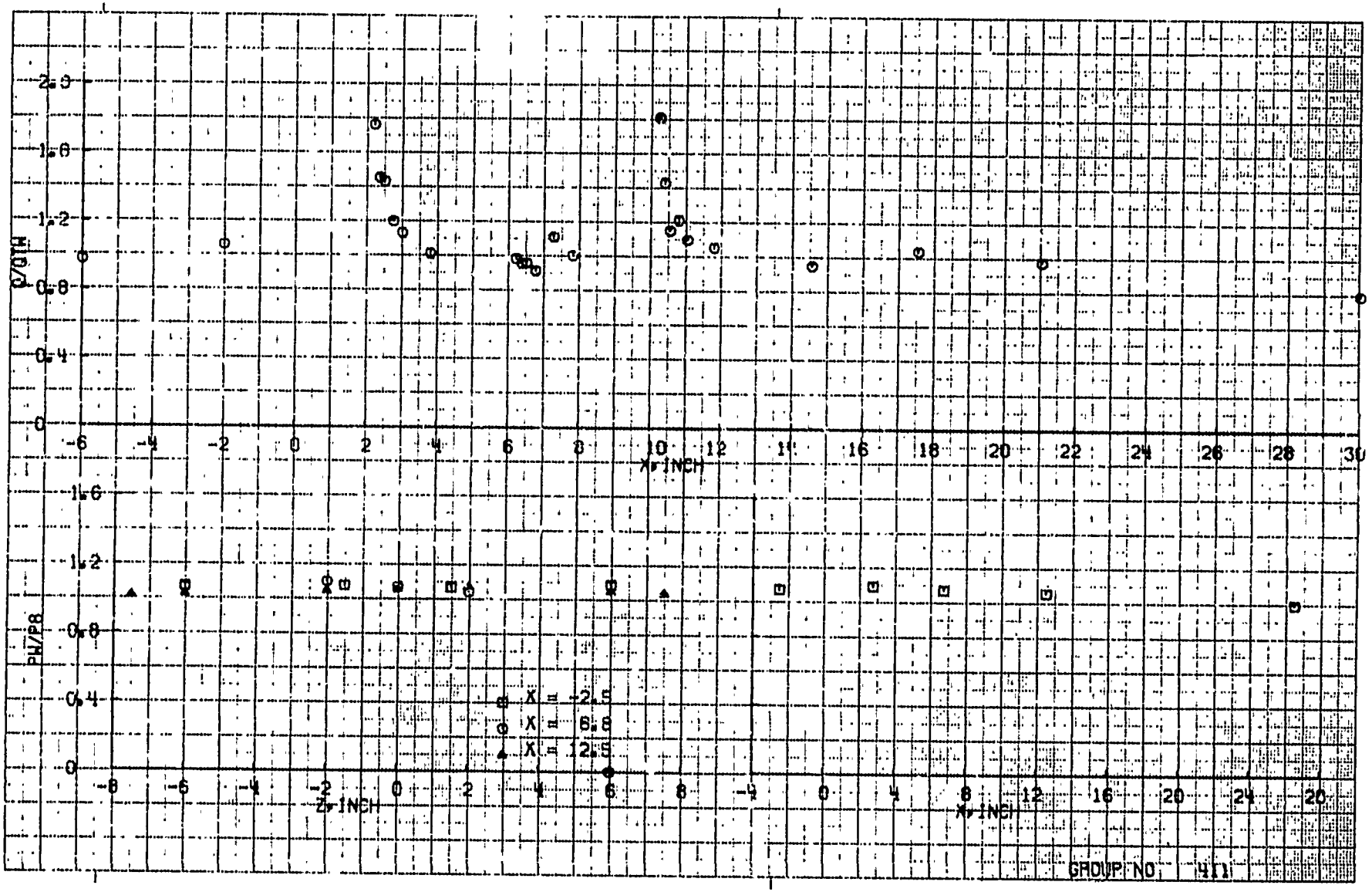
PW/P8
Z, INCH
X, INCH
X = -2.5
X = 6.8
X = 12.5
GROUP NO 411

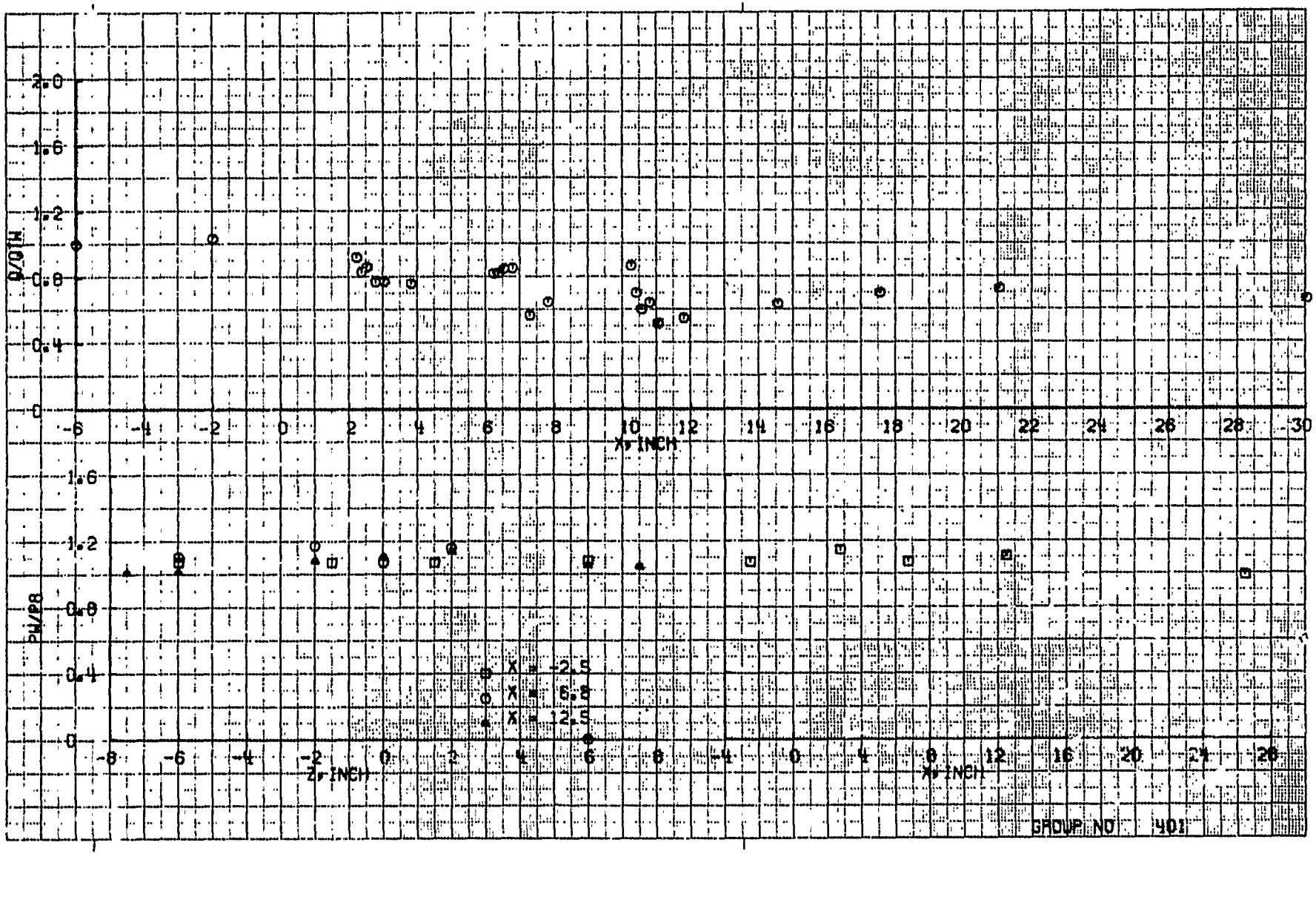
P/P0
Y/D
Xp INCH
Zp INCH
Xp INCH
X = 2.5
X = 5.8
X = 12.5
GROUP NO 401

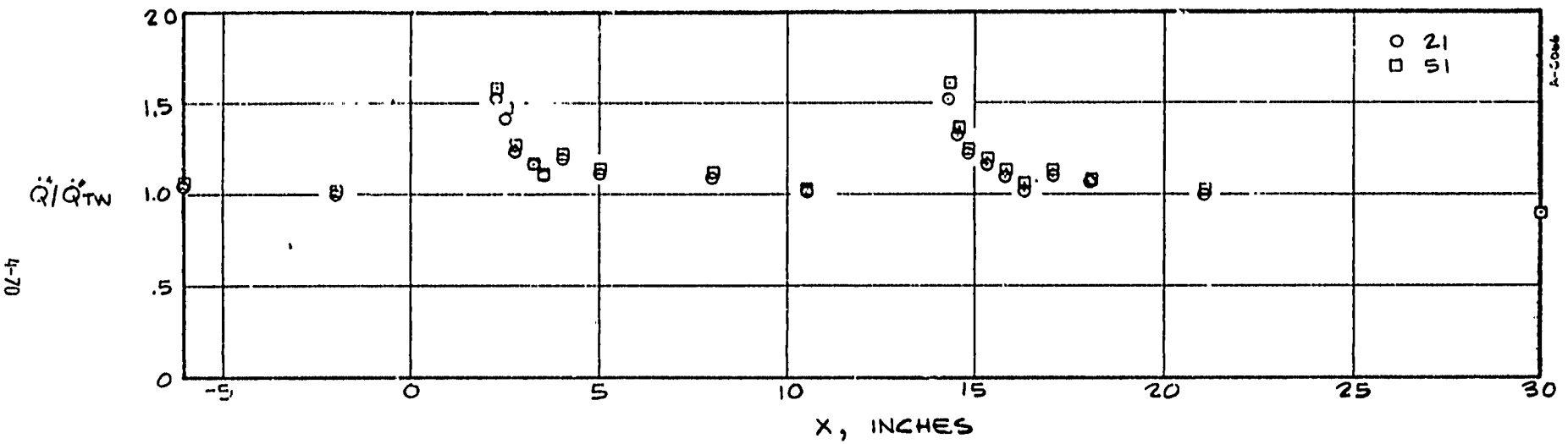

A) 2.0/10.0 MODEL WITH NO BLOWING

Figure 4-31. Comparison of Heat Flux For Duplicate Test Conditions

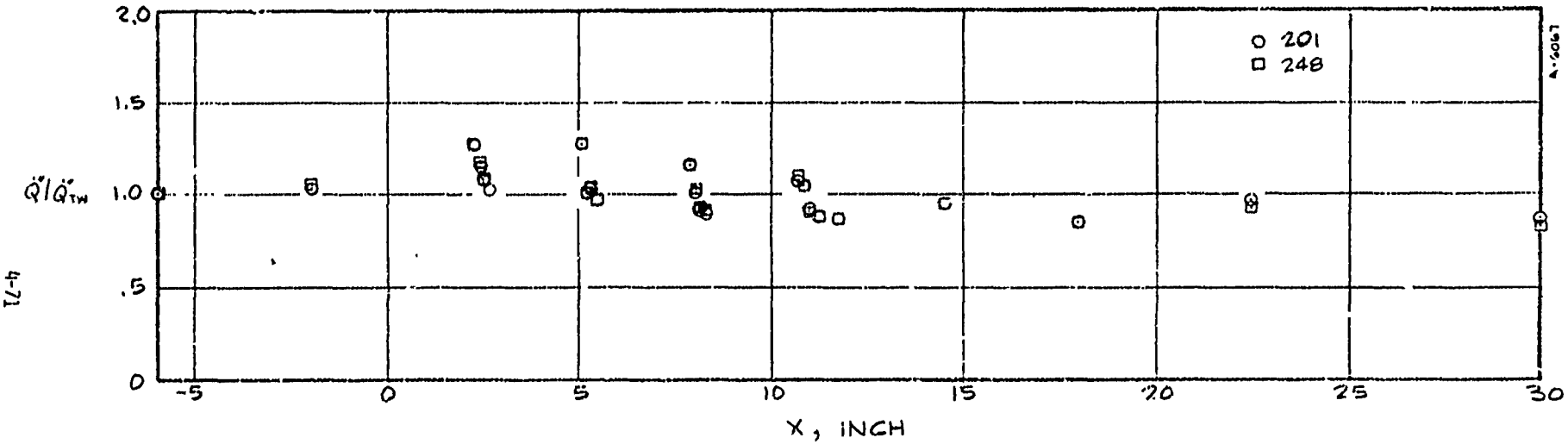

B.) 2.0/.8 MODEL WITH MAXIMUM BLOWING

Figure 4-31. Comparison of Heat Flux For Duplicate Test Conditions

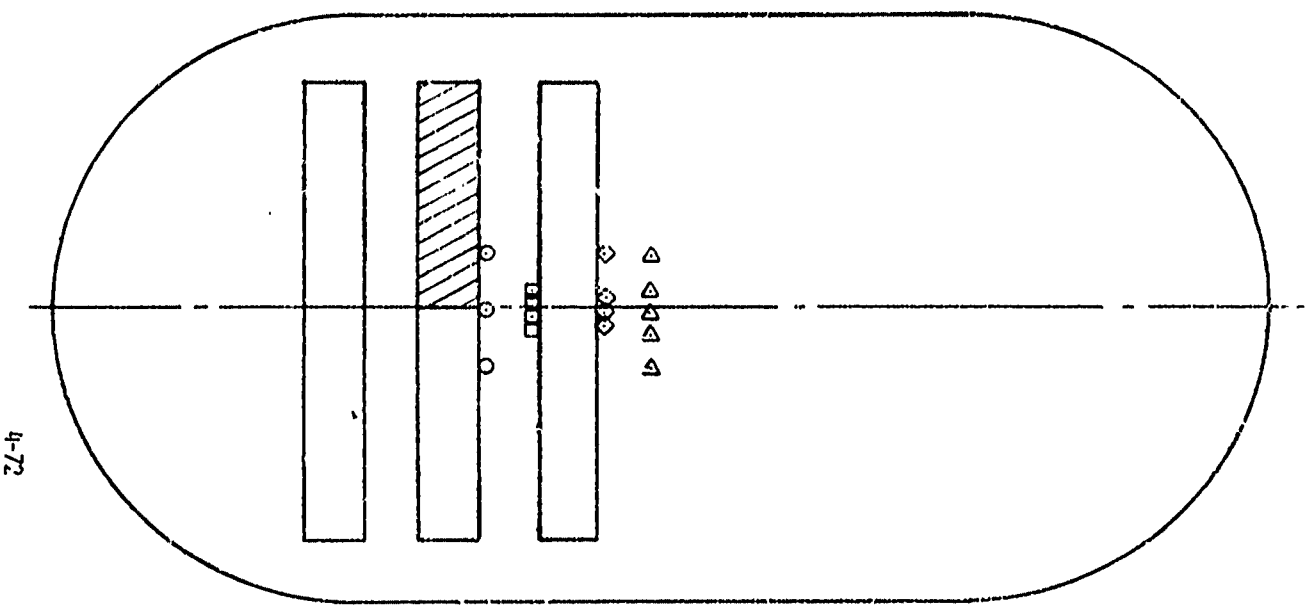

TRANSVERSE GARDON GAGES			
GAGE NO.	SYM	X	Z
7	○	6.23	2.0
8	○	↓	0
9	○	6.23	-2.0
14	□	7.83	.62
15	□	↓	.25
16	□	↓	-.25
17	□	7.83	-.62
18	◇	10.25	2.0
19	◇	↓	.50
20	◇	↓	0
21	◇	10.25	-.50
26	△	11.80	2.0
27	△	↓	.25
28	△	↓	0
29	△	↓	.75
30	△	11.80	2.0

Figure 4-32. Schematic of Transverse Gardon Gage Location

A-6068

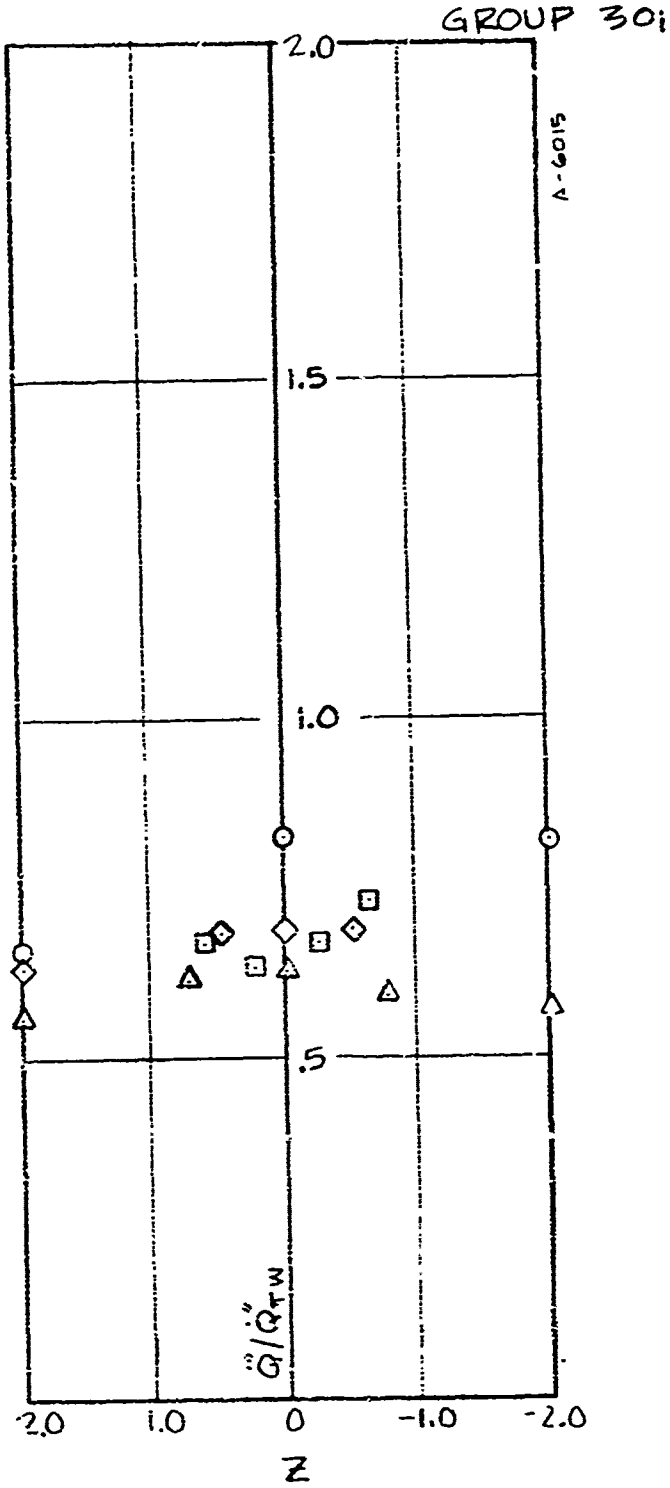

Figure 4-32 (Continued). Transverse Arrays Without Blowing

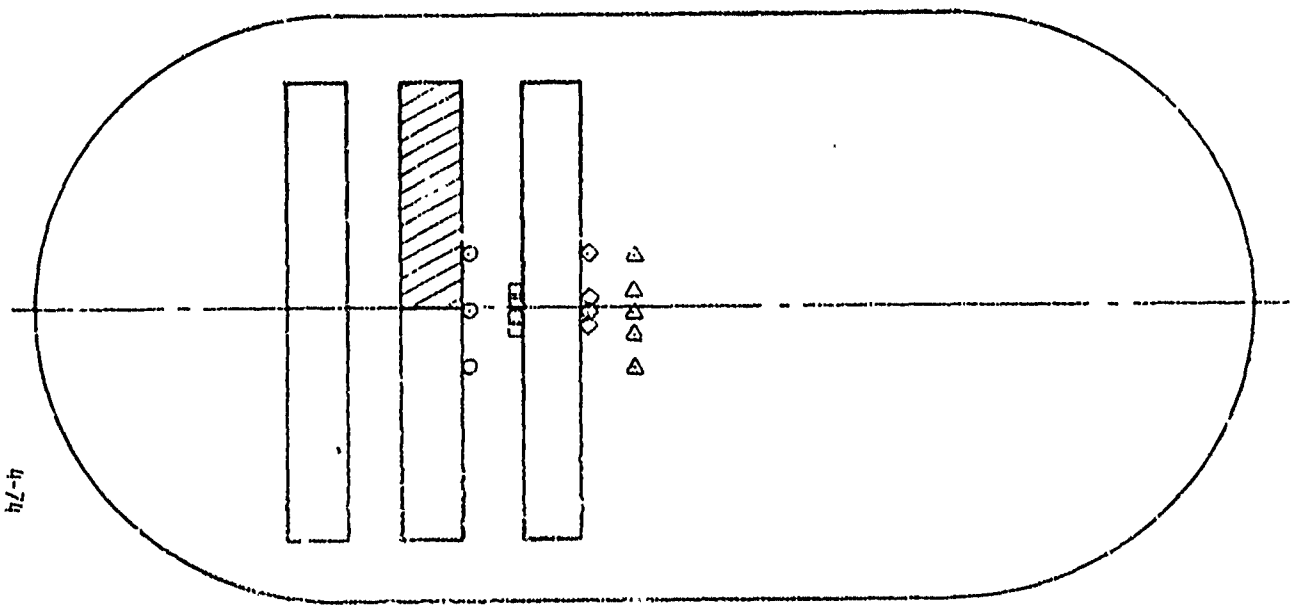

TRANSVERSE GARDON GAGES			
GAGE NO.	SYM	X	Z
7	○	6.23	2.0
6	○	|	0
5	○	6.23	-2.0
14	□	7.83	.62
15	□	|	.25
16	□	|	-.25
17	□	7.83	-.62
18	◇	10.25	2.0
19	◇	|	.50
20	◇	|	0
21	◇	10.25	-.50
26	△	11.80	2.0
27	△	|	.25
28	△	|	0
29	△	|	.75
30	△	11.80	2.0

Figure 4-33. Schematic of Transverse Gardon Gage Location

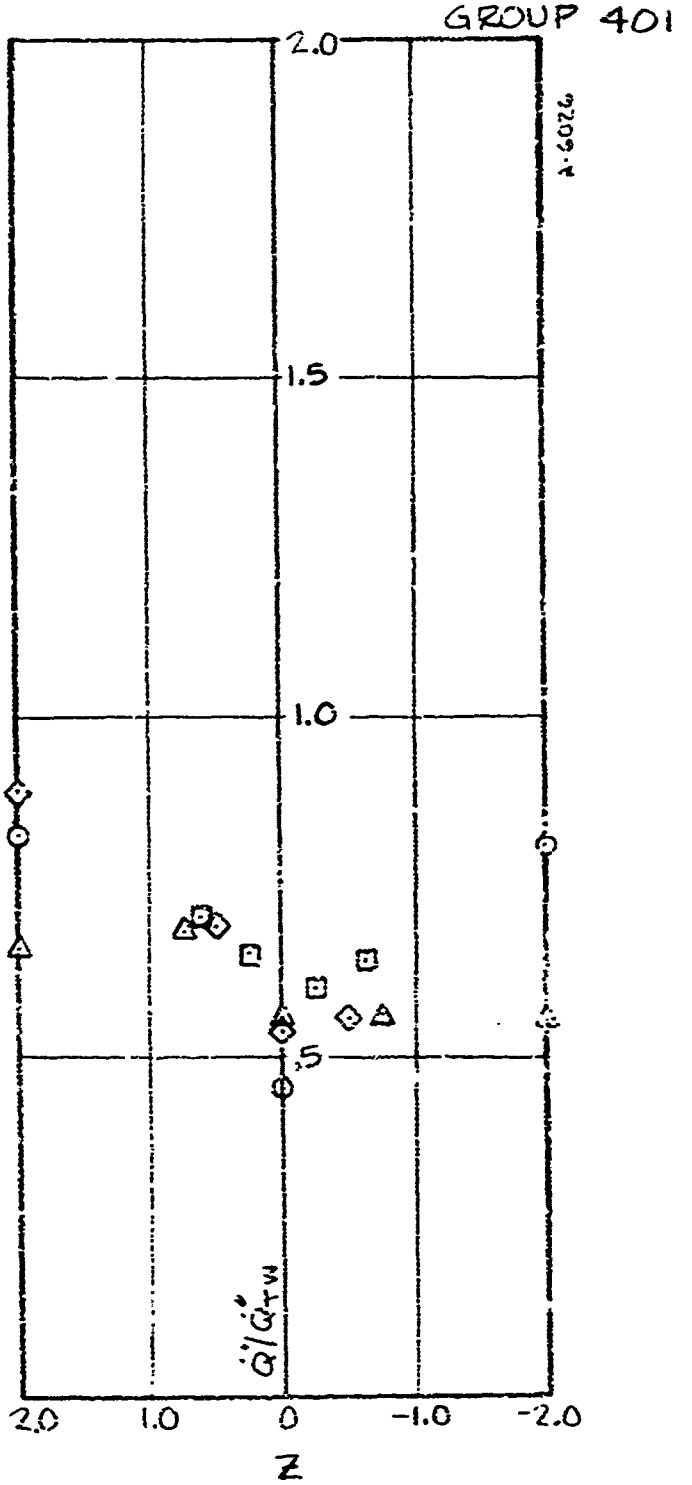

Figure 4-33 (Continued). Transverse Arrays With Blowing

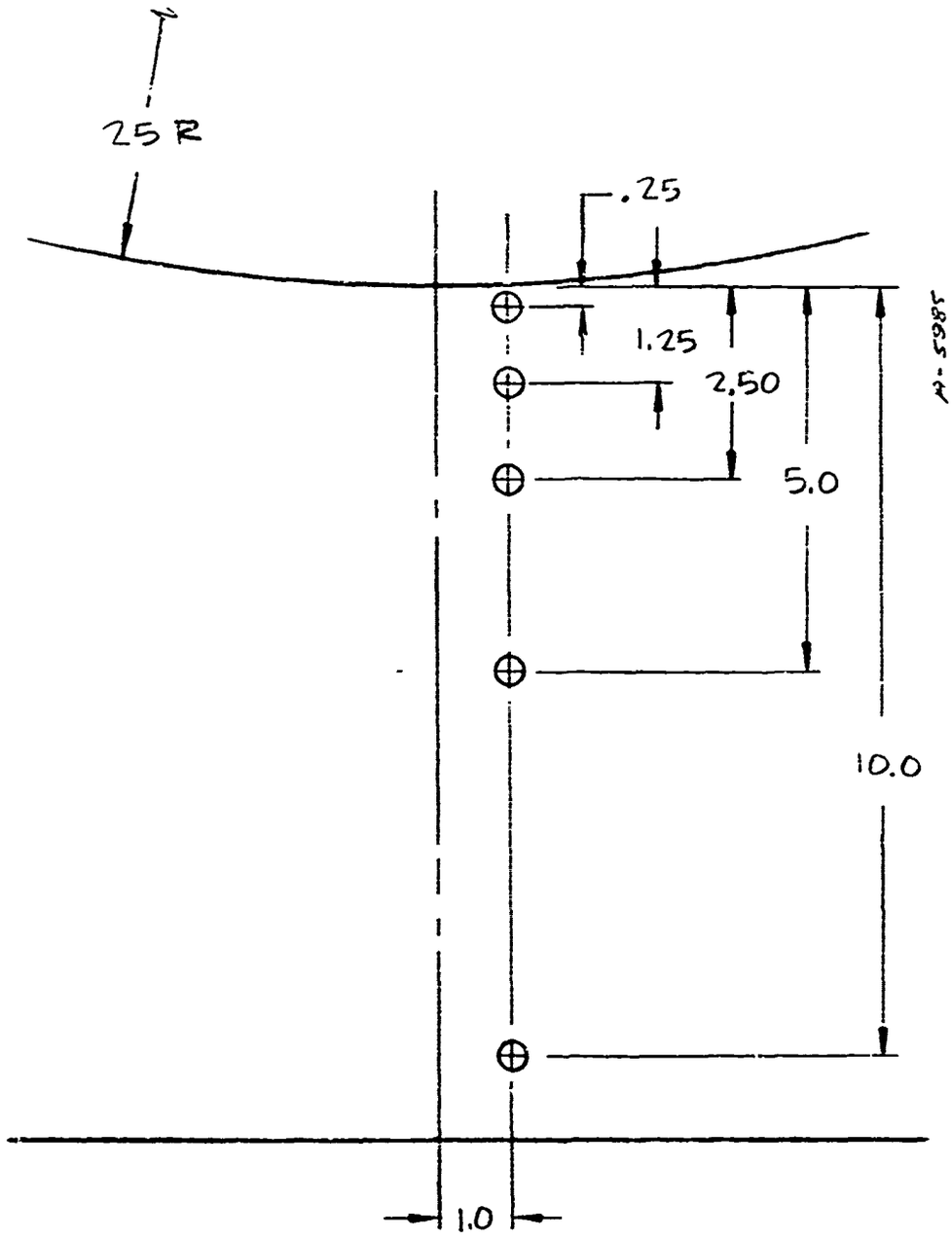

Figure 4-34. Configuration For Sensors in Slot

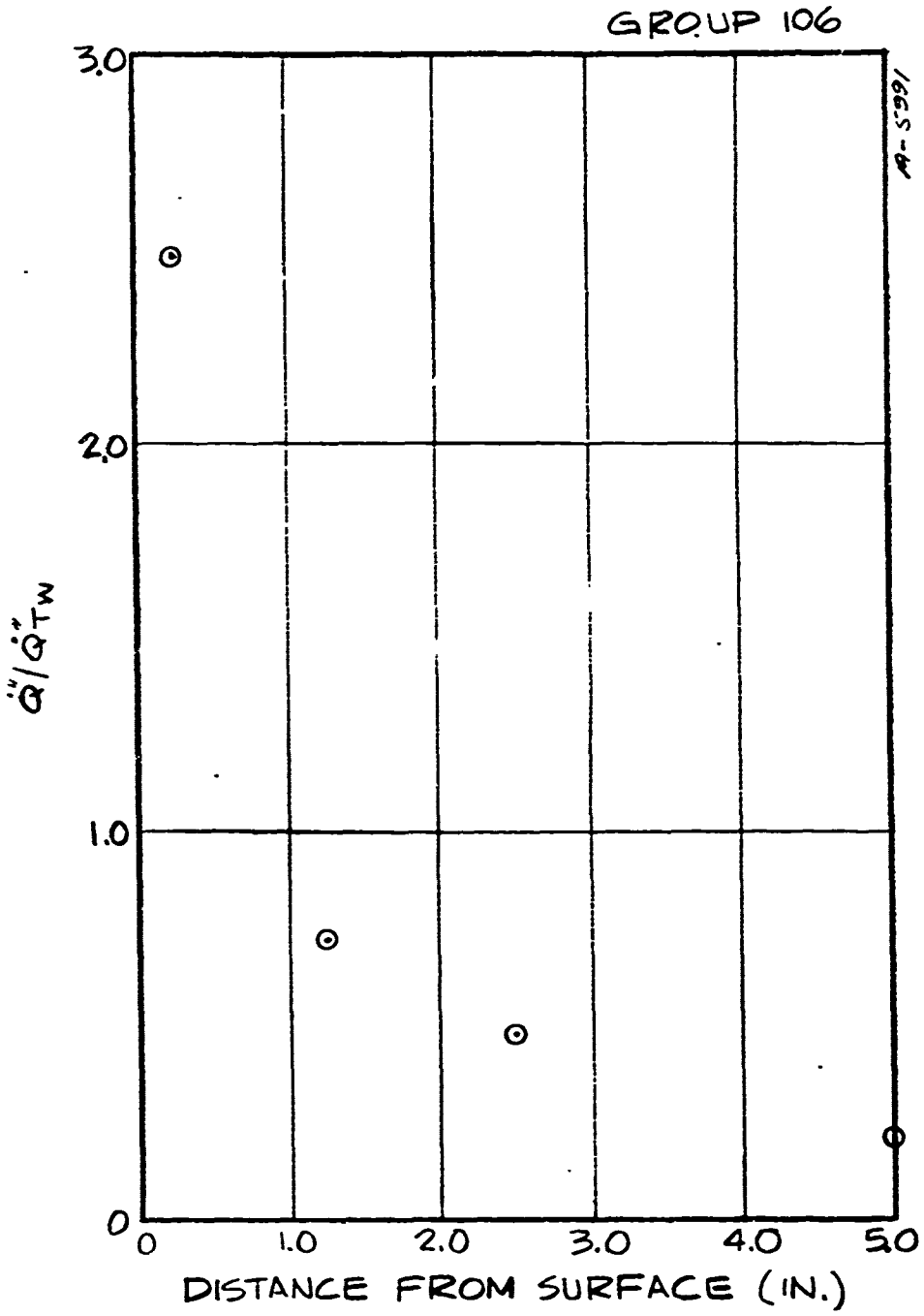

Figure 4-34. (Continued)

does seem to have a more dramatic effect on the in-depth heating than on the surface heat flux, however even tramatic blowing rates reduce the heat flux at the cavity only to the undisturbed value.

The boundary layer data taken is illustrated by Figures 4-35 - 4-39. Each figure includes representative profiles taken with a specifif model configuration. Each set of profiles is accompanied by a sketch showing the locations surveyed and a table of pertinent parameters for the various configurations. While a concerted attempt was made to obtain sufficient profile information to allow estimation of boundary layer behavior, time did not permit comprehensive surveys. The emphasis on surveys at 3 inches up is due to the contour of the plate which resulted in this location allowing maximum resolution with both total temperature and pitot probes without contacting the surface with more fragile temperature probe. The preliminary results of the boundary layer surveys indicate, as might be expected in a seven-inch turbulent boundary layer, that the injection and roughness effects have relatively little impact on the overall boundary layer shape, although these effects obviously drastically affect the behavior at the wall.

4.6 CONCLUSIONS

Representative heat transfer distributions over the four models listed are presented in Figures 4-40 to 4-43. A comparison of these results with boundary layer prediction codes, with no roughness corrections, indicate a roughness dominated phenomena. A list of major conclusions can be drawn from the example data in Section 5.5 and Reference 8:

- The pressure field is not affected by blowing.
- The heat transfer is roughness dominated.
- Roughness heating extends below the surface into the slot.
- Peak heating may be predicted utilizing a base flow correlation technique for flow over the slot.
- Land heating distributions may be correlatable with roughness and downstream cooling curves through the use of an appropriate discrete injection blockage factor (Section 6).

FLOW CONDITIONS

Group	Number of Slots Upstream	Distance Downstream of Previous Slot	$B'_{o\ avg}$	$B'_{o\ slot}$	λ_{avg}	λ_{slot}	$\dot{m}_{slot}$ (lbm/sec)
31	0	-2.0	0	0	0	0	0
34	1	.255					
36		.805					
38		1.255					
40		2.055					
42		8.505					

BOUNDARY LAYER PROPERTIES

Group	Momentum Thickness (in)	Boundary Layer Thickness (in)	Edge Velocity (fps)	Edge Temperature (°R)	Edge Density (lbm/ft^3)	Edge Total Temperature (°R)	Edge Probe Pressure (lbf/in^2)
31	.216	5.639	3831	100.4	.00221	1321.8	6.495
34	.215	5.725	3833	99.9	.00222	1322.3	6.510
36	.216	5.692	3841	101.4	.00219	1329.7	6.467
38	.215	5.641	3827	101.3	.00219	1320.4	6.406
40	.216	5.741	3827	100.2	.00222	1319.3	6.489
42	.217	5.804	3832	100.0	.00222	1322.1	6.517

Figure 4-35a. Investigation of the Boundary Layer Behavior on the First Land of the 2.0/10.0 Model with no Blowing.

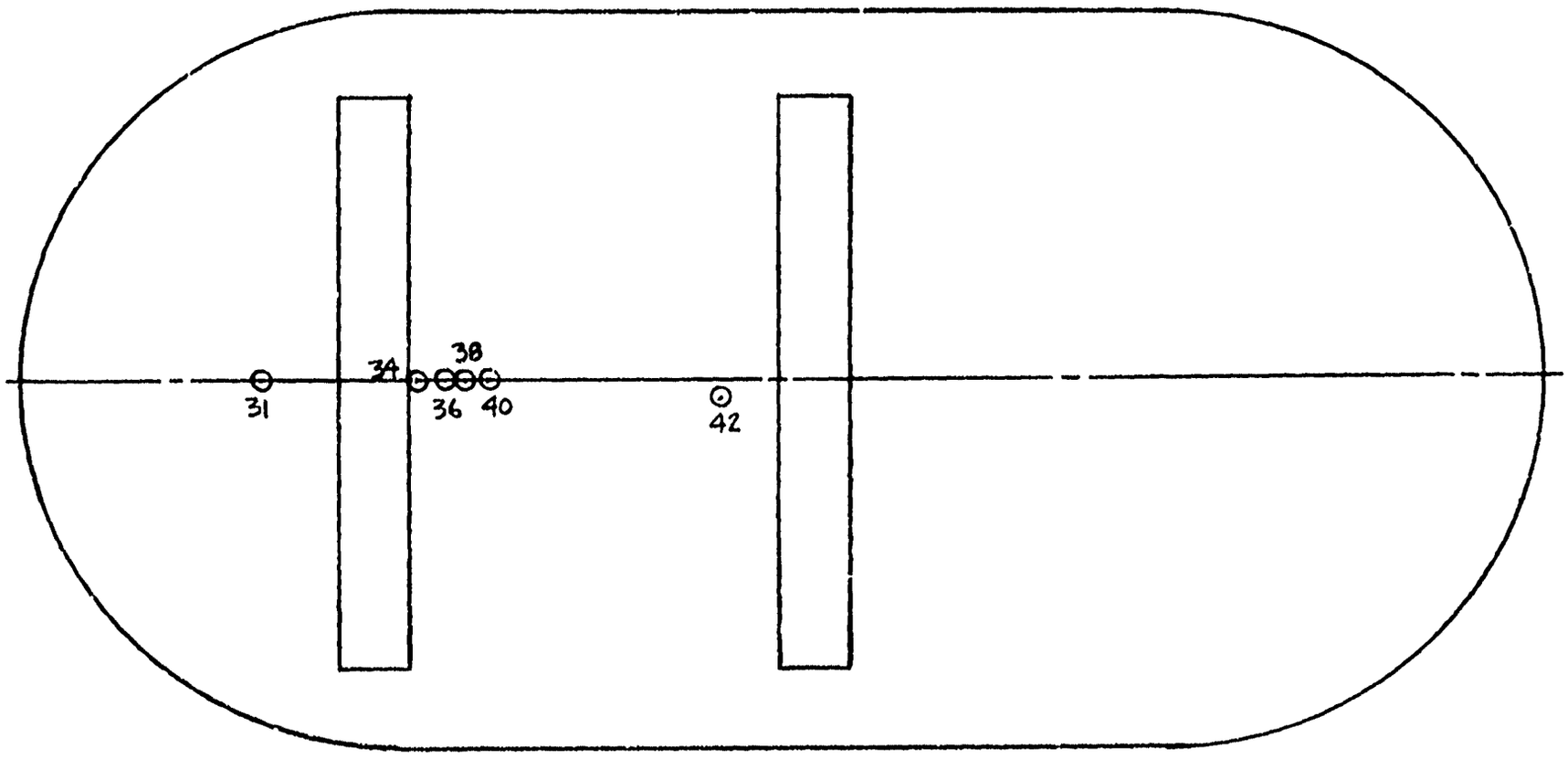

Figure 4-35a. (Continued)

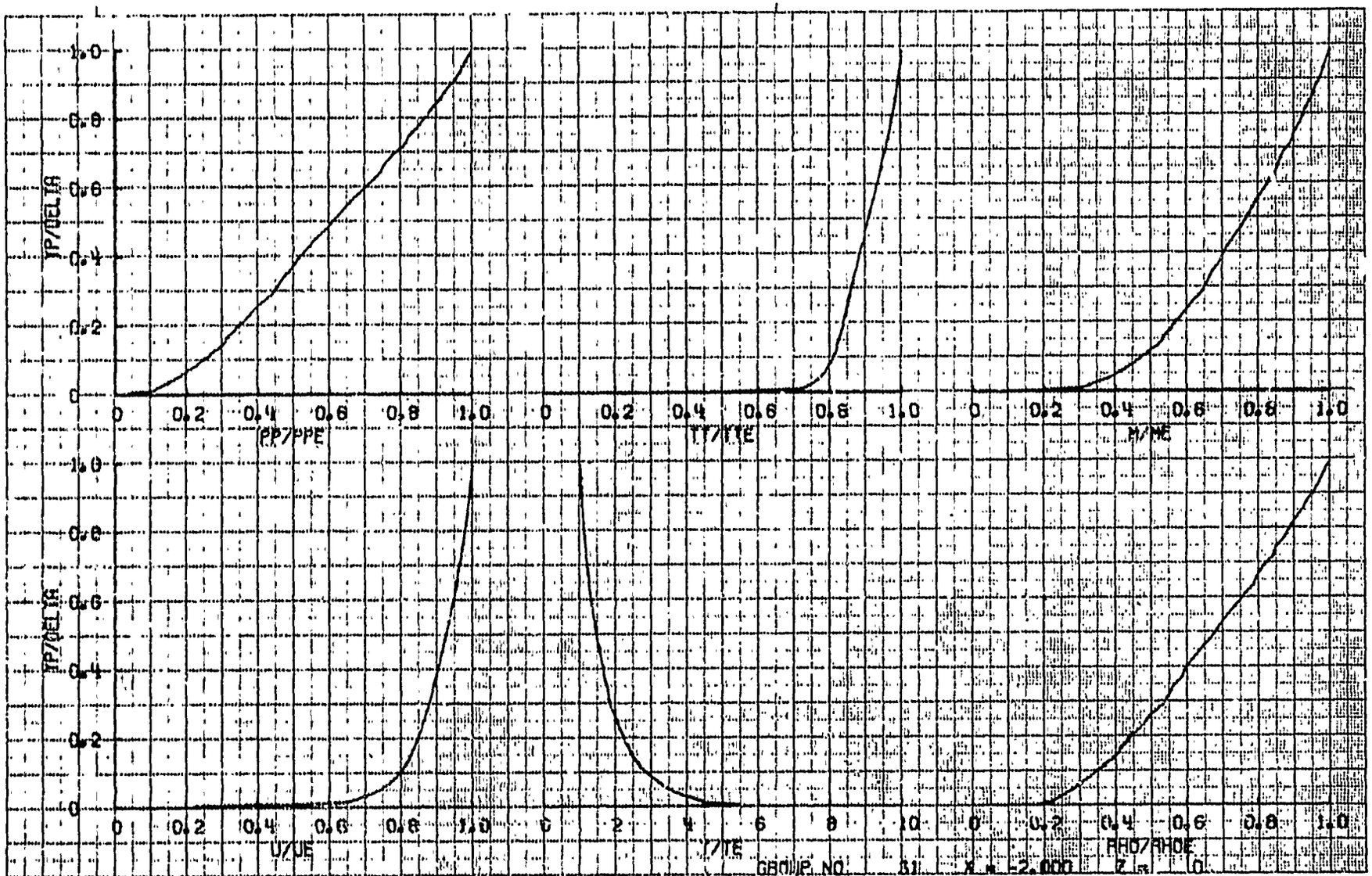
1.0
0.8
0.6
0.4
0.2
0
0.2
0.4
0.6
0.8
1.0
PP/PPE
TT/TTE
M/ME
U/UE
T/TE
RHO/RHOE
GROUP NO. 31
X = -2.000
Z = 0.

FLOW CONDITIONS

Group	Number of Slots Upstream	Distance Downstream of Previous Slot	$B'_{o\ avg}$	$B'_{o\ slot}$	λ_{avg}	λ_{slot}	$\dot{m}_{slot}$ (lbm/sec)
44	2	0.29	0	0	0	0	0
46	|	0.75	|	|	|	|	|
48	|	2.23	|	|	|	|	|
50	|	2.97	|	|	|	|	|

BOUNDARY LAYER PROPERTIES

Group	Momentum Thickness (in)	Boundary Layer Thickness (in)	Edge Velocity (fps)	Edge Temperature (°R)	Edge Density (lbm/ft^3)	Edge Total Temperature (°R)	Edge Probe Pressure (lbf/in^2)
44	.221	5.845	3835	100.5	.00221	1324.4	6.487
46	.220	5.902	3829	100.8	.00221	1321.0	6.469
48	.222	5.875	3826	100.9	.00221	1319.5	6.458
50	.223	5.876	3826	100.6	.00221	1318.9	1339.5

Figure 4-35b. Investigation of the Boundary Layer on the Second Land (Downstream Section) of the 2.0/10.0 Model with no Blowing.

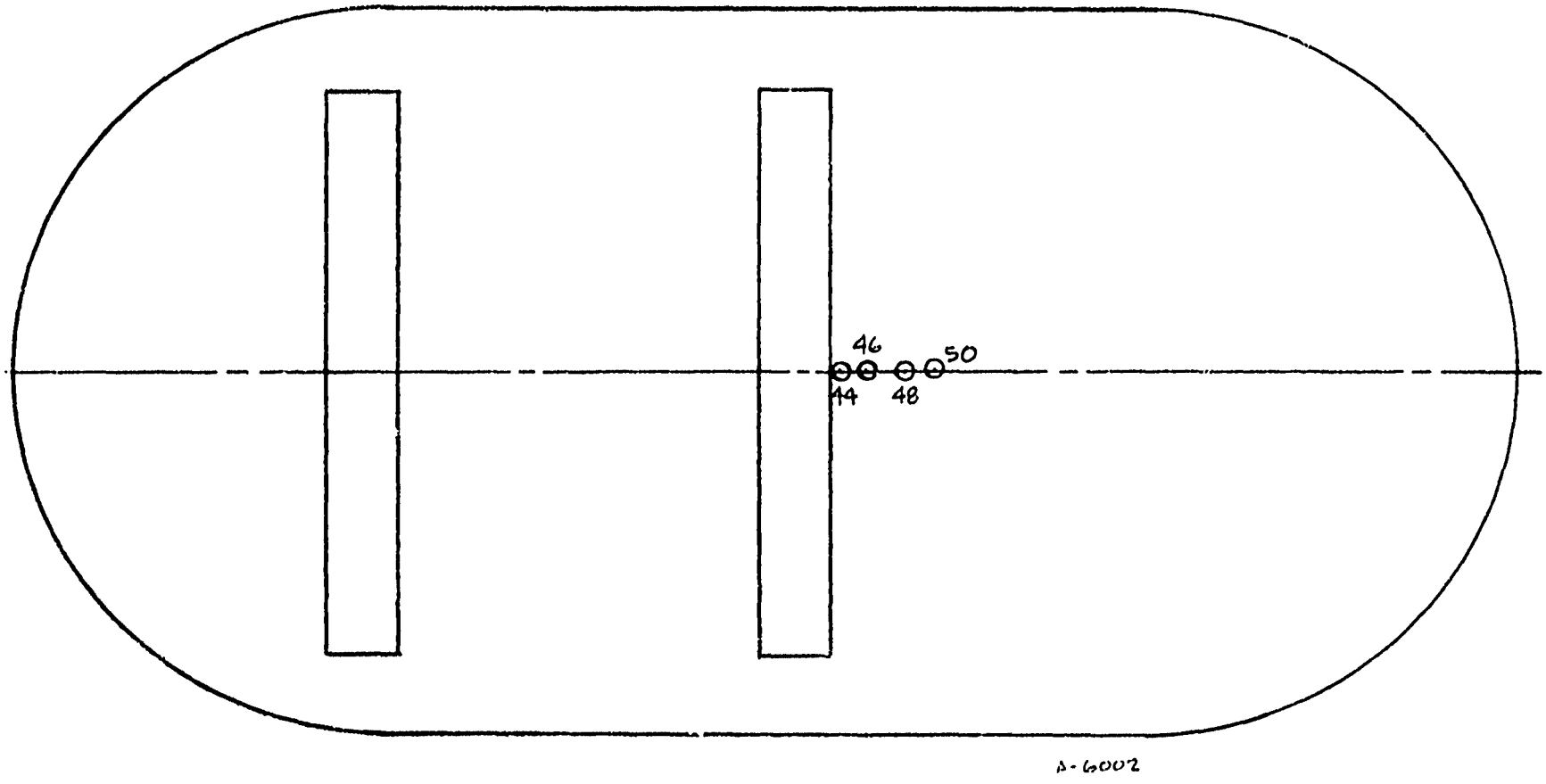

Figure 4-35b. (Continued)

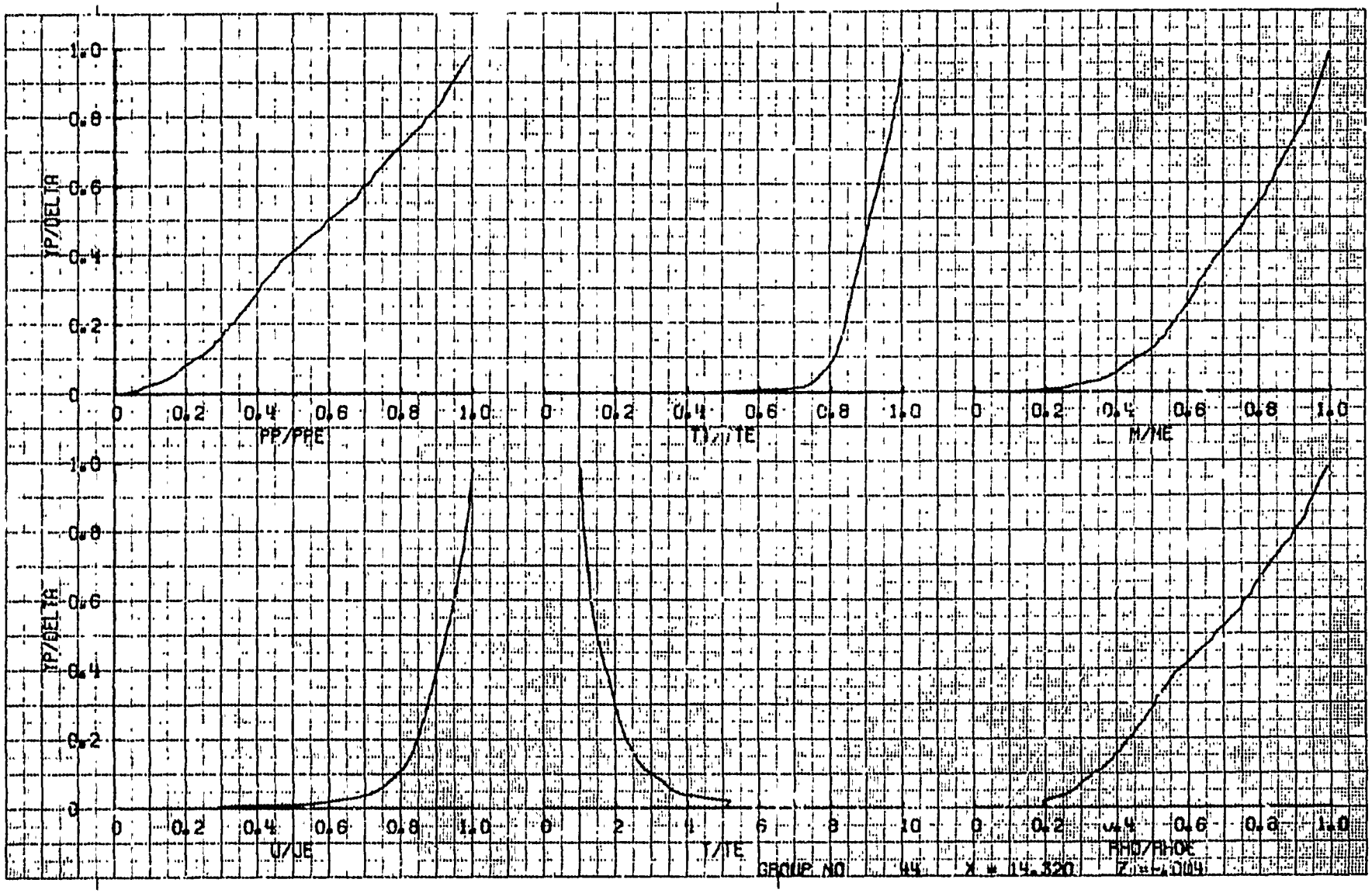
YP/DELTA
PP/PHE
U/UE
T/TE
M/ME
RHO/RHOE
GROUP NO
44
X = 14.320
Z = -.004

FLOW CONDITIONS

Group	Number of Slots Upstream	Distance Downstream of Previous Slot	$B'_{o\ avg}$	$B'_{o\ slot}$	λ_{avg}	λ_{slot}	$\dot{m}_{slot}$ (lbm/sec)
34	1	0.255	0	0	0	0	0
52	|	|	2.36	14.14	.000675	.0040	.0076
58	|	|	3.69	22.15	.00106	.00634	.0119
38	|	1.255	0	0	0	0	0
54	|	|	2.36	14.14	.000675	.0040	.0076
56	|	|	3.78	22.71	.00108	.0065	.0122

BOUNDARY LAYER PROPERTIES

Group	Momentum Thickness (in)	Boundary Layer Thickness (in)	Edge Velocity (fps)	Edge Temperature (°R)	Edge Density (lbm/ft^3)	Edge Total Temperature (°R)	Edge Probe Pressure (lbf/in^2)
34	.215	5.725	3833	99.9	.00222	1322	6.510
52	.213	5.683	3828	100.6	.00221	1320.5	6.458
58	.213	5.673	3828	100.6	.00221	1320.4	6.458
38	.215	5.641	3827	101.3	.00219	1320.4	6.406
54	.216	5.695	3824	100.5	.00221	1338.3	6.450
56	.216	5.709	3825	100.7	.00221	1313.5	6.468

Figure 4-35c. Investigation of the Behavior of the Boundary Layer Behavior at Two Points for Three Flow Rates. First Land, 2.0/10.0 Model.

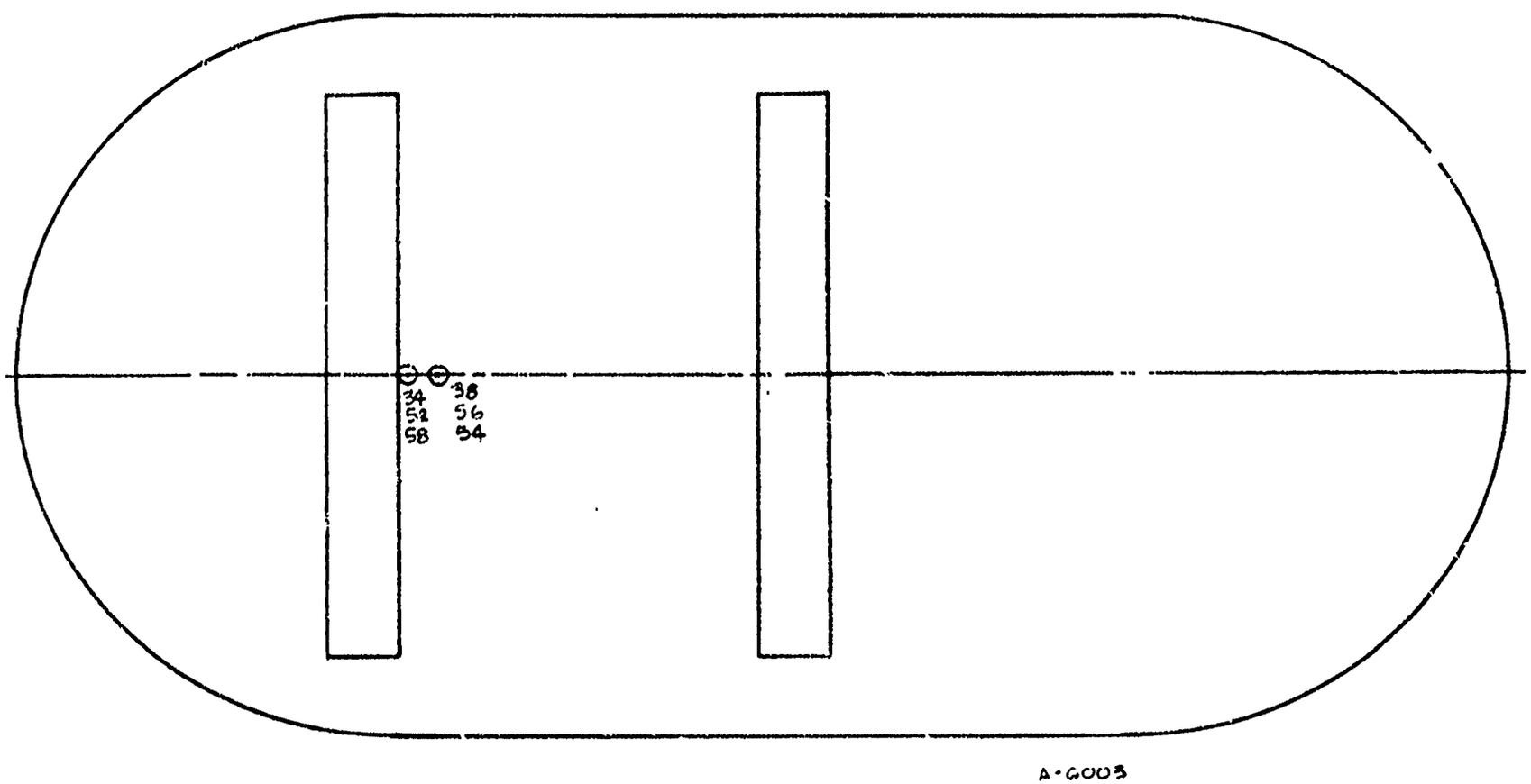

Figure 4-35c. (Continued)

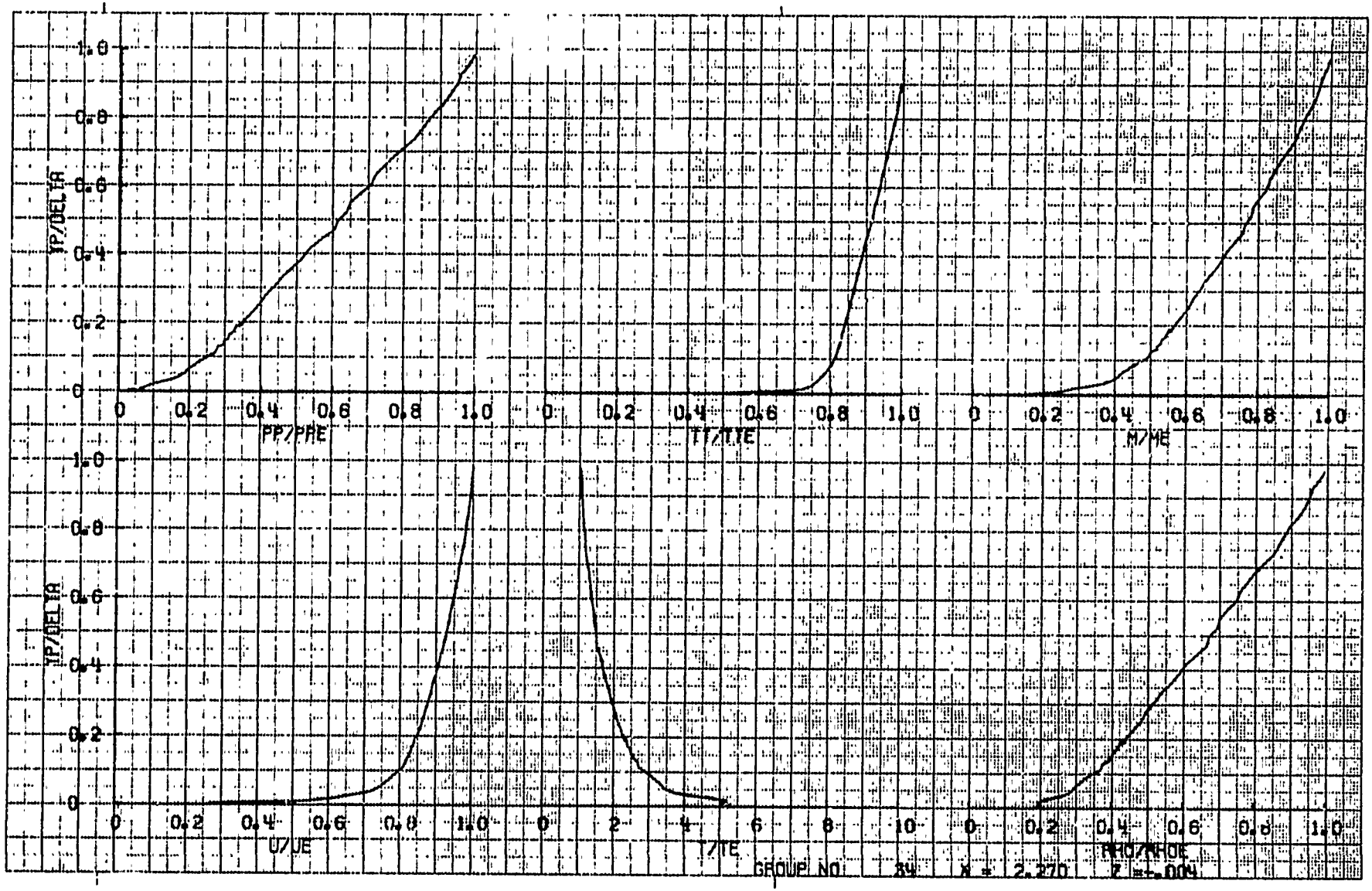
YP/DELTA
PP/PRE
TT/TTE
M/ME
YP/DELTA
U/UE
T/TE
RHO/RHOE
GROUP NO. 34
M = 2.270
Z = -.004

FLOW CONDITIONS

Group	Number of Slots Upstream	Distance Downstream of Previous Slot	$B'_{o\ avg}$	$B'_{o\ slot}$	λ_{avg}	λ_{slot}	$\dot{m}_{slot}$ (lbm/sec)
117	1	0.225	0	0	0	0	0
119		0.735					
121		1.475					
123		1.975					
125		4.475					

BOUNDARY LAYER PROPERTIES

Group	Momentum Thickness (in)	Boundary Layer Thickness (in)	Edge Velocity (fps)	Edge Temperature (°R)	Edge Density (lbm/ft^3)	Edge Total Temperature (°R)	Edge Probe Pressure (lbf/in^2)
117	.215	5.718	3840	100.9	.00220	1349.1	6.483
119	.217	5.716	3843	101.5	.00219	1331.2	6.446
121	.218	5.758	3843	101.4	.00219	1351.1	6.465
123	.220	5.775	3843	100.9	.00220	1351.4	6.484
125	.219	5.822	3853	100.5	.00221	1357.6	6.542

Figure 4-36. Survey of Boundary Layer Behavior on First Land of the 5.0/5.0 Model Without Blowing.

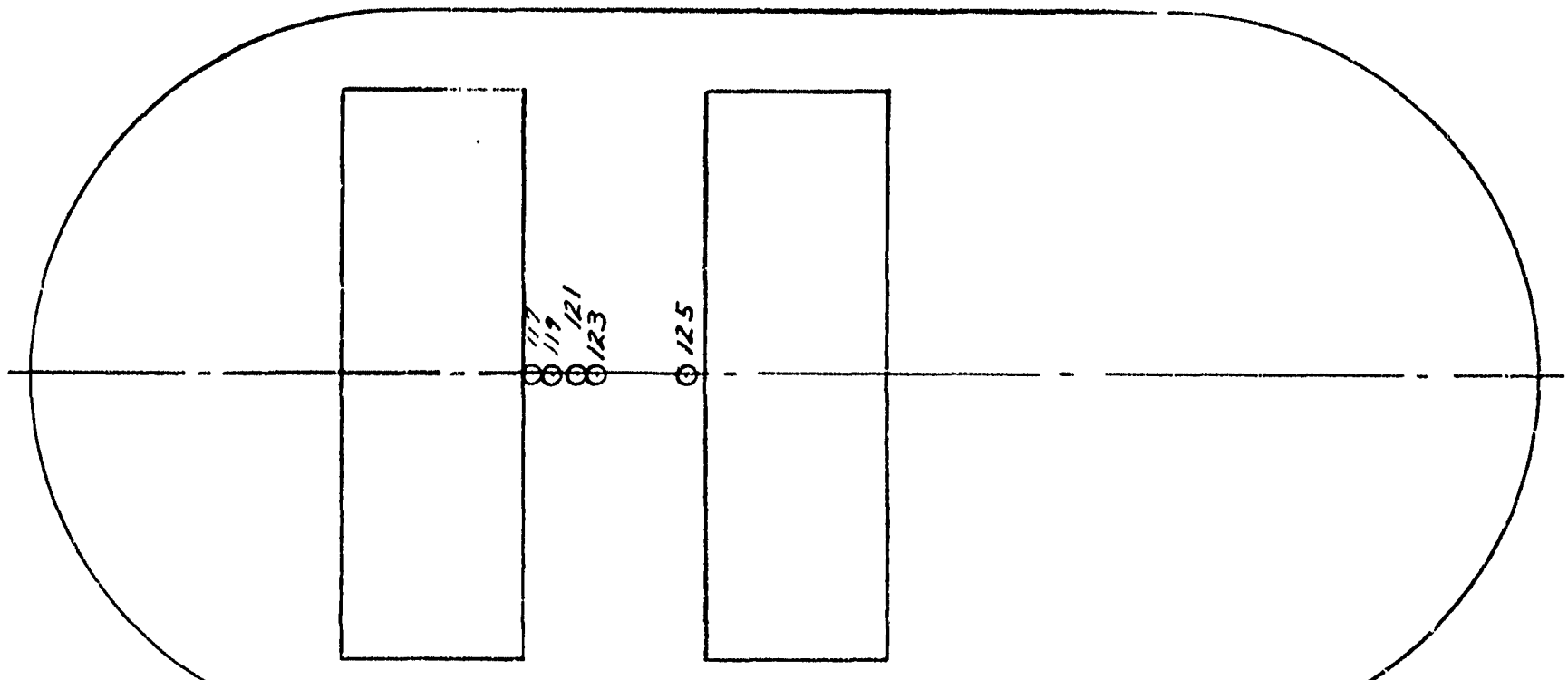

Figure 4-36. (Continued)

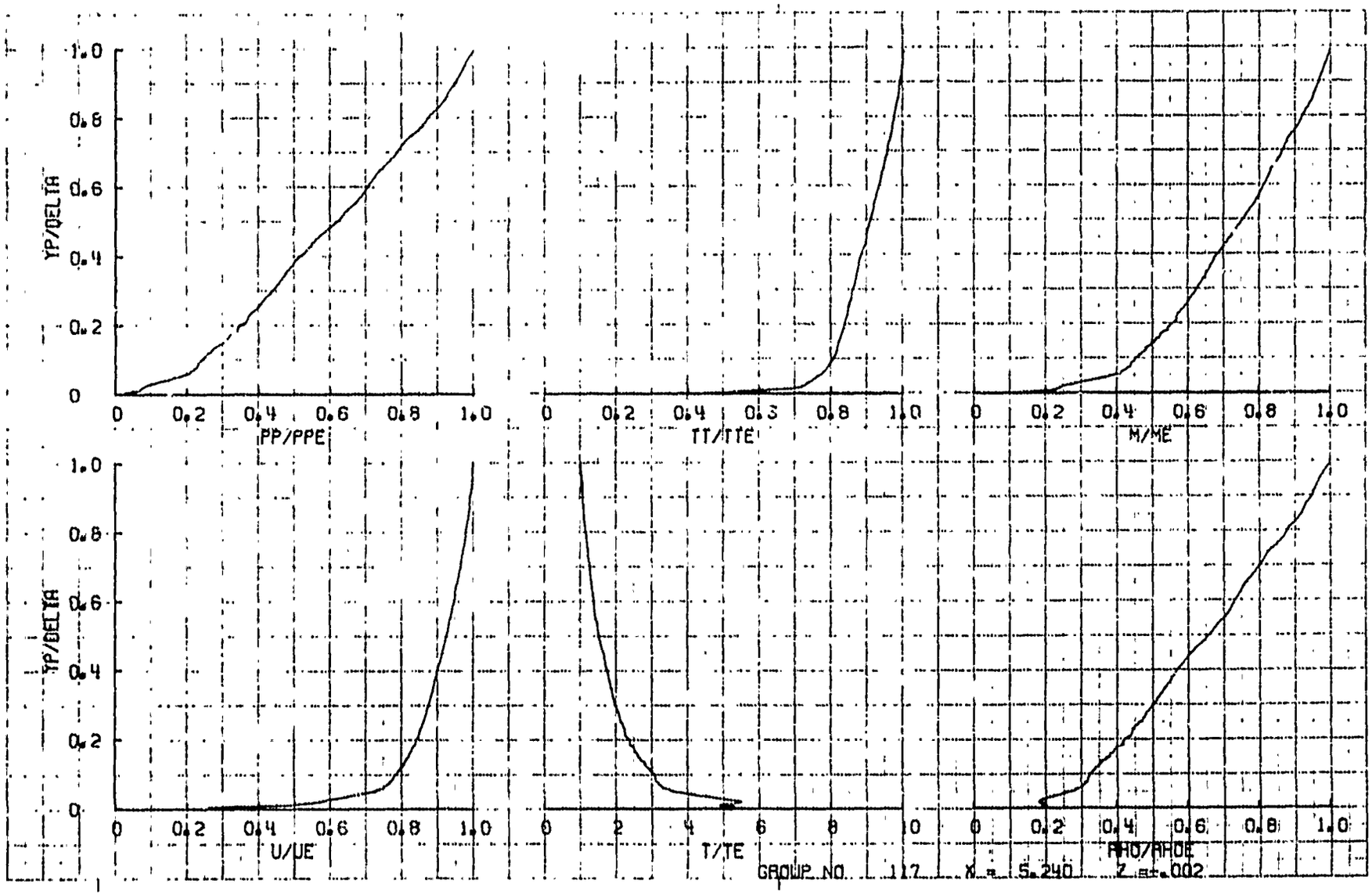
YP/DELTA
PP/PPE
TT/TTE
M/ME
U/UE
T/TE
RHO/RHOE
GROUP NO. 117 X = 5.240 Z = .002

FLOW CONDITIONS

Group	Number of Slots Upstream	Distance Downstream of Previous Slot	$B'_{o\ avg}$	$B'_{o\ slot}$	λ_{avg}	λ_{slot}	$\dot{m}_{slot}$ (lbm/sec)
229	3	0.045	0	0	0	0	0
231	|	0.165	|	|	|	|	|
233	|	0.355	|	|	|	|	|
235	|	0.765	|	|	|	|	|

BOUNDARY LAYER PROPERTIES

Group	Momentum Thickness (in)	Boundary Layer Thickness (in)	Edge Velocity (fps)	Edge Temperature (°R)	Edge Density (lbm/ft^3)	Edge Total Temperature (°R)	Edge Probe Pressure (lbf/in^2)
229	.215	6.070	3834	98.6	.00225	1321.9	6.613
231	.217	6.023	3825	99.0	.00224	1316.7	6.565
233	.213	6.047	3827	98.4	.00225	1317.2	6.597
235	.214	6.073	3827	98.5	.00225	1317.7	6.599

Figure 4-37. Detailed Profile on Initial Downstream Segment After Four Slots on 2.0/0.8 Model Without Blowing.

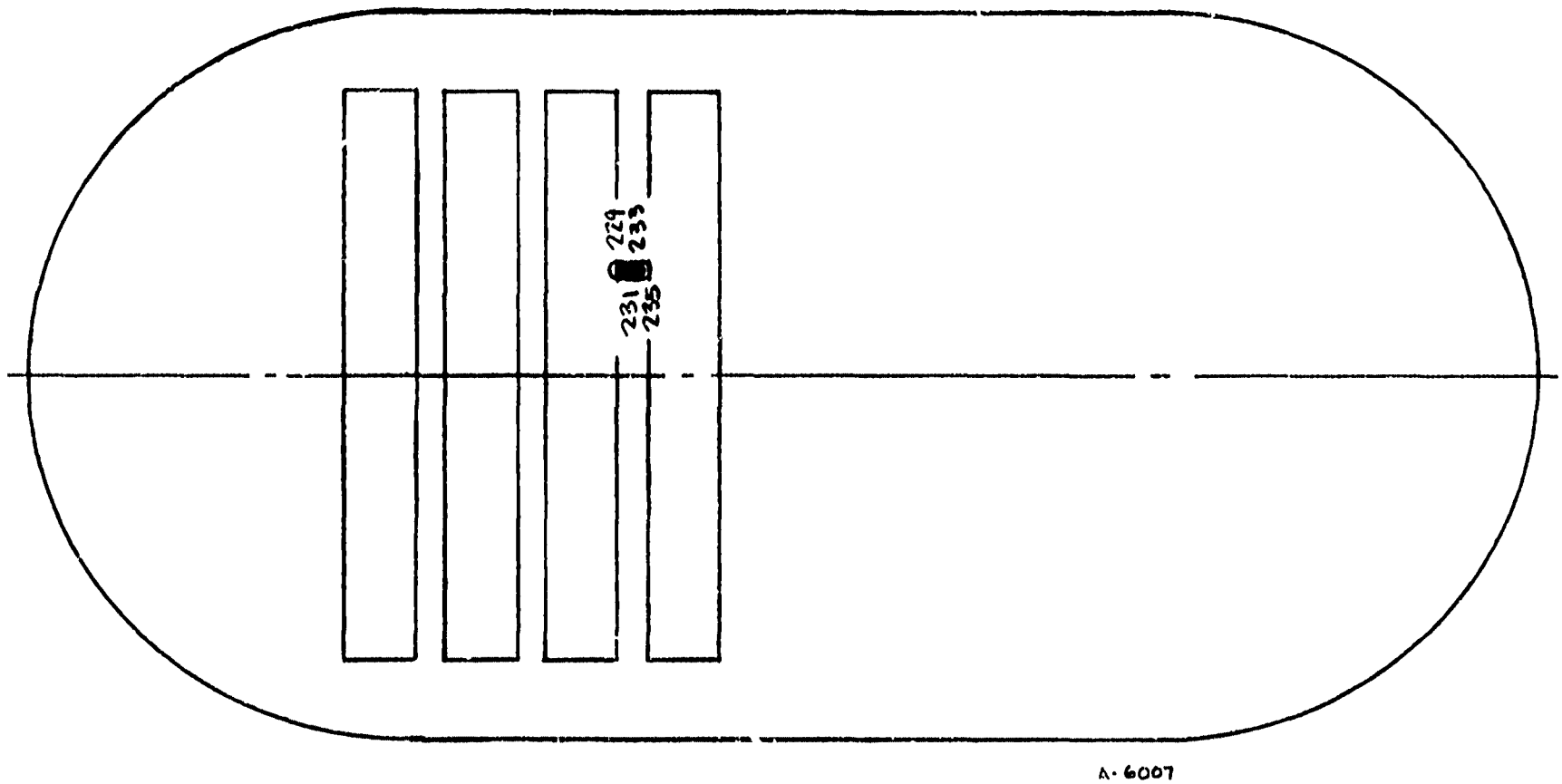

Figure 4-37. (Continued)

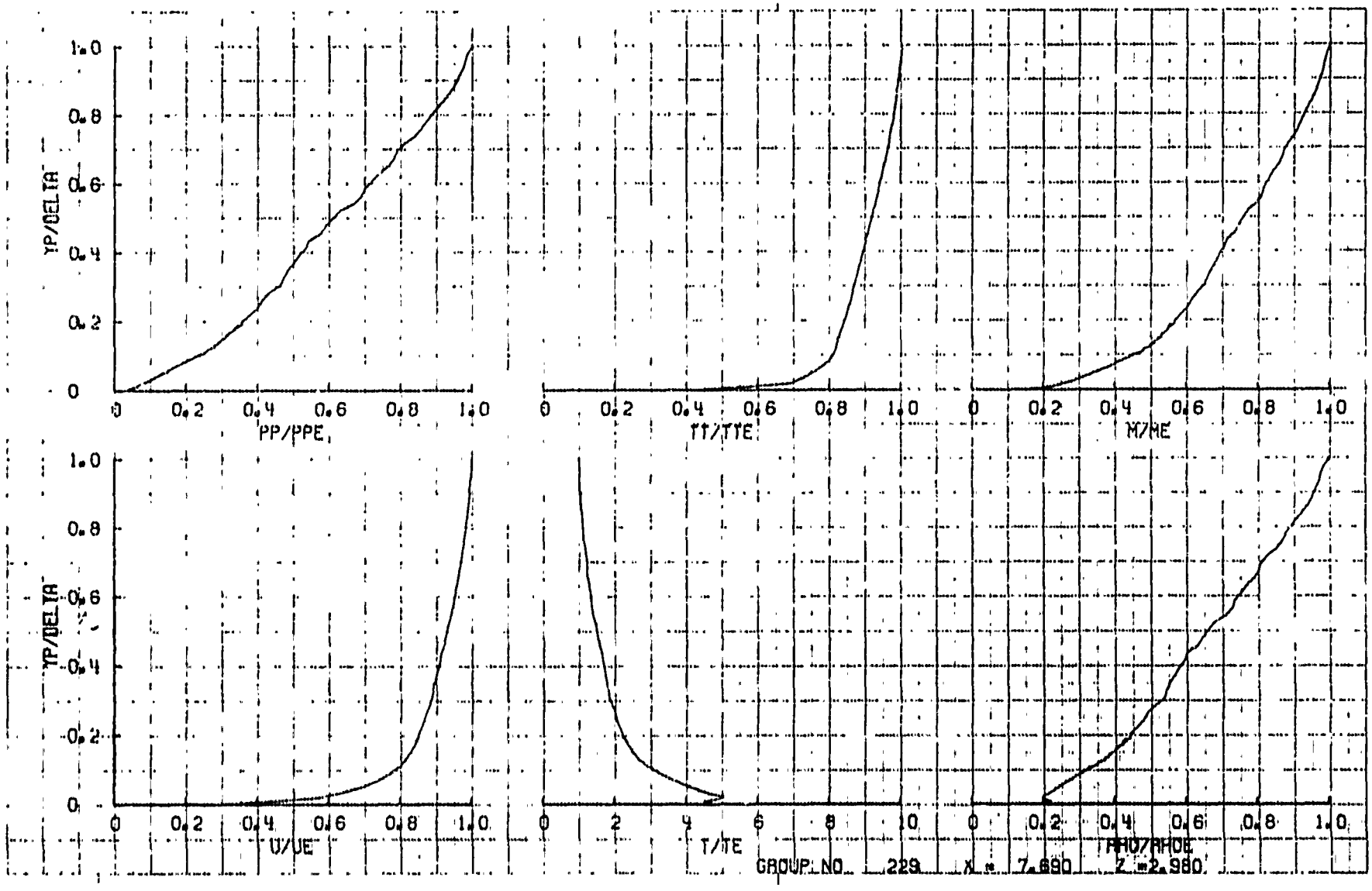
YP/DELTA
PP/PPE
TT/TTE
M/ME
U/UE
T/TE
RHO/RHOE
GROUP NO. 229 X = 7.690 Z = 2.980

FLOW CONDITIONS

Group	Number of Slots Upstream	Distance Downstream of Previous Slot	$B'_{o\ avg}$	$B'_{o\ slot}$	λ_{avg}	λ_{slot}	$\dot{m}_{slot}$ (lbm/sec)
321	2	1.76	0	0	0	0	0
319		0.68					
317		0.28					
315		0.19					
312		0.04					

BOUNDARY LAYER PROPERTIES

Group	Momentum Thickness (in)	Boundary Layer Thickness (in)	Edge Velocity (fps)	Edge Temperature (°R)	Edge Density (lbm/ft^3)	Edge Total Temperature (°R)	Edge Probe Pressure (lbf/in^2)
321	.220	5.972	3841	100.1	.00221	1328.6	6.527
319	.220	5.933	3835	100.9	.00220	1325.3	6.454
317	.220	5.965	3833	100.6	.00221	1323.8	6.478
315	.222	6.218	3835	98.4	.00227	1322.1	6.654
312	.222	6.085	3847	99.1	.00223	1330.5	6.607

Figure 4-38. Detailed Survey of Second Land on the 2.0/2.0 Model to Attempt to Trace Profile Development on a Fine Scale with no Blowing.

Figure 4-38. (Continued)

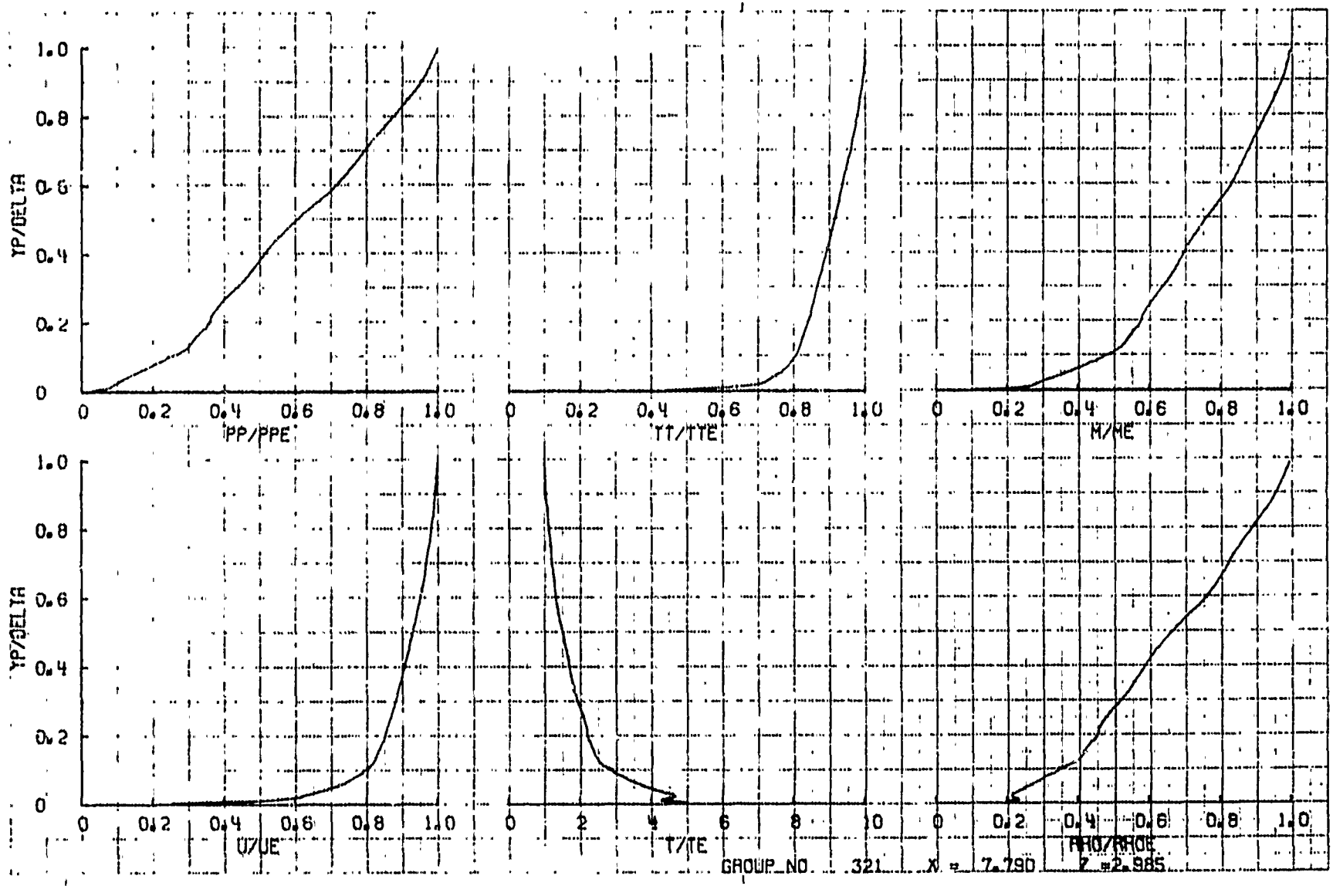
YP/DELTA
1.0
0.8
0.6
0.4
0.2
0
0 0.2 0.4 0.6 0.8 1.0
PP/PPE
TT/TTE
M/ME
U/UE
T/TE
RHO/RHOE
GROUP NO. 321 X = 7.790 Z = 2.985

FLOW CONDITIONS

Group	Number of Slots Upstream	Distance Downstream of Previous Slot		$B'_{o\ avg}$	$B'_{o\ slot}$	λ_{avg}	λ_{slot}	$\dot{m}_{slot}$ (lbm/sec)
			Z(in)					
440	2	0.18	-0.50	0	0	0	0	0
442	|	0.17	-0.20	|	|	|	|	|
444	|	0.16	-0.20	|	|	|	|	|
446	|	0.16	-0.50	|	|	|	|	|

BOUNDARY LAYER PROPERTIES

Group	Momentum Thickness (in)	Boundary Layer Thickness (in)	Edge Velocity (fps)	Edge Temperature (°R)	Edge Density (lbm/ft^3)	Edge Total Temperature (°R)	Edge Probe Pressure (lbf/in^2)
440	.218	5.735	3841	101.1	.00220	1329.1	6.473
442	.223	5.744	3831	99.8	.00222	1321.2	6.504
444	.231	5.825	3826	100.3	.00221	1318.9	6.470
446	.233	5.934	3823	99.1	.00223	1315.8	6.523

Figure 4-39a. Baseline Transverse Profiles Without Blowing for the 2.0/2.0 Configuration with the Filler Block Mounted.

Note that filler block is located at Z = -0.080 in the coordinate system.

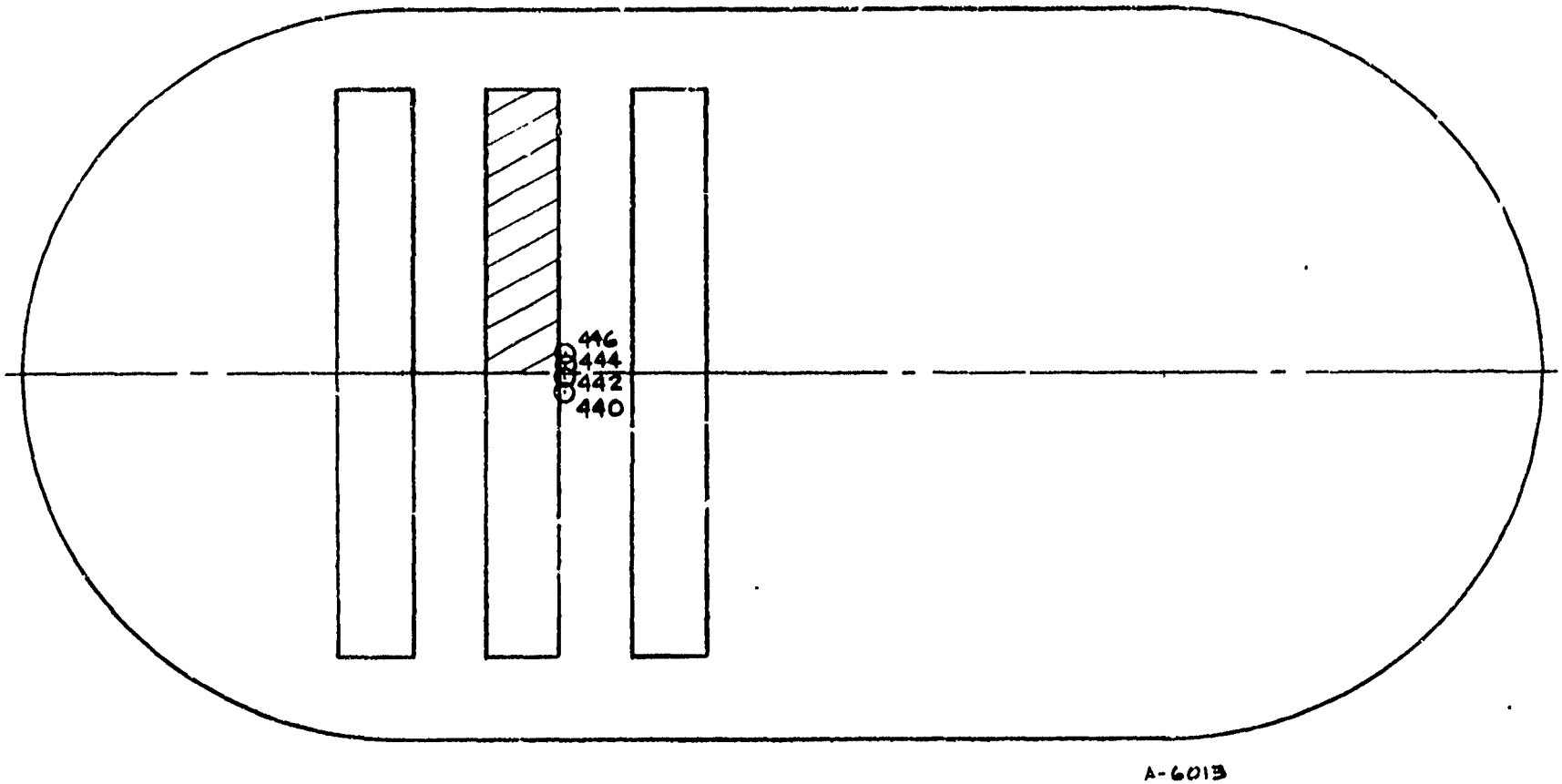

Figure 4-39a. (Continued)

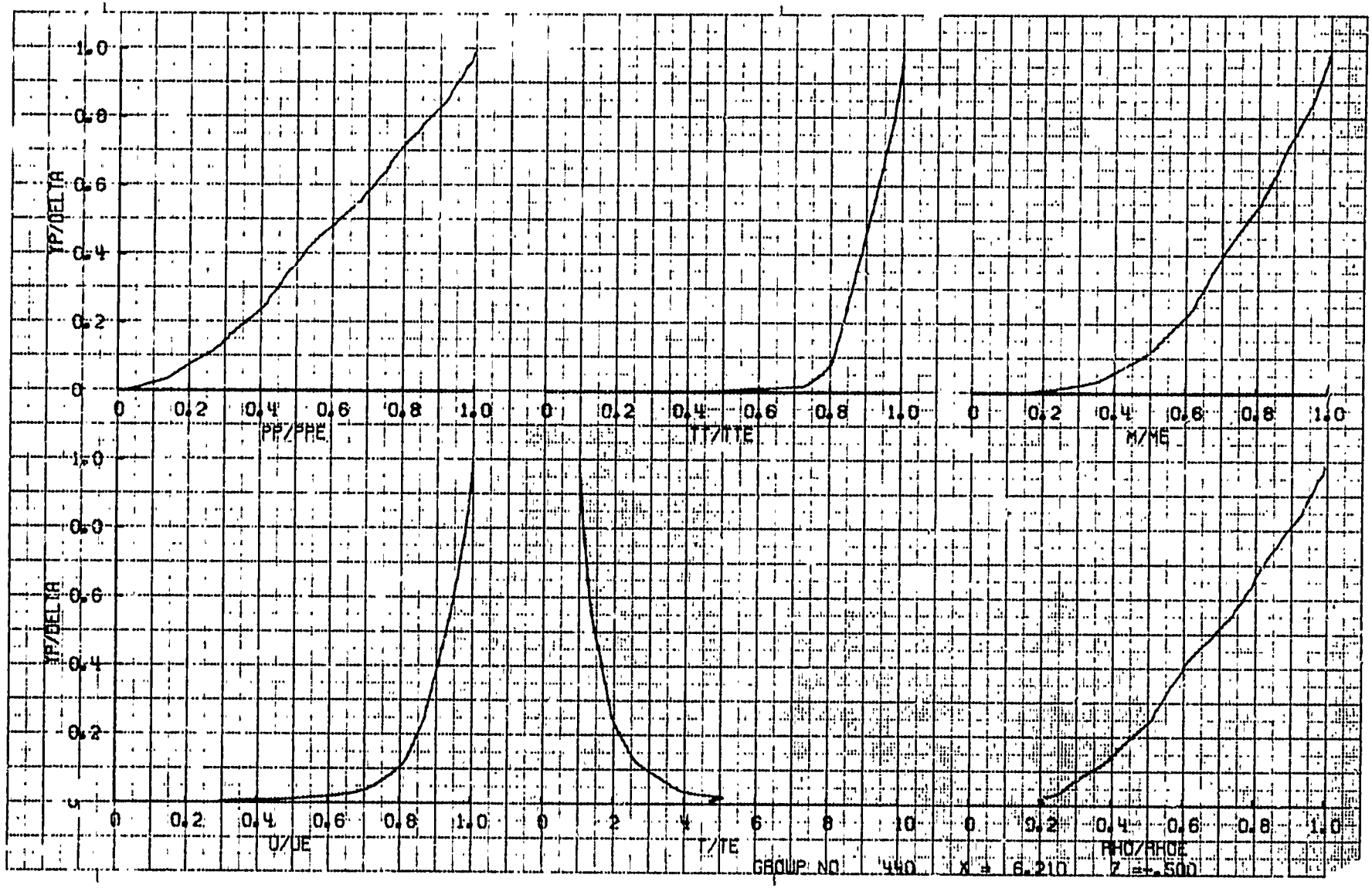
YP/DELTA
PP/PPE
TT/TTE
M/ME
U/UE
T/TE
RHO/RHOE
GROUP NO 440 X = 6.210 Z = -.500

FLOW CONDITIONS

Group	Number of Slots Upstream	Distance Downstream of Previous Slot	Z_{in}	$B'_{o\ avg}$	$B'_{o\ slot}$	λ_{avg}	λ_{slot}	$\dot{m}_{slot}$ (lbm/sec)
420	2	0.14	3.0	5.21	10.42	.00149	.00298	.0056
422		0.16	0.5					
424		0.17	0.2	5.304	10.61	.00152	.00304	.0057
430		0.12	-0.2	5.21	10.42	.00149	.00298	.0056
436		0.17	-0.5					
438		0.14	-3.0					

BOUNDARY LAYER PROPERTIES

Group	Momentum Thickness (in)	Boundary Layer Thickness (in)	Edge Velocity (fps)	Edge Temperature (°R)	Edge Density (lbm/ft^3)	Edge Total Temperature (°R)	Edge Probe Pressure (lbf/in^2)
420	.220	6.016	3836	99.5	.00223	1324.5	6.561
422	.239	5.907	3844	100.7	.00220	1330.4	6.502
424	.231	5.853	3837	100.9	.00220	1326.4	6.462
430	.224	5.845	3838	100.1	.00222	1326.2	6.524
436	.220	5.736	3841	101.0	.00220	1329.2	6.473
438	.221	5.707	3848	102.7	.00216	1335.6	6.405

Figure 4-39b. Transverse Survey Downstream of the Filler Block with Full Mass Injection. Note that the End of the Filler is Actually at Z = -0.080 in this Coordinate System.

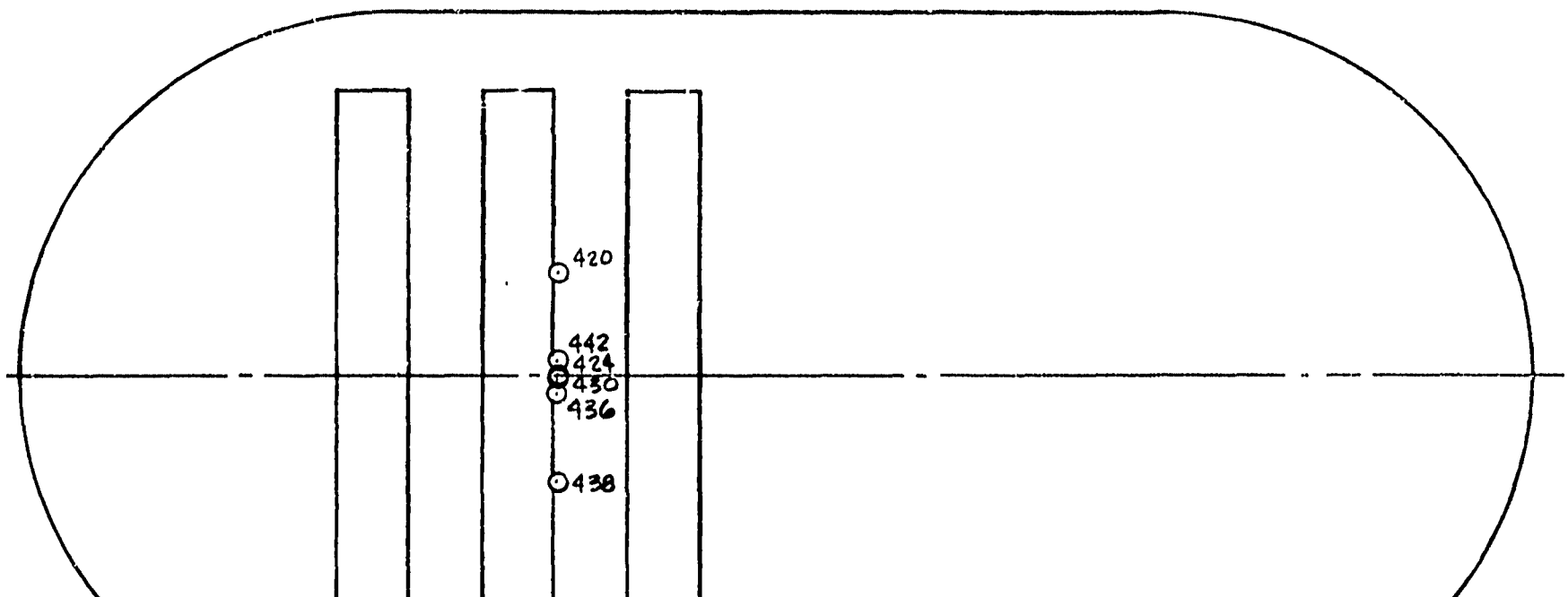

Figure 4-39b. (Continued)

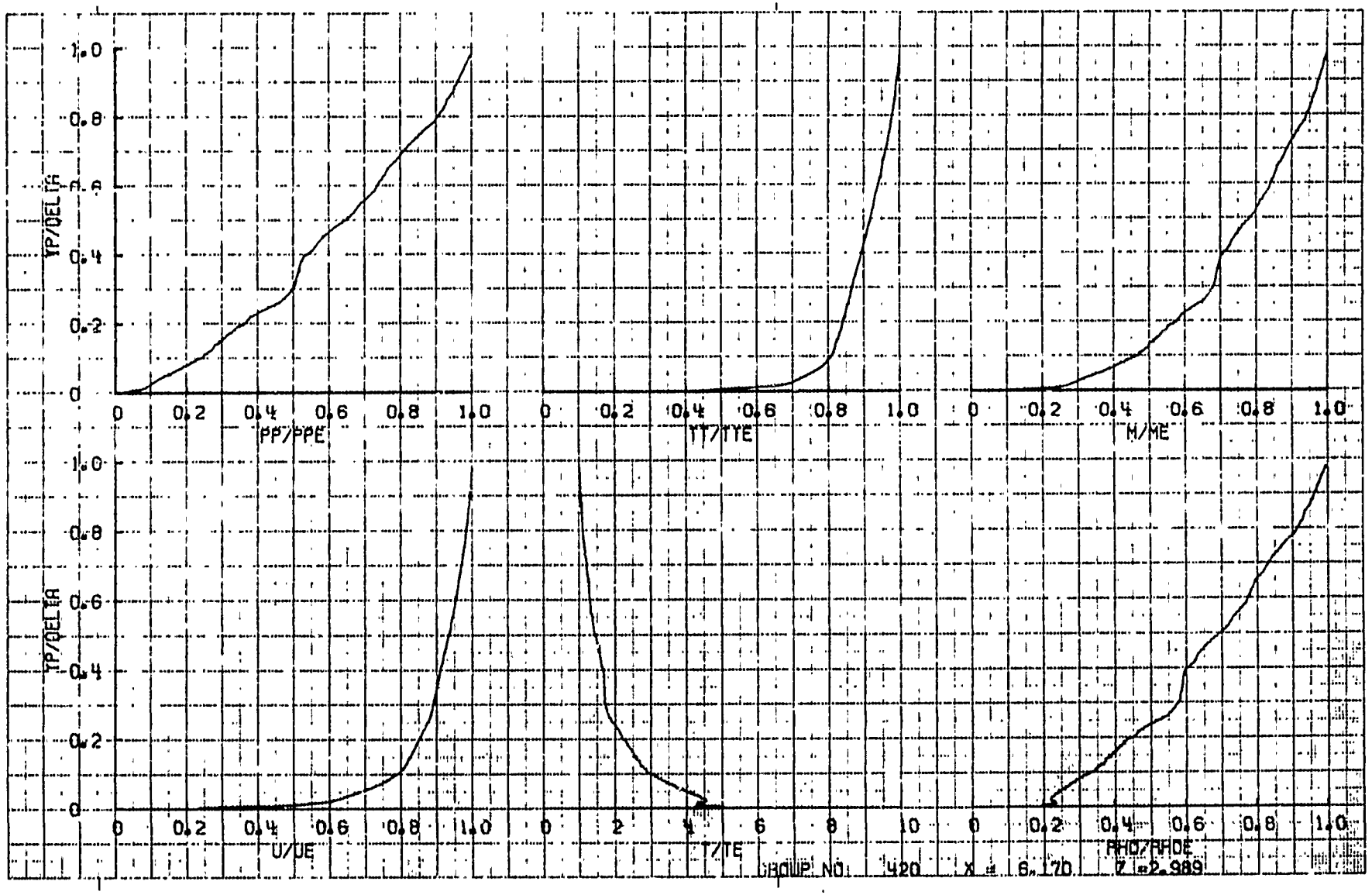
YP/DELTA
1.0
0.8
0.6
0.4
0.2
0
0 0.2 0.4 0.6 0.8 1.0
PP/PPE
0 0.2 0.4 0.6 0.8 1.0
TT/TTE
0 0.2 0.4 0.6 0.8 1.0
M/ME
YP/DELTA
1.0
0.8
0.6
0.4
0.2
0
0 0.2 0.4 0.6 0.8 1.0
U/UE
0 2 4 6 8 10
T/TE
0 0.2 0.4 0.6 0.8 1.0
RHO/RHOE
GROUP NO. 420 X = 6.170
Z = 2.989

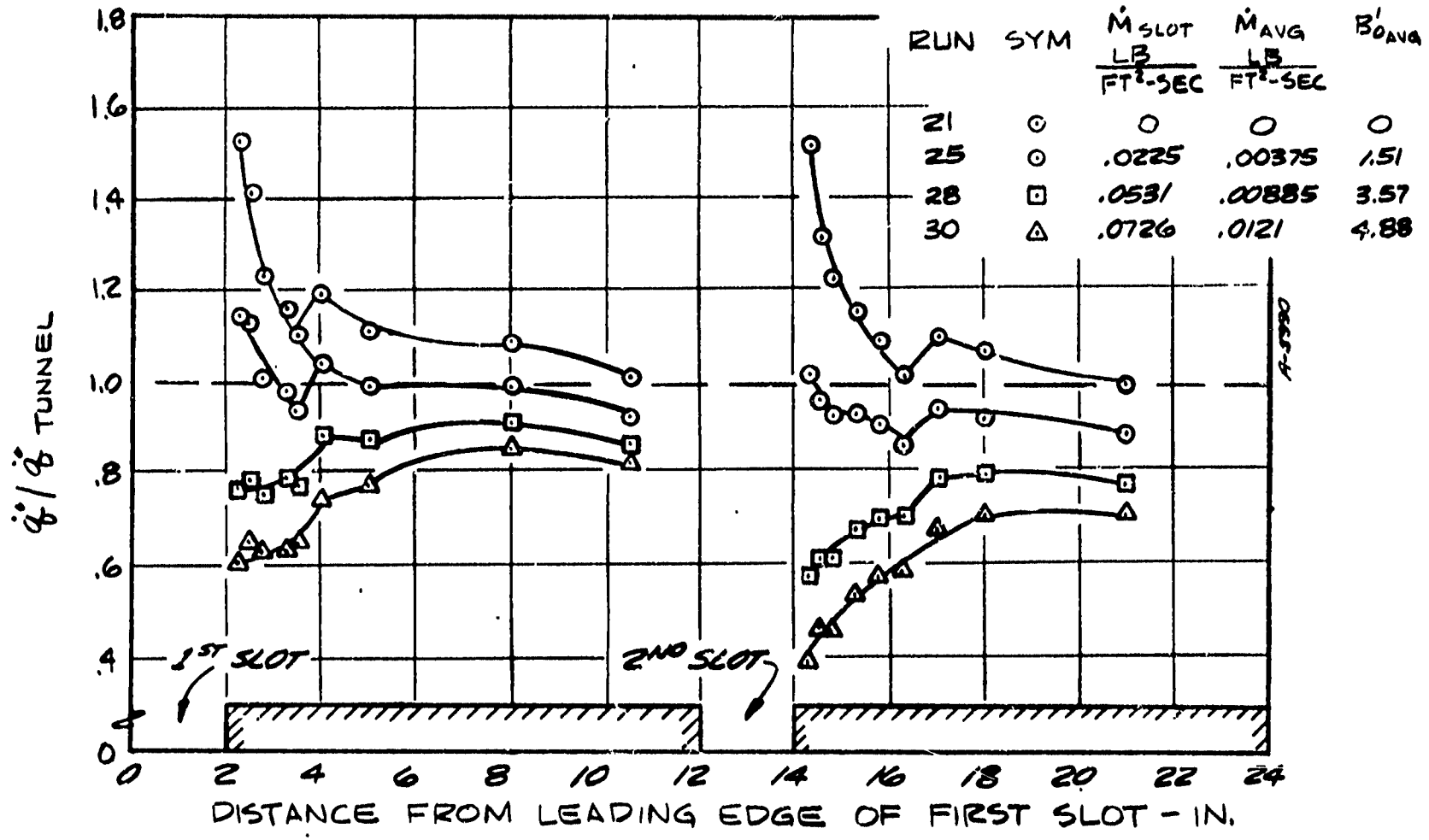

Figure 4-40. Heat Transfer Distribution For 2.0/10.0 Case

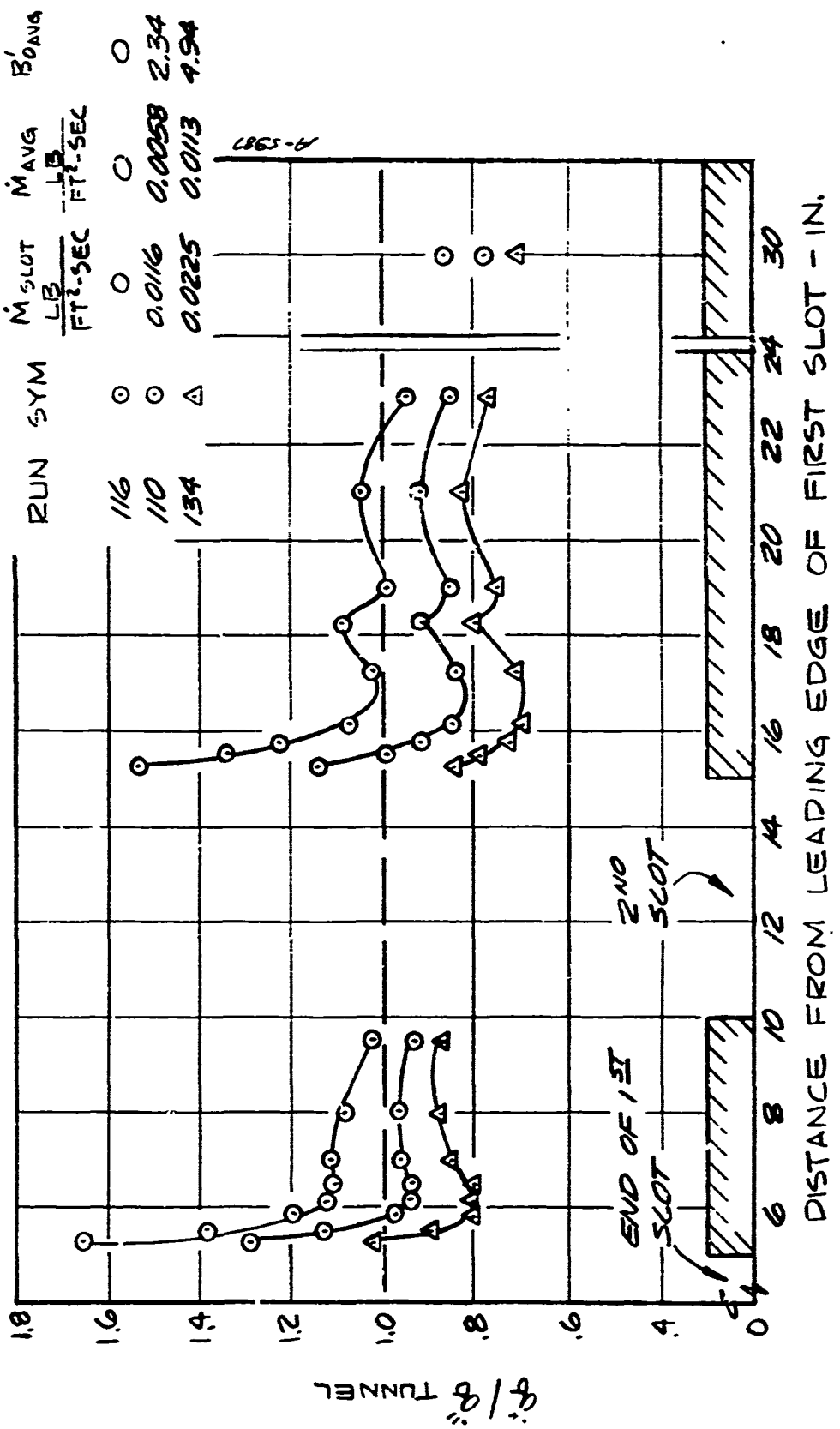

Figure 4-41. Heat Transfer Distribution For 5.0/5.0 Case

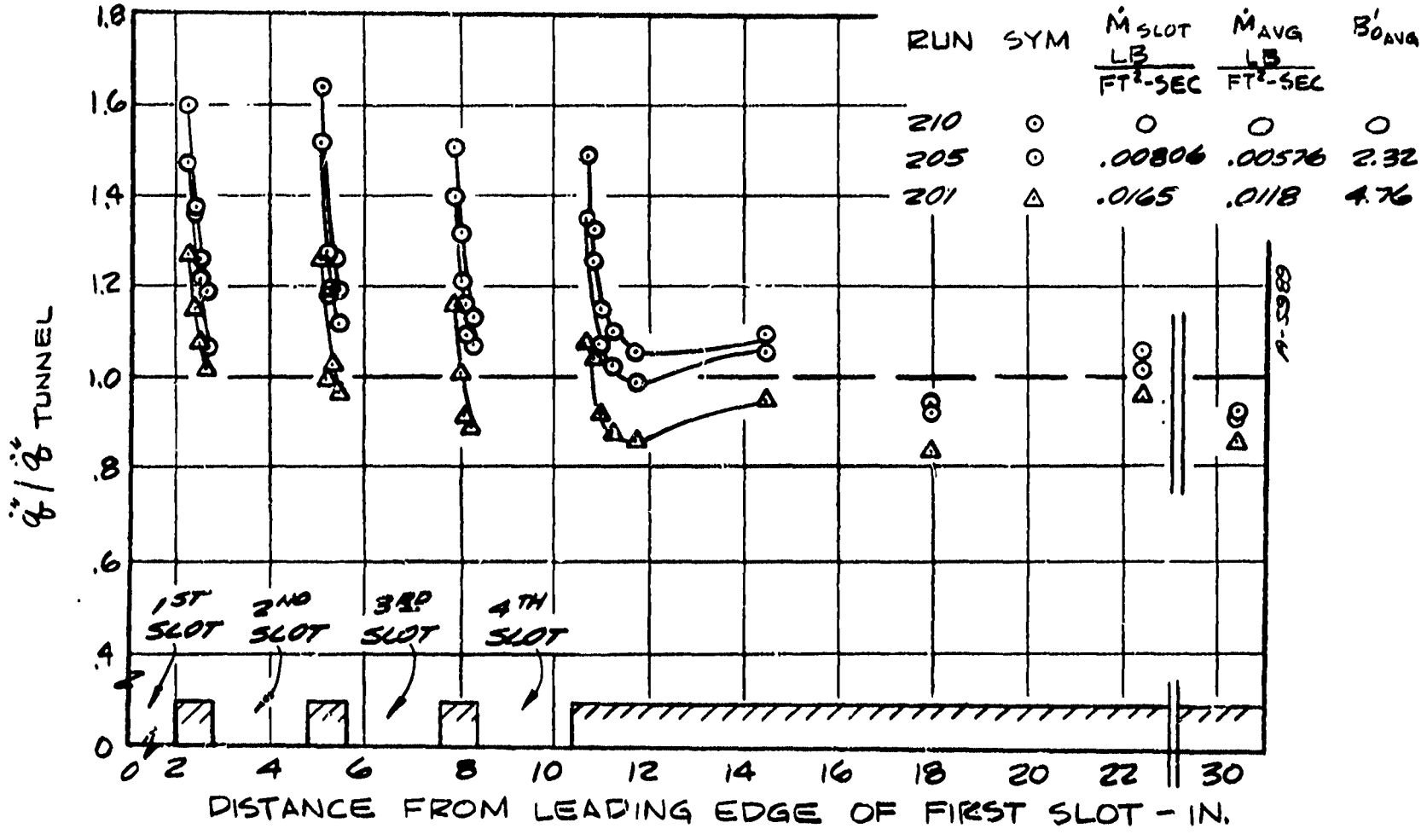

Figure 4-42. Heat Transfer Distribution For 2.0/0.8 Case

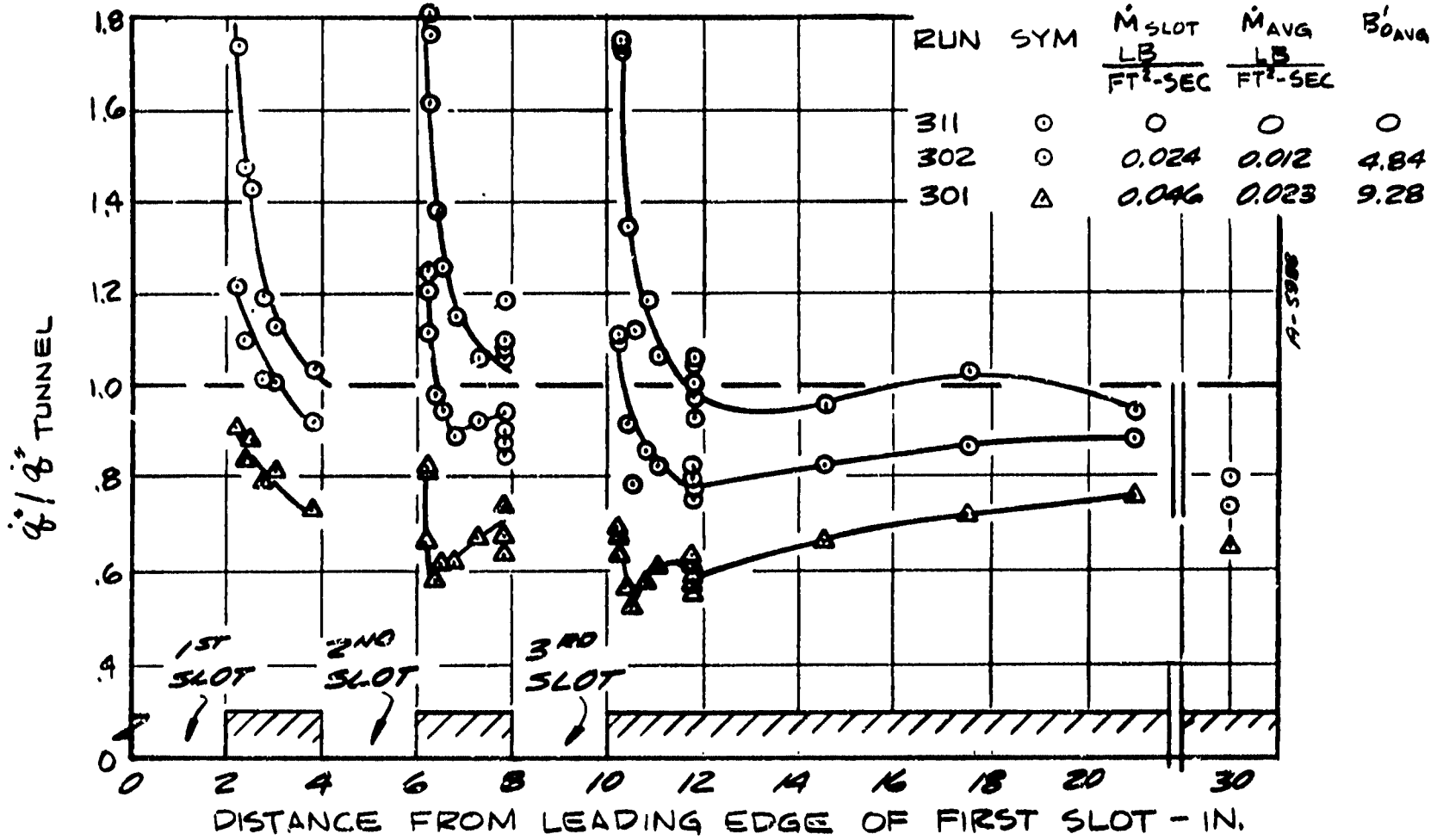

Figure 4-43. Heat Transfer Distribution For 2.0/2.0 Case

SECTION 5

COMBINED COOLING EXPERIMENT

The primary objectives of the Combined Cooling experiment were:

- To perform a fundamental study of discrete injection of either a liquid, two-phase, or gaseous coolant into a turbulent boundary layer.
- To validate and extend the correlations derived from the internal and external cooling experiments.
- To determine downstream cooling effectiveness.

A secondary objective was to compare the performance of discrete and porous injection under identical test conditions.

Since the primary objective of these tests was to obtain data at conditions for which internal and external cooling mechanisms were operative in a coupled mode, a hot test facility was needed. The chosen configuration was a discrete injection model mounted in the floor of the NASA Ames 1 in. x 5 in. turbulent duct facility. This facility was chosen because it can generate a fully turbulent boundary-layer in the test section. Four discrete injection (DI) modules, embodying different slot to land ratios, were tested. The complete model assembly was comprised of a copper water-cooled model holder and a model comprised of the discrete injection module and an instrumented downstream module. The discrete injection module was constructed of quartz in order to simulate flight surface temperatures and in-depth temperature gradients. The entire model assembly was mounted flush with the duct wall. The coolant (water) flow rate was varied over an order-of-magnitude range, from overcooling to undercooling.

Twenty-five successful test runs were performed between May 17 and June 29, 1973. In addition to the DI modules, a porous injection module was tested in order to obtain a comparison of the cooling effectiveness of DI and porous injection under identical test conditions. Extensive instrumentation was used throughout the program. At the injection module, surface and in-depth temperatures were measured with thermocouples, pyrometery, and infrared photography. In addition, the coolant flow was carefully metered and color photography was

used to determine the state of the coolant leaving the slots. At the downstream module, heat flux distributions were measured. The data from the Combined Cooling tests confirm the findings of the External Cooling tests and, for the first time, provide important information concerning the physics of active cooling by discrete injection of a coolant which undergoes a phase change.

The remainder of this section presents brief discussions of the following facets of the combined cooling experiment:

- NASA Ames facility (Section 5.1)
- Models (Section 5.2)
- Instrumentation (Section 5.3)
- Test Matrix (Section 5.4)
- Results (Section 5.5)
- Conclusions (Section 5.6)

Each of the above topics is discussed in much greater detail in either Reference 9 or 10. Due to space limitations, only brief summaries and sample results are presented here.

5.1 FACILITY

5.1.1 Scaling

It was impractical, from both technical and economical points of view, to design a test which duplicated precisely the anticipated flight environments. Therefore, scaling of the important physical phenomena associated with discrete injection was an important phase of the test design. Scaling considerations impacted both the facility selection and the model design (Section 5.2).

Scaling of liquid layer, internal cooling, and external cooling phenomena were considered. The scaling of liquid layer phenomena has been considered in detail in a previous document (Reference 4): the results are summarized here. In particular, the following liquid layer parameters were considered:

a) We_ℓ (film Webers number)

b) We_ℓ/Re_ℓ (film Reynolds number)

c) $[(\rho_e U_e^2)/(\rho_\ell U_\ell^2)]\ We$

d) ℓ/S (film thickness/slot width).

The first three parameters are associated with film formation, film stability, and film entrainment respectively. The last parameter is used to compute the others and is based on a flow margin of unity. (The definition of unity flow margin used in this study is presented in Sections 5.5.3 and 5.5.4.)

In Reference 4 it was concluded that simulation of liquid layer phenomena would be exceedingly difficult, because the present theories are inadequate for treating the occurrence of such phenomena under expected flight conditions. For instance, it is unlikely that a well-defined liquid film would even exist, because the scale of flight nosetip surface roughness is greater than the extremely thin film thicknesses predicted by available theories. In view of these considerations, scaling of liquid layer phenomena was considered to be of only secondary importance.

The problem of simulating heat transfer for internal cooling is illustrated in Figure 5-1. It can be seen that exit coolant temperatures can be increased to a point only limited by the free stream enthalpy potential by decreasing the coolant mass flux $\dot{m}''_s$, the driving potential for internal heat transfer being the temperature drop between fin (land) and coolant (slot). For similar temperature gradients the depth for internal vaporization scales inversely with heat transfer and directly with conductivity. Thus, if a facility is used which provides lower heat fluxes than expected flight values, then the thermal conductivity of the test model must be correspondingly lower than that of the flight hardware.

A code coupling solutions of the fin heat conduction equation to the coolant heat convective equation was utilized to illustrate effects of fin conductivity. Use of the NASA Ames facility, which provides heat fluxes nominally a factor of twenty lower than those calculated for typical flight conditions, was anticipated in making these calculations. Conductivities of 3×10^{-4} Btu/ft sec°R (representative of glass-like materials) and 6×10^{-3} Btu/ft sec°R (representative of stainless steel) were utilized as representative of model and flight hardware materials respectively. Corresponding mass flow rate ratios of 20:1 (flight/test) were used in the computations. Figure 5-2 shows surface temperatures for a model flow rate of 0.05 lbm/ft^{2}sec the corresponding flight value being a factor of 20 larger. It can be seen that for heat transfer rates differing by a factor of 20 reasonably good simulation of temperatures can be attained. For example, for heat transfer rates of 70 and 1400 Btu/ft^{2}sec the surface temperatures are 1200°R and 1500°R for flight and test conditions, respectively. Figure 5-3 illustrates the in-depth penetration (vaporization depth) for the two cases. The simulation, although not exact, is nevertheless good.

The scaling of external cooling was also considered and, in particular, for the anticipated relatively low facility heat transfer rates it could be shown that the blocked values of heat transfer would not necessitate vanishingly small values of $\dot{m}''$ in order to attain high surface temperatures. In order to

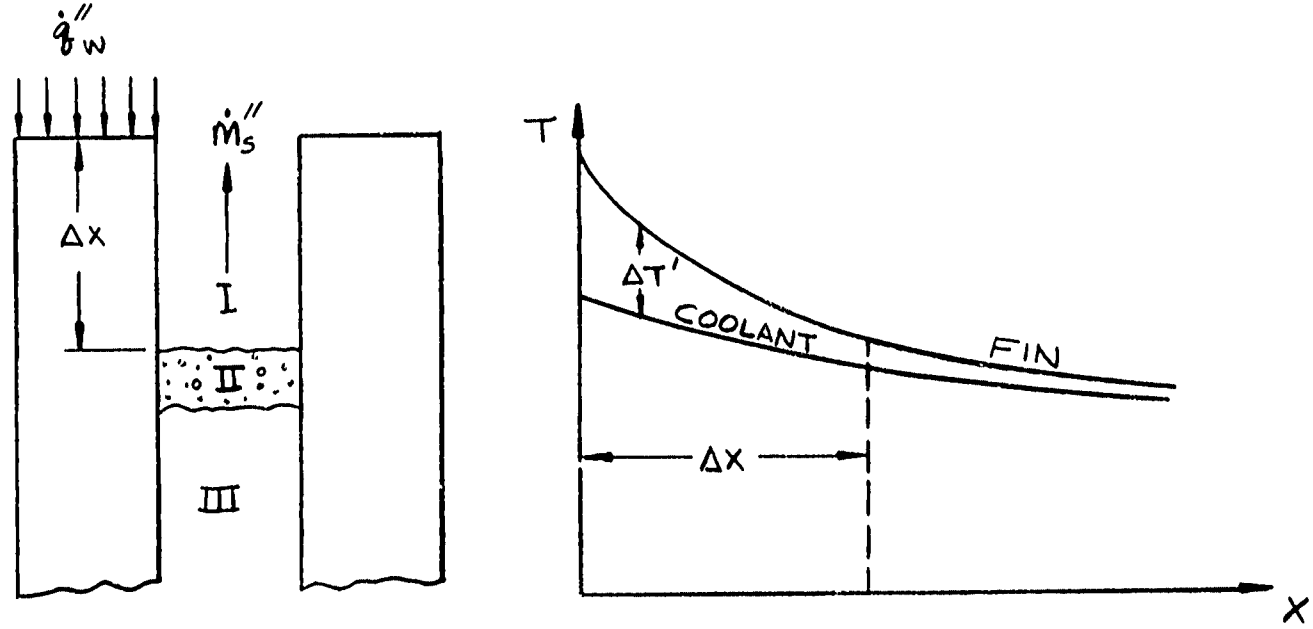

$$\left[\tfrac{1}{2}(T_c - 672) + \lambda_{VAP} + (672 - 532)\right] = \dot{q}''_w / \dot{m}''$$

$$\frac{(\Delta X)_{MODEL}}{(\Delta X)_{FLIGHT}} = \frac{(K_{MODEL})}{(K_{FLIGHT})}\frac{(\rho_{FLIGHT})}{(\rho_{MODEL})}$$

T_c = COOLANT TEMPERATURE AT SLOT EXIT

$\Delta T'$ = FIN TEMPERATURE - COOLANT TEMPERATURE

λ_{VAP} = COOLANT HEAT OF VAPORIZATION

$\dot{q}''_w$ = NET HEAT TRANSFER TO FIN

$\dot{m}''_s$ = COOLANT MASS FLUX

K = THERMAL CONDUCTIVITY

Figure 5-1. Heat Transfer Simulation For Internal Cooling

A-6106

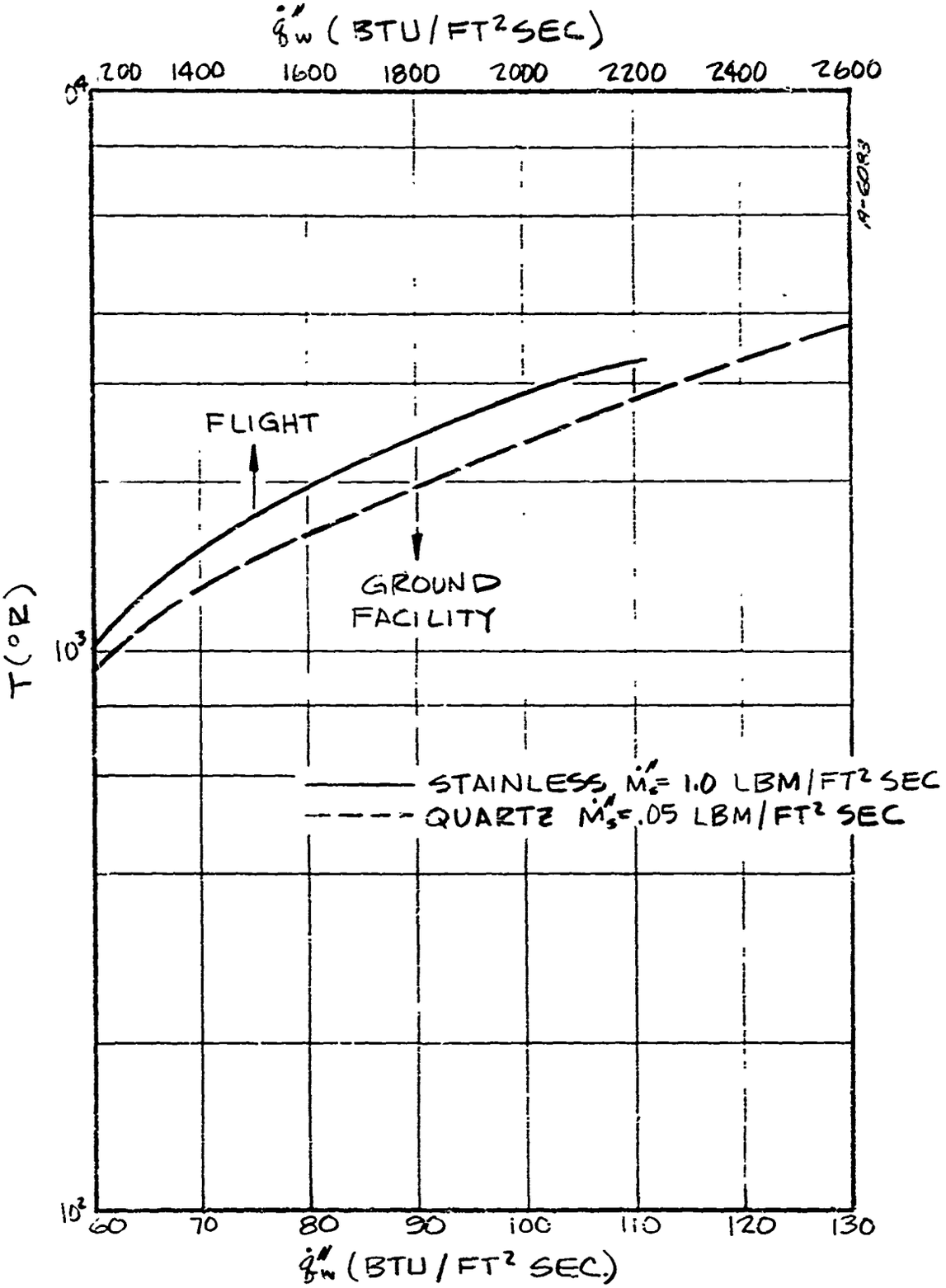

Figure 5-2. Scaling of Land Surface Temperature

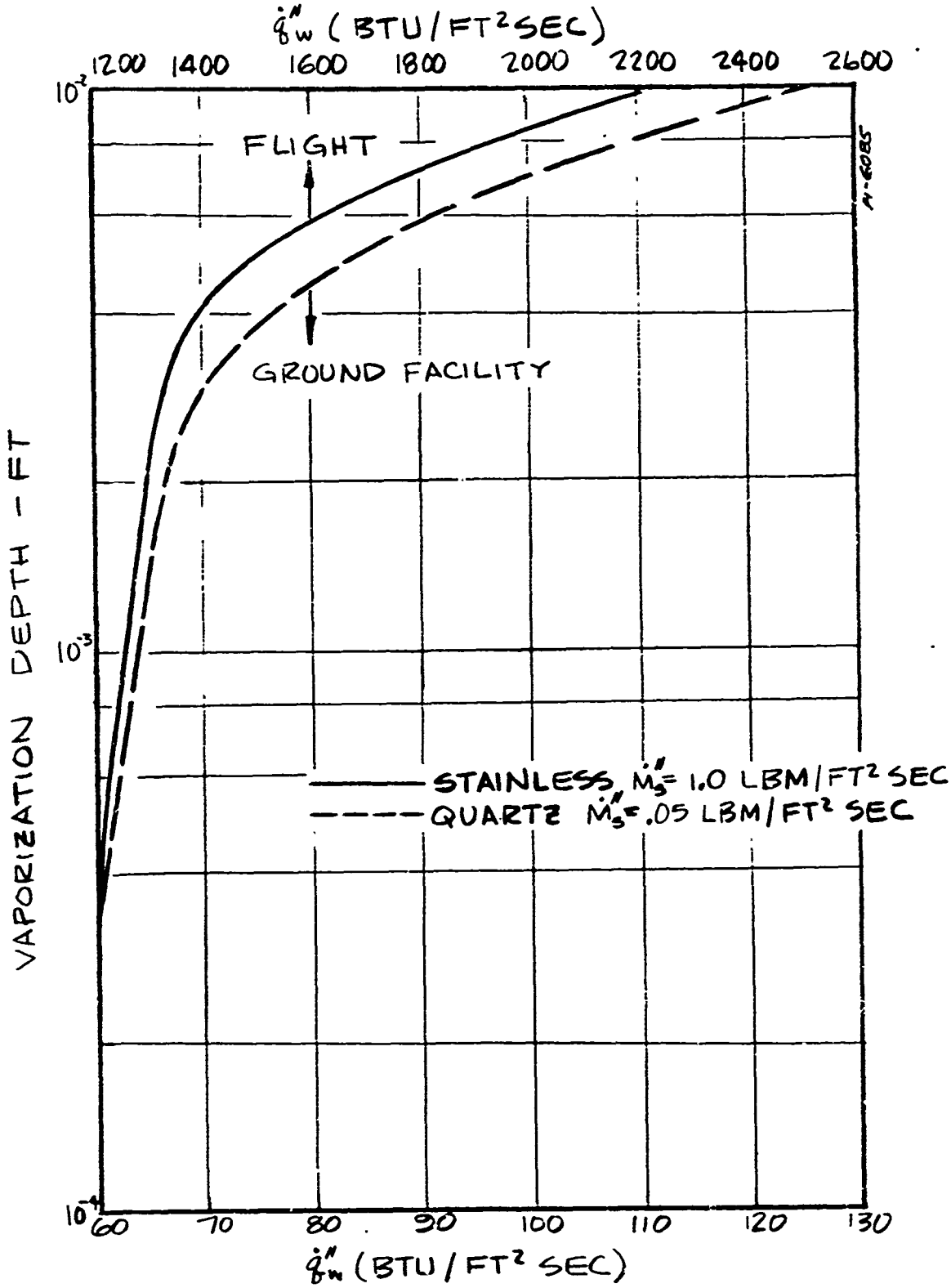

Figure 5-3. Scaling of Vaporization Depth

treat external cooling phenomena, values of unblocked cold wall heat transfer rates $\dot{q}''_o$ and tunnel test stream enthalpies were used together with the blocking correlation of Baronti, Fox, and Soll (Reference 35), based on the blowing parameter F/St_o given by

$$F/St_o = \dot{m}''\Delta H/\dot{q}''_o$$

It is pointed out that for S/L = 1 the value of $\dot{m}''$ appearing in the above relation was taken as one half the actual value of $\dot{m}''_s$ in the slots, since only one half the surface area is protected. The correlation for H_2O is adequately represented by

$$\dot{q}''/\dot{q}''_o = (1 + F/4St_o)^{-3}$$

For mass fluxes ranging from 0.025 to 0.05 lbm/ft^{2}sec and typical facility values of $\dot{q}''_o$ and ΔH, a range for F/St_o of from 0.25 to 0.75 is attainable, yielding a range for $\dot{q}''/\dot{q}''_o$ of from 0.83 to 0.58. For $\dot{q}''_o$ = 100 Btu/ft^{2}sec this range corresponds to a range of blocked heat fluxes from 83 Btu/ft^{2}sec at $\dot{m}''$ = 0.025 lbm/ft^{2}sec to 58 Btu/ft^{2}sec at $\dot{m}''$ = 0.05 lbm/ft^{2}sec.

Scaling of external cooling phenomena also required consideration of the slot size relative to some parameter associated with the gas boundary layer thickness, since heating augmentation due to roughness is a function of these two characteristic lengths. Momentum thickness was chosen as the pertinent boundary layer length parameter, although the laminar sublayer thickness was also considered and resulted in conclusions which differed little from those based upon momentum thickness. Under flight conditions, the ratio of boundary layer momentum thickness to slot size is $0.1 \leq \theta/S \leq 1.0$ around the nosetip when S = 0.005 in. Thus, in order to properly scale the effective surface roughness existing in flight, the slots in the ground test module were selected based upon consideration of the momentum thickness of the test stream boundary layer and the above range of θ/S (see Section 2.3.2).

5.1.2 Facility Selection

As discussed in the previous section, scaling of liquid layer, internal cooling, and external cooling phenomena were considered. It was concluded that, in order to satisfy the objectives of the program, simultaneous scaling of internal and external cooling phenomena in the Combined Cooling experiment was essential, while scaling of liquid layer phenomena was of secondary importance. Hence, the selected test facility had the following features:

- The cold wall, no-injection heat flux was large enough to cause
  - temperatures of the land material at the injection section to reach the melting point of flight hardware
  - subsurface vaporization of the coolant in the injection passages for flow rates approaching zero
- The test stream was supersonic and provided a uniform, fully-developed turbulent boundary layer over the model surface.

Since the flight environments of interest involve stagnation heat fluxes on the order of 10,000 Btu/ft^{2}sec and stagnation pressures on the order of 100 atmospheres, the ideal test facility for the study of the cooling effectiveness of discrete injection would provide a test stream with heat fluxes and pressures at these levels. At the present time, at least two facilities are capable of near-duplication of these conditions: The AFRPL ABRES rocket engine test facility and the AFFDL 50 MW arc facility. However, both of these facilities have several disadvantages, with a major disadvantage being, in both cases, operating expense. In addition, the AFFDL arc facility has a rather small test stream (exit diameter of 1.1 inches), while the ABRES test facility is inherently limited to short duration, long turnaround test runs (15 second firing, maximum of two tests per day). In a facility trade-off study, these disadvantages were found to far outweigh the feature of near-exact duplication of flight conditions. Consequently, the aforementioned scaling techniques were used to select a more economical test facility having the features of large-scale test stream and adequate test duration.

As noted above, a primary requirement for the Combined Cooling experiment was that the boundary layer over the test surface be turbulent. In general, such a turbulent boundary layer is difficult to attain in arc facilities, but is more readily attained in rocket test facilities where high stagnation pressures are easier to achieve and appreciable free-stream turbulent exists. Both the Aerotherm 1.5 MW arc facility and the Avco 10 MW arc facility were considered for the subject test program and ultimately rejected because the existence of a turbulent boundary layer at the test section could not be definitely substantiated. Both sting-mounted and wall-mounted models were considered in the Aerotherm facility, while the configuration considered for the Avco facility was a wedge model attached to the lip of the exhaust nozzle. In general, wall-mounted models are most desirable for the present experimental program because a relatively long running length exists upstream of the test section and thereby increases the changes of obtaining a turbulent boundary layer.

As shown in the previous section, a low-heat-flux facility can be used to achieve surface melt temperatures and subsurface vaporization if a model

surface material with low thermal conductivity is used. The thermal conductivity of the flight hardware (stainless steel) is about 20 Btu/ft hr°R. The lowest thermal conductivity available for model hardware appears to be about 1.0 Btu/ft hr°R, corresponding to glass-like materials. Materials with a thermal conductivity lower than this value, e.g., teflon, are generally structurally unsuitable for construction of the desired test models.

Scaling considerations indicate that use of a model land material with a thermal conductivity lower than flight by a factor of twenty permits the use of a test stream with a cold-wall, no-injection heat flux in the vicinity of 100 Btu/ft^{2}sec. The arc-heated duct facility available at NASA Ames provides a supersonic test stream with heat flux at this level. In addition, it is the only arc-heated duct available which has been demonstrated to have a turbulent boundary layer over the test section. Because of these highly desirable features, the NASA Ames facility was selected for the Combined Cooling test program.

Figure 5-4 presents a schematic of the duct facility at Ames, and the performance of the facility is described in detail in Reference 36. The two-dimensional converging-diverging nozzle described in Reference 36 has recently been replaced by a new nozzle with a more gradual expansion contour, thus providing a more uniform and shock-free test stream at the test section. With this nozzle, the Mach number at the test section is 3.5. The duct is heated by a 5 MW Linde arc heater and is equipped with Gardon gages and pressure taps in the wall opposite the test section which are used for calibration purposes. The Combined Cooling model described in Section 5.2 below is inserted into the 4 in. x 6 in. test area designated in Figure 5-4.

Considerable effort has been devoted to demonstrating the existence of a turbulent wall boundary layer in the NASA Ames duct, since the facility was originally designed for testing space shuttle thermal protection materials in the turbulent heating regime. Experimentally-measured Stanton numbers have been compared with those predicted by both laminar and turbulent theories and have been found to clearly agree best with the latter theory. In addition, cross-hatch ablation patterns have been observed on uncooled teflon models installed flush with the duct wall at the test section. Such cross-batch recession patterns are indicative of supersonic turbulent boundary layer flow.

5.1.3 Facility Specifications

5.1.3.1 Arc Heater Specifications

A Linde N-4000 high-pressure arc heater is used to provide a high-temperature air stream for the rectangular duct. For this test program, power input ranged from 2.92 to 3.65 MW, with arc current ranging from 600 to 700 amps

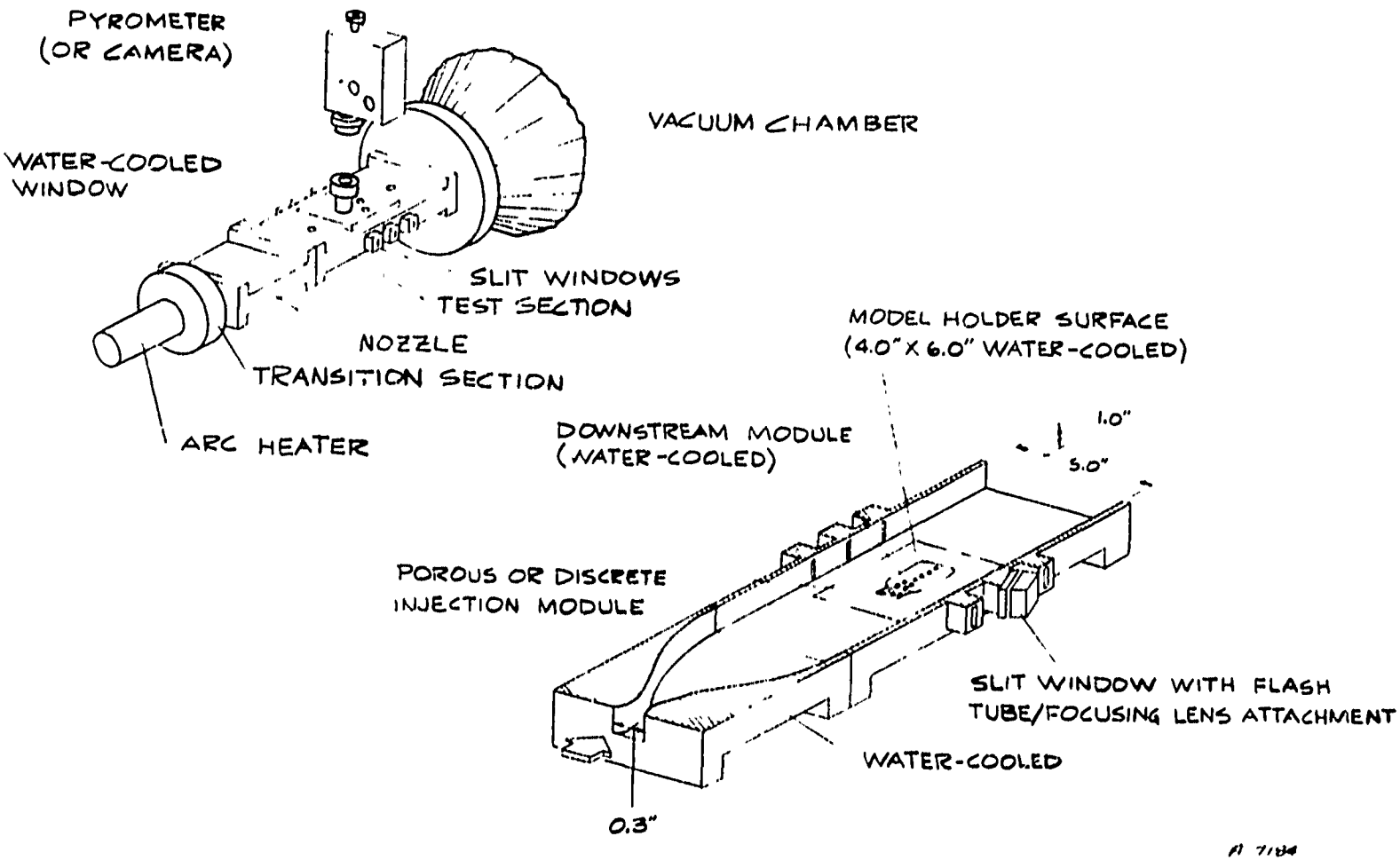

Figure 5-4. Schematic of the Arc-Heated Turbulent Duct Facility at NASA Ames, with Aerotherm Model and Instrumentation in Position

and arc voltage ranging from 4300 to 5900 volts. The total mass flowrate ranged from 0.755 to 1.23 lbm/sec, resulting in a test gas mixed-mean total enthalpy ranging from 1100 to 2150 Btu/lbm.

5.1.3.2 Nozzle and Test Section Specifications

The interior configuration of the test section was rectangular with a 1 in. x 5 in. cross-section. The test model was inserted into the floor of the duct, and seven Gardon gages and eight pressure taps were located in the ceiling of the duct, as shown in Figure 5-4. The third Gardon gage downstream was removed and replaced with a water-cooled window assembly for overhead pyrometry or photography. Three slit windows are mounted on each side of the duct at the test section for test stream and model observation. One of the center windows was replaced with a special window designed and fabricated at Aerotherm for flash illumination during photography of the injection module surface.

The two-dimensional converging-diverging nozzle was 16.25 in. long with a throat cross-section area of 1.0 in. x 0.334 in., which resulted in an exit/throat area ratio of 15.0 and a nominal exit Mach number of slightly over 3.5.

5.1.3.3 Data Acquisition System Specifications

The NASA Ames facility provided a Beckman ANSCAN Digital Recording System and a CRC strip chart recorder for recording all instrumentation output. The only data channels recorded on the strip chart recorder were those corresponding to the duct wall static pressures. All other data channels were recorded on the ANSCAN.

The ANSCAN can accommodate up to 100 channels of information and also provides digital output of any selected channel. Twenty-three channels were used for the Combined Cooling test program. For each injection flowrate, data were recorded for a 10-second interval at a sampling rate of three per second. The magnetic tape record provided by the ANSCAN was reduced via a computer code provided by the Ames facility.

5.2 MODELS

5.2.1 Design Guidelines

The program objectives stated in the beginning of this section dictate that the Combined Cooling test section be comprised of separate injection and downstream modules. Figure 5-5 presents a sketch of the Combined Cooling model which was inserted into the Ames rectangular duct. A copper, water-cooled

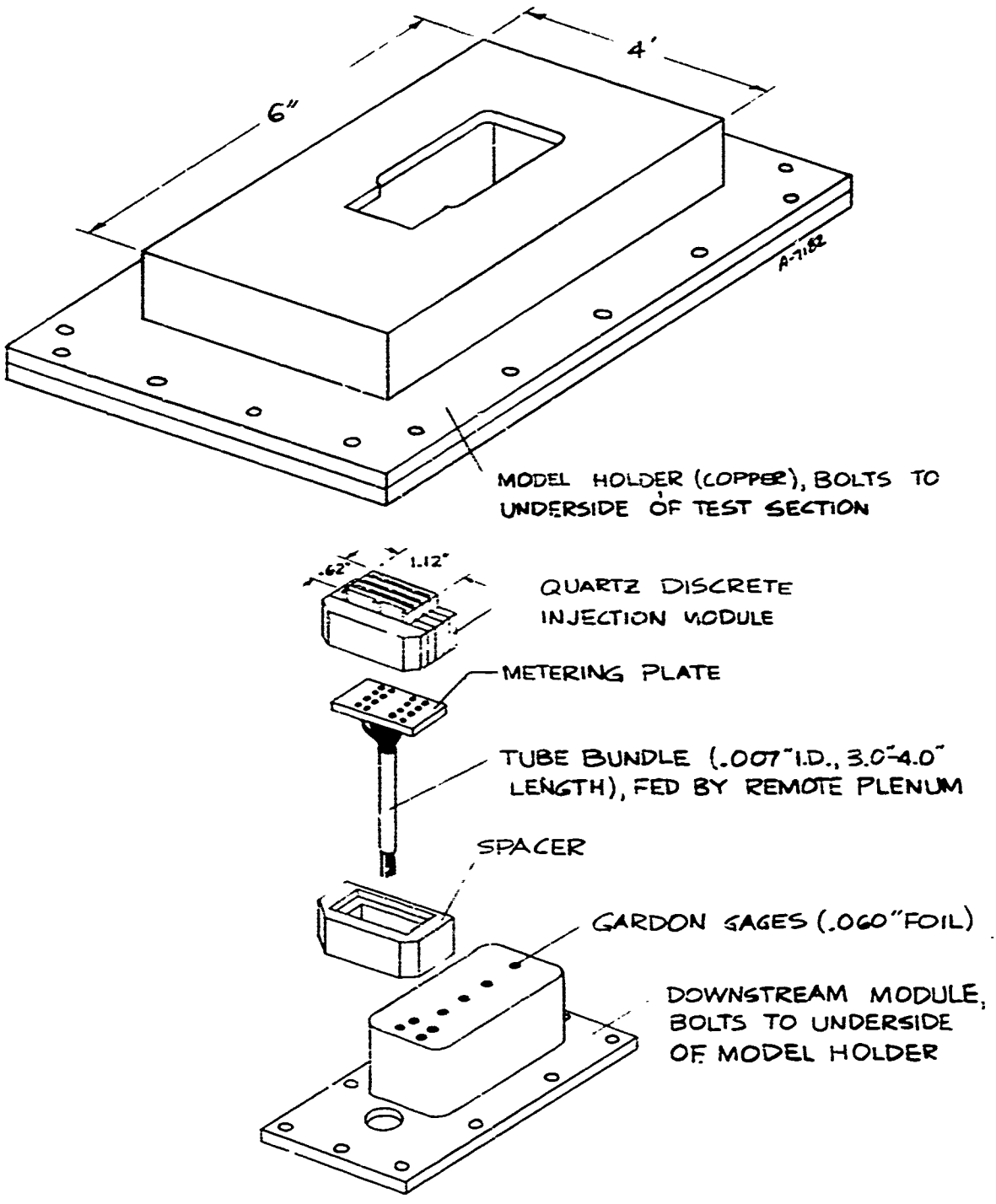

Figure 5-5. Schematic of Combined Cooling Model Assembly

model holder with 4 in. x 6 in. test surface interfaced with the opening in the Ames rectangular duct. The Combined Cooling model within the model holder was comprised of the discrete (or porous) injection and downstream modules. As outlined in Section 5.3, the injection module was instrumented to observe phenomena in the immediate vicinity of injection, and the downstream module was instrumented to observe phenomena downstream of the injection area.

The slot/land geometry and slot arrangements selected for the DI module were based upon the existing Aerotip configuration illustrated in the photographs of Figure 5-6. These photographs reveal that the slots are staggered from row to row and that the slot-width-to-slot thickness ratio is from five to ten. Table 5-1 summarizes the five slot/land combinations which were considered in the subject test program. In all cases the slot depths were sufficient to obtain fully-developed flow well before the coolant reached the slot exit.

The smallest slot size in the test matrix, S = 0.010 in., approximately duplicated the slot size in the actual flight hardware. This value of S was included in order to study boiling and heat conduction phenomena in small slots and lands. The largest slot size, S = 0.189 in., was chosen to scale boundary layer momentum thickness to slot dimensions (see Section 5.1.1). Flight values of the ratio θ/S, where θ is the boundary layer momentum thickness, vary from 0.1 to 1.0 when S = 0.005 in. In the Ames duct, θ is roughly 0.10 in., so that the facility θ/S was around 0.53 for S = 0.189 in.

The smallest land width was 0.020 in., which represents a practical minimum for quartz fabrication. A quartz land of smaller width is susceptible to excessive chipping and cracking during the grinding process. The three intermedicate values of S and L were chosen to study the effects of varying S/L for fixed S or fixed L. The study of external heating phenomena documented in Reference 1 indicated that the S/L range of interest is $0.25 \leq S/L \leq 2.50$, so this range was used as a guideline in selecting the three intermediate S and L values. For these S and L values there are only two slots per row, which reflects the desire to simplify fabrication of the discrete injection module while still maintaining the staggered slot configuration.

As indicated in Figure 5-5, the total width of the exposed surface of the discrete injection module was nominally 1.12 in. for all slot/land combinations, so that the number of slots per row ranged from 1 to 10. The total running length of the same surface was always 0.62 in. Therefore, only a single model holder was required for all tests. This was essentially mandatory since the model holder must interface with the Ames duct and must be water cooled, making the design and fabrication of more than one model holder uneconomical.

AEROTHERM
ACURTEX Corporation

COMBINED COOLING-FLIGHT AND GROUND TEST INJECTION SURFACES

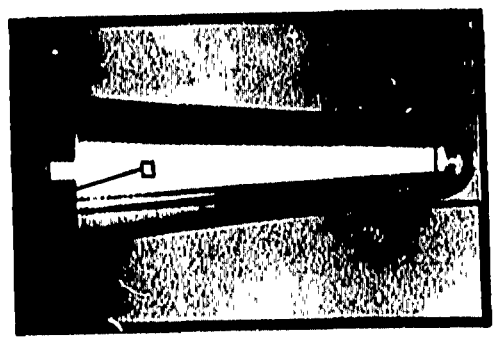

FLIGHT AEROTIP

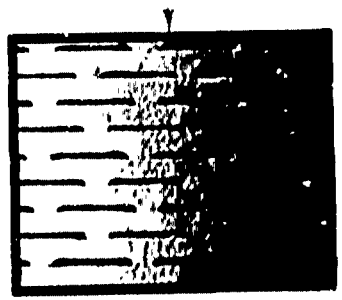

SKIRT REGION

MODEL MOUNTED ON DUCT WALL

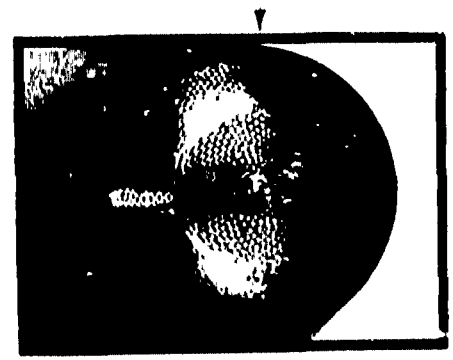

CAP REGION

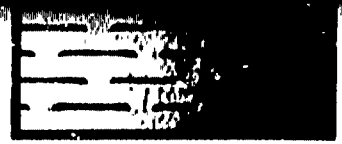

SKIRT REGION

MODEL MOUNTED ON DUCT WALL

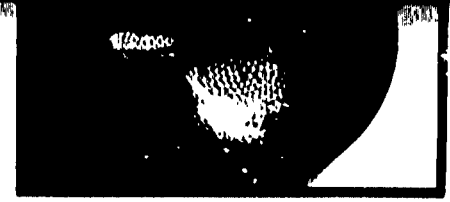

CAP REGION

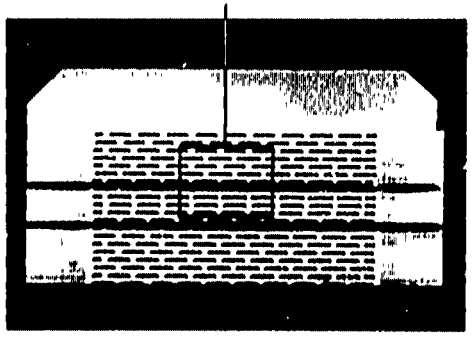

S=.010/L=.020

S=.051/L=.051

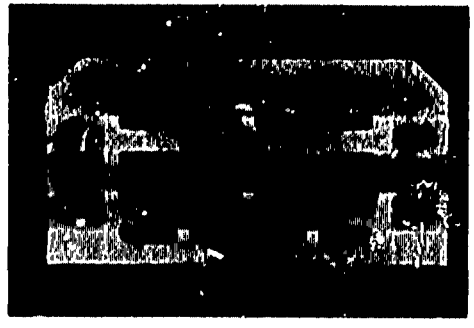

S=.051/L=.102

S=.102/L=.051

FIGURE 5-6

TABLE 5-1

SLOT/LAND CONFIGURATIONS

S (in)	L (in)	W (in)	S/L (-)	Percent Open Area (%)	No Slots/Row (-)	No Rows (-)
0.010	0.020	0.100	0.50	33.3	10	20
0.051	0.051	0.510	1.00	50.0	2	6
0.051	0.102	0.510	0.50	33.3	2	4
0.102	0.051	0.510	2.00	66.7	2	4
0.189	0.188	1.020	1.01	66.8	1	2

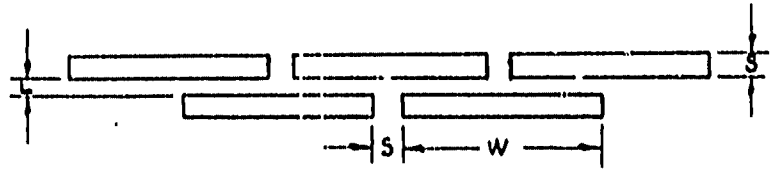

Because the total cooled area (0.62 in. x 1.12 in.) was the same for each slot/land combination, the total mass flowrate (lbm/sec) injected in the DI section for a specified average coolant mass flux (lbm/ft^{2}sec) was independent of the slot/land configuration. This simplified the interpretation of data obtained on the downstream coolant effectiveness and eliminated the need for major coolant supply variations for the different DI modules. Finally, the one-inch width selected for the DI module minimized the effects of transverse nonuniformities in the test stream.

Based upon the analyses of Reference 34, to observe the 90 percent recovery point downstream of injection, for an isothermal surface and typical injection rates, the running length of the downstream test surface must be approximately 2.5 times that of the cooled section. The downstream length of 2.25 in. satisfied this requirement and was the maximum feasible, since the coolant channel in the model holder occupied a certain amount of running length on the model holder surface.

The discrete injection module was fabricated from quartz (fused silica). Quartz was chosen solely because its thermal conductivity of 0.8 Btu/hr°F is approximately twenty times lower than that of the flight hardware, thereby permitting scaling of internal heating phenomena in the Ames turbulent duct which provides heat fluxes two orders of magnitude lower than flight. Unfortunately, the flight hardware is fabricated from stainless steel which, for a metal, has low thermal conductivity. Therefore, although metals were desirable for test fabrication purposes their thermal conductivities were unacceptably high. In general, materials with thermal conductivities in the range of that for quartz, e.g., electrical ceramics and epoxies, cannot be fabricated in the small-slot configurations required for this experiment since casting and molding processes are involved. Also, materials with thermal conductivities below that of quartz, which conceivably could have been used in this experiment - e.g., teflon, are too soft and/or flexible.

Table 5-2 presents the thermophysical properties of quartz. Compared to flight hardware (stainless steel), quartz has a higher melting temperature and a much lower coefficient of thermal expansion. Consequently, quartz has very good thermal shock resistance, a very desirable feature for this test program. The single major disadvantage with quartz is its susceptibility to chipping and cracking, both during the module fabrication process and under the typical mechanical loadings exerted on the module when it was mounted in the model holder.

As mentioned at the beginning of this section, the secondary objective of the Combined Cooling experiment was to test a porous injection module under the same conditions as used for the discrete injection modules, thus providing

TABLE 5-2

THERMOPHYSICAL PROPERTIES OF QUARTZ (from Reference 9)	
Property	Value
Thermal Conductivity	0.8 Btu/hr ft°F
Specific Heat	0.18 Btu/lb°F
Melting Point	3652 °R
Softening Point	3492 °R
Annealing Point	2543 °R
Strain Point	2417 °R
Specific Gravity	2.2
Coefficient of Thermal Expansion	3×10^{-7}/°F
Hardness	4.9 mohs

a common basis for comparison of porous versus discrete cooling performance. A porous material manufactured at NASA Ames was chosen for the present tests. The material is fabricated by mixing silica fibers with an epoxy-type binder and sintering the mixture at an elevated temperature. Because the solid matrix of the porous material is fused silica, its thermal conductivity is essentially the same as that for the solid lands in the DI modules. Thus, internal heating phenomena were scaled equally in both porous and DI modules.

5.2.2 Model Hardware Specifications

Figures 5-6 and 5-7 contain photographs of the primary components of the Aerotherm model assembly. In the following subsections, brief descriptions of most of these components are presented.

5.2.2.1 Model Holder

The model holder was machined from copper and was comprised of two parts, a backing plate and a mounting plate. When these two plates were bolted together the model holder coolant channel was formed. Coolant requirements were approximately 3.0 gpm at 60 psi. All features of the external configuration of the model holder were designed to permit inserting the model holder in the Ames duct without modifying the latter.

5.2.2.2 Discrete Injection Model Assembly

The discrete injection model assembly was comprised of three primary components:

- Slotted quartz module
- Metering plate
- Metering plate holder/plenum

The S = 0.010 in. module was fabricated before the other modules and subjected to extensive laboratory testing. Based on the findings of this testing, some features in the design of the remaining quartz modules were different from the S = 0.010 in. module:

- The mounting flange was made thicker for increased mechanical strength
- The leading land was replaced by an open slot in order to eliminate a large surface area of uncooled quartz.
- The trailing row of slots was replaced by a land in order to achieve better sealing at the interface between the module and the metering plate.

AEROTHERM
ACUREX Corporation

COMBINED COOLING GROUND TEST HARDWARE

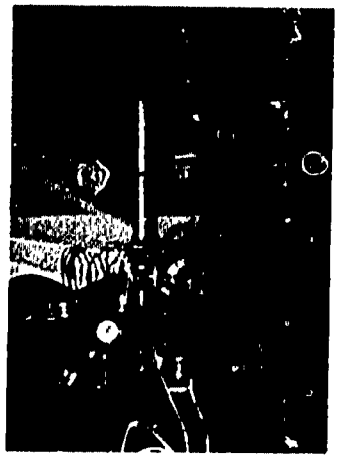

TOP VIEW TEST DUCT WITH CAMERA IN POSITION

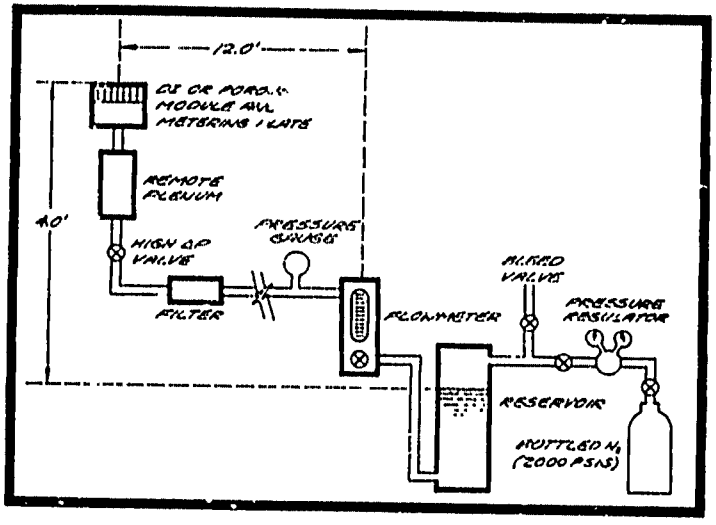

COOLANT SUPPLY SYSTEM

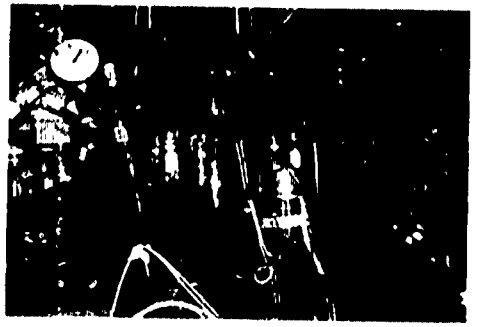

SIDE VIEW TEST DUCT

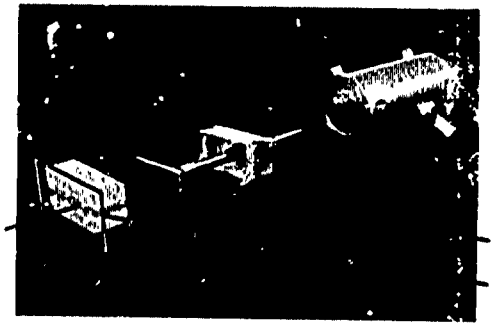

DI MODULE METERING

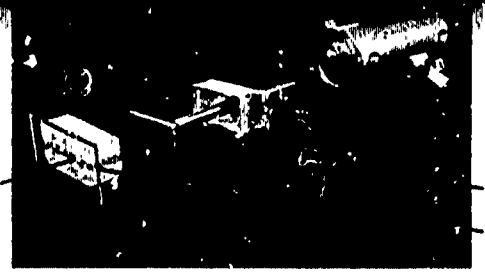

DI MODULE METERING PLATE AND PLENUM ASSEMBLY

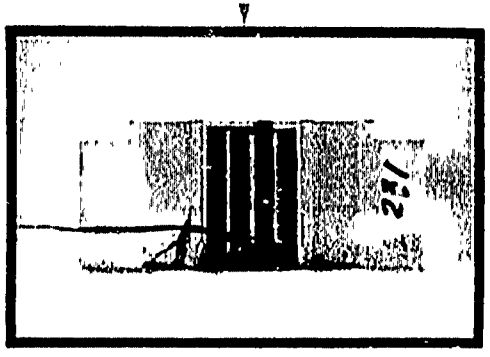

IN-DEPTH VACUUM DEPOSITED THERMO-COUPLES (FE/NI)

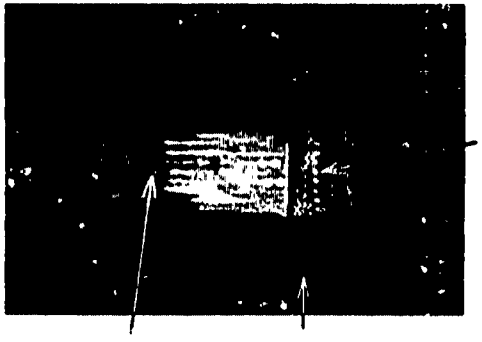

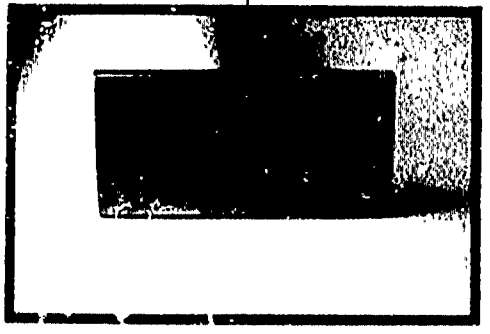

FRONT VIEW METERING PLATE

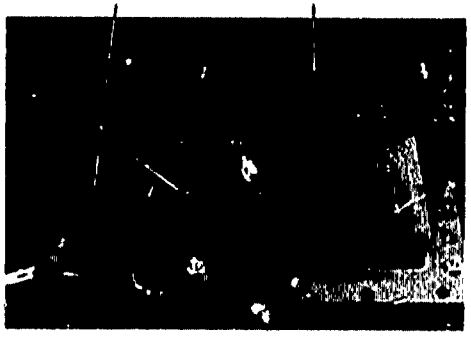

DOWNSTREAM MODULE

MODEL HOLDER

FIGURE 5-7

The basic quartz module fabrication procedure was to first grind channels into several identical quartz platelets, and then glue these platelets together to form a slotted block of quartz. The final grinding operations, i.e., cutting of the flanges and surface lapping, were then carried out on the glued assembly. Finally, the entire assembly was unglued for inspection for possible cracks and fractures in the individual channeled platelets. Insaco Co. (Quakerstown, Penn.) was responsible for fabrication of all quartz modules.

When the quartz module was inserted into the model holder, each platelet or subassembly was allowed to float free from adjacent platelets, in order to reduce the possibility of thermal stresses being set up which would result in fractures. However, all faces of the flanges on the assembled model were coated with a thin layer of RTV adhesive/sealant. This coating served to seal against possible water leaks out the side of the module and also provided a cushion between the quartz/copper interface where possible chipping could occur.

Figure 5-5 depicts the type of metering plate used for the larger-slot DI modules. Figure 5-7 contains a photograph of such a metering plate. Two versions of the tube-bundle metering plate were built, with 0.30-0.45 in. and 3.0-4.5 in. long metering tubes. The short-tube version was designed for high flowrates ($6 \leq M \leq 12$), and the long-tube version was designed for the low flowrate regime ($1 \leq M \leq 6$).

Figures 5-5 and 5-7 also indicate the holder for the aforementioned metering plates. This component held the metering plates in place, and located the tubes of the metering plates directly under the slots of the quartz modules.

For the S = 0.010 in./L = 0.020 in. module, it was not possible to use the tube-bundle-type metering plate because the slots were too small and too numerous. Instead, a porous stainless steel plate (Poroloy, Bendix Corporation) was used. The Poroloy metering plate was characterized at flowrates of interest so that nonuniformities in coolant flux over the plate could be accounted for. Flow uniformity tests of both the porous and tube-bundle metering plates are discussed in greater detail in Section 5.3.6.

5.2.2.3 Porous Model Assembly

The porous model assembly was comprised of two primary components:

- Porous module
- Holder.

There was no metering plate required for the porous module testing.

The porous module was fabricated of re-usable surface insulation (RSI) with a density of 23 lb/ft^3. RSI is a material comprised of silica fibers combined with a binder, raised to an elevated temperature, and subjected to high pressure to compress it. The RSI material was supplied and machined by NASA Ames. The porous module was designed to be placed in the cavity of the model holder with the exposed surface flush with the floor of the test duct and to be supported by an existing metering plate holder.

In bench tests performed at Aerotherm, the physical permeability of the porous module material was found to be approximately 1.45×10^{-11} ft^2.

5.2.2.4 Downstream Module

Figures 5-3 and 5-7 indicate the main features of the downstream module. This module was fabricated from copper and had its own separate coolant circuit. Coolant requirements were approximately 1.0 gpm at 60 psi. In addition, it was instrumented with eight Gardon gages. Additional details on the gages are presented in Section 5.3.7. The entire downstream module was manufactured by Thermogage, Inc. (Frostburg, Maryland).

5.2.2.5 Injection Module Coolant System

Figure 5-7 presents a schematic of the coolant supply system which was used to provide coolant to the injection module. The basic concept for the design of this system was that the flowrate must be varied by varying the system back pressure, rather than by varying a valve adjustment in a constant-back-pressure system.

Inherent in the coolant requirements for the DI and porous modules were two somewhat unique and troublesome features:

- The total flowrates were extremely low, 60 cc/min at maximum
- The static pressure of the test stream into which the water was injected was subatmospheric.

As a consequence, the fluid flow friction (pressure drop) in the lines of the supply system was negligible because of the low flowrates, and dissolved air in the water tended to come out of solution because of the subatmospheric pressure.

Normally, the pressure drop in the lines of a coolant system is comparable to the pressure drop present in the metering valve. Thus, when the valve position is varied to achieve a different flowrate, the pressure drops through various portions of the system adjust quickly and the transient period in the flowrate is of short duration. However, when flow friction in the system lines is negligible compared to friction at the metering valve, most of the pressure

drop from supply to sink occurs at the valve. In this situation, flow transients of several minutes can occur when the metering valve is adjusted from one position to another. In order to circumvent this problem, variations in the flowrate were obtained by varying the system back pressure.

Whenever the pressure in the coolant supply system was significantly below one atmosphere, air bubbles tended to form because air dissolved in the water came out of solution. Because flow velocities were extremely low (1.0 in./sec for 60 cc/min of water in a 0.25 in. ID tube), these bubbles were able to coalesce and form large air voids in the supply lines. Such air voices created highly sporadic and, therefore, undesirable injection at the surface. This problem was essentially eliminated by placing a large-pressure-drop valve as close to the remote plenum as possible. This ensured that most of the water in the supply system was at a pressure sufficiently high to prevent air desorption.

Before a test run, the large-pressure-drop valve located near the plenum was set to give the maximum flowrate of interest when the pressure over the coolant resevoir was approximately 120 psig. Then, to obtain lower flowrates, the bleed valve between the reservoir and the pressure supply was opened and the regulator on the nitrogen cylinder was shut off. This allowed some of the nitrogen over the reservoir to escape, resulting in a reduction in back pressure.

As described in Section 5.2.2.2, several of the metering plates used in the test had 3.00 in. or 4.50 in. long metering tubes. These tubes were too long to be contained within the model holder. For each such metering plate, the tubes were gathered into a bundle, and a sheath (a length of stainless steel tubing) was placed around the bundle. The tube bundle and its sheath extended below the lower surface of the model holder, and the remote plenum was placed at the entrance to the metering tubes to provide acceptably low entrance velocities to the metering tubes.

5.3 INSTRUMENTATION

Extensive and state-of-the-art instrumentation was used in the Combined Cooling experiment. Much of this instrumentation required calibration in bench tests carried out at Aerotherm. The details of the calibration procedures and the calibration results are presented in Reference 10. Space limitations preclude more than the brief summary of the instrumentation given below.

Table 5-3 summarizes the instrumentation used in the Combined Cooling experiment.

TABLE 5-3

SUMMARY OF MEASUREMENTS AND INSTRUMENTATION FOR THE COMBINED COOLING EXPERIMENT

Location	Measurement	Instrument or Data Source
Discrete Injection Module	Average surface temperature at center of module	Pyrometer
	State of coolant exiting slot (formation and motion of liquid layer, droplets, rivulets, etc.)	Sequence photography - color film
	Land surface temperature distribution	Sequence photography - infrared film + microdensitometer
	Land in-depth temperature distribution	Vacuum-deposited and wire thermocouples
	Total coolant flowrate to DI module	Rotameters
	Individual slot coolant flowrate	Metering plate
Downstream module	Streamwise heat flux distribution	Gardon gages
Duct wall opposite model holder	Cold wall, no-injection heat flux distribution	Gardon gages
	Cold-wall, no-injection wall pressure distribution	Pressure transducers
Miscellaneous	Temperature of coolant in DI section	Thermocouple probe
	Temperature of coolant leaving downstream module	Thermocouple probe
	Temperature of coolant leaving model holder	Thermocouple probe
	Arc heater chamber pressure	NASA/Ames data recording
	Arc heater power input	NASA/Ames data recording
	Test stream mass flowrate	NASA/Ames data recording

5.3.1 Pyrometer: Average Surface Temperature at Injection Module

Because of the smallness of the lands in the DI modules and the presence of a high-temperature supersonic test stream, the most straightforward approach to the measurement of land surface temperatures without disturbing the test stream was pyrometry. However, by virtue of the very small land dimensions a pyrometer is capable of measuring only the average temperature over either a single land, for those modules with $L \geq 0.100$ in, or several slots and lands, for the module with $L = 0.020$ in. and $S = 0.010$ in. Nevertheless, for the purpose of real-time monitoring of the average temperature at a spot on the injection module surface, whether it was the porous or DI module, the pyrometer reading provided essential data concerning the surface thermal state. Furthermore, it is doubtful that a thermocouple or thin film gage installed on a land surface could have survived the severe heating environment.

Because a pyrometer window was already available in the duct wall opposite the test section, the location of the injection module was directly below this window. Figure 5-4 illustrates the orientation of the pyrometer relative to the test section. The pyrometer senses radiation from the target surface in the wavelength range 3.5 to 4.1μ. The transmission of radiation in this wavelength regime by a quartz sample more than 1 mm thick is quite small, so that a true surface temperature was detected.

To make an accurate measurement via pyrometry, spectral absorption and emission characteristics of the medium between the pyrometer lens and the target must be considered. In the present application, absorption and emission of 3.5 - 4.1μ wavelength radiation in the following media were of concern:

- The air environment between the instrument and the duct window
- The duct window material
- The arc-heater air test stream in the duct
- Liquid and vapor-phase water at the surface of the DI section.

As discussed in References 9 and 10, calculations were carried out which indicated that absorption by any of the above intercepting media would be negligible. As a precautionary measure, however, the pyrometer was calibrated under conditions which duplicated very closely the actual test environment. A full-scale plywood model of the Ames test section was constructed, and the Ames water-cooled window assembly and a small slotted block of quartz with a surface thermocouple were mounted in the ceiling and floor of the duct, respectively. The quartz block was convectively heated with a natural gas/oxygen torch capable of delivering heat fluxes up to 300 Btu/ft^{2}sec. For a range of heating levels, the pyrometer and thermocouple surface temperature

readings were compared and the pyrometer surface emissivity adjustment was set to bring the two temperatures into approximate agreement.

The calibration data indicated that the emissivity of the quartz surface was essentially unity, but that viewing through the Ames water-cooled window assembly reduced the effective surface emissivity to 0.385. This was found to be a result of aperature limitations imposed by the window assembly, rather than absorption effects in the window material.

A Thermodot Model TD-17G pyrometer (Infrared Industries, Inc.) was used to measure the average land surface temperature. The primary features of this instrument are the following

- Temperature ranges : 200 - 400, 350 - 860, 700 - 2600°C
- Focus range : 12 - 24 inches
- Spectral range : 3.5 - 4.1 microns
- Response time : 0.3 seconds
- Minimum object area : 0.1 in. square
- Accuracy : ± 2 percent of temperature range, or ± 10°F, whichever is greater.

A Thermodot Model A-1 Accessory Unit was used in conjunction with the TD-17G to provide a convenient remote operator panel. Real-time monitoring of the temperature measured by the pyrometer was done at the Accessory Unit. Also, the unit was used to change temperature ranges, adjust response time, actuate and adjust the calibrate signal, adjust the recorder output level, and control the AC input power.

5.3.2 Color Photography: State of Coolant Exiting Slots

Sequence photography was used to determine the state of the coolant leaving the slot exit and to observe how the ejected fluid then flows downstream. The results of the Internal Cooling experiment (Reference 6) revealed that for small slots, S = 0.005 in., the state of the coolant leaving the slot depends on the heating conditions and the coolant and may be in liquid, spray, globule, or vapor form. As the injectant then moves downstream, it may assume liquid layer, droplet, or rivulet forms. During selected test runs, these events at the surface of the DI section were monitored with sequence photography. Referring to Figure 5-4, the camera replaced the pyrometer and used the same duct window during these selected runs. A flash tube was attached to one of the slit windows in the side of the duct to provide synchronized illumination.

A Nikon F 35 mm camera with Photomic FTN Finder was used. Because the test cell was isolated when the arc heater was operating, the camera was remotely controlled. This was accomplished with a Nikon F-36 Motor Drive and Battery Pack which was attached to the camera and actuated via a push-button mechanism at the end of a 25 foot extension cord. Depressing the push-button mechanism both released the shutter and advanced the film to the next frame. Since the aperature and shutter speed could not be controlled remotely, they were preset at f3.5 and 1/30 sec, respectively. Kodak High Speed Ektachome (ASA 160) color slide film with standard Kodak processing was used.

The camera was equipped with a 135 mm lens attached to a 16 in. extension tube. This rather unique lens/extension combination was required to provide a magnified image filling the entire frame under the constraint that the front of the lens could be no closer than 4 in. from the injection module surface, due to the space occupied by the water-cooled window. Image magnification was 2 1/2 - 3X, and further magnification via 3 in. x 5 in. prints or slide projection was accomplished without loss of detail. Depth of field was approximately ± 0.020 in.

The electronic flash unit used consisted of a 1 in. long flash tube with 13 joules output in 1/1000 sec. Power was provided by a battery pack, and the flash was synchronously triggered by the camera. As indicated in Figure 5-4, the flash was mounted on the side wall of the duct in a specially-designed window which replaced the existing duct window assembly.

5.3.3 Infrared Photography: Injection Module Surface Temperature Distribution

Infrared photography was used to provide a quantitative estimate of the temperature variations over the surface of the injection module. Interpretation of the infrared photographs was performed by color enhancement of the film via micro densitometry.

To expose the infrared film, the camera arrangement discussed in the previous section was used, without the flash tube and with the addition of a Nikon R60 (red) filter. Kodak High Speed Infrared (black and white) film was used. Bench tests carried out at Aerotherm indicated that the optimum aperature was f5.6 and the optimum shutter speed was in the range of one to ten seconds.

The infrared film is sensitive to radiation with wavelengths up to 0.95μ. The red filter eliminated all radiation below 0.62μ, so the wavelength regime which was recorded on the film was the red/infrared regime, $0.62 \leq \lambda \leq 0.95$. Note that no radiation in the visible regime $\lambda < 0.62$ (except red) was recorded (including stray light which might have entered the camera from the laboratory surroundings). In fact, for the surface temperatures of interest, $400 \leq T \leq 1500°F$,

emitted radiation was heavily weighted toward the maximum wavelength recorded, $\lambda \cong 0.95\mu$ (see Reference 7). Therefore, the image recorded on the infrared film under the conditions of interest was entirely beyond the visible regime and provided a true "thermal recording."

In order to deduce local temperature from examination of the exposed negative, a relation between negative density and temperature of the photographed object must be established. In Reference 10 it is shown that when radiation from a source with surface temperature in the range $400 \leq T \leq 1500°F$ and with wavelengths in the range $0.62 \leq \lambda \leq 0.95\mu$ is incident upon the infrared film, the resulting film density is linearly related to the inverse of the surface temperature; that is, when the temperature of the object increases, the density of the exposed negative increases.

Local densities on the exposed negative were measured with a microdensitometer manufactured by International Imaging Systems (Mountain View, California). This device measures the percentage transmission of a known quantity of light at a point on the negative, where transmission is defined as

$$\tau = \frac{\text{Transmitted Light}}{\text{Incident Light}}$$

By definition, the film density is

$$D = \log \frac{1}{\tau}$$

The International Imaging Systems (I^2S) microdensitometer was equipped with an electronic package which converted local τ to local D and assigned a selected color to a given range of D values. The unit used in this work had a thirty-two-color scale, so that the full range of film densities (surface temperatures) was portioned into thirty-two increments. The full color pattern corresponding to a 35 mm negative was projected onto a television screen and permanently recorded on Kodachrome X 35 mm color slide film.

Since the relationship between D and $1/\tau$ is linear, a complete calibration required independent knowledge of the temperatures at two locations in the thermal recording or two different temperatures at the same location in two different recordings. This data was provided by the pyrometer measurement of the surface temperature. Once such a calibration was obtained, it could be used for all of the thermal recordings as long as each roll of film was developed under precisely repeatable processing and only negatives with the same exposure time were compared. All processing of infrared film in the present study was performed by Aerotherm personnel to ensure that such processing repeatability was maintained.

5.3.4 Vacuum-Deposited and Wire Thermocouples: Slot In-Depth Temperature Distribution

Temperatures and temperature gradients in selected coolant channels of the DI module were monitored with thermocouples. Two methods were used:

- Vacuum-deposited thermocouple junctions
- Small-diameter wire thermocouples.

For the quartz module with S = 0.010 in. and L = 0.020 in., only vacuum-deposited thermocouples were used since the small slot widths rendered installation of wire thermocouples impractical. For all other modules, both types of thermocouples were used.

A photograph of the vacuum-deposited thermocouples in the quartz DI module with S = 0.050 in. and L = 0.50 in. is included in Figure 5-7. The quartz subassembly was first grooved as shown to allow passage of the lead wires to the side. The surface to be deposited on was then polished with an abrasive slurry to obtain as smooth a finish as possible. Then, thin films of iron and nickle approximately 1μ thick were deposited on the polished surface (only pure metals, as opposed to metal alloys, can be reliably deposited). The iron was deposited first, and when the nickel was deposited a small overlap onto the iron film in the three locations indicated in the photograph was permitted. These three regions of overlap formed the bimetal junctions which acted as thermocouples.

After the iron and nickel films were deposited, a film of SiO was deposited over the entire area, except at the bottom of the subassembly where the lead wires were attached, in order to prevent oxidation of the films from occurring due to the high-temperature air environment. No special procedure for electrical insulation of the backside of the thin films was required by virtue of the insulative quality of the quartz itself.

The lead wires were soldered to the thin films in the locations shown and seated in the grooves with epoxy. All grooves were filled with epoxy and ground flush in order to ensure a close fit with the adjacent quartz subassembly and to prevent coolant flow from one slot to an adjacent slot.

A single wire thermocouple was installed in selected quartz subassemblies. The bead of the thermocouple was located in the web, as close as possible to the land surface, and was cemented in place with high-temperature quartz cement. The leads were brought out to the side of the subassembly in a manner similar to that used for the vacuum-deposited thermocouples.

Wire leads of 0.002 in. diameter were used for all thermocouples. These lead wires were brought out of the bottom side of the model holder to an attached terminal board. A calibration curve for the iron-nickel thermocouple junction is presented in Reference 10.

5.3.5 Rotameters: Total Coolant Flowrate to Injection Module

As described in Section 5.4 below, the Combined Cooling Test matrix considered total coolant flowrates to the DI module up to .002 lbm/sec (55 cc/min), corresponding to a theoretical margin factor of approximately six and the highest heat flux attainable. The total coolant flowrate was continuously monitored throughout a given test run.

Two SK type 20-7050V rotameters were selected for the coolant flowrate measurement. One of the rotameters covered the flowrate range 0 - 6 cc/min ($0 - 2.2 \times 10^{-4}$ lbm/sec) and the other covered the range 0 - 60 cc/min ($0 - 22 \times 10^{-4}$ lbm/sec). Both meters have a quoted accuracy of ± 2 percent of full scale. However, a checkout of the meters revealed the accuracy to be much less than ± 2 percent. Therefore, the meters were calibrated over their entire ranges. Calibration curves are presented in Reference 10.

5.3.6 Metering Plates: Individual Slot Coolant Flowrate

In order to make a meaningful interpretation of all data taken at the DI module, the coolant flowrate through each slot, especially the instrumented slots, must be known. Ideally, the flowrates in all slots should be equal. However, if all slots are fed by a common plenum, it is possible that nonuniform slot-to-slot flow can develop if the pressure drops through the slots are not equal from slot to slot. This condition can arise when, for instance, local boiling occurs at one slot but not the others, thus giving rise to nonuniform slot-to-slot flow characteristics (friction factor).

In order to ensure that the flow rate in each slot is independent of the state of the fluid or other flow phenomena in the slot, flow metering must occur just upstream of each slot. Metering was accomplished by placing a metering plate on the upstream side of the quartz DI module, as illustrated in Figure 5-5. The plate is an effective metering device whenever the pressure drop through it is substantially larger than the pressure drop through an individual slot. A mesh-type gasket was placed between the quartz module and the metering plate in order to prevent slot-to-slot crossflow between the plate and the module.

Slot pressure drop calculations were carried out for a total coolant flowrate of 0.002 lbm/sec (roughly the maximum considered in the tests) and the smallest slot-size module, S = 0.010 in. This module has 200 slots, so that the flowrate in each slot, under uniform conditions, was 10^{-5} lbm/sec. For such a small flowrate, laminar flow prevails for both liquid and vapor phase coolant. Using the standard friction-factor correlation for fully-developed laminar flow in rectangular passages, slot pressure drops of 0.0032 psi and 0.037 psi were calculated for all liquid and all vapor flow, respectively. These extremely

small pressure drops imply that flow friction was negligible compared to gravity and surface tension effects. This is substantiated by the fact that the pressure below a column of liquid-phase water 0.2 in. high is 0.007 psig, and the pressure drop across a bubble assumed to form over the slot exit was calculated to be 0.083 psi.

Using the above pressure-drop calculations as a guideline, the decision was made to design a metering plate which provided at least a 2.0 psi pressure drop for a flowrate of 0.002 lbm/sec through a flow area of 1.0 in. x 0.6 in. A 2.0 psi pressure drop is sufficient to dominate the various slot pressure drops calculated above.

For the small-slot DI module, S = 0.010 in., there were a total of 200 slots in the nominally 1.0 in. x 0.6 in. injection area. The most practical metering plate for this module was one comprised of a porous metal. The plate used was 1/16 in. thick Porolcy (Bendix Corporation). Typically, such porous material has inherent nonuniformities which occur during the fabrication process. Therefore, the plate was calibrated and well-characterized before it was used in the actual tests. The plate calibration procedure and results are presented in Reference 10. Flowrate nonuniformities at positions where instrumentation was located did not exceed ± 30 percent.

All other DI modules had fewer slots which were much larger in cross-sectional area. This made the tube-bundle metering plate approach depicted in Figure 5-5 quite attractive. In this approach, each full slot was fed by two hypodermic tubes and each half-slot was fed by one tube. Using the fully-developed laminar-flow circular-tube friction-factor correlation f = 16/Re, the tube length required to achieve a 2.0 psi pressure drop for a specified tube diameter and flowrate was determined. In all cases the tube OD was 0.013 in. and the ID was 0.007 in. The major difficulty encountered in assembling the tube-fed metering plates was cutting the required tube lengths from the commerically-available stock. Special care was required to ensure that each cut was clean and free of burrs or other distortion of the tube ends. A number of the tubes were bench tested at Aerotherm to verify that uniform flow characteristic prevailed from tube-to-tube. The data scatter in these tests did not exceed 15 percent.

In addition, bench test data were taken on one of the assembled tube-fed metering plates. The flow issuing from each of the sixteen holes in the plate was measured with a small sampling tube. The maximum percent deviation from the average was 15 percent, which was felt to be quite acceptable.

In order to permit considering a wide range of flowrates during the testing program, two tube-bundle metering plates were made for each model, one giving

a 2.0 psi pressure drop and the other a 20.0 psi pressure drop. The 2.0 psi pressure drop plates had tube lengths between 0.30 and 0.45 inches long and were fed by the spacer/plenum located within the model holder. The 20.0 psi pressure drop plates had tube lengths between 3.0 and 4.5 inches long, requiring that a remote plenum be used to feed the tubes. The remote plenum is included in one of the photographs of Figure 5-7.

Bench tests were also performed at Aerotherm to determine the pressure drop across the porous model supplied by NASA Ames. Pressure-drop data were obtained for a cylindrical sample with both cross-sectional area and depth identical to the module actually tested. The pressure drop for the maximum flowrate considered in the actual testing was 4.0 psi. A physical permeability range of 1.415 to 1.526 x 10^{-11} ft^2 encompassed all of the data taken.

5.3.7 Gardon Gages: Downstream Heat Flux Distribution

As discussed in Section 5.2.2.4, the downstream module was fabricated from copper and was water-cooled. Consistent with the test objectives stated in the beginning of Section 5, this module was instrumented for the purpose of measuring the effects of the coolant injection upstream. The streamwise heat flux distribution over the downstream section was chosen as the parameter most indicative of downstream cooling effectiveness. A series of Gardon gages was installed at the surface of the downstream module for the purpose of making this measurement.

Eight Gardon gages with 1/8 in. body diameter were located as indicated in Figure 5-5. Gages with a 1/8 in. body diameter were the smallest currently available. The gages at the leading edge were separated by the smallest feasible web thickness, 0.020 in. The first four gages were staggered to achieve the largest possible packing density. The transverse distance between these gages (0.220 in.) was large enough to maintain structural rigidity of the copper surface during the press fit of the individual gages. However, the transverse distribution of wall heat flux in the Ames duct shows variations of 15-20 percent in 0.400 inches. This imposed a restriction on the maximum transverse gap between the first four gages. Accordingly, the design indicates a dimension of 0.345 inches from outside edge to outside edge of the gages. The maximum possible gage packing density was required at the leading edge of the downstream module in order to record the recovery gradient.

The downstream module and associated Gardon gages were designed and fabricated by Thermogage, Inc. (Frostburg, Maryland). Each gage was calibrated at Thermogage after being press-fitted into the copper module and lapped to a finish flush with the module surface. The resulting calibration curves are presented in Reference 10.

5.3.8 Opposite-Wall Gardon Gages and Pressure Tops: Cold-Wall, No-Injection Heat Flux and Pressure Distributions

This instrumentation was already available in the Ames duct (Reference 36). Static pressure was measured at the centerline and two off-centerline stations; heating rate was measured at five centerline and two off-centerline locations. Pressures were measured with variable capacitance diaphragm-type cells, while heat flux was measured with water-cooled steady state calorimeters.

5.3.9 Miscellaneous Instrumentation

Primarily as a safeguard to prevent destruction of the test hardware, the coolant temperatures in the following locations were continuously monitored:

- Injection module plenum
- Coolant exit at downstream module
- Coolant exit at model holder

Cooper-constantan thermocouple probes were used for these measurements. The arc-heater would have been shut down if, for any reason, these temperatures exceed 150 - 175°F. However, these temperatures were observed to remain within acceptable limits throughout the entire testing program.

Measurement of the following test facility operating parameters was required:

- Arc heater chamber pressure
- Arc heater power input
- Test stream mass flowrate

Knowledge of these parameters permits calculation of the mixed-mean stagnation and static enthalpies of the test stream. The stagnation enthalpy can be computed by two different methods. In the first method, it is given by

$$h_o = \frac{N\mathcal{E}I}{\dot{m}_t}$$

where $\mathcal{E}$ is the total applied voltage, I is the total arc current, $\dot{m}_t$ is the test stream flowrate, and N is the arc heater efficiency (nominally 50 percent). In the second approach, the sonic flow method described in Reference 10 was used to determine the stagnation enthalpy as a function of duct throat area, total mass flowrate and nozzle upstream pressure.

5.4 TEST MATRIX

5.4.1 Overview

The Combined Cooling test program was performed in two separate testing periods. The first period occupied three weeks between May 14 and June 1, 1973. The second period was one week in duration, from June 25 to June 29, 1973.

A total of twenty-five successful test runs was made during the one month of testing. Table 5-4 summarizes the test program, including the model configuration, window diagnostic, and data associated with each test run. It will be recalled that only one window was available in the duct which permitted viewing the injection region in the direction normal to the surface. Since three separate diagnostic tools required this window (pyrometry, infrared photography, color photography), at least three test runs were performed for each cooled model.

As indicated in Table 5-1, the discrete injection S = 0.189 in./L = 0.188 in. module was not tested. In the test planning, this model was included to investigate roughness effects associated with very large slots relative to the boundary layer momentum thickness. However, these effects were delineated clearly in the S = 0.102 in./L = 0.051 in. module, so testing of the S = 0.189 in./L = 0.188 in. module was deemed unnecessary. The uncooled teflon models tested in Runs 020 and 021 were provided by NASA Ames. They were 4 in. x 6 in. flat plate models which were mounted into the floor of the duct, thus replacing the entire Aerotherm model holder assembly. The purpose of testing the teflon models was to investigate the extent and degree of test stream heat flux nonuniformities over the test section by observing the ablation patterns on these models after a thirty-second exposure.

In terms of test runs per day, the first two weeks of the test program were much less efficient than the last two weeks. This was due to initial facility preparation, conflicts with other test stands, and arc electrode failures. The first three days were spent making the appropriate modifications to facility plumbing and electrical systems, in order to accommodate the Aerotherm model. Throughout the first two weeks, several interruptions occurred because other test stands at NASA Ames utilizing the same data recording, air supply, and steam ejection vacuum systems as the turbulent duct facility were involved in test programs. Finally, the operating conditions required for the Combined Cooling test program involved a higher arc heater chamber pressure and longer test duration than utilized in past test programs. As a result, electrode failures were more frequent than usual. After the first two weeks of testing, the life of a single electrode became predictable and therefore permitted replacement of the electrode before it failed. Performing the replacement before failure eliminated interruption and subsequent repeat of a given test run.

TABLE 5-4

SUMMARY OF TEST RUNS

Run #	Model Configuration	Window Diagnostic	Date
001	DI, S = 0.010"/L = 0.020"	Pyrometer	May 17
002	↓	Infrared	18
003		Infrared	22
004		Color	22
005	DI, S = 0.051"/L = 0.051"	Pyrometer	25
006	↓	Pyrometer	29
007		Infrared	30
008		Color	30
009	DI, S = 0.051"/L = 0.102"	Pyrometer	31
010	↓	Infrared	31
011		Color	31
012	DI, S = 0.102"/L = 0.051"	Pyrometer	June 1
013	↓	Infrared	1
014		Color	1
015	DI, S = 0.010"/L = 0.020"	Pyrometer	25
016	↓	Infrared	25
017		Color	25
018		Color	26
019	Teflon, Uncooled	Infrared	26
020	↕	Color	27
021	Porous	Infrared	27
022	↓	Pyrometer	28
023		Pyrometer	28
024		Infrared	29
025		Color	29

5.4.2 Procedures

Due to the complexity of the Combined Cooling test models and testing sequence, a rather elaborate procedure was followed throughout the test program. This procedure is outlined in broad detail below.

5.4.2.1 Pretest

At the beginning of the program, the coolant supply system for the injection module, described in Section 5.2.2.5, was installed at the Ames facility. A table just outside the test cell was utilized to support the flometers, coolant reservoir, and high-pressure N_2 cylinder. Several feet of 0.25 in. polyflo tubing was installed leading from the monitoring table to the duct inside the test cell. A control valve and filter were installed in this line, about one foot from the connection to the remote plenum feeding the injection module.

Several one-time plumbing and electrical facility modifications were also carried out at the beginning of the test program. Special coolant lines were installed for connecting a 5 hp-pump-driven coolant supply to the coolant circuits for the model holder and downstream module. Several electrical cables were installed, leading from a terminal box beneath the test cell to the test duct, for the purpose of connecting all Aerotherm instrumentation with the Beckman ANSCAN recorder described in Section 5.1.3.3. Finally, the Thermodot Model A-1 Accessory Unit (Section 5.3.1) was installed on the table outside the test cell so that the pyrometer output could be monitored on a real-time basis.

All components of the test model were assembled at Aerotherm before a given test run. The assembly process started with the assembly of the injection module. In the case of the DI module, (in contrast to the porous module), the quartz platelets were first aligned and then glued together with a light coat of RTV adhesive/sealant on all exposed surfaces except the exit and entrance planes of the slots. The assembled injection module was then placed in the model holder and the thermocouple lead wires were routed to the bottom side of the model holder and attached to a terminal block. Next, the proper metering plate for a given module was mounted in the metering plate holder and sealed with RTV. The neoprene-coated nylon mesh was then placed on the back side of the injection module and the metering plate/holder assembly was placed in the model holder. Finally, the downstream module, which holds the entire injection model assembly in place, was bolted into position in the model holder. At this point, continuity of the slot indepth thermocouples was checked at the terminal block on the back side of the model holder, in order to verify that all circuits were still intact.

The assembled model was then transported to the Ames facility for final installation. First, the model was bolted into place in the duct. Then, the three coolant supplies were connected: injection module, downstream module, and model holder. Lastly, all electrical connections were made, involving slot indepth thermocouples, coolant thermocouples, and downstream Gordon gages.

In Figure 5-7 is presented a side view photograph of the test duct with the model holder installed and associated cooling lines and electrical leads connected.

During every test run either the pyrometer or the camera was used as a window diagnostic. Both of these instruments required similar installation procedures: mounting, aligning, focusing, and connecting with remote control and flash (camera) or readout cable (pyrometer).

A photograph of the camera mounted in position for a test run is included in Figure 5-7. The camera is aimed vertically downward, so that the line-of-sight passes through the window on the top side of the duct and intercepts the injection surface on the floor of the duct.

After all equipment and the model were mounted and in position, a thorough checkout procedure was undertaken. Continuity of all instrumentation was checked at the Beckman ASCAN Recorder, and any short or open circuits were eliminated. All coolant systems were turned on so that water leaks in the vicinity of the arc heater could be located and remedied. In addition, the downstream end of the duct was put under vacuum and the air supply was turned on to allow cold air to flow through the test section.

As a final step before actual testing, the various instrumentation signals were calibrated for recording purposes. Also, the valve in the injection coolant supply system immediately upstream of the remote plenum was adjusted to obtain a 120 psig back pressure at the highest flowrate to be considered in the ensuing test.

For those test runs utilizing color photography, two shots were taken with water injection into the cold test stream.

5.4.2.2 Test

After the test stand was completely checked out for water leaks and instrumentation continuity, all personnel were removed and the test cell was closed and locked. The injection coolant flowrate was then set at the maximum value to be considered in the test, usually $6 \leq M \leq 8$, in order to provide adequate protection against the short-term, high-level heat pulse which occurs during arc startup.

Approximately two seconds before arc initiation, the cold gas flow was shut off. This was required to reduce the chamber pressure in the arc heater and thereby permit electrical breakdown of the cold air. Once the arc was initiated flow was reestablished and approximately two minutes was required to attain the desired operating conditions (current, voltage, and flowrate). The time period during which the air in the system was stagnant was purposely kept to a maximum in order to prevent any of the injected water from diffusing upstream into the arc heater. Of course, the injected coolant had to be flowing before arc initiation so that a protective film was well established before the injection surface was exposed to the transient startup heat pulse.

The sequence of flowrates considered in a given test depended upon whether pyrometry or photography was being used. With the pyrometer in position, the flowrate regime bounding the extremes in surface temperatures was determined by observing the pyrometer readout on the Model A-1 Accessory Unit dial as the flowrate was varied from high to low values. Usually, seven to eight flowrates were considered. After each flowrate value was set, by establishing a certain back pressure on the coolant reservoir, roughly thirty seconds was allowed for a steady-state to be achieved at the injection region. Then the flowrate and pyrometer readings were recorded at the monitoring table, and all other data were recorded on the ANSCAN tape recorder and a strip chart recorder (duct wall pressures only) in the control room. The ANSCAN recorded for a period of ten seconds at a sampling rate of three per second.

When photography was being used, four specific flowrate values were preselected. These flowrates were based upon the previous pyrometer data for the same injection module. A high flowrate, two flowrates around the "knee" of the surface-temperature-versus-flowrate curve, and a low flowrate were selected. For color photography, two shots were taken at each flowrate, with a thirty-second wait between each shot to permit the flash unit to fully recharge. For infrared photography, three shots were taken at each flowrate, with shutter speeds of 1, 3 and 10 seconds (and aperture set at f5.6).

5.4.2.3 Post Test

After each test, the model surface was inspected either by removing the entire model from the duct, when the final test on a given injection module had been performed, or by removing one of the slit window assemblies in the duct side-wall and viewing the surface while the model was mounted in position. In those cases where the model was removed, it was then returned to Aerotherm and completely disassembled. During disassembly the injection module was closely examined to determine whether or not any significant coolant leaks between metering plate and slots had occurred.

The data recorded on magnetic tape by the ANSCAN was reduced at the Ames Computer Center with an Ames data reduction computer program. The reduced data consisted of calibrated voltage outputs for each data channel with three values per second for the ten-second interval for each injection flowrate. Averages of the recorded voltages over the ten-second interval were also provided by the data reduction program. Calibration curves were then used to convert these average voltages for each data channel into physical quantities such as temperature or heat flux. The strip chart recorder data were converted to duct wall pressures using the known value of the pen displacement for a calibration voltage and a scale to measure the actual displacement recorded during the test run.

5.5 RESULTS

All of the test data obtained is included in Reference 10. Due to space limitations, in certain instances only a representative portion of the total amount of data obtained is presented below.

5.5.1 Arc Heater Operating Conditions

Table 5-5 presents the arc heater operating conditions for the entire Combined Cooling test program. Arc voltage E, arc current I, chamber pressure P_c, and manifold pressure P_m are measured during each test run. The test stream flowrate was determined as a function of P_m. Since the manifold supplies air to the chamber, the total flowrate is a unique function of P_m whenever the jets feeding the heater chamber are choked. However, the unusually high chamber pressure used in the present test program prevented choked flow from occuring at the jets. Therefore, a Venturi gage upstream of the manifold was used to obtain the calibration curve of $\dot{m}_t$ versus P_m.

The arc heater power input P is simply the product of E times I.

The nozzle pressure P_n is the pressure immediately upstream of the converging-diverging rectangular duct. This pressure is somewhat lower than the arc heater chamber pressure P_c due to the long electrode and significant mechanical losses associated with tangential injection. P_n was obtained as a function of P_c from special calibration runs during which P_c was measured directly. In runs 024 and 025 the magnetic field coil which stabilizes the arc was connected so that the field vector was in the same direction as the injected air swirl vector. In all other runs the reverse connection was used so that these two vectors opposed one another.

Stagnation enthalpy h_o was obtained from the sonic flow method mentioned in Section 5.3.9 above, and efficiency N was calculated from the energy balance given in that section.

TABLE 5-5

ARC HEATER OPERATING CONDITIONS

Run No.	E (volts)	I (amps)	P_c (psia)	P_m (psia)	$\dot{m}_t$ (lbm/sec)	P (MW)	P_n (psia)	h_o (Btu/lbm)	N (-)
001	4940	600	500	915	0.785	2.934	421	2050	0.579
002	4860	604	500	905	0.775	2.935	421	2100	0.585
003	5250	600	497	890	0.765	3.150	419	2150	0.551
004	5200	600	500	900	0.770	3.120	420	2150	0.560
005	5200	600	500	900	0.770	3.120	420	2150	0.560
006	4720	600	500	940	0.810	2.832	421	1885	0.569
007	4650	603	505	940	0.807	2.804	425	1950	0.592
008	4650	600	500	930	0.800	2.790	421	1950	0.590
009	4540	700	505	885	0.760	3.178	425	2050	0.517
010	4370	700	495	880	0.755	3.059	417	2100	0.546
011	4300	700	497	900	0.770	3.010	419	2150	0.580
012	5980	605	700	1312	1.127	3.600	581	1850	0.611
013	5900	600	690	1300	1.120	3.540	573	1825	0.609
014	6000	600	700	1300	1.120	3.600	580	1900	0.624
015	5600	600	700	1300	1.120	3.360	580	1900	0.670
016	5520	604	690	1330	1.145	3.330	573	1725	0.626
017	5520	605	695	1340	1.137	3.340	578	1800	0.647
018	5560	600	700	1360	1.179	3.340	581	1675	0.624
019	5600	604	698	1350	1.178	3.380	580	1650	0.607
020	5600	600	700	1350	1.180	3.360	580	1650	0.611
021	5650	605	715	1415	1.209	3.420	593	1650	0.615
022	5480	608	700	1315	1.172	3.330	581	1700	0.631
023	5400	614	685	1325	1.121	3.320	569	1800	0.641
024	4860	600	690	1425	1.225	2.920	496	1100	0.487
025	4860	600	690	1420	1.161	2.920	496	1200	0.503

5.5.2 Test Section Cold-Wall Heat Flux and Static Pressure

Figure 5-8 presents the duct wall static pressure distributions for several of the test runs. The pressure taps were located on the wall opposite the model. The wall pressure at the test section varied from 2.9 to 5.4 psig. At 21 inches from the nozzle throat, transverse variations in pressure over two inches never exceeded 25 percent.

Figure 5-9 presents the cold-wall heat flux distributions measured at the wall opposite the model for each test run. For all runs except 024 and 025, $\dot{q}''_o$ at the test section varied from 87 to 131 Btu/ft^{2}sec. As pointed out in Section 5.1.1, the magnetic field coil polarity in the last two runs was changed, resulting in lower arc heater efficiencies which gives lower values for $\dot{q}''_o$.

5.5.3 Thermodynamic and Fluid Mechanic Parameters at the Test Section

Table 5-6 presents the test section static conditions and recovery enthalpy for each test run. These quantities were calculated using References 37 and 38, experimental values of P_w and P_n, and values of h_o from Table 5-5.

Table 5-7 presents the ideal injection flowrate associated with each test run. For continuous injection at a porous surface, the ideal injection rate is that rate at which the blocked heat flux is precisely offset by vaporization of the coolant. Thus,

$$\dot{m}''_{ideal} = \frac{\dot{q}''_b}{\Delta h_L}$$

The ratio $\dot{q}''_b/\dot{q}''_o$ was taken to be equal to St/St_o, where the latter quantity was taken from Figure 5-10 (taken from Reference 35). The nondimensional injection rate F/St used in conjunction with Figure 5-10 was computed from

$$B'_{ideal} = \frac{\dot{m}''_{ideal}}{\rho_e U_e St} = \frac{\dot{m}''_{ideal}(h_r - h_w)}{\dot{q}''_b} = \frac{h_r - h_w}{\Delta h_L} = \frac{F}{St}$$

where Reynold's analogy is assumed, and $\Delta h_L \cong 1000$ Btu/lbm and $h_w \cong 150$ Btu/lbm at the water saturation temperature corresponding to the average measured wall static pressure. The ideal injection rate for the entire module was computed from

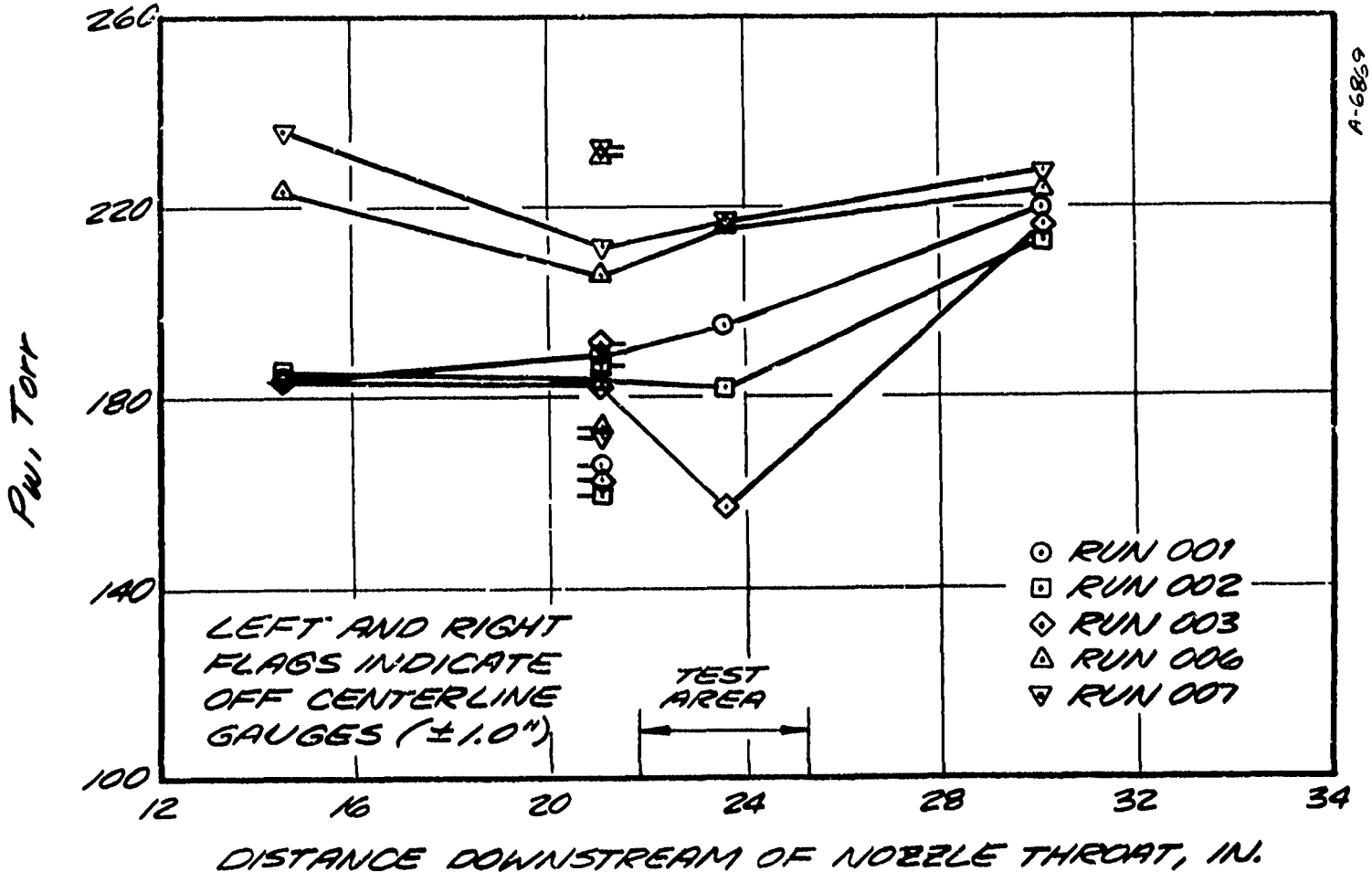

Figure 5-8. Duct Wall Static Pressure Distributions

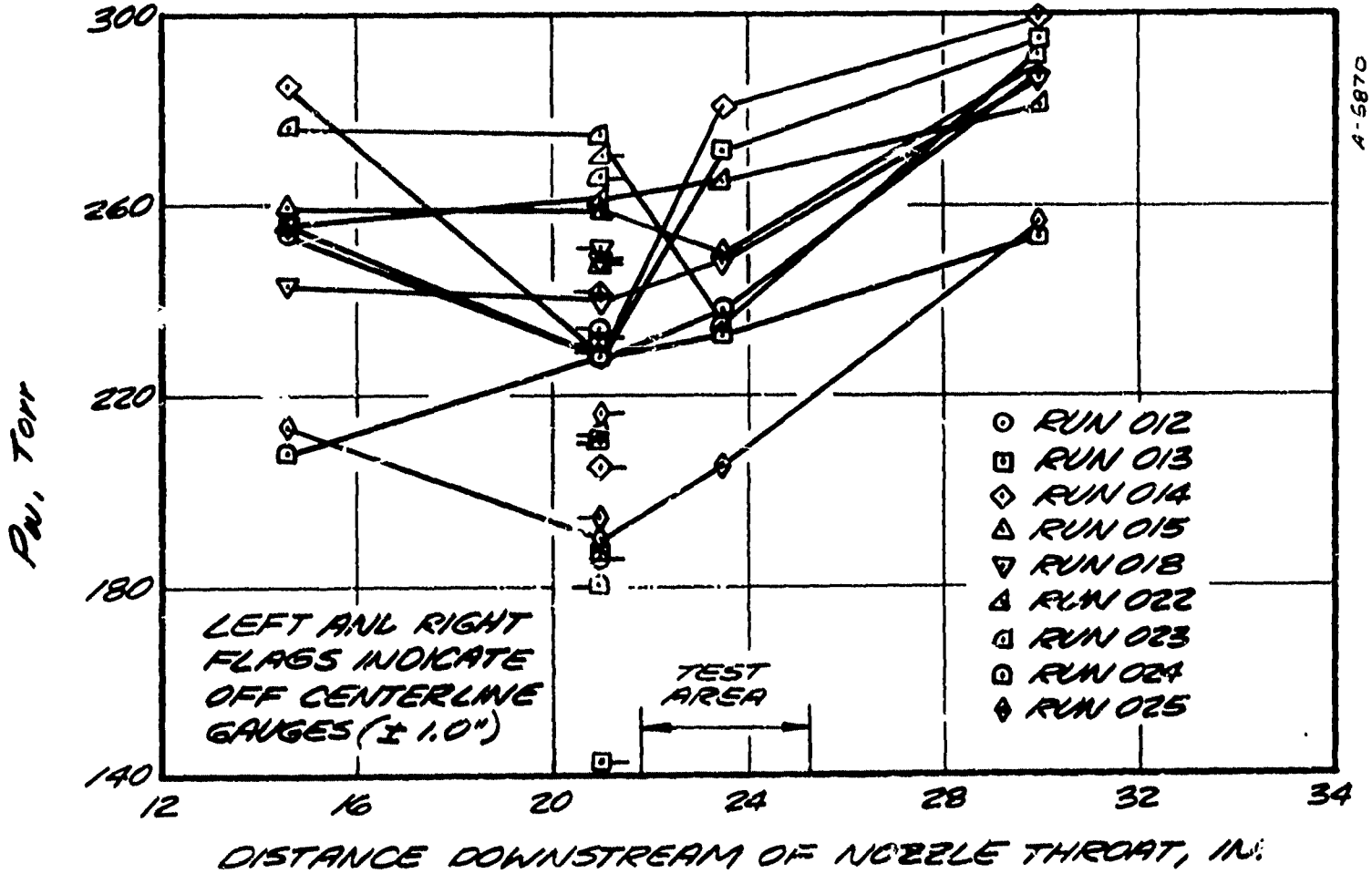

Figure 5-8. Concluded

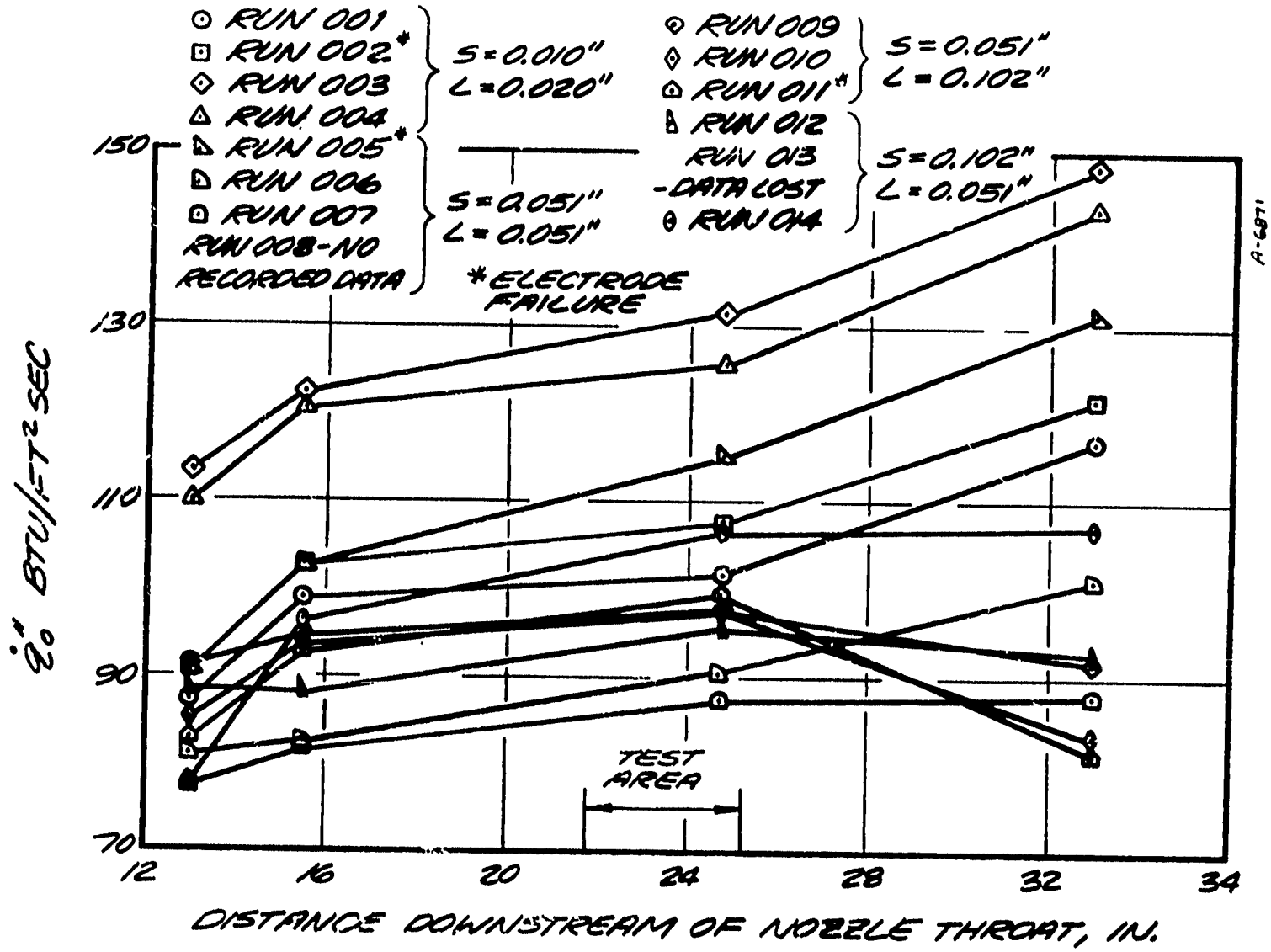

Figure 5-9. Duct Cold-Wall Heat Flux Distributions

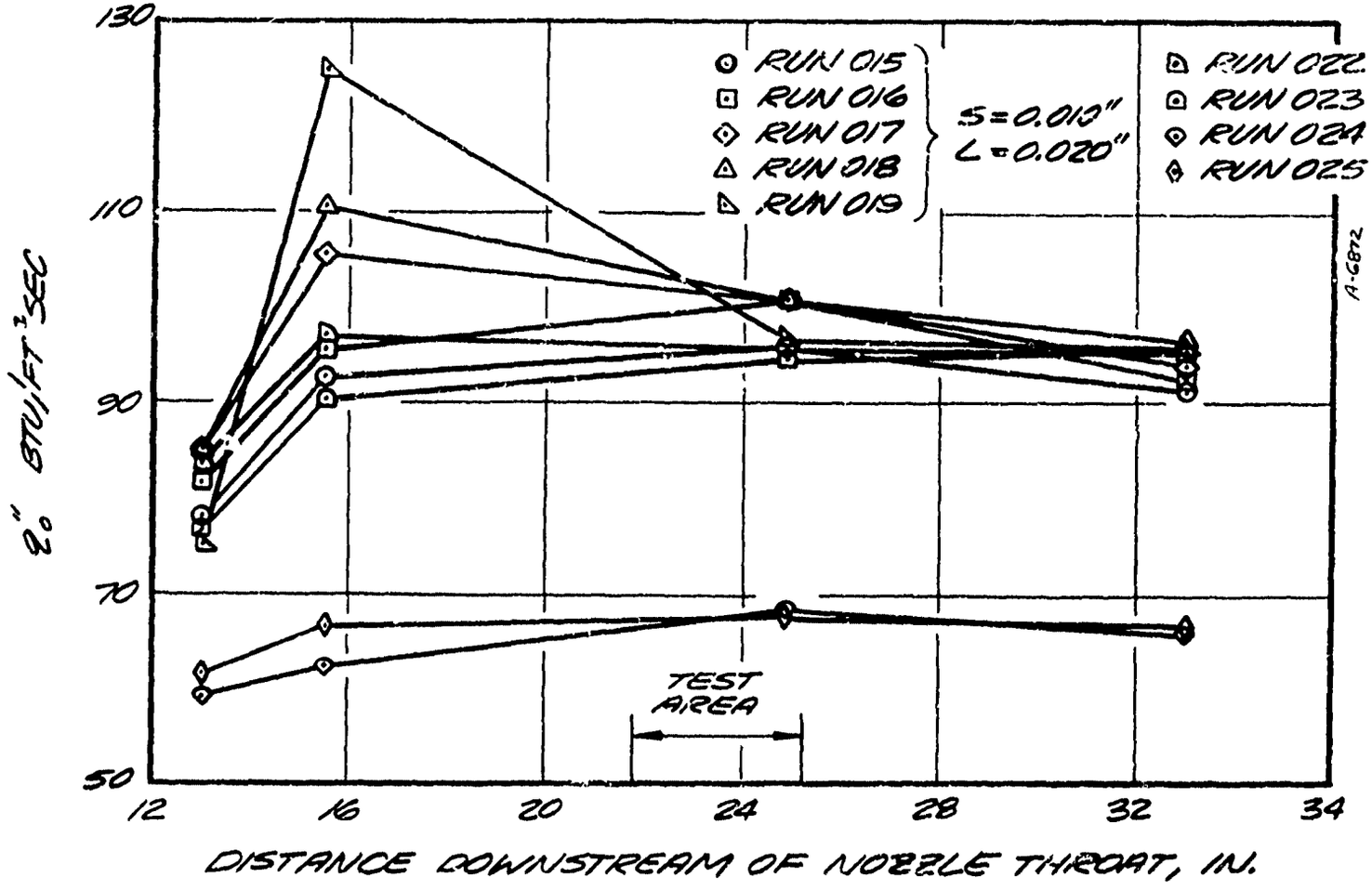

Figure 5-9. Concluded

TABLE 5-6

TEST SECTION STATIC CONDITIONS AND RECOVERY ENTHALPY

Run No.	h_o (Btu/lbm)	P_w (atm)	P_r (atm)	$\dot{m}$ (-)	T_e (°R)	h_e (Btu/lbm)	h_r (Btu/lbm)
001	2050	0.256	28.64	3.52	2490	640	1892
002	2100	0.239	28.64	3.58	2390	615	1934
003	2150	0.207	28.50	3.64	2450	630	1980
004	2150	0.207	28.57	3.65	2450	630	1980
005	2150	0.206	28.57	3.65	2450	630	1980
006	1885	0.284	28.64	3.47	2210	565	1737
007	1950	0.286	28.91	3.47	2490	640	1803
008	1950	0.286	28.64	3.47	2490	640	1803
009	2050	0.284	28.91	3.48	2490	640	1892
010	2100	0.284	28.37	3.47	2490	640	1936
011	2150	0.284	28.50	3.47	2490	640	1981
012	1850	0.313	39.52	3.60	2200	560	1705
013	1825	0.358	38.98	3.51	2216	565	1684
014	1900	0.368	39.46	3.50	2350	600	1754
015	1900	0.329	39.46	3.58	2334	600	1754
016	1725	0.329	38.98	3.56	1914	480	1674
017	1800	0.329	39.32	3.56	2150	540	1659
018	1675	0.326	39.52	3.58	1934	485	1542
019	1650	0.326	39.46	3.58	1934	485	1519
020			Transient				
021							
022	1700	0.349	39.52	3.53	2132	540	1570
023	1800	0.313	38.71	3.59	2184	555	1660
024	1100	0.372	33.74	3.41	1376	335	1014
025	1200	0.271	33.74	3.59	1400	345	1104

TABLE 5-7

IDEAL INJECTION FLOWRATE

Run No.	h_r (Btu/lbm)	F/St (-)	St/St_o (-)	$\dot{q}''_o$ (Btu/ft²sec)	$\dot{q}''_b$ (Btu/ft²sec)	$\dot{m}''_{ideal}$ (lbm/ft²sec)	$\dot{m}_{ideal}$ (lbm/sec)
001	1892	1.74	0.525	102.0	53.4	.0534	2.57×10^{-4}
002	1934	1.78	0.525	108.0	56.5	.0565	2.72×10^{-4}
003	1980	1.83	0.520	132.0	68.4	.0684	3.30×10^{-4}
004	1980	1.83	0.520	126.0	65.4	.0654	3.15×10^{-4}
005	1980	1.83	0.520	115.0	59.9	.0599	2.89×10^{-4}
006	1737	1.59	0.550	90.5	49.8	.0498	2.40×10^{-4}
007	1803	1.65	0.530	87.4	46.3	.0463	2.23×10^{-4}
008	1803	1.65	0.530	87.4	46.3	.0463	2.23×10^{-4}
009	1892	1.74	0.525	97.7	51.3	.0513	2.47×10^{-4}
010	1935	1.79	0.525	97.7	51.3	.0513	2.47×10^{-4}
011	1981	1.83	0.520	99.4	51.7	.0517	2.49×10^{-4}
012	1705	1.56	0.550	95.6	52.6	.0526	2.54×10^{-4}
013	1684	1.53	0.550	95.6	52.6	.0526	2.54×10^{-4}
014	1754	1.60	0.540	107.0	57.5	.0575	2.77×10^{-4}
015	1754	1.60	0.540	95.8	51.7	.0517	2.49×10^{-4}
016	1674	1.52	0.560	101.0	56.5	.0564	2.72×10^{-4}
017	1659	1.51	0.560	101.0	56.5	.0564	2.72×10^{-4}
018	1542	1.39	0.590	101.0	59.5	.0595	2.87×10^{-4}
019	1519	1.37	0.590	96.8	57.1	.0571	2.75×10^{-4}
020	Transient						
021							
022	1570	1.42	0.590	95.8	56.5	.0562	2.71×10^{-4}
023	1660	1.51	0.560	94.5	52.9	.0529	2.55×10^{-4}
024	1014	0.86	0.650	68.5	44.5	.0452	2.18×10^{-4}
025	1104	0.95	0.640	67.6	43.3	.0433	2.09×10^{-4}

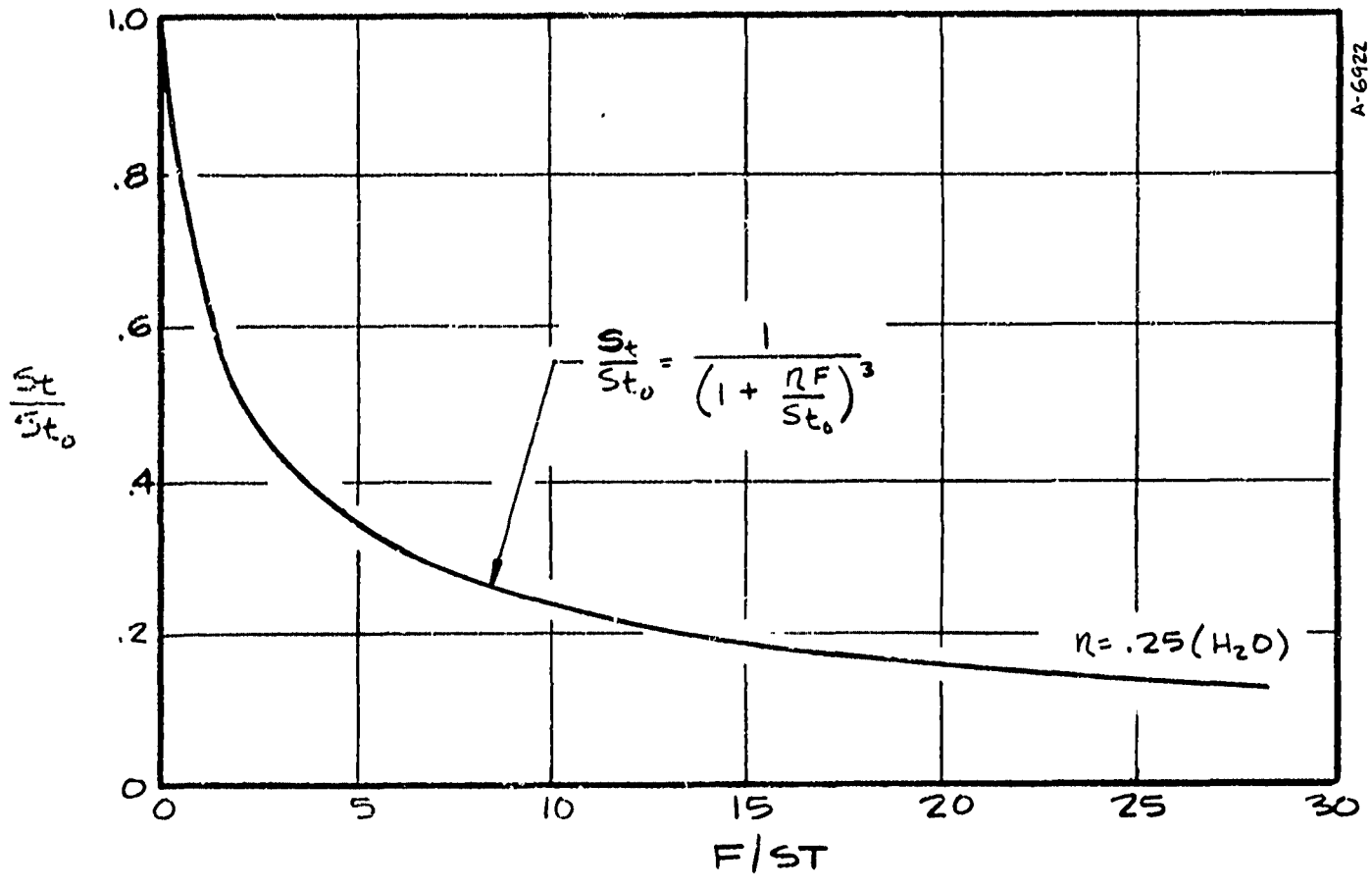

Figure 5-10. Turbulent Flow Heat Blockage for a Flat Plate

$$\dot{m}_{ideal} = \dot{m}''_{ideal} A_I$$

where A_I is the total area of the injection region.

5.5.4 Pyrometer and Slot Indepth Thermocouples

Figure 5-11 presents the surface and in-depth temperatures versus total injection flowrate for all injection modules considered in the test program. There were no subsurface thermocouples in the porous module. During the early portion of the first test run with the S = 1.102 in./L = 0.051 in. DI module, the ANSCAN recorder was inadvertantly shut off so that no data were recorded. When the test points were rerun and recorded no signals were obtained from the vacuum-deposited thermocouples, indicating that they had been destroyed while the ANSCAN was down. Thus, no indepth data was obtained for this slotted module.

An interesting phenomena exhibited by the temperature data is the occurrence of random "hot spots". For instance, during run 015 the surface temperature and intermediate-depth slot temperature reached much higher temperature levels at a given flowrate than in runs 001 and 002 involving the same slot and land sizes and heat flux levels. It will be recalled that the intermediate-depth thermocouple junction is on one side of the common iron leg, while the top and bottom thermocouples are on the opposite side (see Figure 5-9). Apparently, then, coolant nonuniformities within a single slot can be large enough to result in a portion of the slot being relatively uncooled. In addition, the results of runs 016, 017 and 018 indicate that such a hot spot was not necessarily repeatible. During these runs, the heating levels were similar to that of run 015 but all indepth temperatures were lower at a given flowrate.

The hot spot phenomena also occurred for the S = 0.051 in./L = 0.102 in. DI module during runs 009 and 010. In these runs (as in all runs), the pyrometer was aligned over the center slot, as opposed to the aft slot. During run 009, the pyrometer and center-slot thermocouples indicated unusually high temperatures even at the highest flowrate considered. However, in the next run (010) the surviving slot thermocouples indicated much lower temperatures for the same coolant flowrate range.

As indicated in Figure 5-11, the wire thermocouples on the webs consistantly indicated fairly low temperatures. This was most likely due to three factors. First, none of the wire thermocouples was located closer than 0.012 in. from the surface, so that temperatures at the thermocouple location were considerably lower than the surface temperature due to the low thermal conductivity of the

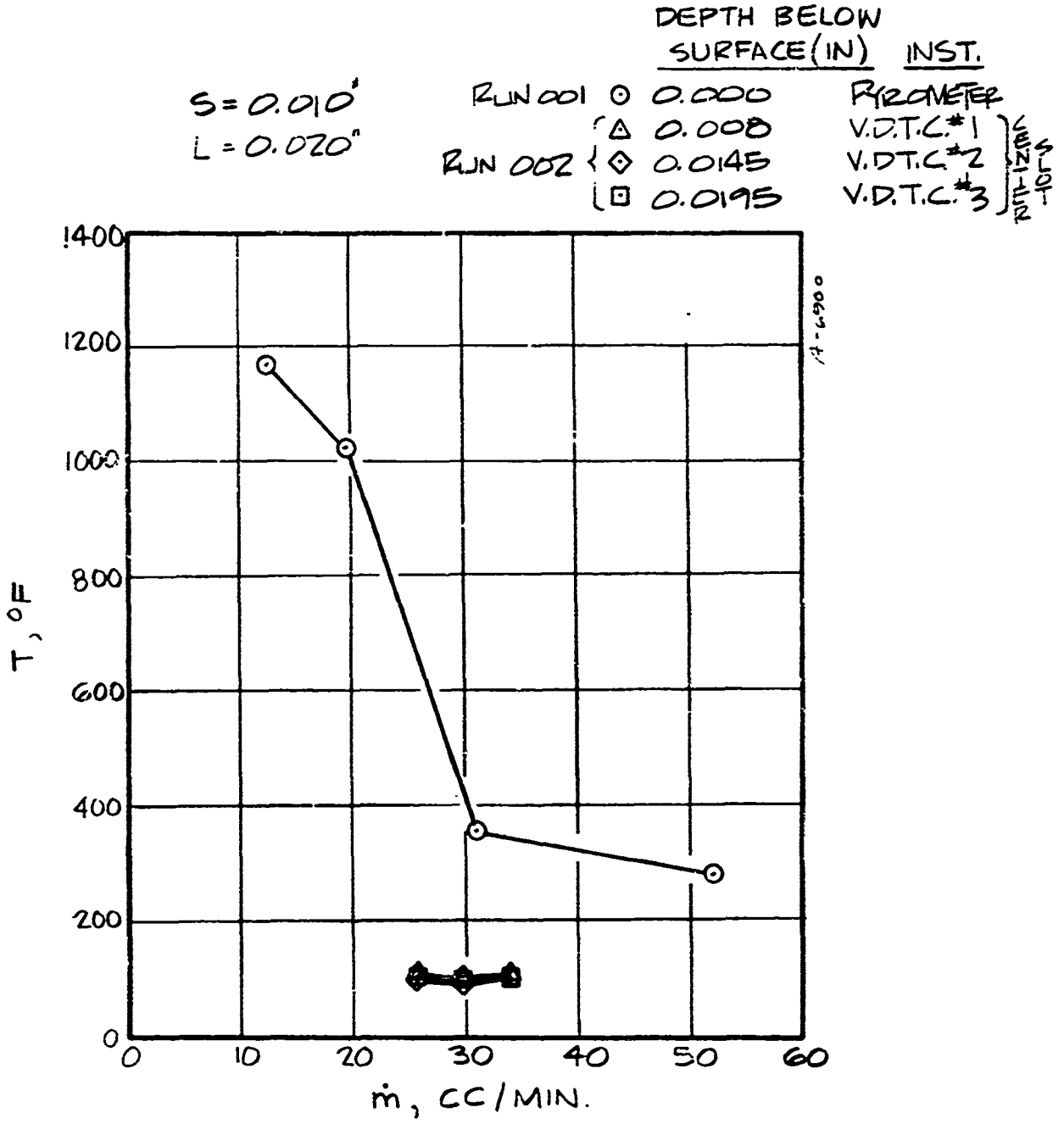

Figure 5-11. Surface and Indepth Temperatures vs. Total Injection Flowrate

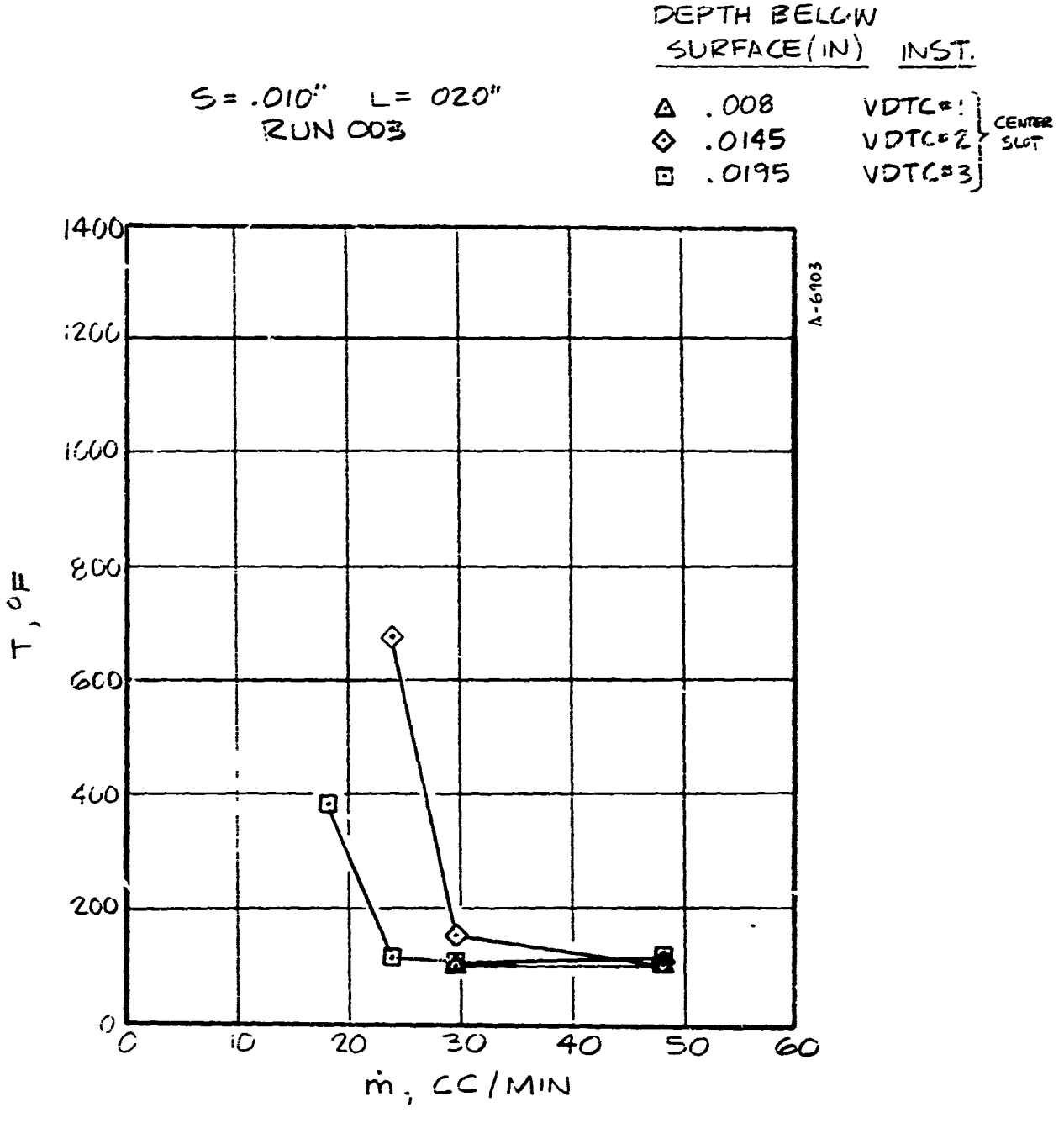

Figure 5-11. Continued

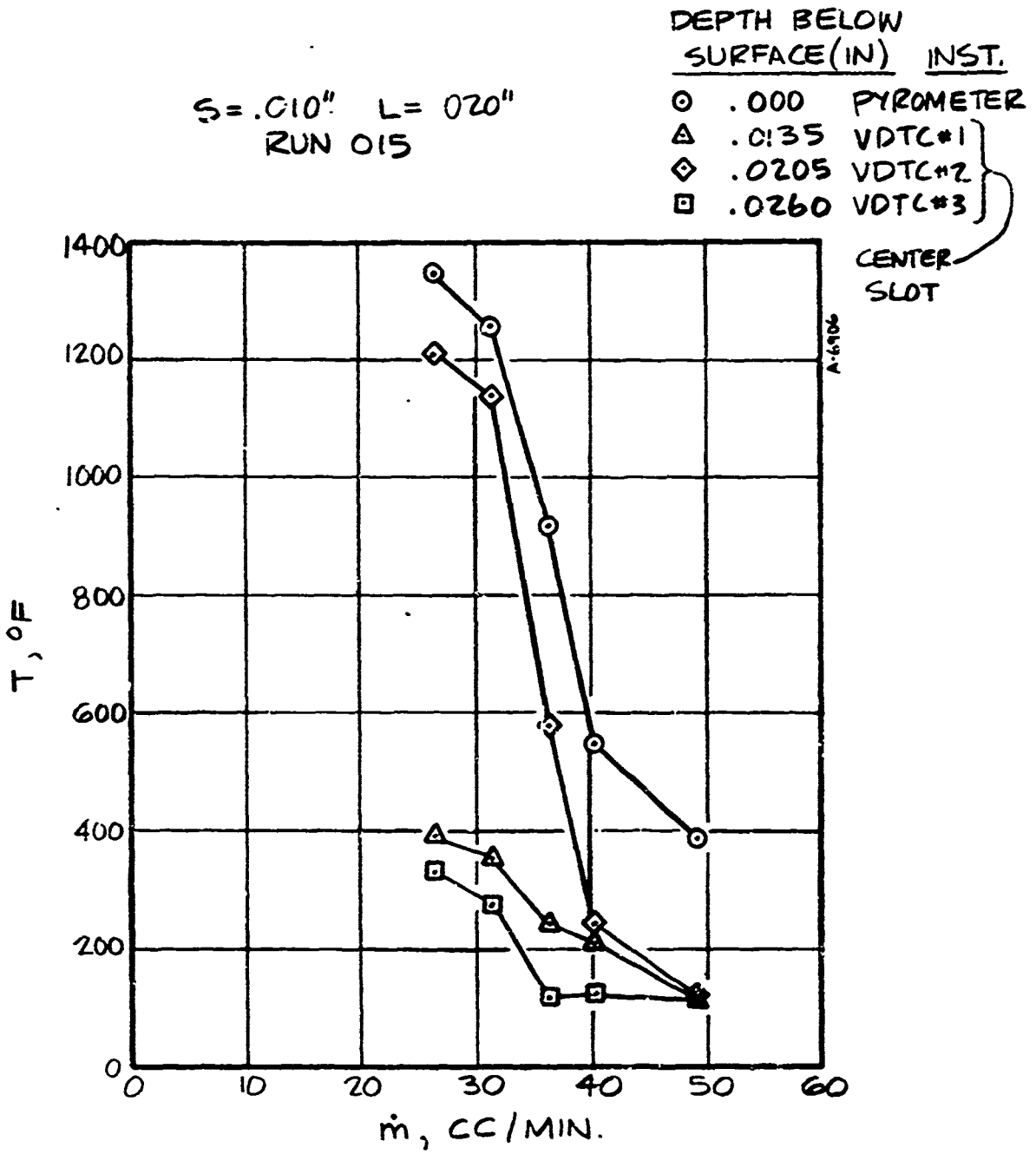

Figure 5-11. Continued

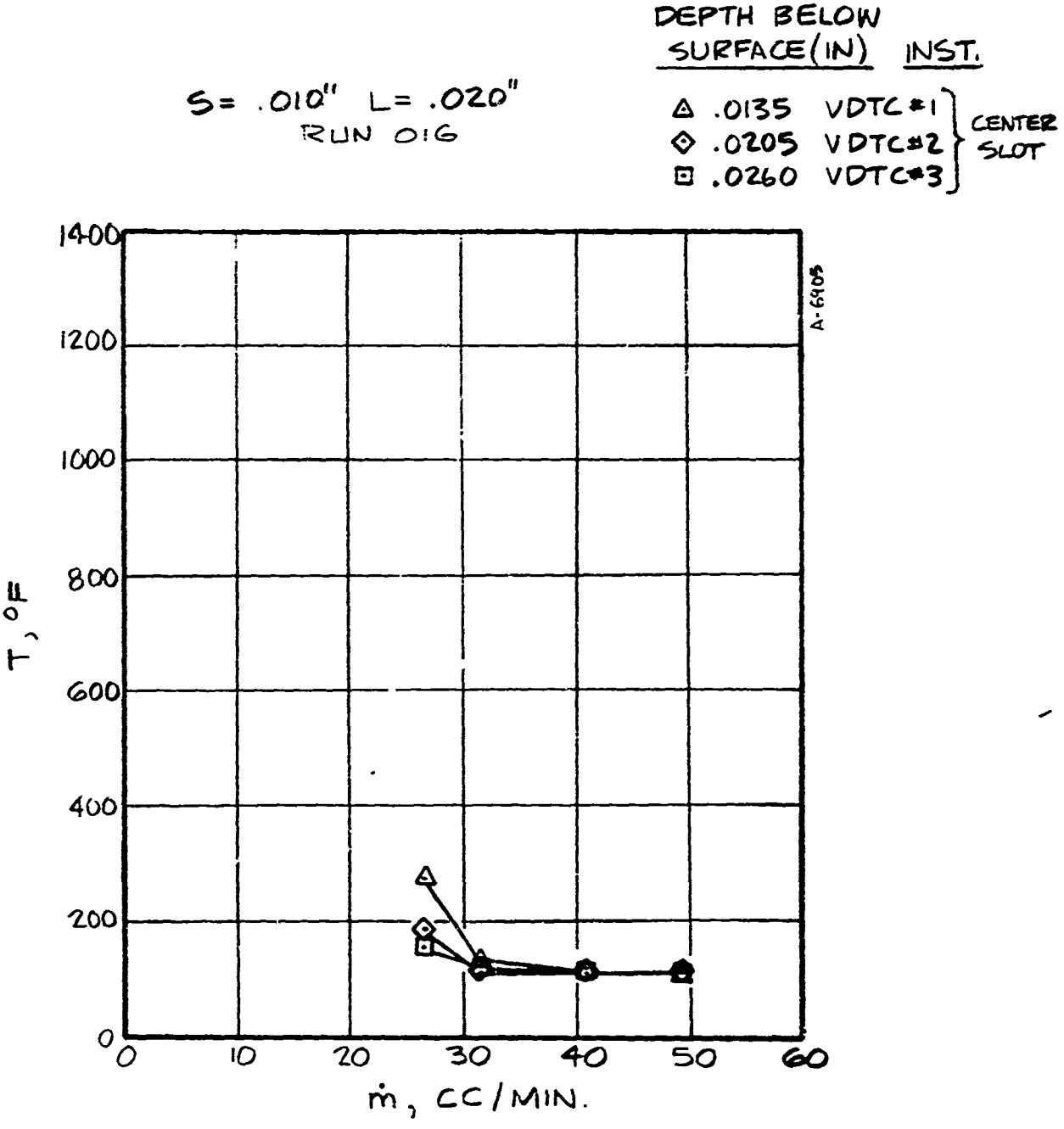

Figure 5-11. Continued

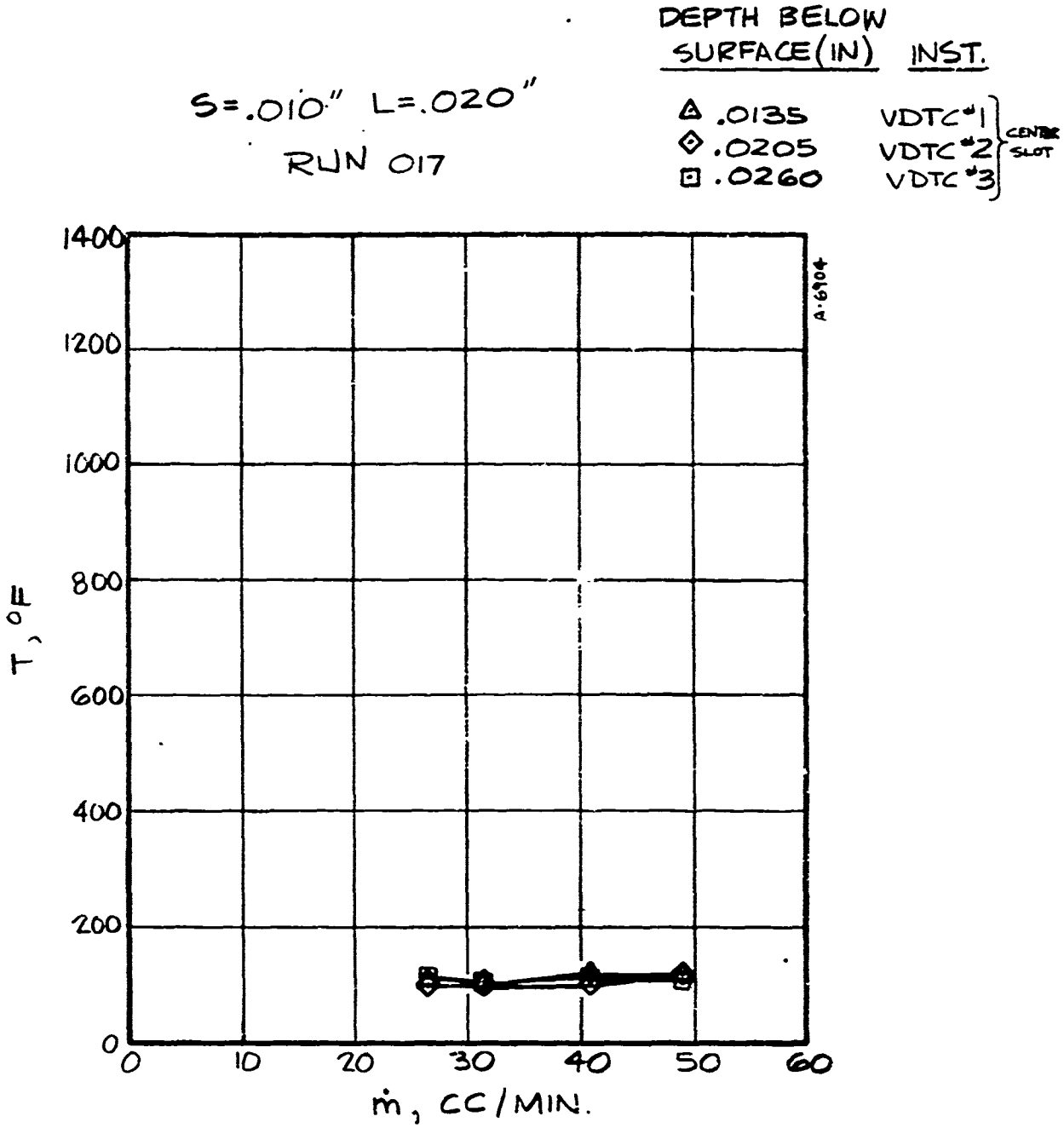

Figure 5-11. Continued

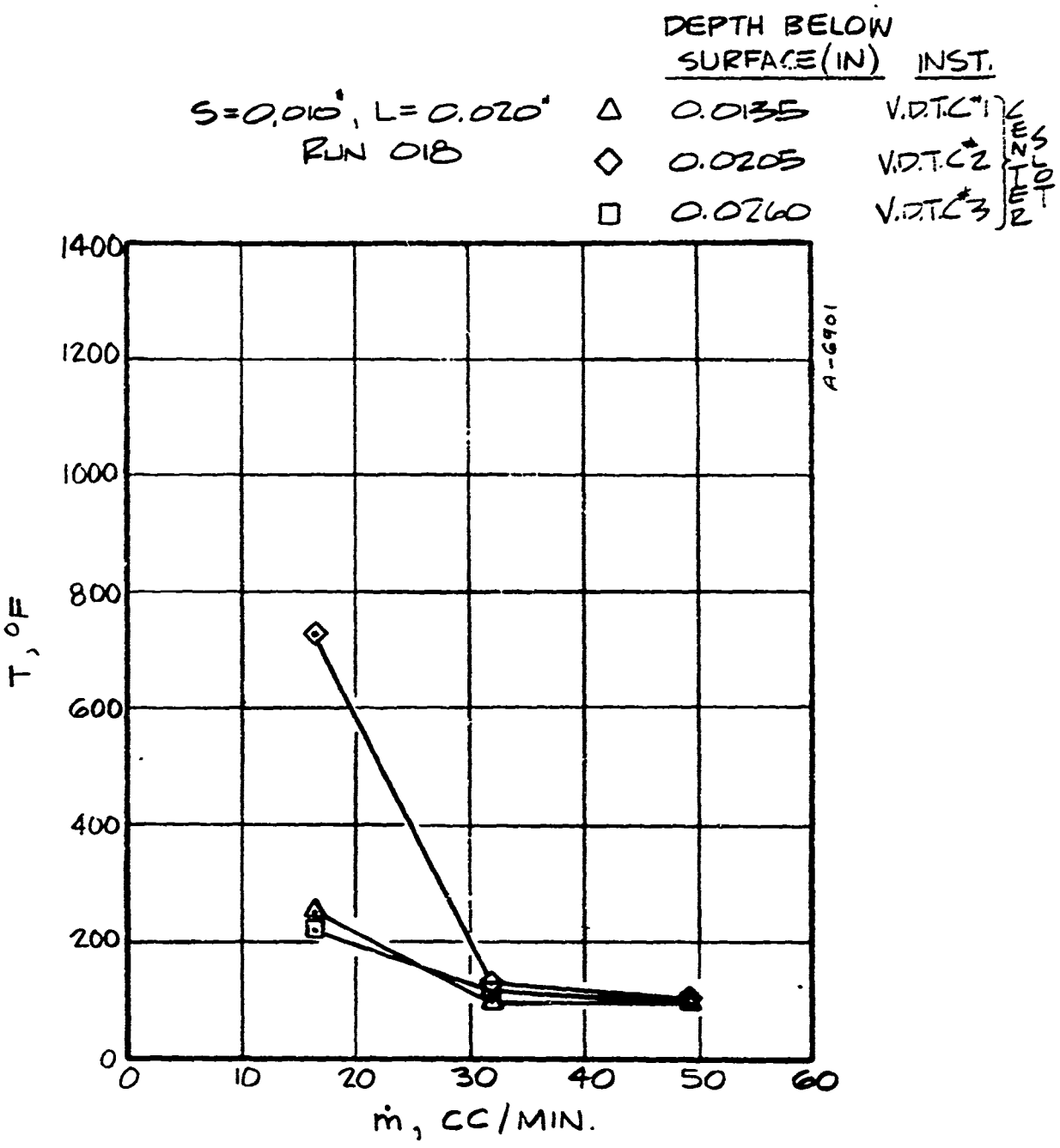

Figure 5-11. Continued

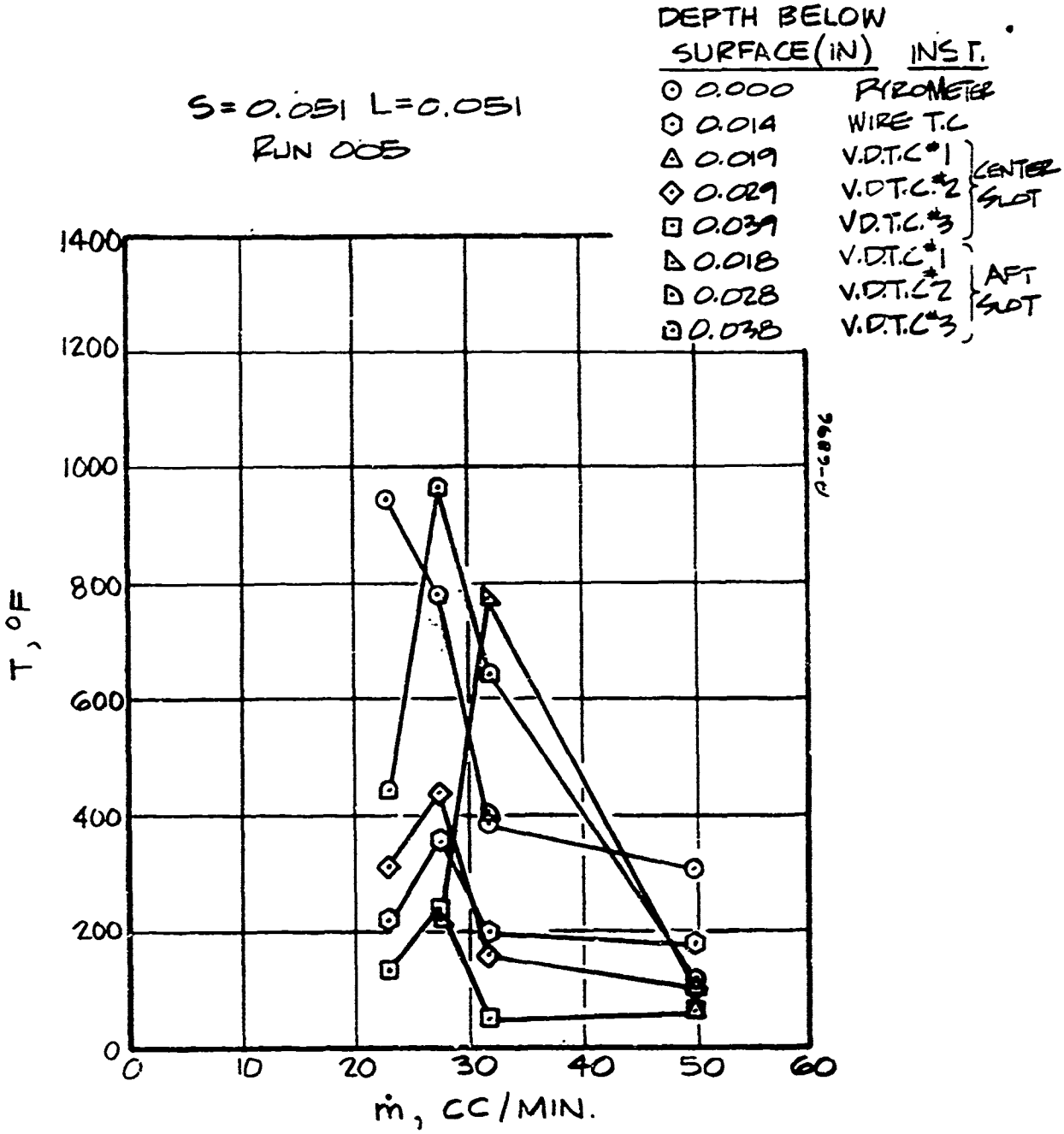

Figure 5-11. Continued

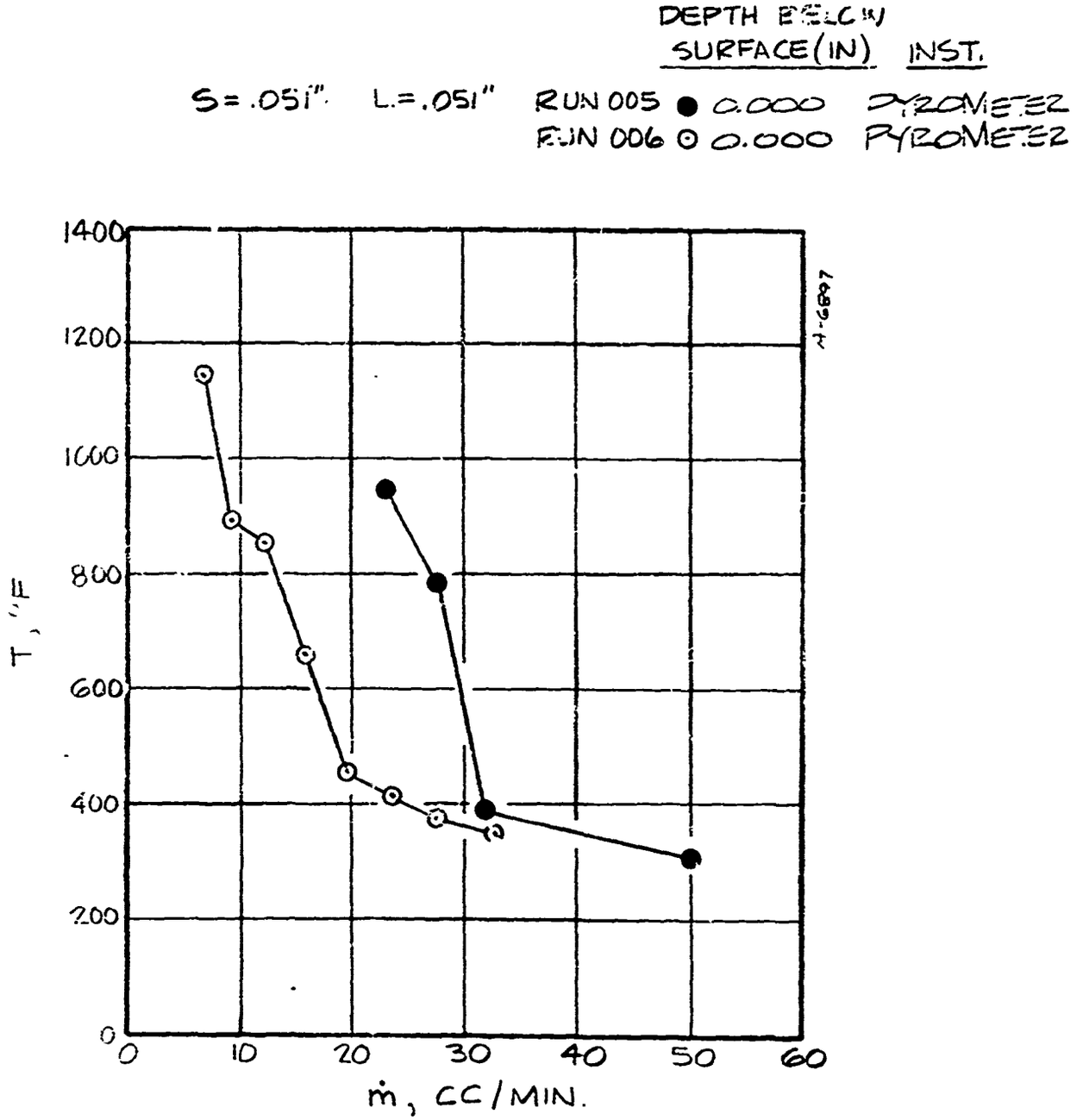

Figure 5-11. Continued

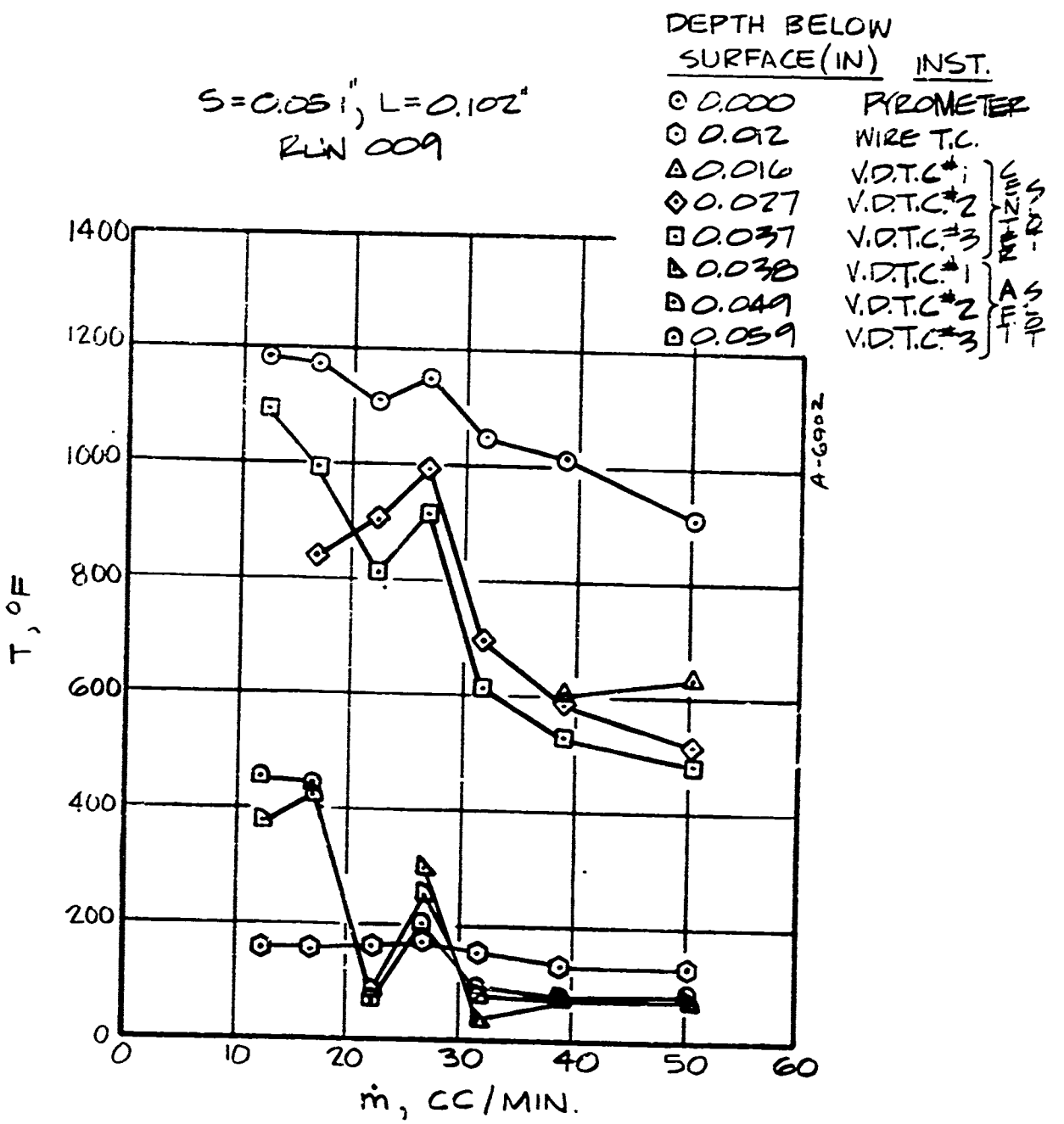

Figure 5-11. Continued

S = .051" L = .102"
RUN 010

	DEPTH BELOW SURFACE (IN)	INST.
⊡	.037	VDTC #3, CENTER SLOT
⊡	.049	VDTC #2, AFT SLOT
⊡	.059	VDTC #3, AFT SLOT

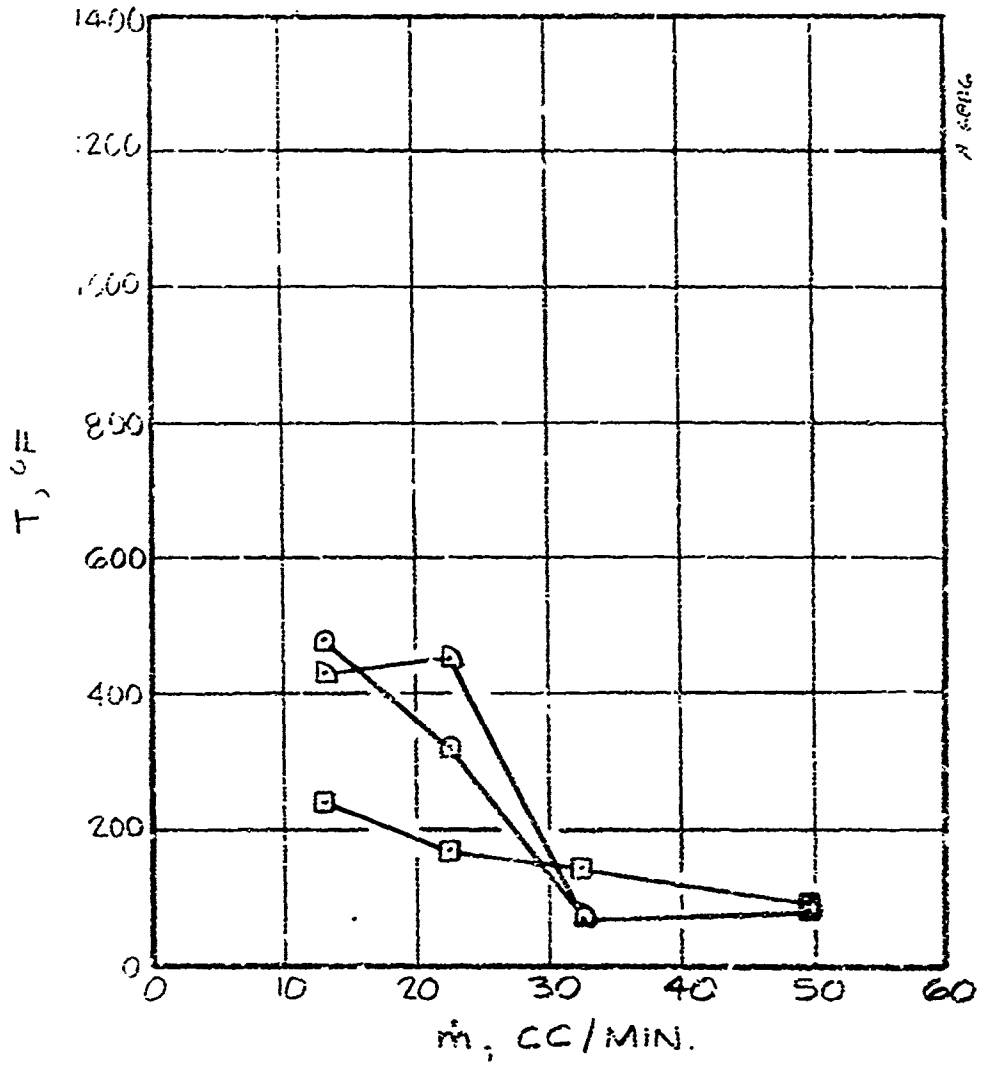

Figure 5-11. Continued

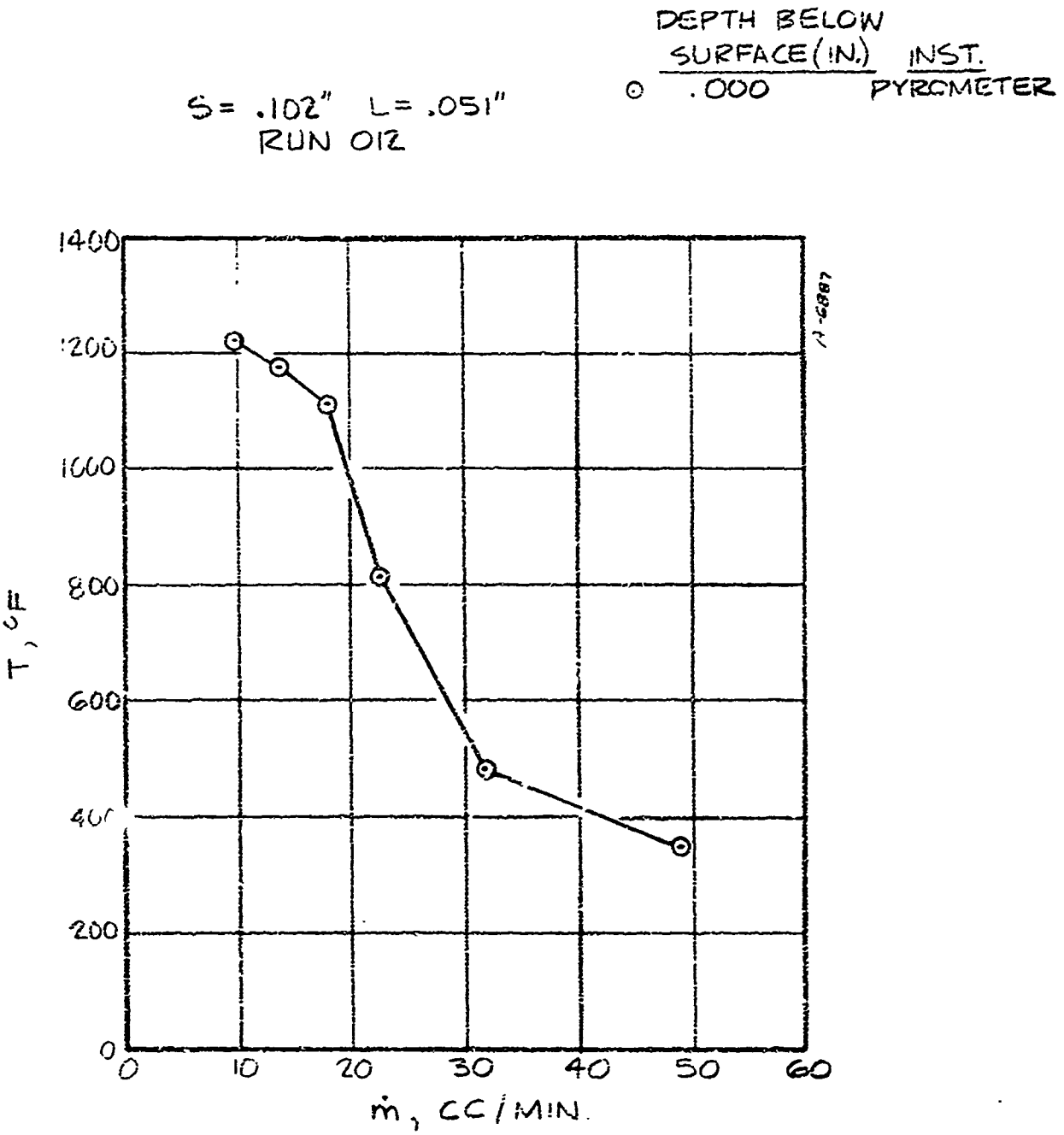

Figure 5-11. Continued

POROUS
RUN 023

DEPTH BELOW SURFACE (IN)	INST.
⊙ .000	PYROMETER

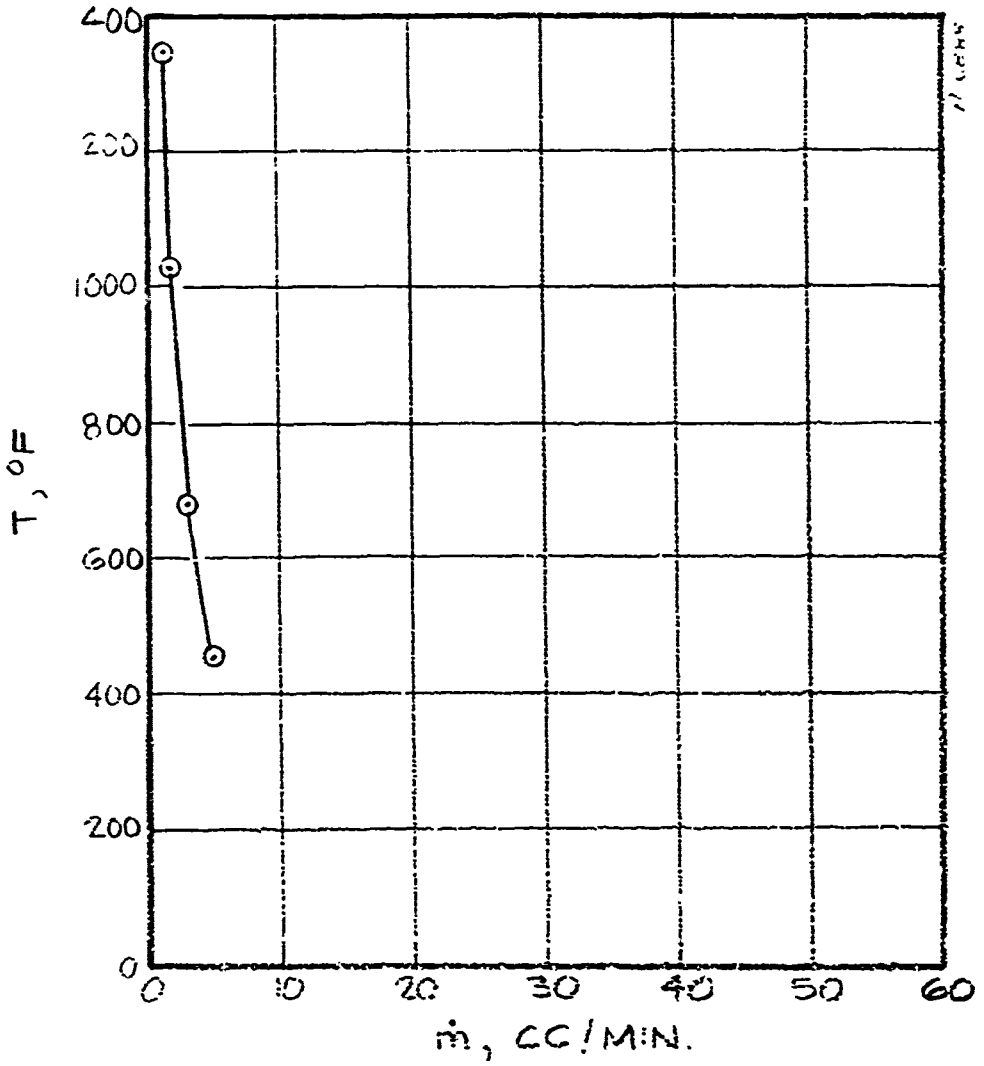

Figure 5-11. Concluded

quartz web. Second, the color photographs (Section 5.4.1) indicated that the coolant tended to adhere to the sides of the webs rather than adhering to some other portion of the slot. Third, the web thermocouples were located some distance from the leading edge of the upstream land, where enhanced heating would be expected. In summary, the web thermocouples appear to have been located in the most shielded and most efficiently cooled region of the DI module.

Figure 5-12 is a plot of the pyrometer data for all injection modules as a function of margin factor M. The margin factor is defined as

$$M = \frac{\dot{m}_{actual}}{\dot{m}_{ideal}}$$

where $\dot{m}_{ideal}$ is taken from Table 5-7 for each test run. In addition, for the S = 0.010 in./L = 01020 in. module, $\dot{m}_{actual}$ is multiplied by the factor 0.7 to account for the metering plate nonuniformity. Due to the definition of $\dot{m}_{ideal}$, the margin factor implicitly accounts for variations in test conditions ($\dot{q}''_c$) from run to run.

A few general conclusions can be made from examination of Figure 5-12. First, the porous module was much more thermally efficient than any of the slotted modules, because much lower injection flowrates were required to give elevated surface temperatures. In fact, the porous module performed very close to theory, since an extrapolation of the T_p (M) curve to $T_p \cong 150°F$ (the water saturation temperature at test conditions) gives a margin factor very close to unity. At this time, the poorer performance of the slotted modules is attributed to augmented heating developed at the injection surface due to its roughness. In addition, the local cooling effectiveness appears to be a function of the degree of surface roughness. If runs 009 and 015 are ignored (since they are identified with the hot spot phenomena discussed above), the remaining pyrometer data indicate that the margin at which a certain low value of T_p is exceeded, say 300°F, increases with increasing effective roughness: porous, S = 0.010 in., S = 0.051 in., and S = 0.102 in. A final observation from Figure 5-9 is that the slope dT_p/dM is significantly steeper for the porous module, indicating that when it does fail, it fails faster than a DI surface.

Figure 5-13 presents most of the slot indepth temperature data contained in Figure 5-12, plotted versus the depth below the surface. The saturation or vaporization temperature of the coolant is also included in Figure 5-13. The main significance of this data is that once the coolant margin drops below 2.0 for the S = 0.010 in./L = 0.020 in. module and 4.0 for the larger-slot module,

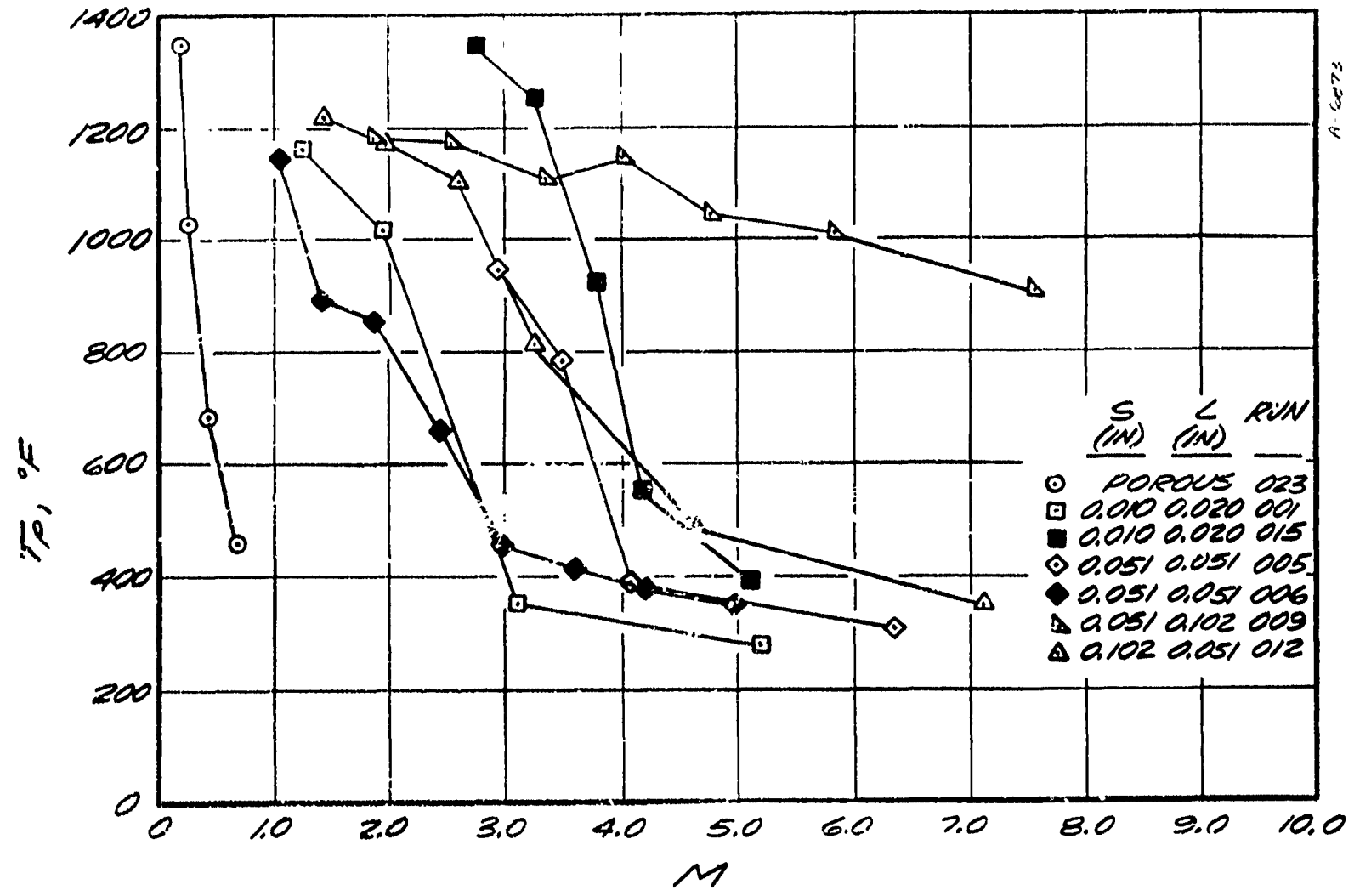

Figure [illegible] surface [illegible]

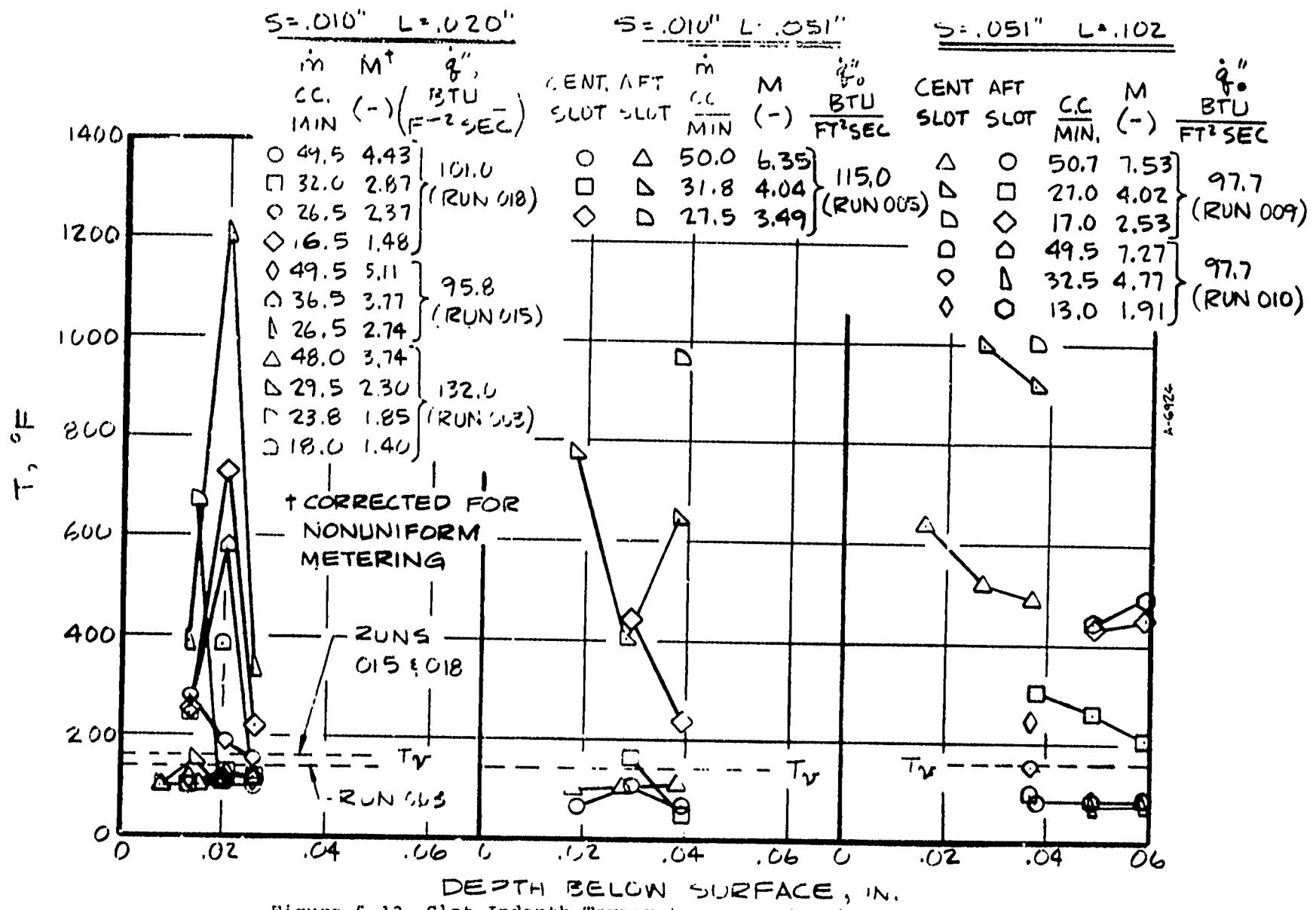

Figure 5-13. Slot Indepth Temperatures vs. Depth Below Surface and Margin Factor

the in-depth temperatures, from 0.008 to 0.060 inches below the surface, are greater than the saturation temperature. If the apparent roughness were not a factor, these temperatures would have remained at or below T_v for $M \geq 1.0$.

5.5.5 Downstream Gardon Gages

Figure 5-14 presents most of the downstream heat flux data taken during the test program. In contrast to the temperature plots presented in the preceding section, the margin factor M for the S = 0.010 in./L = 0.020 in. DI module has not been corrected for local nonuniformities at the injection surface, since the overall average injection rate is the important parameter for downstream cooling.

For the porous and S = 0.010 in./L = 0.020 in. modules, good downstream cooling for 2-3 injection lengths was achieved for $M \geq 2.0$, while for the largest slot module downstream cooling was ineffective even for M = 6.0. Again, the effective roughness at the injection region correlates these findings. Also, it is noted that the peak heating near the leading edge of the downstream module at low values of M appears to increase with effective surface roughness at the injection region.

Figures 5-15 and 5-16 are presented to permit comparison of downstream cooling performance from module to module and to substantiate the conclusions stated above regarding roughness effects. Figure 5-15 shows that at $M \cong 4.5$ the modules with the lowest effective surface roughness provide good downstream cooling, while the rougher modules give downstream heating enhancement up to 1.6 times the cold-wall value. Figure 5-16 shows that at $M \cong 1.0$ none of the modules provide downstream cooling, and the peak heating increases as the effective surface roughness increases. Note that even for the smooth porous module downstream heating is significantly higher than the cold-wall value. This is due to the fact that the downstream module is water-cooled so that its surface is relatively cold, while the surface at the injection region is hot. It can be shown that a hot upstream running length results in enhanced heating from the boundary layer when it reaches the cooled surface. The relaxation length over which the heat flux decays to the cold-wall level appears to be three to four injection lengths.

5.5.6 Photography

5.5.6.1 Color

Figure 5-17 contains a matrix of color photographs taken during the test program. These photographs illustrate the appearance of the DI surface and the coolant in the vicinity of the slot exits under various flowrate conditions,

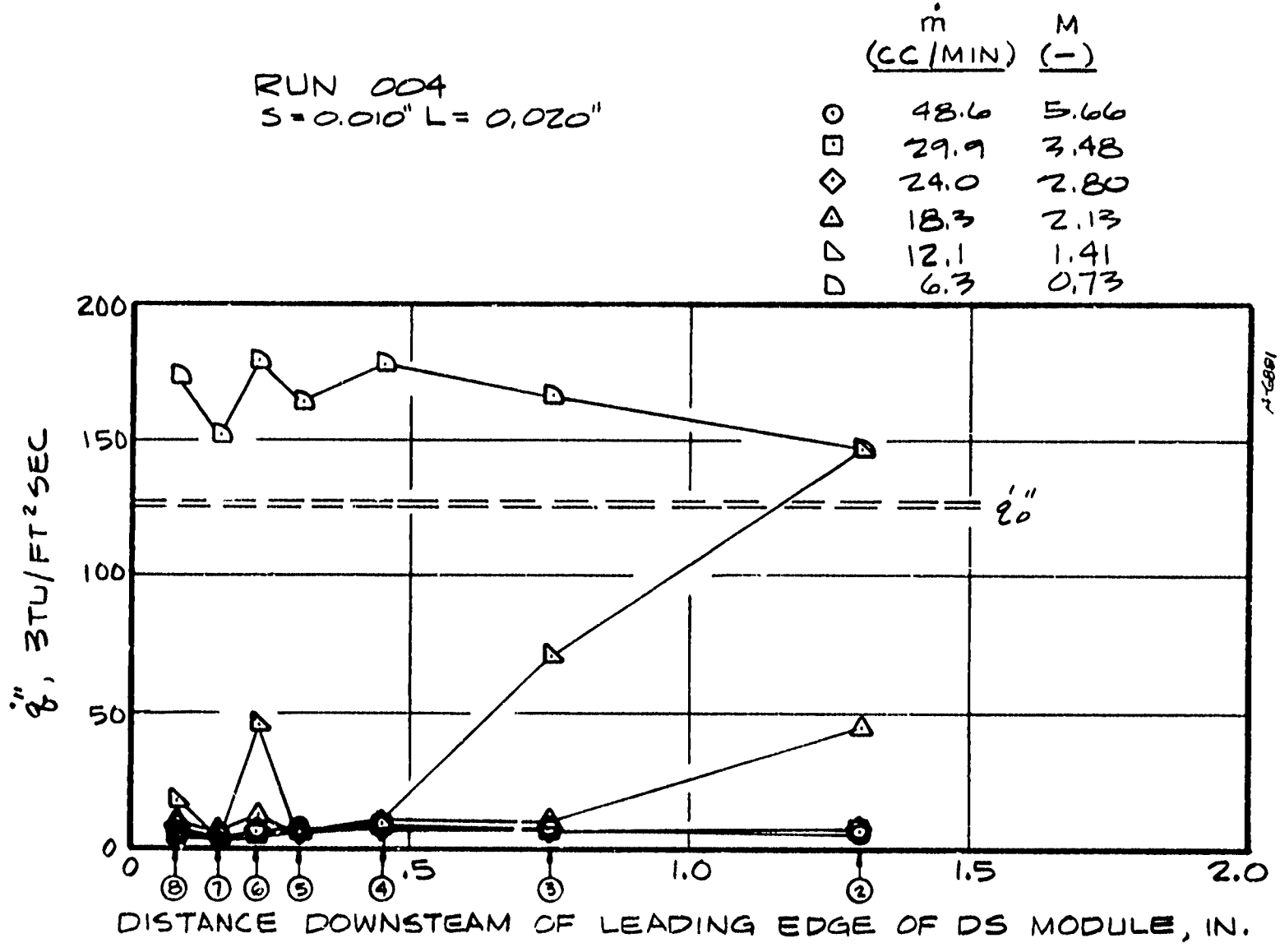

Figure 5-14. Downstream Heat Flux Distribution versus Margin Factor

RUN 018
S = .010" L = .020"

	$\dot{m}$ (CC/MIN)	M (–)
⊙	49.5	6.33
⊡	32.0	4.10
◇	16.5	2.11
△	7.0	.89

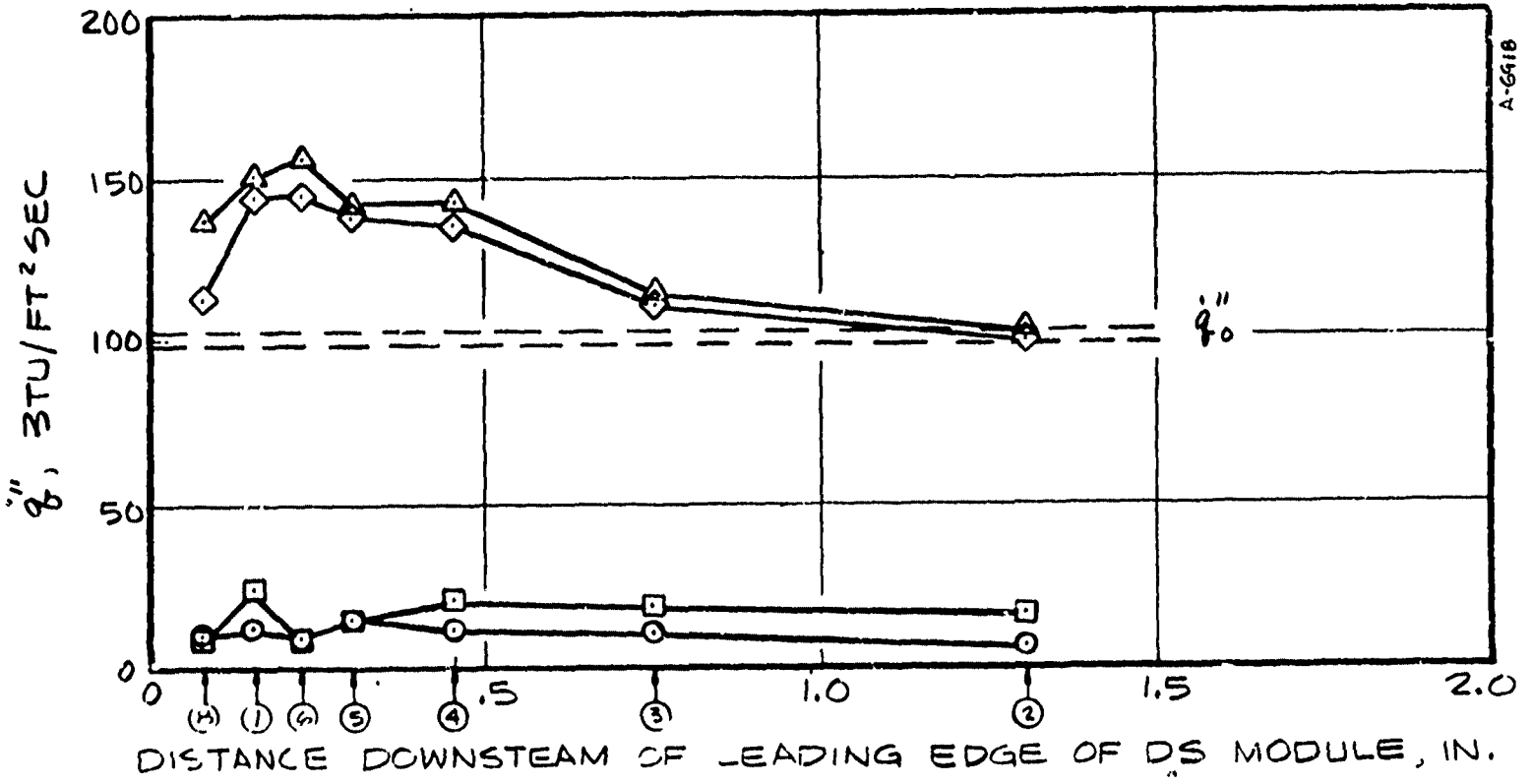

Figure 5-14. Continued

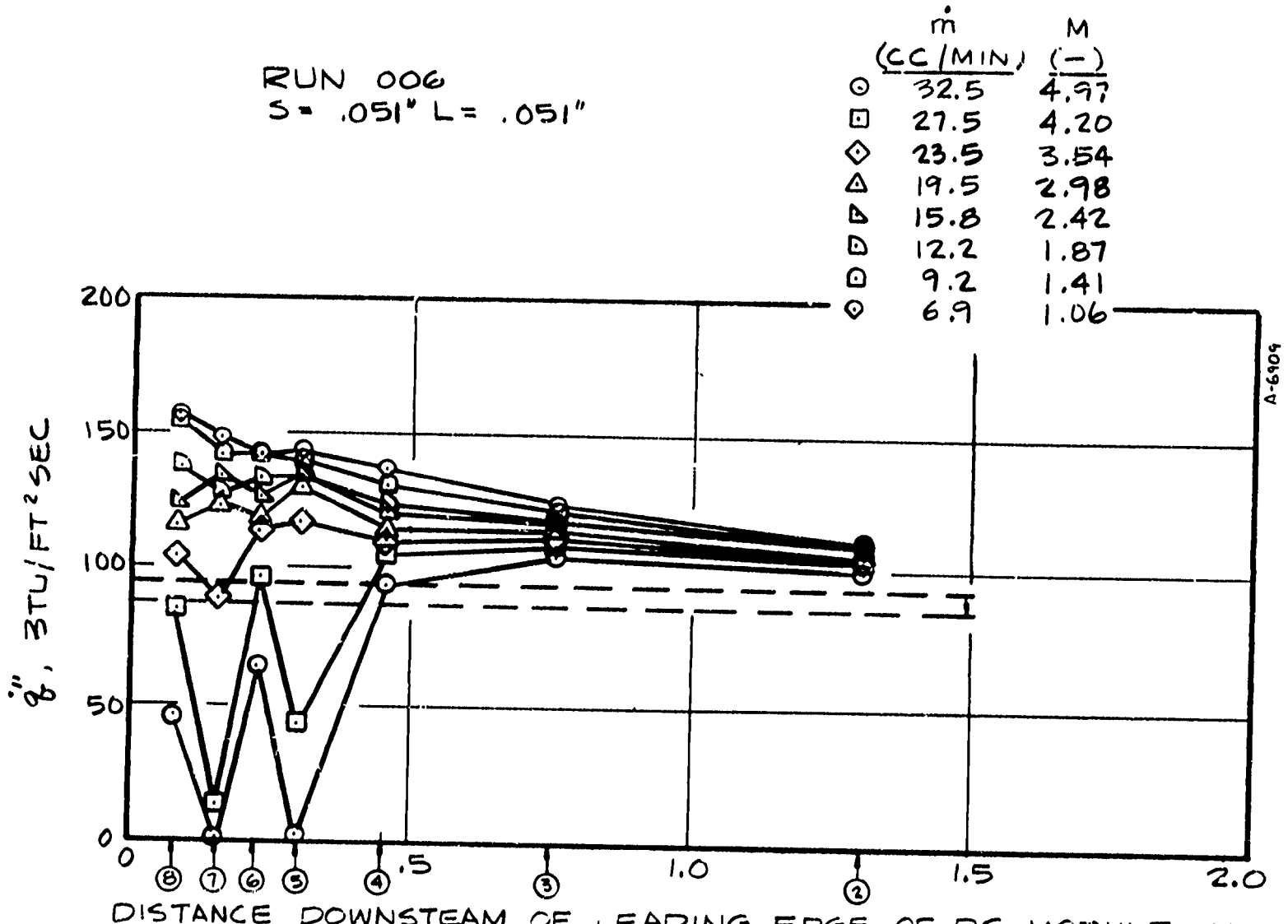

Figure 5-14. Continued

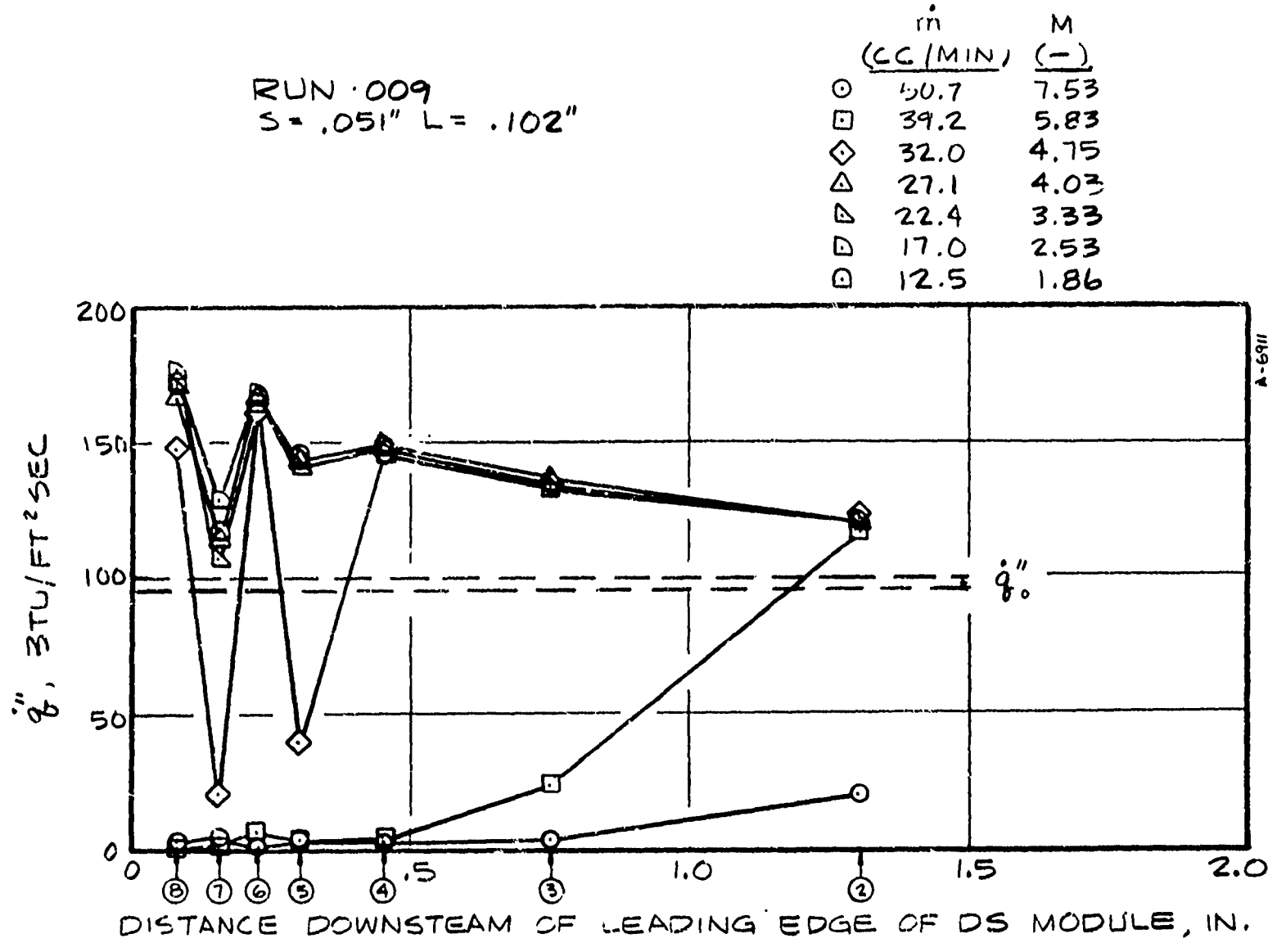

Figure 5-14. Continued

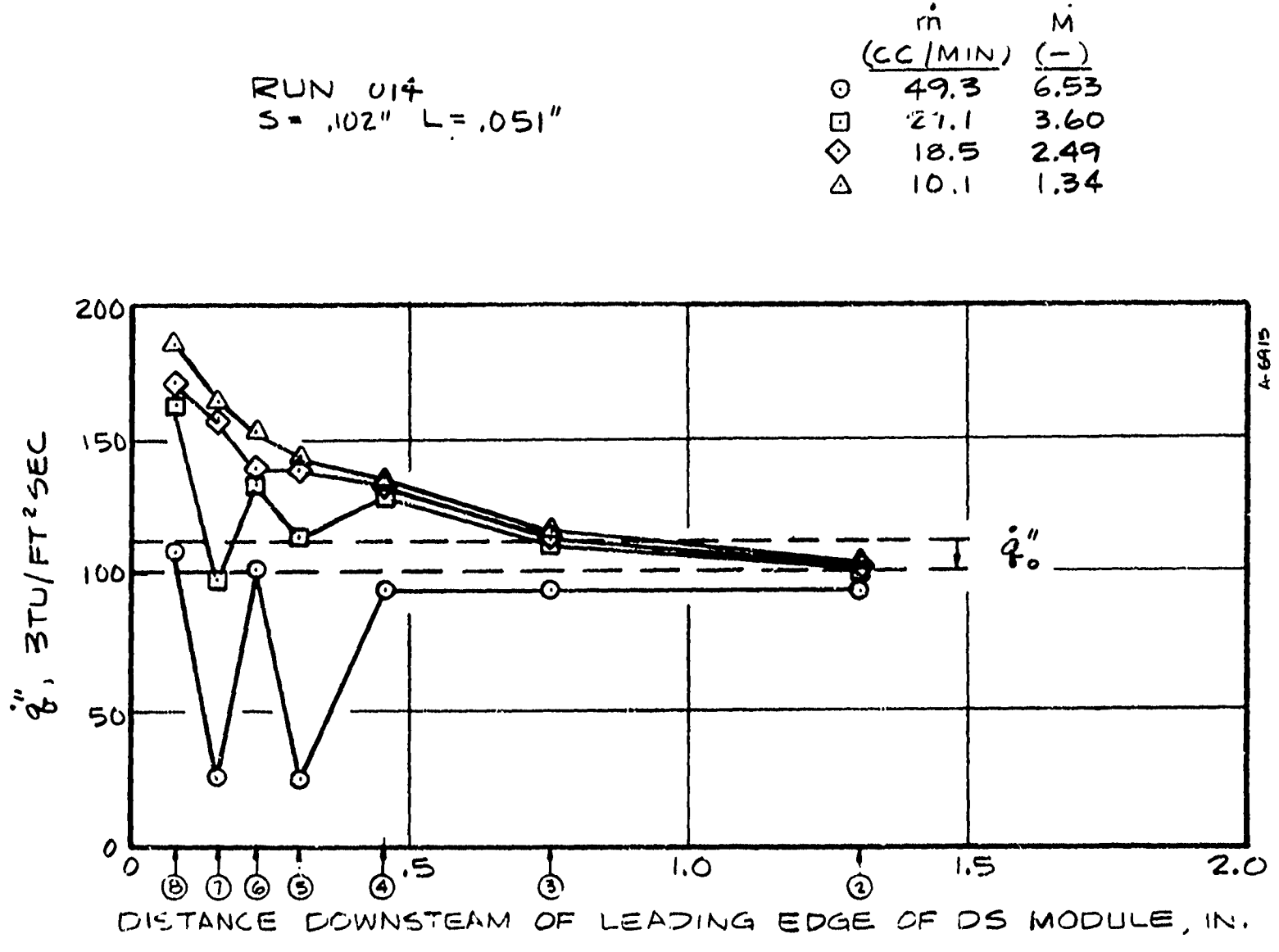

Figure 5-14. Continued

RUN 022
POROUS

	$\dot{m}$ (CC/MIN)	M (−)
○	51.1	6.92
□	40.0	5.41
◇	24.0	3.25
△	6.9	.93
▷	4.8	.65

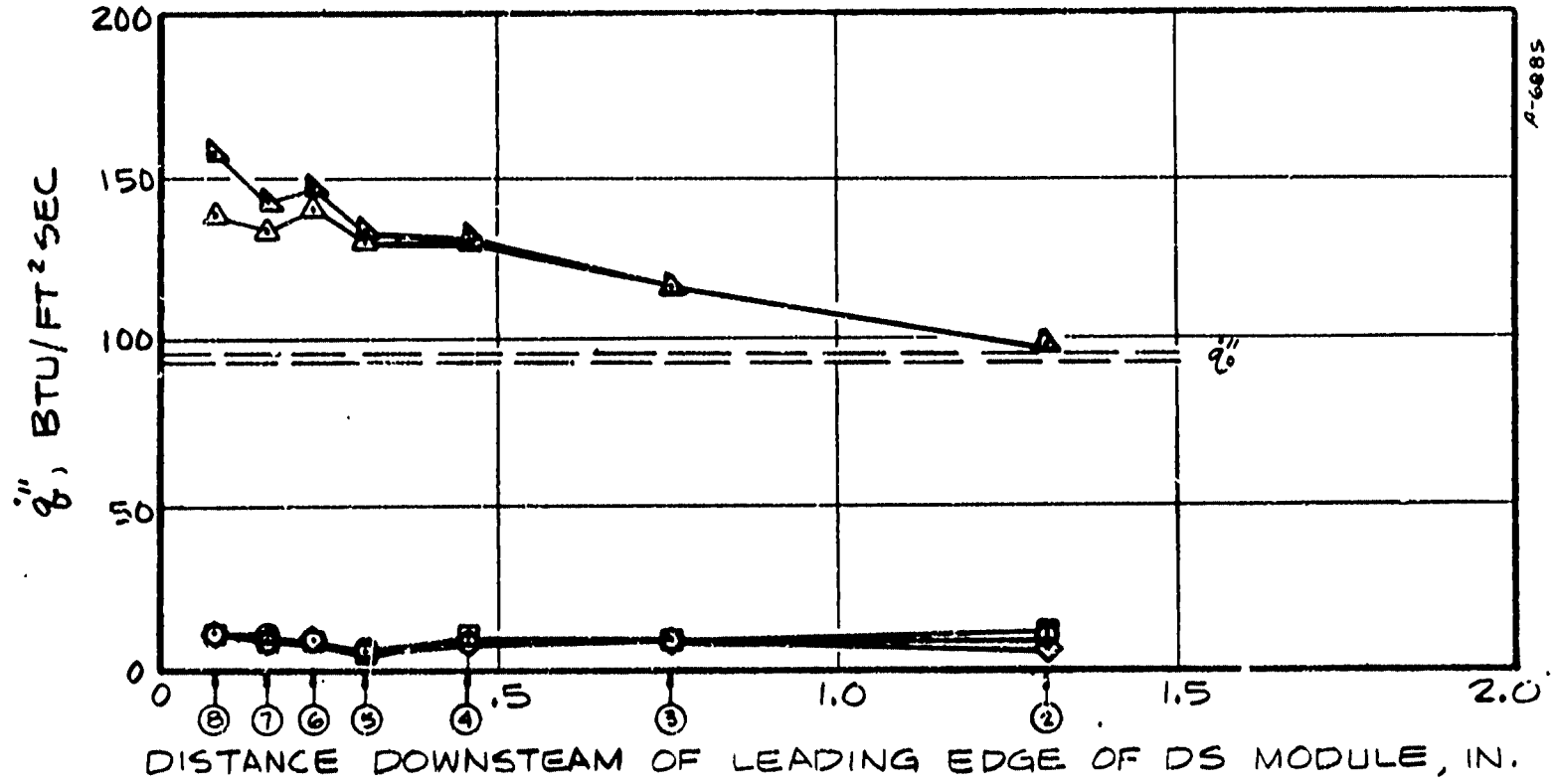

Figure 5-14. Continued

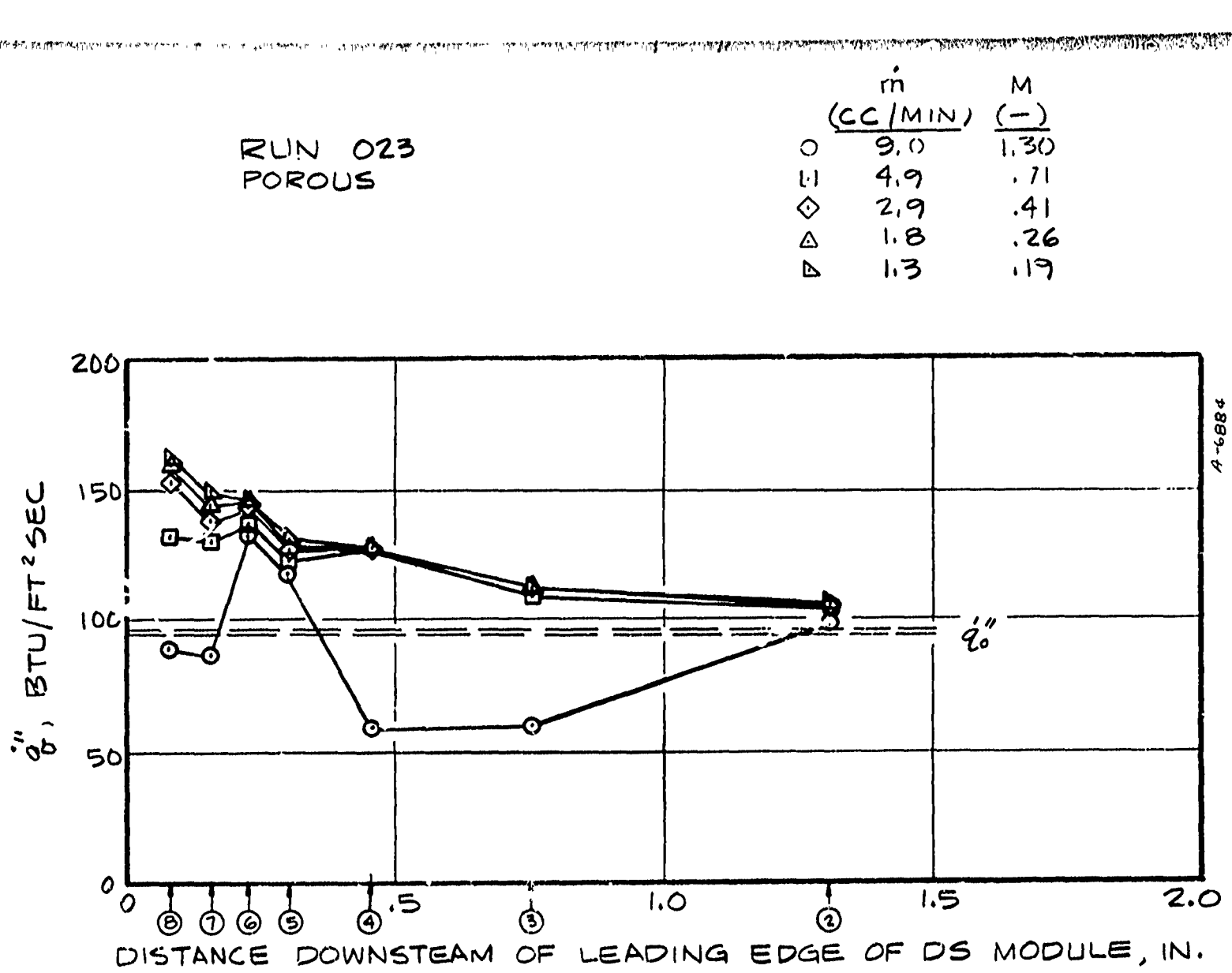

Figure 5-14. Concluded

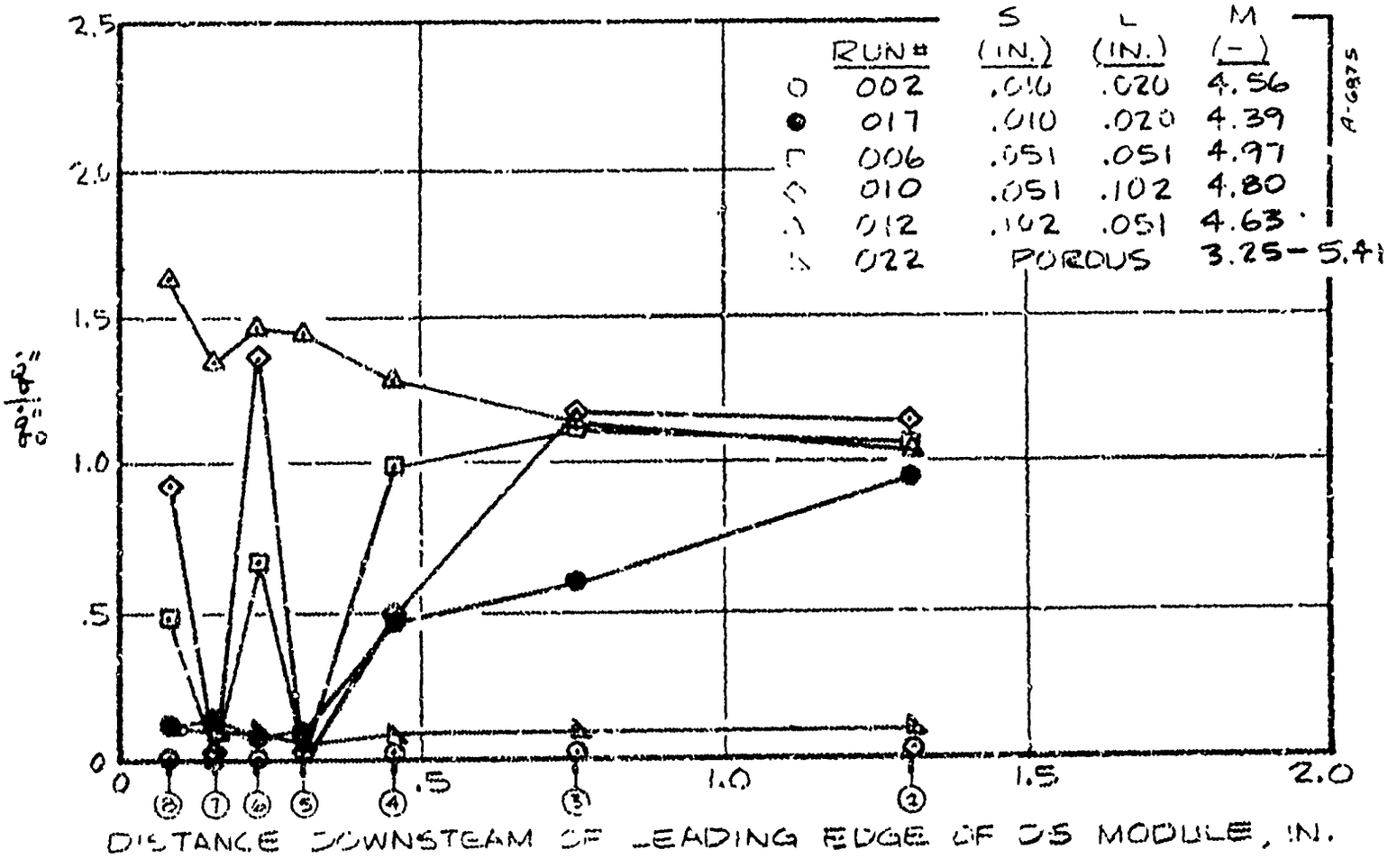

Figure 5-17. Normalized Downstream Heat Flux Distributions at M = 4.5

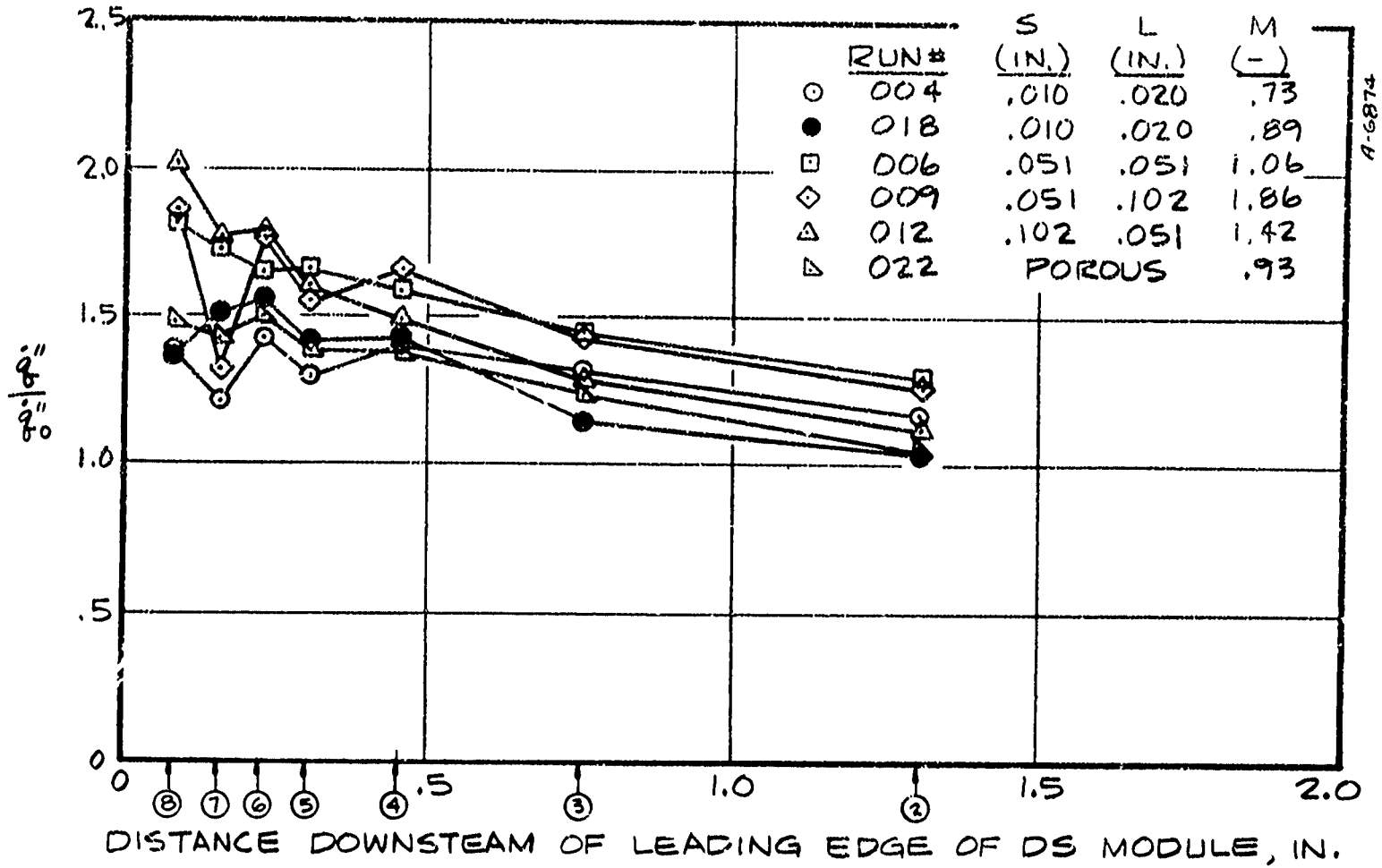

Figure 5-16. Normalized Downstream Heat Flux Distributions at M ≅ 1.0

AEROTHERM
ACUREX Corporation

COMBINED COOLING-
COLOR SLIDE PHOTOGRAPHY

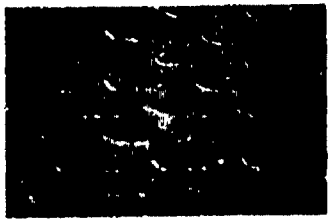

NO FLOW

NO FLOW

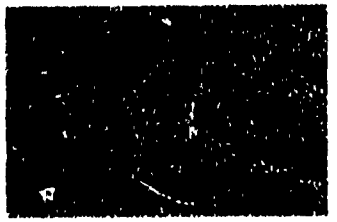

NO FLOW

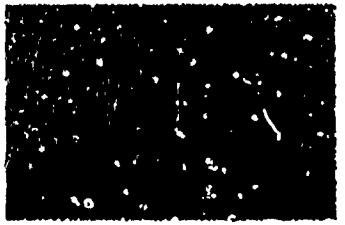

NO FLOW

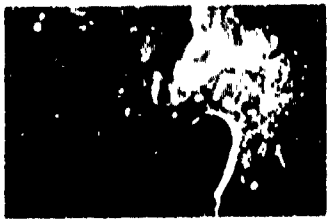

COLD FLOW

COLD FLOW

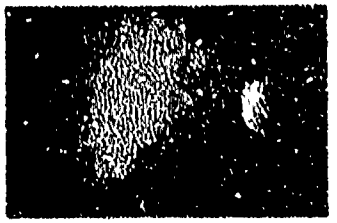

COLD FLOW

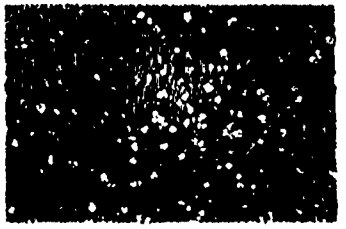

COLD FLOW

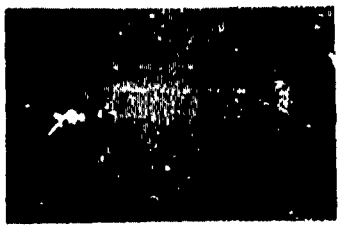

M=6.5

M=3.0

M=7.0

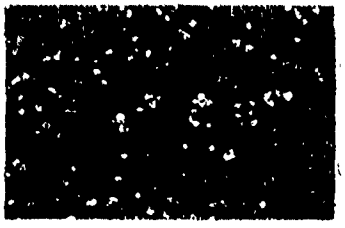

M=6.5

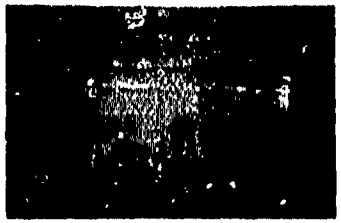

M=6.5

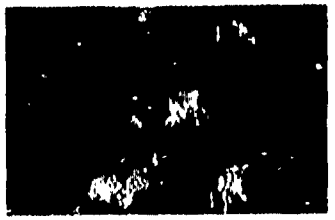

M=8.0

M=7.0

M=6.5

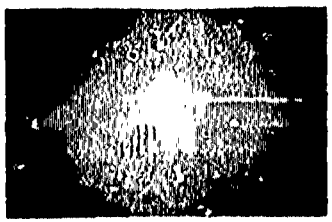

M=4.0

M=3.5

M=3.5

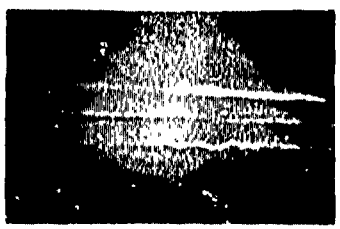

M=2.0

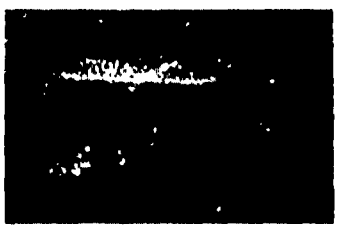

M=2.0

M=2.5

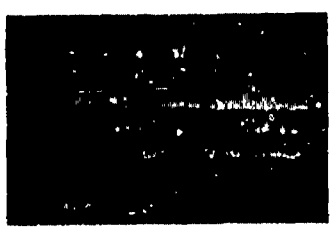

M=1.0

M=1.0

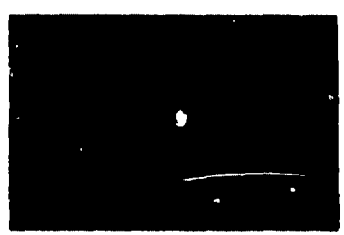

M=1.5

AEROTHERM
ACUREX Corporation

COMBINED COOLING INFRARED PHOTOGRAPHY

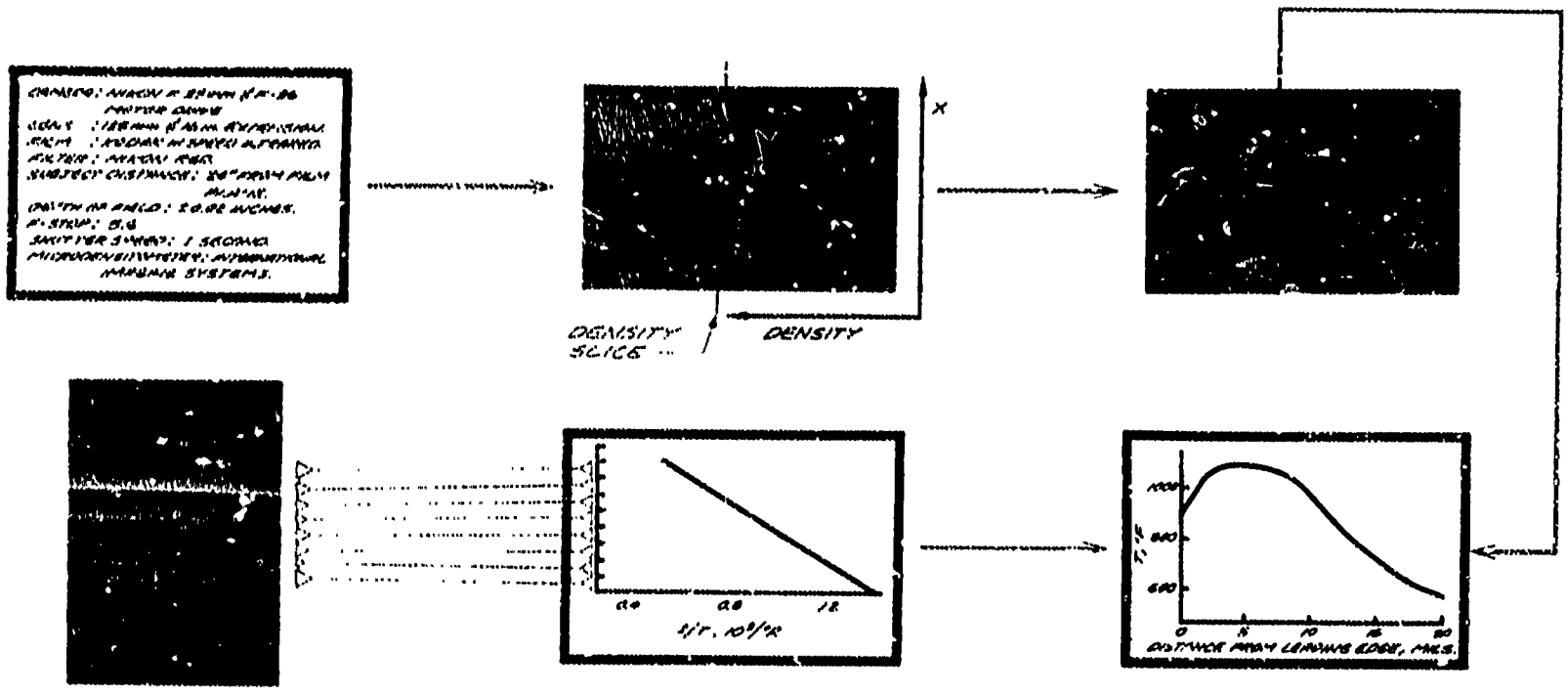

S=.010
L=.020

S=.051
L=.051

S=.051
L=.102

S=.102
L=.051

M=7.0

M=3.0

M=7.5

M=7.0

M=4.5

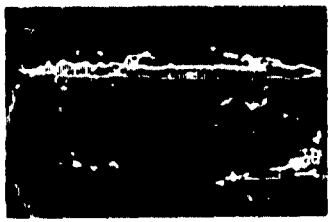

M=2.0

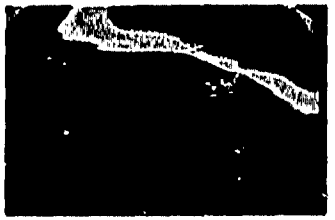

M=5.0

M=4.0

M=2.0

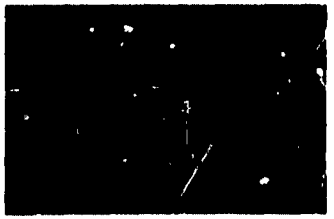

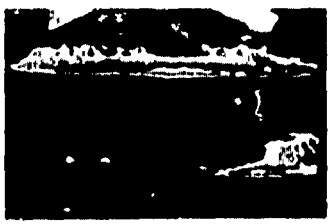

M=1.5

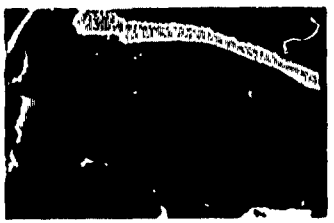

M=3.5

M=2.5

FLOW DIRECTION

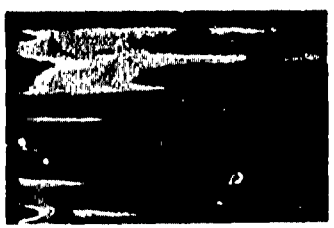

M=1.0

M=1.0

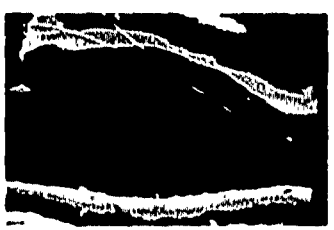

M=2.0

M=1.5

ranging from zero coolant flowrate and injection at a high margin factor into a cold test stream, to injection over a range of margin factors into a hot test stream. The photographs reveal that under no conditions, including injection into a cold test stream, is a smooth liquid layer formed. At high margins with a hot test stream, the coolant appears to have been entrained into the boundary layer in the form of a mist or tiny liquid-phase droplets. Also, at high margins and with $S \geq 0.051$ in., the liquid-phase coolant below the slot exit plane did not entirely fill the slot. Rather, "threads" of liquid coolant usually attached themselves to the webs separating adjacent slots. As the margin decreased to 3.5 - 4.0, evidence of mist entrained into the boundary layer diminishes, implying that all coolant entering the boundary layer is in the gaseous phase. At M = 1.0 - 1.5, there is no evidence of liquid-phase coolant above or even to some distance below the slot exits, and the red-hot appearance of the lands indicates they reached elevated temperatures (as substantiated by the pyrometer data).

A limited number of color photographs were also obtained for the porous module (see Figure 5-20 below). They indicate that at M = 1.5 a smooth liquid layer is not formed even over a smooth porous surface.

5.5.6.2 Infrared

Figure 5-18 contains a matrix of color-enhanced infrared photographs taken during the test program. Also included is a schematic of the procedures used both to obtain the color-enhanced "thermal maps" and to use them for arriving at a quantitative estimate of land temperature distributions. These procedures are also discussed in Reference 10.

The calibration curve presented in Figure 5-18 is used to make a quantitative interpretation of the color-enhanced infrared photographs. The calibration was obtained using the pyrometer data for the indicated test runs. A ±15 percent uncertainty has been attached to this calibration curve.

Several general conclusions can be stated based upon Figure 5-18. In general, there were gross, or large-scale, nonuniformities in the surface temperature distributions at low coolant margins. This was due to uneven coolant distribution within a single slot for the larger-slot modules and uneven slot-to-slot metering for the S = 0.010 in./L = 0.020 in. module. As a rule, the web separating two adjacent slots was the coolest region on the surface. This was most likely due to two effects: the color photographs indicate the coolant in the slots tends to adhere to the sides of the webs, and the web does not have an exposed leading edge which experiences enhanced heating like that which occurs on the lands. A final observation is that very small scale surface imperfections experience enhanced heating.

Figure 5-19 presents illustrative land surface temperature distributions obtained to date. Locations on the photographs where slot coolant distributions were fairly uniform were selected for analysis (these locations are noted on Figure 5-18). Three features are evident in Figure 5-19: The peak temperature was slightly downstream of the leading edge, the smaller land had steeper temperature gradients, and the decay in the direction downstream from the peak temperature is nearly linear.

Figure 5-20 includes color-enhanced infrared photographs of the porous module surface. The main conclusion to be drawn from these thermal maps is that, like the DI modules, large scale nonuniformities in surface temperature occured at the low coolant margin factors, because of coolant nonuniformities at the surface.

5.5.7 Teflon Models

Teflon models were tested during runs 022 and 023. The test duration in each case was approximately 30 seconds with an initial 15 second transient. Post test examination of these models indicated recession patterns very similar to those obtained in the study described in Reference 36. It is therefore concluded that heating nonuniformities did not exceed ±10 percent over the injection or downstream modules.

5.5.8 Correlations and Comparison with Flight Data

Two correlations based upon the Combined Cooling experimental data were derived to substantiate conclusions already mentioned above relating to roughness effects. Figure 5-19 is a plot of the margin factor for which the pyrometer-indicated temperature is 300°F, versus the equivalent sand grain roughness of the corresponding injection surface. The roughness parameter K_s is defined in the Appendix of this report. The essence of this correlation is that with increasing surface roughness the coolant flowrate required to keep the surface at 300°F increases very rapidly at first and then approaches an asymptotic value of about 9.0.

Figure 5-21 is a similar threshold margin plot. The "downstream threshold" is defined as the point at which most of the Gardon gages change from indicating low heat fluxes (~10 Btu/ft^{2}sec) to indicating high heat fluxes (~100 Btu/ft^{2}sec). As demonstrated in Figure 5-14, this decrease in downstream cooling effectiveness occurs over a relatively narrow coolant flowrate range. The curve of Figure 5-22 resembles that of Figure 5-21, with an apparent asymptotic threshold margin factor of about 9.0.

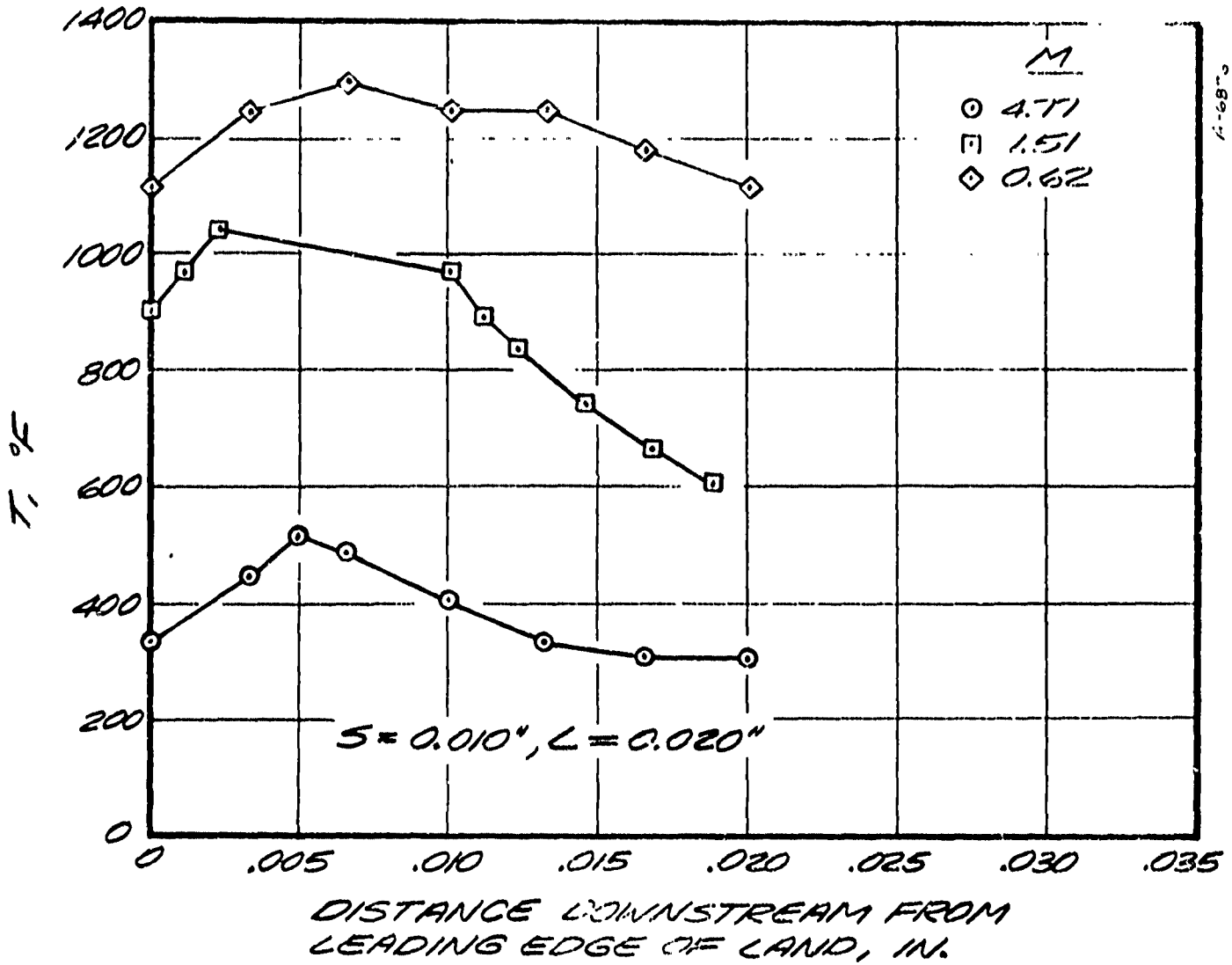

Figure 5-19. Land Temperature Distributions (from Infrared Photography)

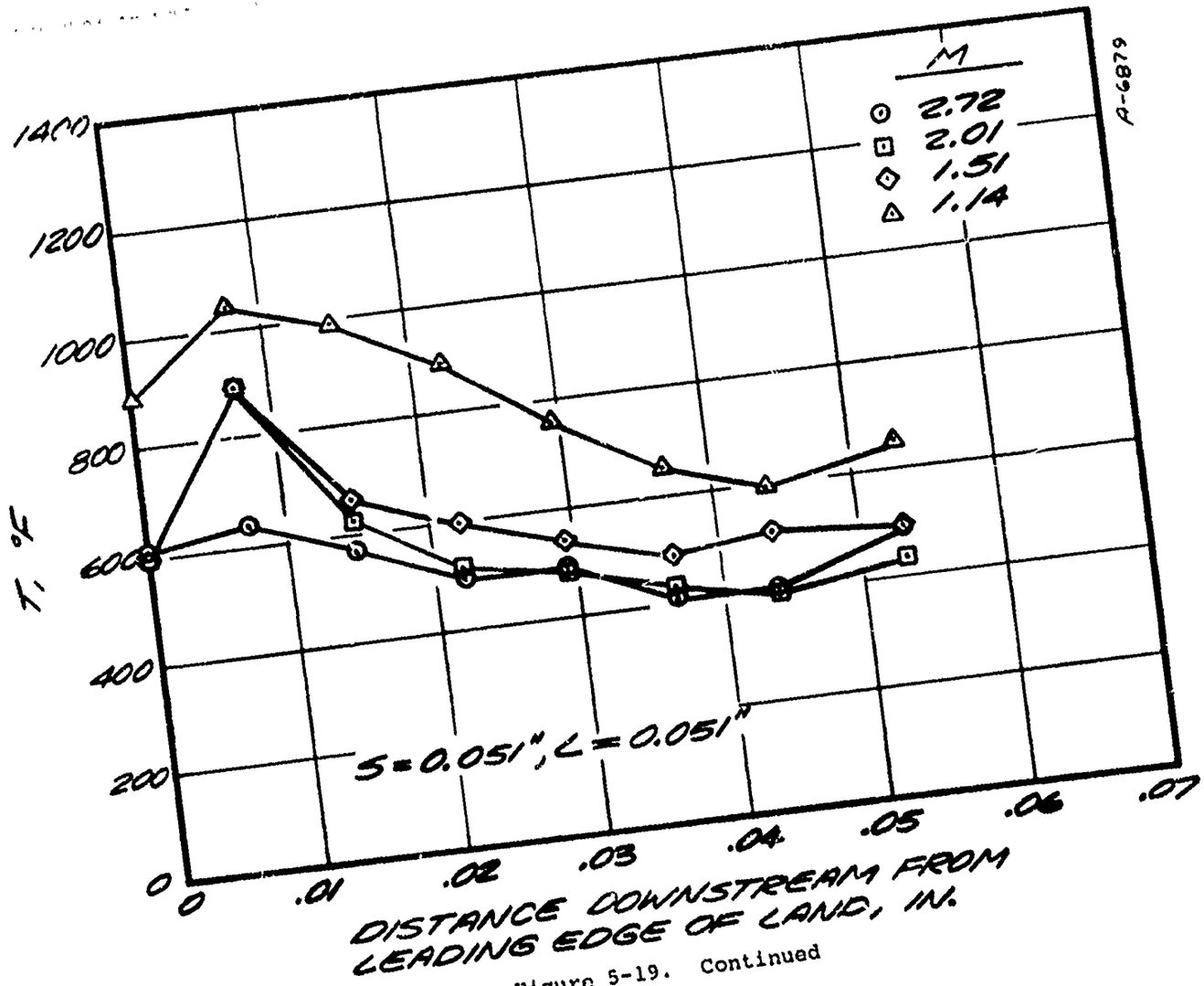

Figure 5-19. Continued

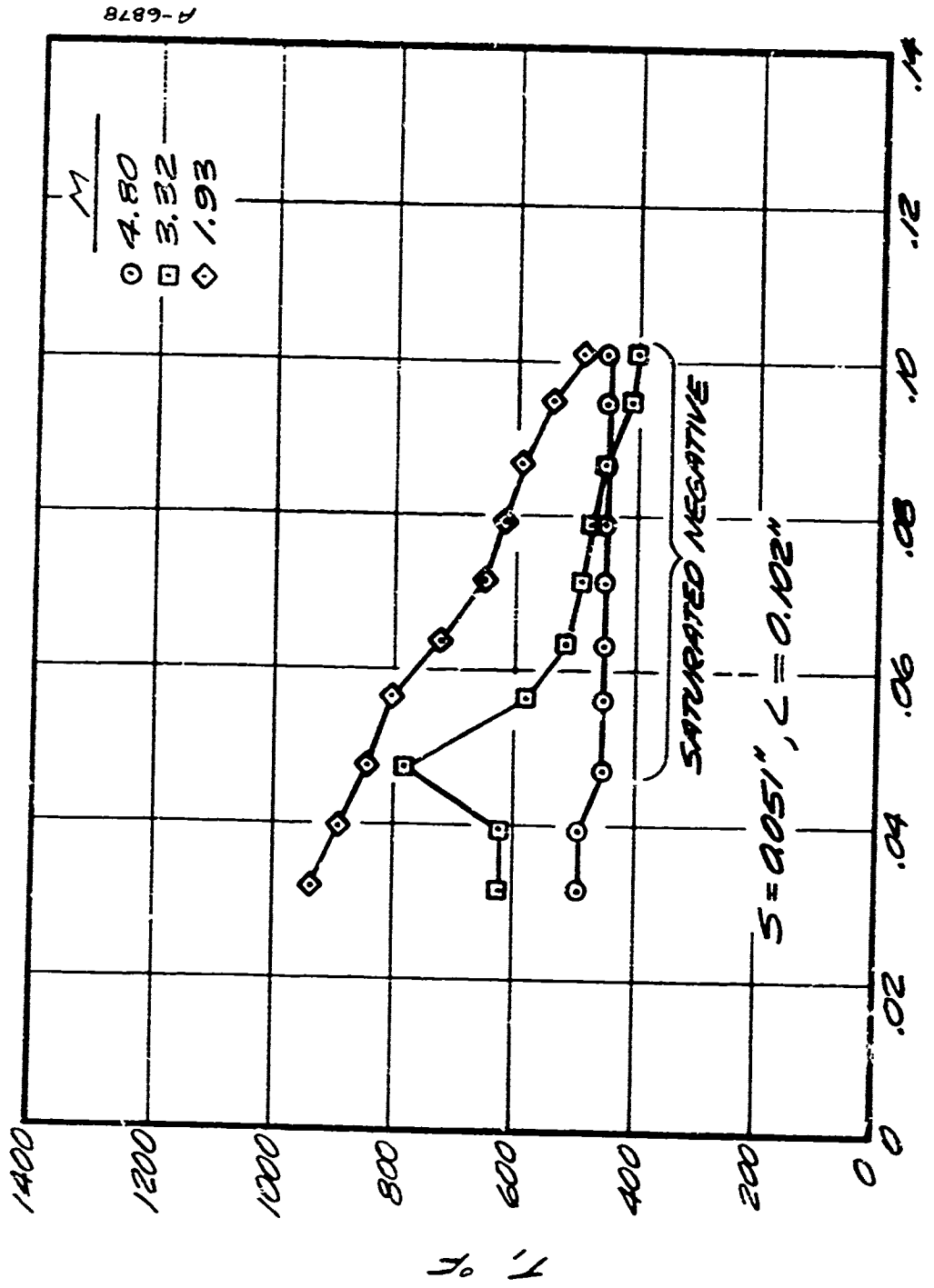

Figure 5-19. Continued

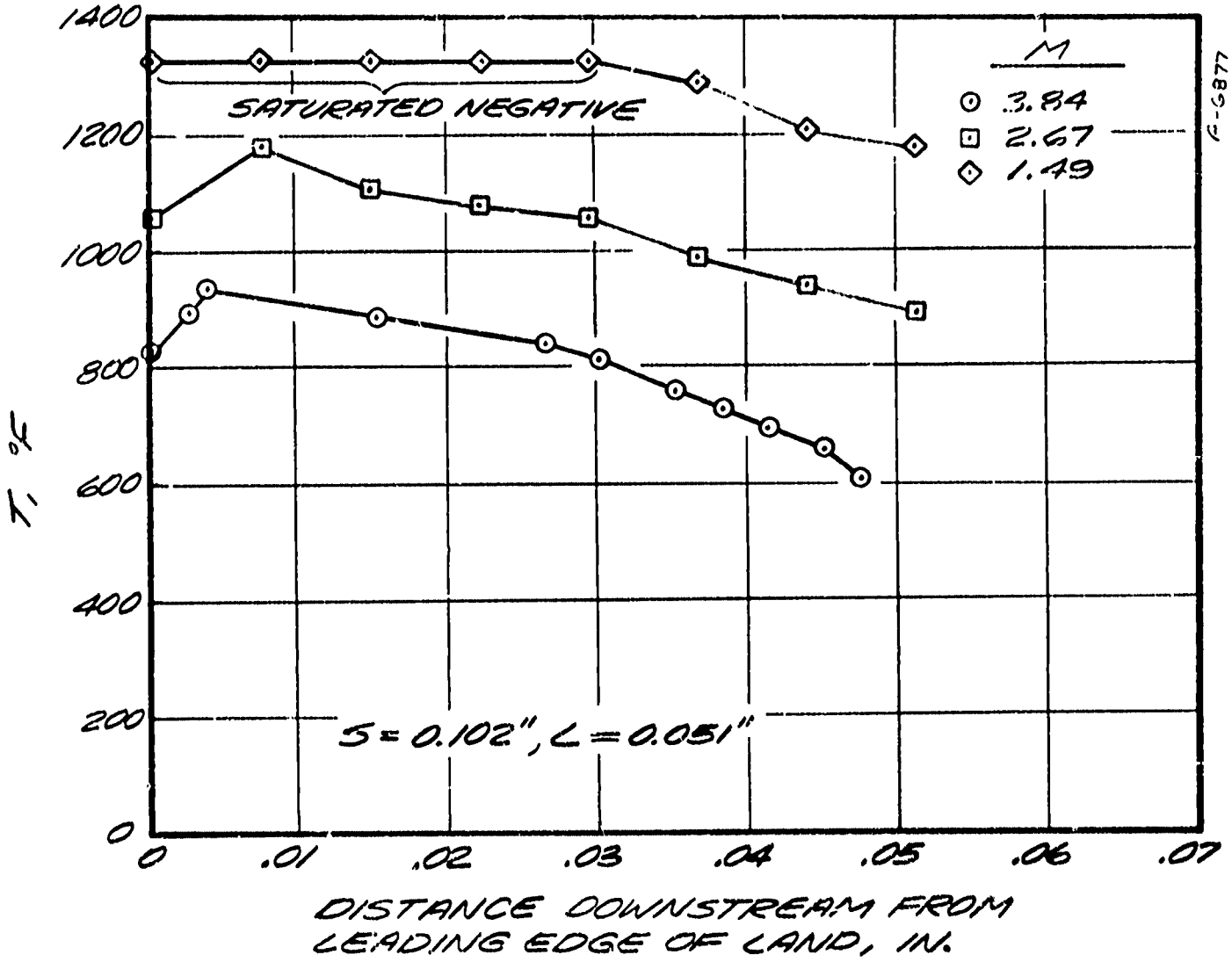

Figure 5-19. Concluded

AEROTHERM
ACUREX Corporation

COMBINED COOLING COMPARISON OF DISCRETE AND POROUS INJECTION

DISCRETE INJECTION

POROUS INJECTION

NO FLOW

NO FLOW

M = 1.0

M = 1.0

FLOW VISUALIZATION FROM NOZZLE TO JET

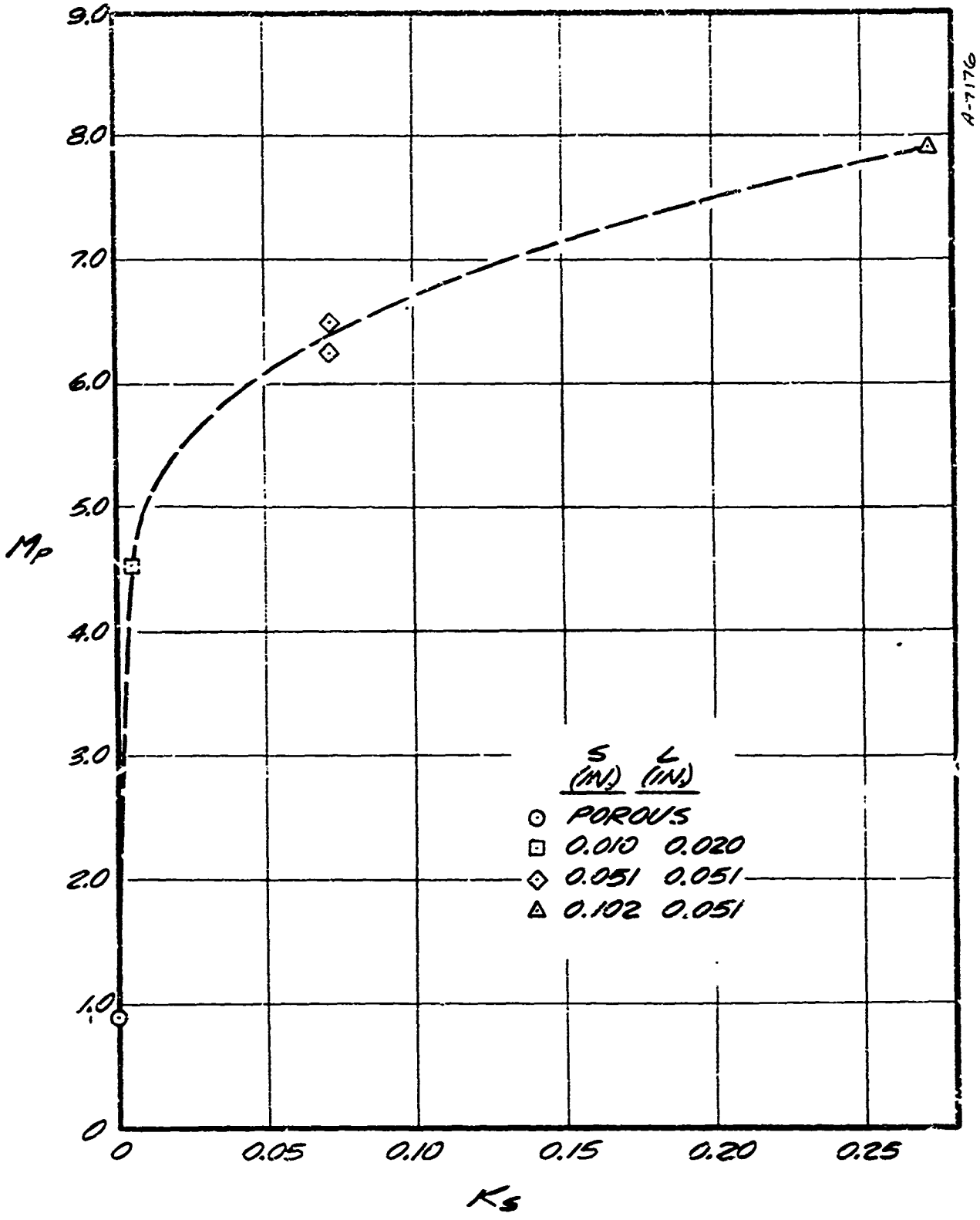

Figure 5-21. Margin at T_p = 300°F Equivalent Sand Grain Roughness

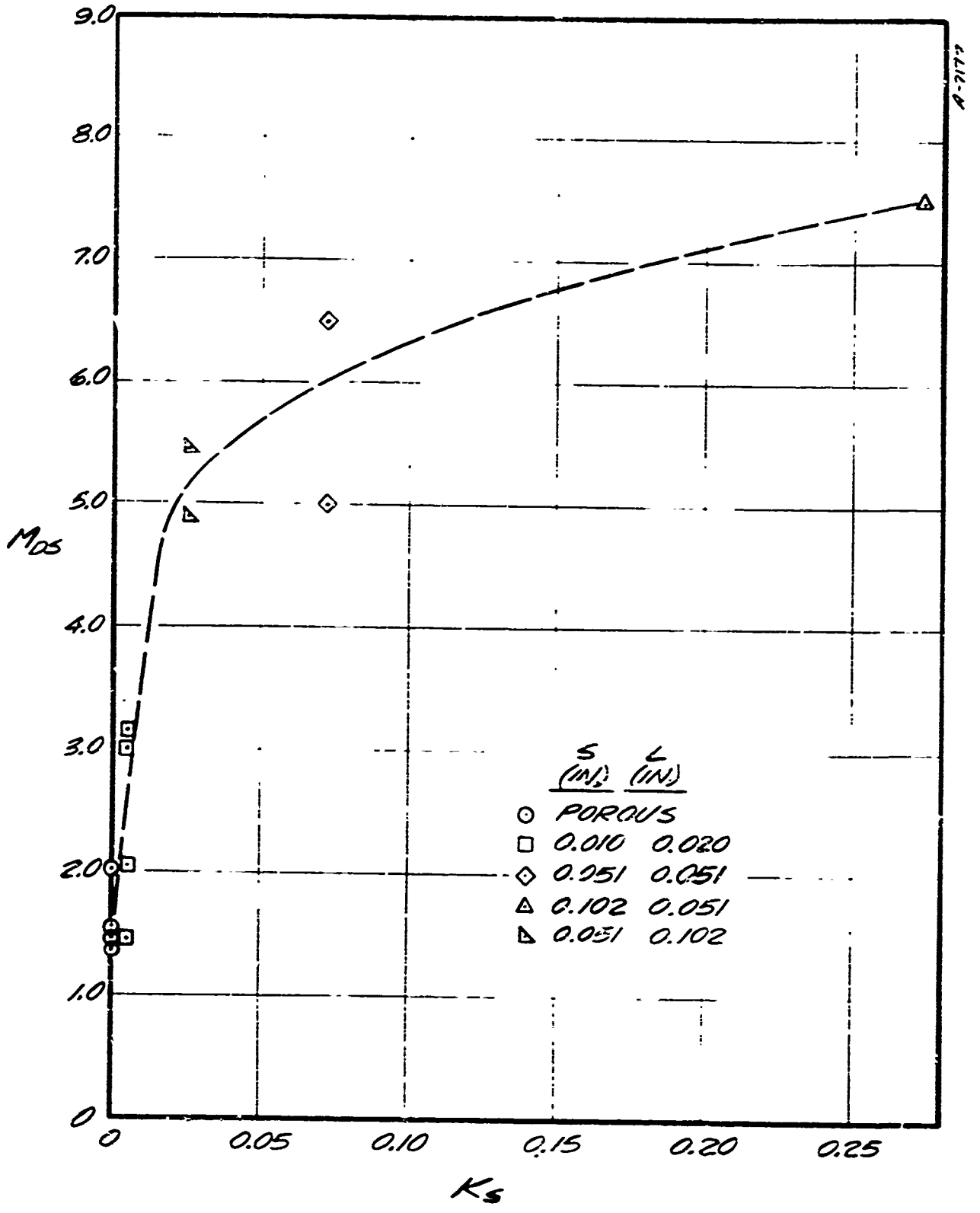

Figure 5-22. Margin at Downstream Threshold Versus Equivalent Sand Grain Roughness

Figure 5-23 compares the slot indepth temperatures measured in the Combined Cooling experiment with those measured in a flight test. A stainless steel Aerotip (see Figure 5-6) was used in the flight test, and most of the thermocouples were located in the skirt region. For similar depths below the exposed surface, the ground test thermocouples indicated temperature liftoff with decreasing coolant flowrate before the flight test thermocouples. In all probability this was due to the discrepancy in thermocouple location. As described in Section 5.3.4, the ground-test thermocouples were vacuum-deposited on the exterior of a land, facing in the upstream direction. In contrast, in the flight hardware the thermocouples were imbedded in the interior of a land and, consequently, were considerably more protected. Nevertheless, the agreement between flight and ground test data must be considered quite good, which substantiates the low-heat-flux facility/low-thermal-conductivity-model approach taken in the Combined Cooling experiment.

5.6 SUMMARY AND CONCLUSIONS

Twenty-five successful test runs have been performed in the NASA-Ames turbulent duct facility during the Combined Cooling Test Program. A flat-plate type model was mounted on the floor of the rectangular converging-diverging duct. At the 1 in. x 5 in. test section, the boundary layer was turbulent and the free stream Mach number was 3.5. The cold-will heat flux and static pressure at the test section were nominally 100 Btu 1 ft^2sec and 4.0 psia, respectively. The model was comprised of separate injection and downstream modules, with indepth and surface temperature measurements and photographs taken at former and heat flux distributions measured at the latter. Four quartz DI modules were considered, with slot/land dimensions of 0.010 in./0.020 in., 0.051 in./0.051 in., 0.051 in./0.102 in. and 0.102 in./0.051 in. In addition, a porous model fabricated from a sintered silica fiber matrix was tested.

Based upon an examination of the reduced experimental data, the following observations and conclusions have been made:

1. The injection surface temperature T_p rose rapidly above the saturation temperature T_v when the coolant flowrate was reduced to a threshold margin factor M_{th} of 3.0-6.0 for the DI modules and 1.0 for the porous module. Thus, the porous module had a greater local cooling efficiency. Also, the threshold margin M_{th} increased with increasing injection surface roughness for the DI modules.

2. In the region of rapid temperature rise, $|dT_p/dM|$ for the porous module was greater than that for any of the DI modules, indicating that when failure does occur, it happens more rapidly on a porous surface.

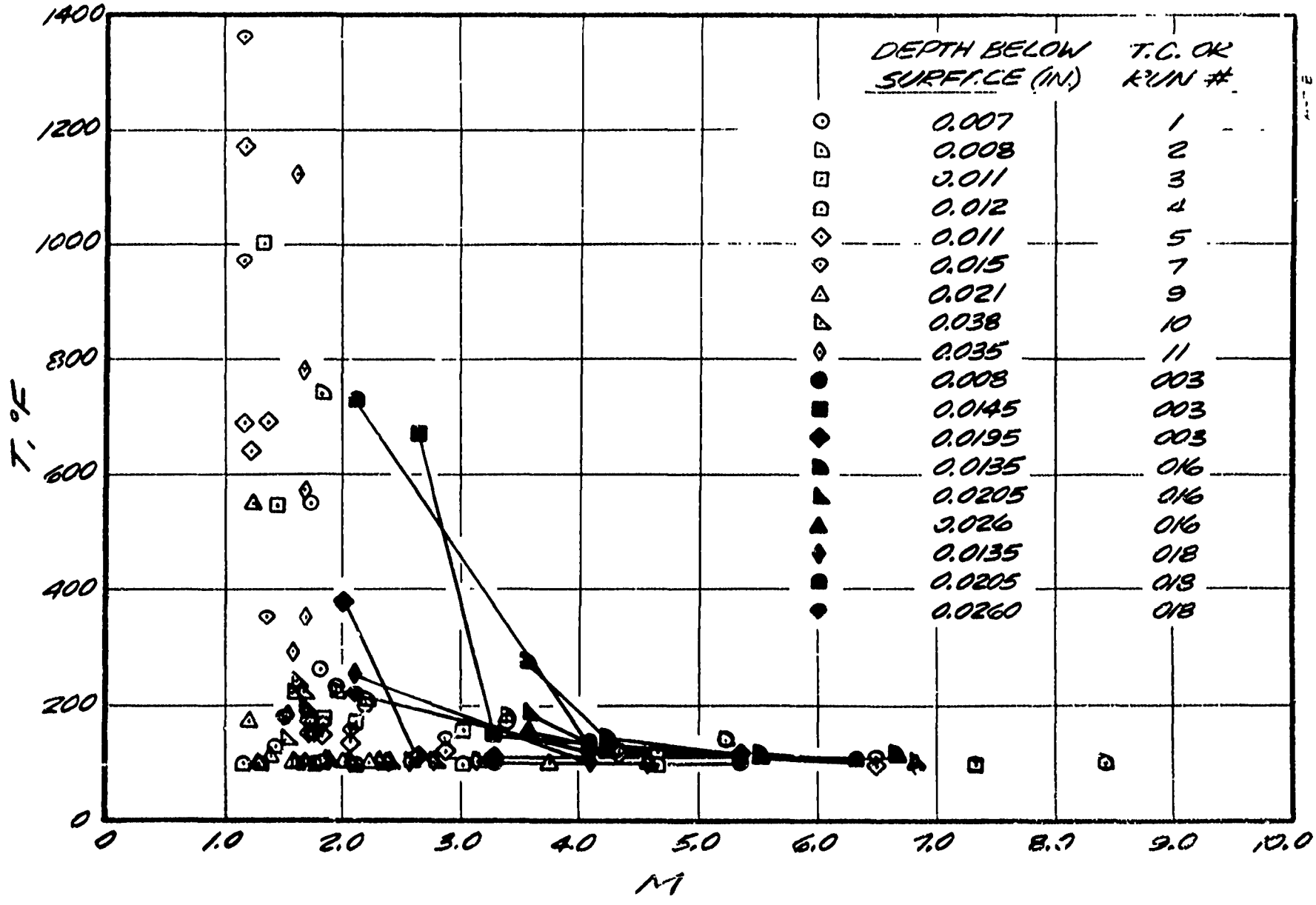

Figure 5-23. Comparison of Combined Cooling Slot In-Depth Temperatures With Those From Flight Test

3. Randomly-occurring hot spots were occasionally observed on the DI surfaces, due to fluctuations in the coolant distribution in a single slot. When such a hot spot occurred during a given test run, it remained for the duration of the run but did not reappear during the following run with the same injection module.

4. At $M = 1.0$, the indepth slot temperatures for all DI modules were significantly greater than T_v (~150°F) for depths up to 0.060 in. For the S = 0.010 in./L = 0.020 in. module, slot temperatures were at or below T_v when $M \geq 2.0$. For the DI modules with larger slots, $M \geq 4$ was required to reduce slot temperatures to T_v. These findings indicate that appreciable heating extended down into the slots for margins significantly greater than unity. This is in contrast to a model based upon continuous injection from a smooth surface which predicts that indepth temperatures will not exceed T_v until $M < 1.0$.

5. Good downstream cooling for 2-3 injection lengths was achieved with the porous and S = 0.010 in./L = 0.020 in. modules when $M \geq 2.0$, but for the DI module with the largest slots downstream cooling was ineffective for $M \leq 6.0$. These observations are correlated with the effective surface roughness of the injection module. In addition, for $M \leq 1.0$, peak heating downstream increased with increasing injection surface roughness.

6. Under none of the test conditions did a smooth liquid layer form on the injection surface. Even for $M \geq 6.0$, the coolant was entrained into the boundary layer in the form of a mist of small liquid droplets, rather than forming a cohesive liquid film. For $M = 1.0 - 1.5$, there was no evidence of liquid-phase coolant above or even to some distance below the slot exits, indicating the coolant was entirely vaporized (and probably superheated) at these margins.

7. At $M \cong 1.0$, there were large-scale nonuniformities in the injection surface temperature distributions, due either to coolant nonuniformities in a single slot or from slot-to-slot (S = 0.010 in./L = 0.020 in.) or point-to-point (porous). When a land was hot and had a transversely uniform coolant distribution, the peak temperature occured slightly downstream of the leading edge. Generally, the web separating two adjacent slots was the coolest region on a DI surface. Also, very small scale surface inperfections were observed to experience enhanced heating.

The essence of the above conclusions is that the roughness of the injection surface reduces both local and downstream cooling efficiency, that hot spots can

develop on both DI and porous surfaces due to coolant distribution nonuniformities, and that even at high coolant margins the formation of a cohesive liquid layer is unlikely. The effects of surface roughness observed in this experiment are substantiated by the findings of the earlier Large Slot External Cooling Tests (Reference 8). The formation of water flobules at the slot exits, which were observed in the Internal Cooling Tests (Reference 6), were not observed in the present tests. This is probably due to the fact that the slots themselves were not heated in the former tests.

SECTION 6

ANALYSIS PROCEDURE

6.1 GENERAL DESCRIPTION

The analysis procedure for discrete injection hardware, developed under the Nose Cooling Technology Program can be divided into the following three steps:

I Prediction of environment (SAANA)

II Prediction of slotted surface roughness augmented heating with mass transfer.

III Prediction of surface temperature and internal temperature distribution from internal heat transfer model

A flow diagram depicting this procedure is shown in Figure 6-1. Steps II and III specifically are the outgrowth of the present program.

6.1.1 Correlation Analysis

A series of experimental programs have been performed to identify the critical aerothermodynamic parameters associated with discrete injection transpiration cooling systems. In addition, an analysis of the sensitivity of coolant mass flux rates required to maintain a given surface temperature was performed which was related to uncertainties in these identified parameters. The objective of the NCT Data Correlation task was to quantify these parameters in such a manner that a user oriented discrete injection cooling correlation technique may be obtained. This correlation would then be validated against the data obtained from the NCT experimental programs and a prediction would be made over an Aerojet Discrete Injection Nosetip in the ABRES RPL Rocket facility (Section 7).

6.1.1.1 Data Availability and Applicability

A series of three distinct experimental programs were performed to obtain the data needed in formulating a useable discrete injection correlation procedure. Specifically, the objectives of each program can be summarized in Table 6-1. Results of experiment 3 indicated that the internal heat paths

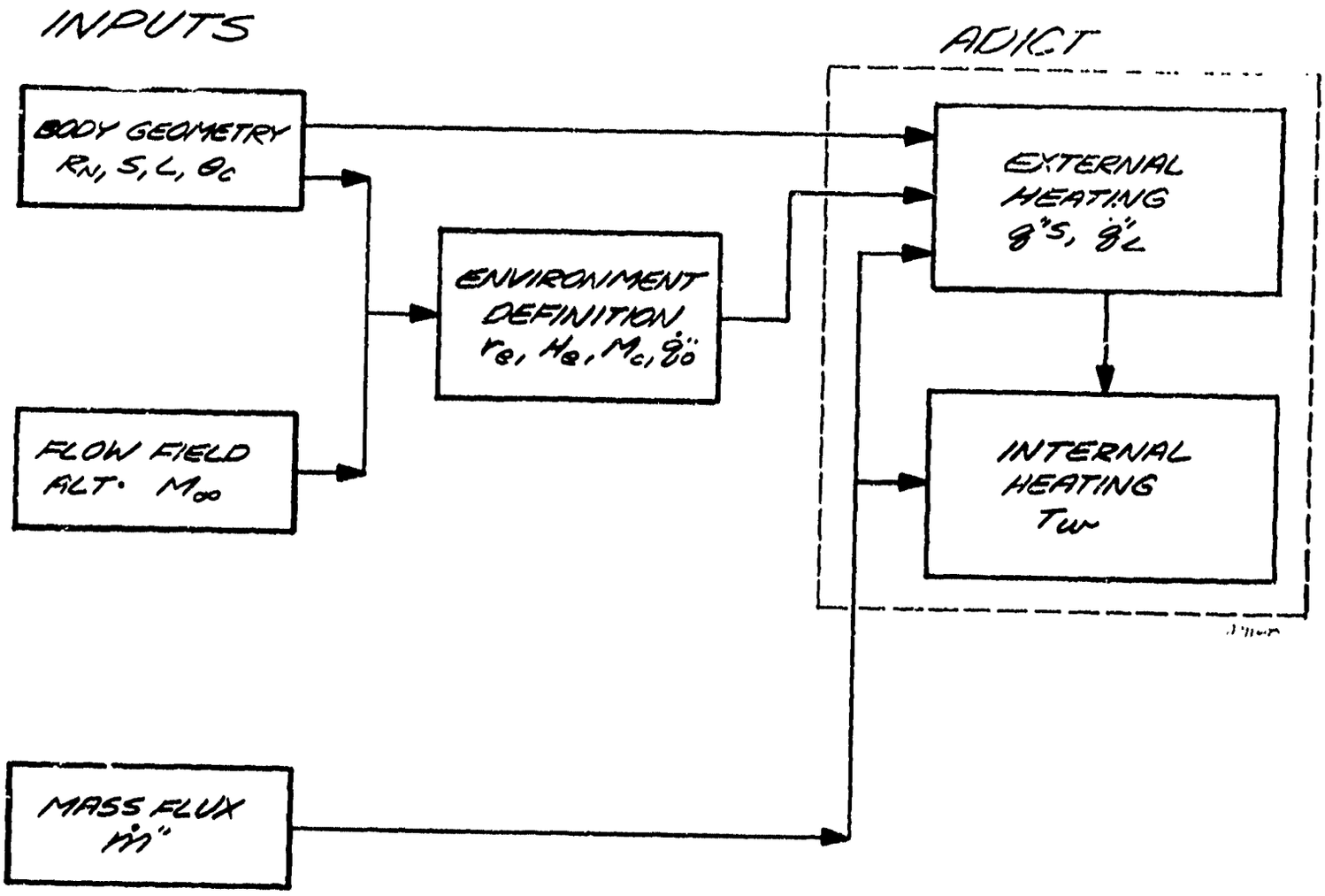

Figure 6-1. Schematic of Correlation Procedure

TABLE 6-1

Test Program	Primary Objectives	Impact on Correlation Study
1. Internal Cooling Experiment	- obtained internal film heat transfer coefficients characterizing nature of two phase flow in small passages - identify internal heat paths and thermodynamic state at exit plane of slots	- technical difficulties led to limited use of this data in correlation development; reference Section 3 and 6.2
2. External Cooling Experiment	- determined detail heat flux and temperature distributions over scaled up versions of slot land configurations - isolated and identify contributions of roughness heating augmentation and effective film cooling data - determine the downstream effectiveness of film cooling - determine three dimensional contributions of stagged slot-land configurations - obtain fundamental fluid mechanic data relating to turbulent boundary layer flow over slots with and without blowing and localized separation phenomena	- this test program provided the detailed data upon which the correlation technique was built; reference Section 4 for a complete overview
3. Combined Cooling Experiment	- obtain an understanding of gaseous, two-phase or liquid injection of a coolant into a hot turbulent boundary layer - to validate and assess the correlation procedures developed from Experiments 1 and 2 to determine the downstream effectivenss of multiphase film cooling	- this test program provided the necessary data to validate the NCT correlation procedure. It also provides valuable visual information pertaining to the aerothermodensity pehnomena occuring over realistic discrete injection configurations under a scaled flight environment; reference Section 5.

were not properly simulated in experiment 1; hence, the results of this experiment were not directly applicable to the development of a correlation. Let us now restrict our attention to experiments 2 and 3. Table 6-2 identifies the types of data taken during each test program and identifies those data which impacted the correlation procedure.

The basic groundwork in formulating the correlation procedure was performed as the external cooling test data was being reduced and evaluated. Simultaneously the final inputs to the combined cooling experiments were being addressed. As a result, a conscience effort was placed upon obtaining that information which would produce the most effective cross-coupling of data between the experiments. This served two purposes:

1. Validation of the experimental procedures
2. Validation of the correlation procedure

This data cross-coupling proved most useful in the identification and the optimum utilization of the revalent aerothermodynamic parameters.

6.1.1.2 External Heat Transfer Correlation

The Aerotherm heat transfer correlation is based upon the generation of two basic curves:

- The no-blowing, roughness augmented heat transfer distribution.
- The "fully-blown" heat transfer distribution (defined such that $\dot{q}''$ at X_L = 0 is zero). We will refer to this as our film cooling profile

Consider the following sketch:

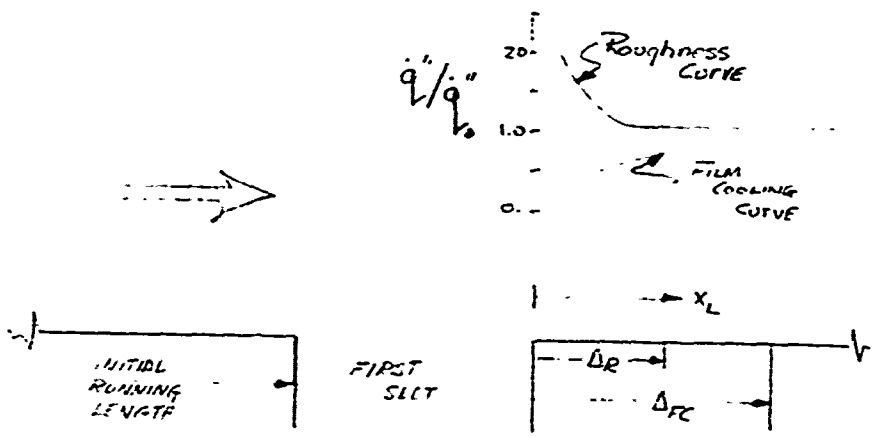

Δ_R = Relation length for roughness profile

Δ_{FC} = Relaxation length for film cooling profile

TABLE 6-2

Experiment	Data Taken	Major Contributor To a Fundamental Fluid Mechanical Understanding	Contributor NCT Correlation Procedure
	Over Slot-Land Configuratives		
2. - External Cooling Experiment • $M_\infty \approx 8.$ • $\dot{q}_o^{\prime\prime} \approx 0.5 \frac{Btu}{ft^2 sec}$ • $B'_{SLOT} = 0 - 20.$ • Four Models Tested 1. 2.0"/10.0" 2. 2.0"/2.0" 3. 2.0"/0.8" 4. 5.0"/5.0"	1. Surface Temperature (S,L)*		
	2. Surface Pressure (S,L)	X	
	3. Surface Heat Transfer (S,L)		X
	4. In-depth Heat Transfer	X	X
	5. In-depth Pressure	X	
	6. Mass Flux	X	X
	7. Boundary Layer Survey (S)	X	
	Downstream Section		
	8. Surface Temperature (S)		
	9. Surface Pressure (S)		
	10. Surface Heat Transfer (S)	X	X
	Over Slot-Land Configuratives		
3. - Combined Cooling Experiment • $M_\infty \approx 3.75$ • $\dot{q}_o^{\prime\prime} = 100 \frac{Btu}{ft^2 sec}$ • $B'_{SLOT} = 1. - 20.$ • Four Models Tested 1. .010"/.020" 2. .051"/.051 3. .102"/.051" 4. .051/.102" • One Porous Model $\rho = 23$ lbm/ft^3 $k = 1.45*10^{-11}$ft^2	1. Pyrometer - Average Surface Temperatures	X	X
	2. Mass Flux	X	X
	3. In-depth Temperatures	X	
	4. Color Photograph	X	X
	5. Infra-red Photograph	X	X
	Downstream Section		
	6. Surface Heat Transfer (S)	X	X

*S = Streamwide distributions
L = Laterial distributions

It is postulated that any other heating distribution over a land due to any other blowing rate in a slot must lie between these two bounding profiles.

6.1.1.3 Determination of the Roughness Augmented Heating Distributions

The roughness augmented heating distribution is dependent upon three key parameters:

- Stagnation peak heating
- Relaxation length
- Decay rate

The value of peak heating is found by calculating a discrete roughness height associated with an individual slot-land configuration and converting this height into an equivalent sand-grain roughness model. The discrete roughness height is obtained by calculating the separation angle through which the flow field expands as it passes over the first slot. This is done by calculating an effective base pressure, P_b, from the simple expression:

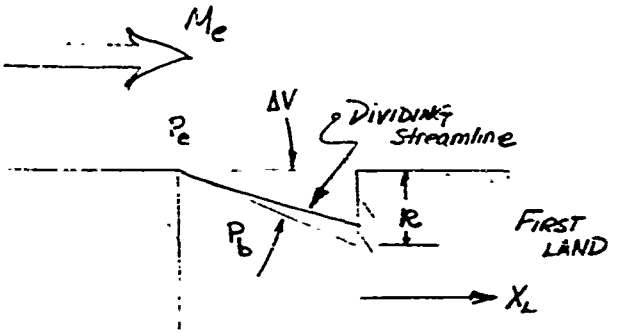

$$\frac{P_b}{P_e} = \left[\frac{1 + \frac{\gamma-1}{2} M_e^2}{1 + \frac{\gamma-1}{2}\left(M_e^2/(1-\phi^2)\right)}\right]^{\gamma/(\gamma-1)}$$

where M_e is the edge Mach number and ϕ is the velocity ratio of the dividing streamline. This expression is adopted simply because it relies on the least amount of physical modeling and uncertainty. We can obtain ϕ from the following curve, Reference 39.

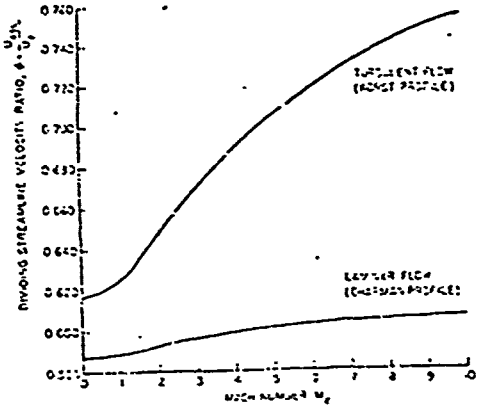

Knowing the base pressure (cavity pressure) the flow field can be expanded into the cavity by an amount equivalent to the Prandtl-Meyer turning angle for the given ratio of P_b/P_e namely ΔV. Out discrete roughness height is now simply $k = \tan(\Delta V)*S$ where S is the slot opening. An equivalent sand grain roughness can then be obtained using the method described in Reference 40. Once this is obtained, the roughness augmented heating factors can be found using the Powars' correlation, Reference 41, for example. The large slot data gives augmented heating rates of the order of 2.5.

The remaining two parameters, relaxation length and decay rate, are postulated solely from the data behavior of the large slot tests.

6.1.1.4 Decay Rate and Relaxation Length

Consider the problem of the formation of a new laminar boundary layer in an already established turbulent high speed boundary layer. In particular, concern is with the problem of where the lower portion of the boundary layer is scraped off. That is:

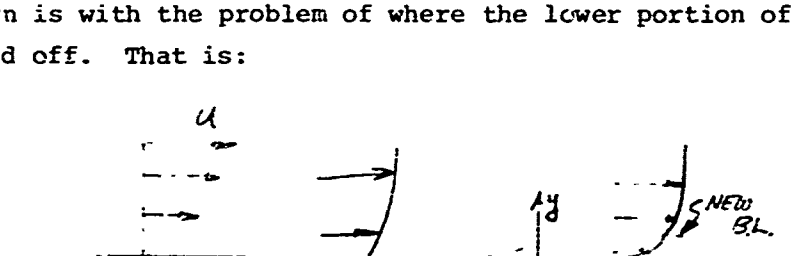

The new laminar b.l. (LBL.) developes from x = 0 and with edge conditions determined from the local properties of the turbulent BL (T.B.L.) at a distance y above the surface. If in fact, the L.B.L. grows as $X^{1/2}$ and one can assume a profile for the T.B.L. (e.g. 1/10th, 1/2, log, etc.), and one can obtain the local edge conditions as a function of x. This technique has in fact been attempted with only moderate success. In fact, the difficulty stems from the assumed shape of the T.B.L. This difficulty suggests several problems:

1. Either the entire approach is wrong, namely, the L.B L. does not grow like $x^{1/2}$ and edge conditions cannot be obtained from the T.B.L.
2. The L.B.L. grows like $x^{1/2}$ but since the surface conditions are so sensitive to the assumed T.B.L. profile that the technique is unreliable
3. A combination of (1) and (2).

In problem (1) lies the crux of the difficult. The L.B.L. grows under a variable edge condition environment. The approach orginally outlined is in

fact a convenient technique for determining the surface conditions providing one is of sufficient distance from the leading edge. How far is "sufficient" is left open temporarily, however, there does exist enough data base to get a handle on this number. In any event, "sufficient" length will be many times the length that would exist in a constant free stream edge environment. In fact, what is being proposed is a long region of strong interaction L.B.L.

The strong interaction B.L. comes about when one can no longer dis-associate the external environment from the boundary layer development. In fact the solution of both becomes a coupled problem in which an iteration is necessary to obtain a consistent solution.

Consider the strong interaction laminar boundary layer growth over a flat plate

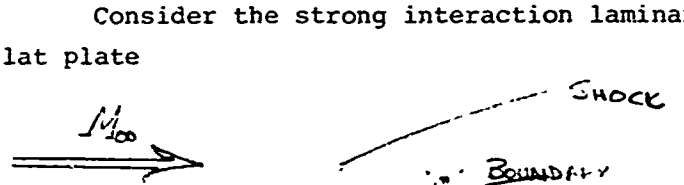

The edge pressure is approximated by a series expansion as

$$\frac{p_e}{p_\infty} \sim \frac{d\delta^*}{dx}$$

since

$$\delta^{*2} = \frac{x^2}{R_e}$$

then

$$\frac{p_e}{p_\infty} \sim \frac{1}{\sqrt{R_e}} \sim \frac{1}{x^{1/2}} \sim x^{-1/2}$$

{ referred to as the over pressure

Similarily, we can show

$$q/q_o \sim \left(\frac{p_e}{p_\infty}\right)^{-1/2} \sim x^{-1/4}$$

where $\dot{q}''_o$ is the no interaction heat transfer. Essentially, what is being postulated is:

1) A model in which a variable Mach number boundary layer impinges on a land producing a weak shocklet and a laminar strong interaction boundary layer.

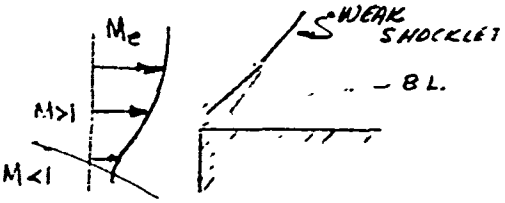

2) This L.B.L. grow in such a manner that the heat transfer is not a function of $x^{-1/2}$ but rather $x^{-1/4}$

3) Data is shown to substantiate this model in Figure 6-2.

6.1.1.5 Film Cooling Distribution

The lower boundary in the heat transfer model is represented by a film cooling profile in which $\dot{q}'' = 0$ at $X_L = 0$. Using this condition in conjunction with a method for predicting the downstream cooling effectiveness in a turbulent high speed boundary layer, Reference 42, allows us to obtain the film cooling distribution. Laganell's technique employs a Von Karmen Integral Momentum approach wherein Eckert's Reference Enthalpy method is utilized for compresibility corrections. The film cooling equation becomes

$$\frac{S_T}{S_{To}} = 1 - \eta$$

where

$$\eta = \frac{1}{1 + \frac{1}{5}\frac{C_{P_E}}{C_{P_C}}\xi\,\varepsilon}$$

and

C_{P_C} = coolant specific heat at constant pressure

C_{P_E} = edge specific heat at constant pressure

$\varepsilon = 1/(1 + .13\,M_e^2)^{.8}$ - Mach number correction

$$\xi = \frac{x}{\dot{m}s}\left|Re_s \frac{\mu_c}{\mu_e}\right|^{-.25}, \quad \mu_c = \text{coolant viscosity}$$

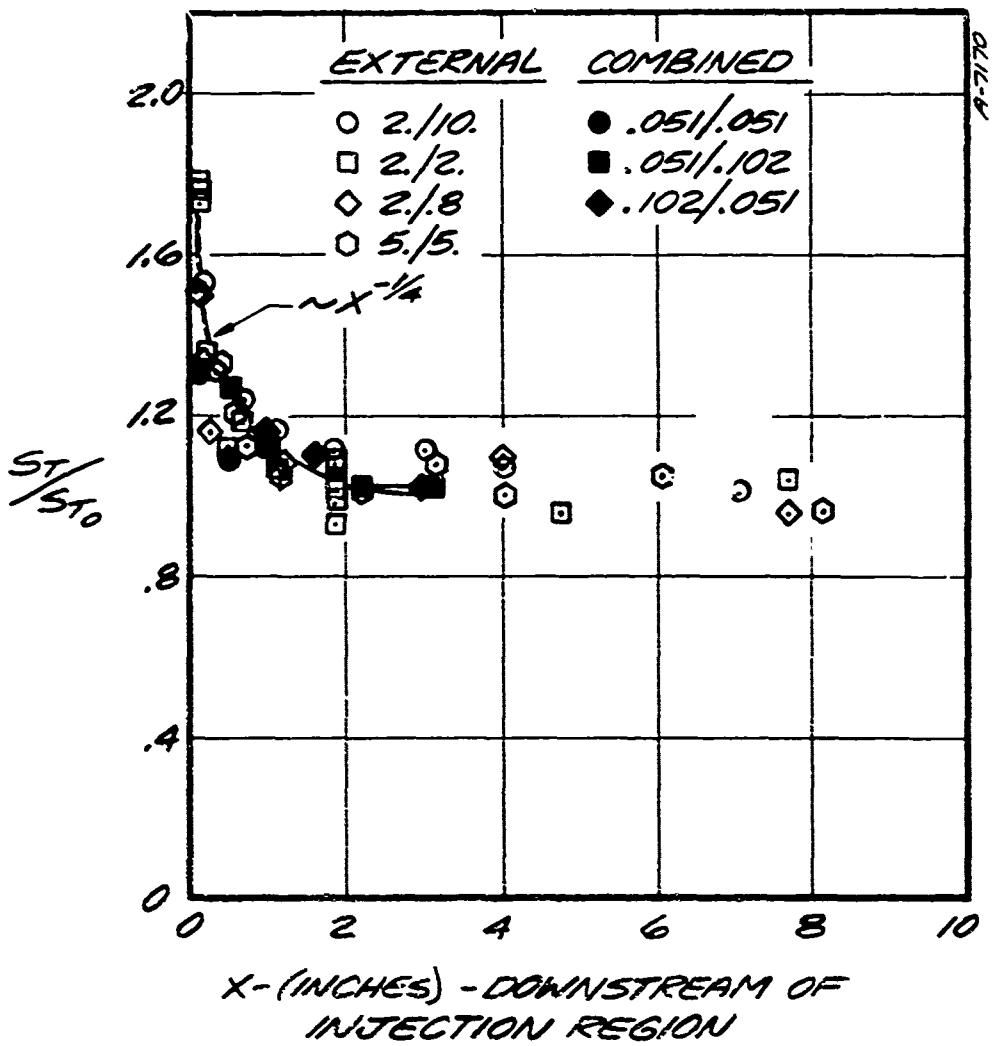

Figure 6-2. Downstream Cooling Effectiveness Correlation

Since the correlation was used for determining the downstream cooling effectiveness of an upstream porous plate, this equation was modified slightly. The modification accounted for

- Injection length being a discrete injection surface
- Multiple slot openings

This modification was based solely on the data trends and can be rewritten as

$$\eta = \frac{1}{1 + \frac{1}{2}\frac{C_{P_E}}{C_{P_C}}\xi\,\varepsilon}$$

where S is one slot opening.

6.1.1.6 Intermediate Blowing Rates

Perhaps some of the most consistent correlatable data to be obtained in the NCT Program has been the ratio of (peak heating) $B' \neq 0$ to (peak heating) $B' = 0$ as a function of $B' = F/S_{T_o}$ where $F = \rho_w u_w/\rho_e u_e$, and S_{T_o} = Smooth wall Stanton number. All of data is shown to collapse onto a single curve in Figure 6-3, where Δ is defined as

$$\Delta = S_T/S_{T_{B'=0}}$$

this ratio is applied across the entire region of interest, X_L, to obtain the heating distribution over the slot- land configuration. For example, for a blowing rate, B':

$$\dot{q}/q_{ref} = \Delta * (\dot{Q}_R(X_L) - \dot{Q}_{FC}(X_L)) + \dot{Q}_{FC}(X_L)$$

where Δ is from Figure 6-3, $\dot{Q}_R$ is from Section 6.1.1.3 and $\dot{Q}_{FC}$ is from Section 6.1.1.5. It is also interesting to see the effect of S/L on the discrete injection blockage factor, Figure 6-4.

Finally, a few remarks pertaining to the similarity between the NCT testing configurations and the in-flight hardware should be mentioned. The large slot tests scaled boundary layer and slot-land dimensions to in-flight numbers. However, heating rates and liquid mass transfer effects were not simulated. The combined cooling test also scales boundary layer and slot-land

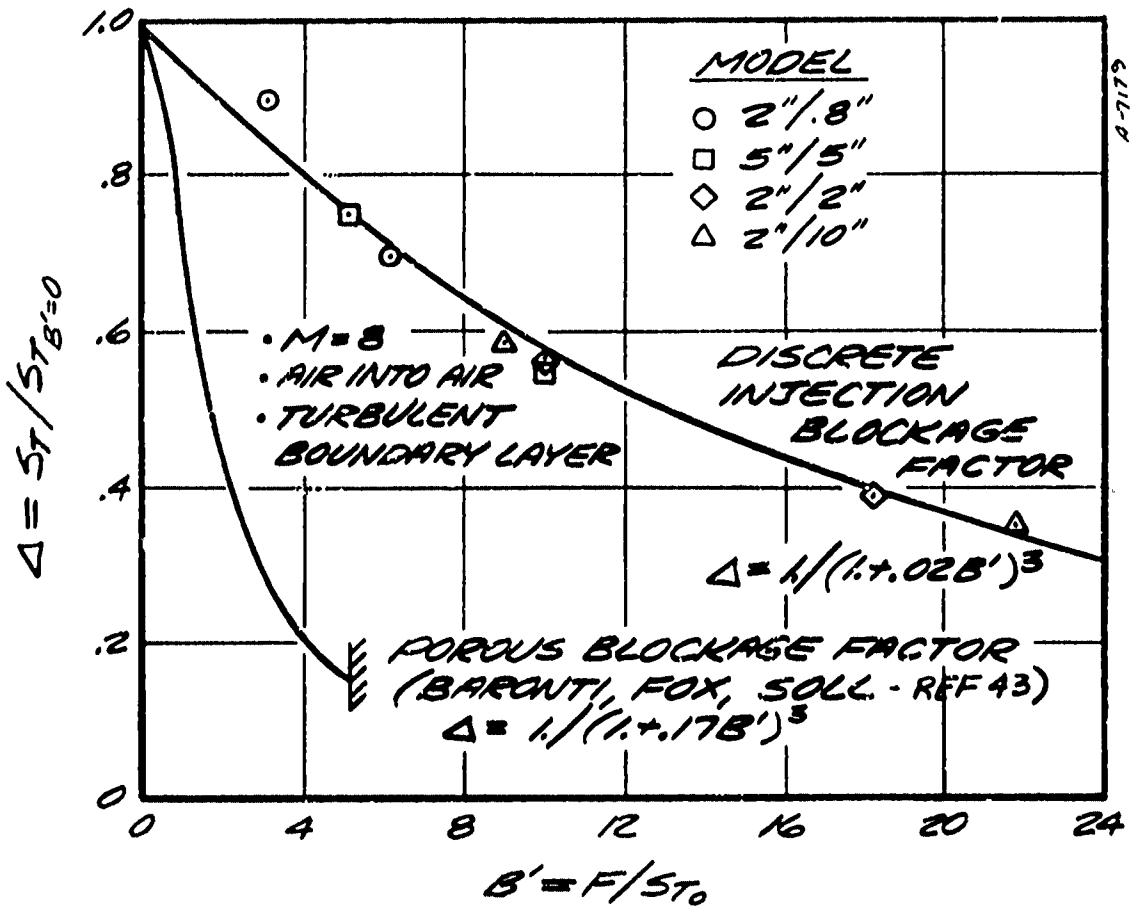

Figure 6-3 Discrete Injection Blockage Factor Based on Slot Area

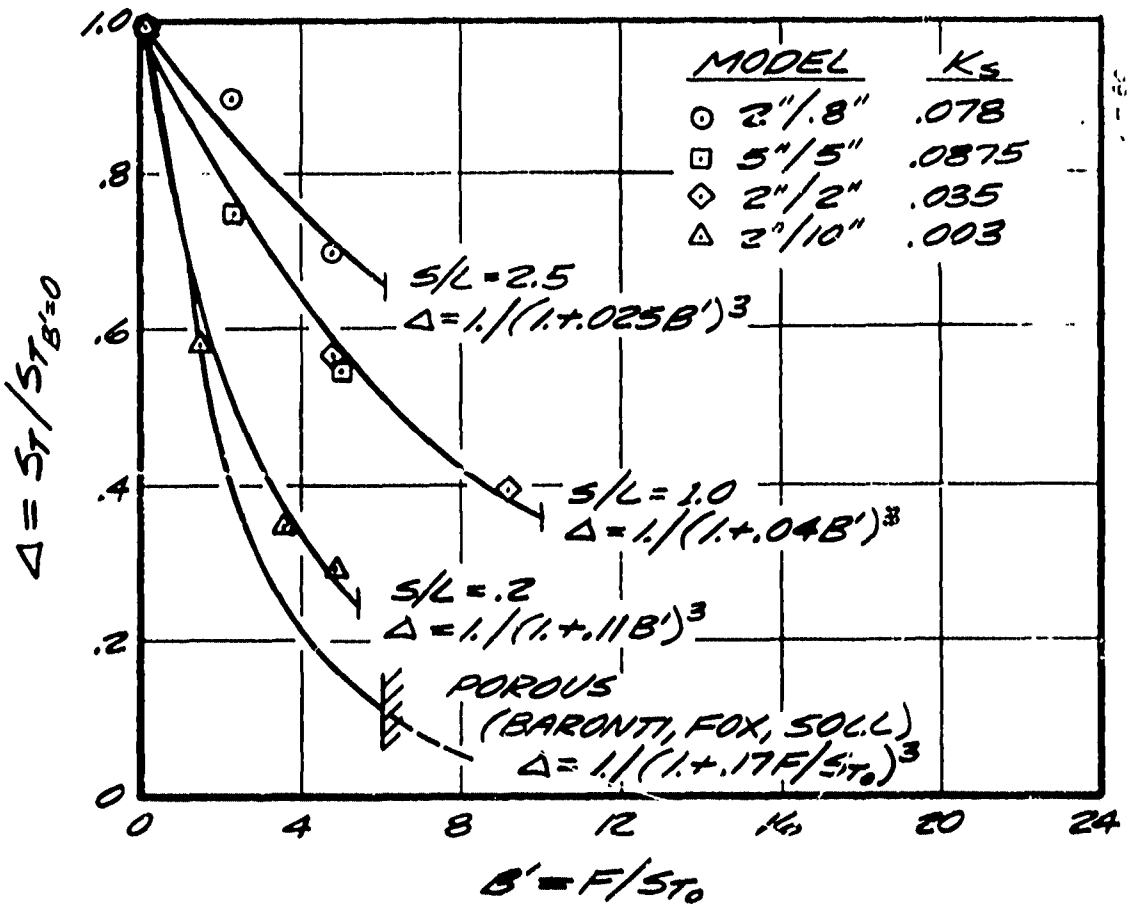

Figure 6-4. Discrete Injection Blockage Factor Based on Total Area

openings and, in addition, duplicates the flight environment and liquid cooling effects more closely. In neither case has actual nosetip geometries been utilized and subsequently these effects (which may and may not be sizeable) have not been accounted for. Therefore, the extension of this correlation to other configurations should be done with reasonable care and measureable apprehension.

6.1.2 Internal Cooling Analysis

The system being analyzed is schematically represented in Figure 6-5. For the purpose of anlaysis the system was divided into three regions, a gas phase region, a two phase region, and a liquid phase region. The largest portion of the total in-depth temperature drop, as observed from the internal cooling experiment, combined cooling experiment, and flight test occurs near the surface (within 10 slot diameters). Hence, a fine nodal network is employed to represent this region as shown in Figure 6-6.

For the in-depth nodes it is assumed that there is no temperature variation across a slot or across a given land. Thus within a slot or land, energy is only transferred in the y direction. Due to roughness effects there are axial temperature gradients as well as in-depth temperature gradients in the lands near the surface. Therefore in order to model roughness effects a nodal distribution in the axial direction is utilized in the land for the first two rows (Δy intervals). Energy balances for the j-th slot and land nodes are given below:

Slot

$$C_S(T^S_{j-1} - T^S_j) + H(T^L_j - T^S_j) = C_S(T^S_j - T^S_{j+1}) + M(T^S_j - T^S_{j+1})$$

Land

$$C_L(T^L_{j-1} - T^L_j) = C_L(T^L_j - T^L_{j+1}) + H(T^L_j - T^S_j)$$

where

$$C_S = [k_S(S/2)/\Delta y]$$

$$C_L = [k_L(L/2)/\Delta y]$$

$$H = h\,\Delta y = (k_S Nu_m/S)\Delta y$$

$$M = \dot{m}\,C_{P_S}\,(S/2)$$

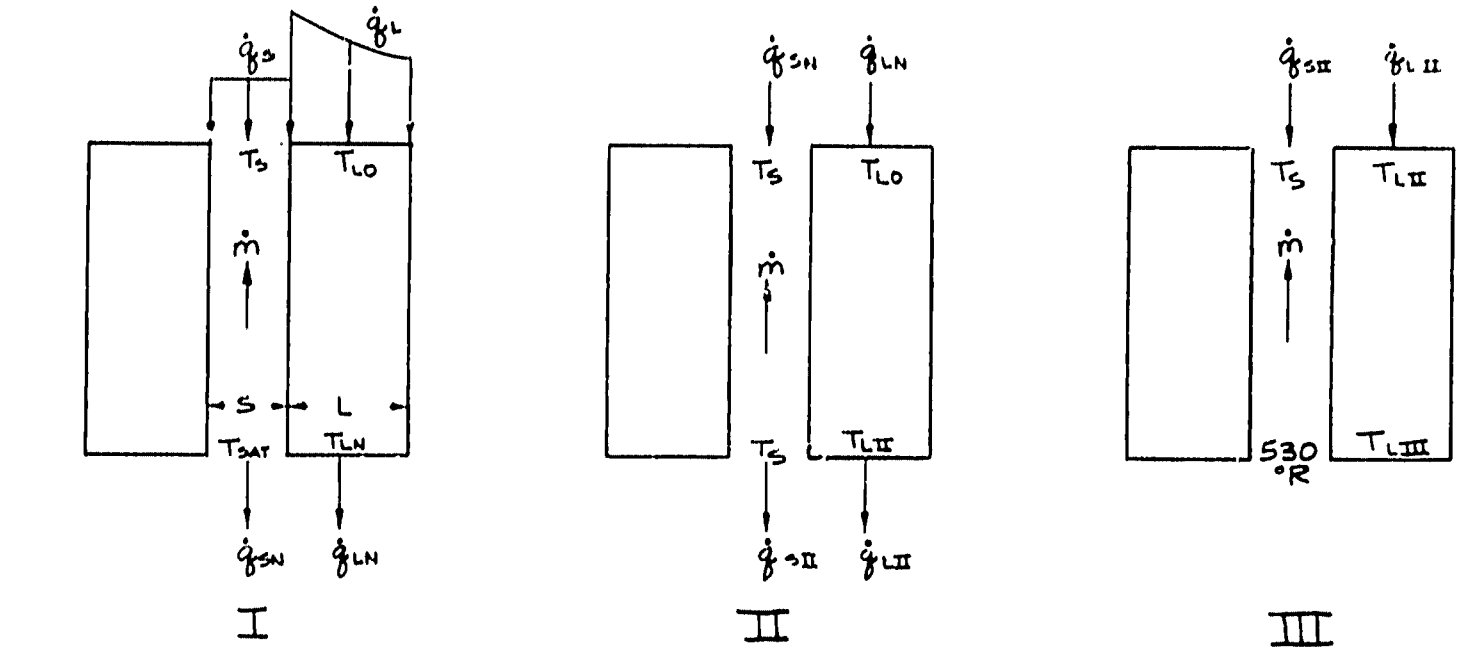

Figure 6-5. Internal Cooling Analysis Schematic

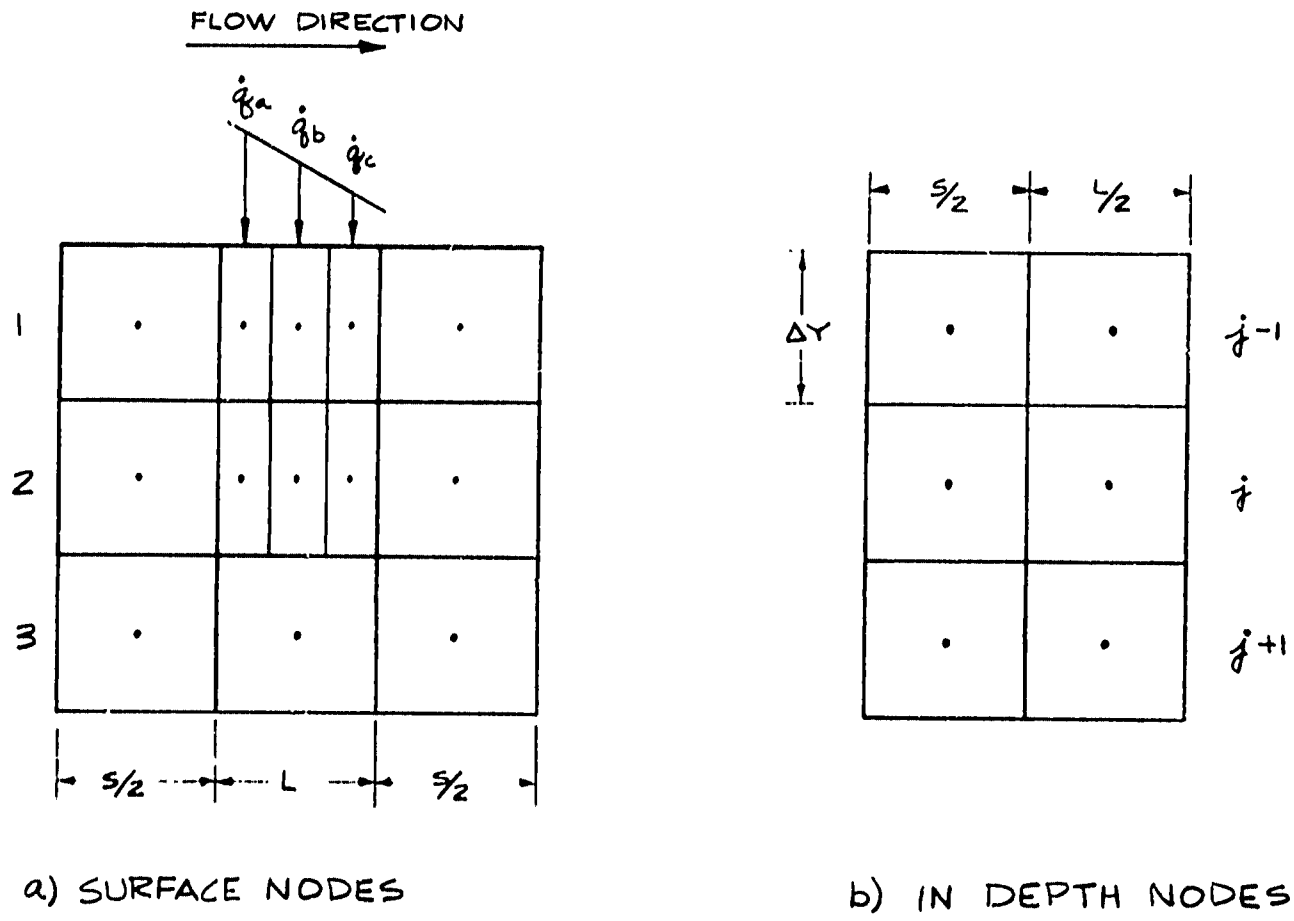

Figure 6-6. Internal Nodal Network Schematic

The boundary conditions are

$$\dot{q}_s \text{ (specified for first slot model)}$$

$$\dot{q}_a,\ \dot{q}_b,\ \dot{q}_c \text{ (specified for first layer of land nodes)}$$

$$T = T_{sat} \text{ (last slot nodes)}$$

$$q_{SN}(S/2) + q_{LN}(L/2) = \dot{m}(S/2)[C_{p_w}(T_S - T_R) + \lambda_{vap}] \text{ (Nth land and slot nodes)}$$

As was mentioned the last node corresponds to the location at which two phase flow begins within a slot. The last boundary condition, stated above, is required in order to raise the coolant from its reservoir temperature to its saturation temperature and vaporize the coolant.

An appropriate Nusselt number for laminar channel flow taken from Reference 28 (Knudsen and Katz) is used to obtain the convective heat transfer coefficient from land to slot. The Nusselt no. is related to Reynolds number and Prandtl and is given by

$$Nu_m = \frac{0.664\ \phi^{1/2}}{Pr^{1/2}}\left(1 - 6.27\left(\frac{Pr}{\phi}\right)^{4/9}\right)^{1/2}$$

where

$$\phi = RePr$$

For the two phase and liquid regions the temperature variation is smaller than for the surface region and approximations are used to represent in-depth temperature distributions. For the two phase region within the slot, $T = T_{sat}$. For the remaining land regions and the liquid phase slot region the following approximation is employed.

$$T_\ell^L = T_o^L + \frac{\left(\frac{\partial T}{\partial y}\right)_o^L + \left(\frac{\partial T}{\partial y}\right)_\ell^L}{2}\,\ell$$

where ℓ corresponds to the length of any given region and

$$\left(\frac{\partial T}{\partial y}\right)_o^L = -\frac{\dot{q}_o^L}{k}$$

$$\left(\frac{\partial T}{\partial y}\right)_\ell^L = -\frac{q_\ell^L}{k}$$

Superscript L denotes a land region. A similar expression can be written for the liquid phase region in a slot. In order to complete the system of equations required to compute temperatures on the boundaries of the various regions, expressions are required for the convective heat flux from land to slot. An expression for the single phase heat transfer coefficient has been given; for two phase heat transfer the following expression obtained from Reference 29 is used

$$Nu_{2\phi} = Nu_{\text{mist flow}} + Nu_m$$

where Nu_m is given above and

$$Nu_{\text{mist flow}} = \frac{h\ s}{k_{\ell iq}} = 0.08\ (\frac{\dot{m}\ x}{\mu_{\ell iq}})^{0.87} Pr_{\ell iq}^{0.4}$$

where x in the quality of the two phase mixture. An additional boundary condition imposed on the system is that their is zero heat transfer out of the system (i.e., adiabatic back face). Continuity of temperature and heat flux are used as matching conditions at region interfaces.

The above treatment can be employed to obtain detailed in-depth temperature distributions in the wall region and interface temperatures for the remaining regions.

6.2 DATA COMPARISON

6.2.1 External Cooling Data Correlation Comparison

Figures 6-7 through 6-10 present the comparison of the ADICT solutions for downstream cooling effectiveness with the data from the external cooling experiment shown also in Figures 4-40 through 4-43.

6.2.2 Combined Cooling Data Correlation Comparison

Figure 6-2 presents the comparison of the ADICT solution for the downstream cooling effectiveness with the data from the combined cooling experiment.

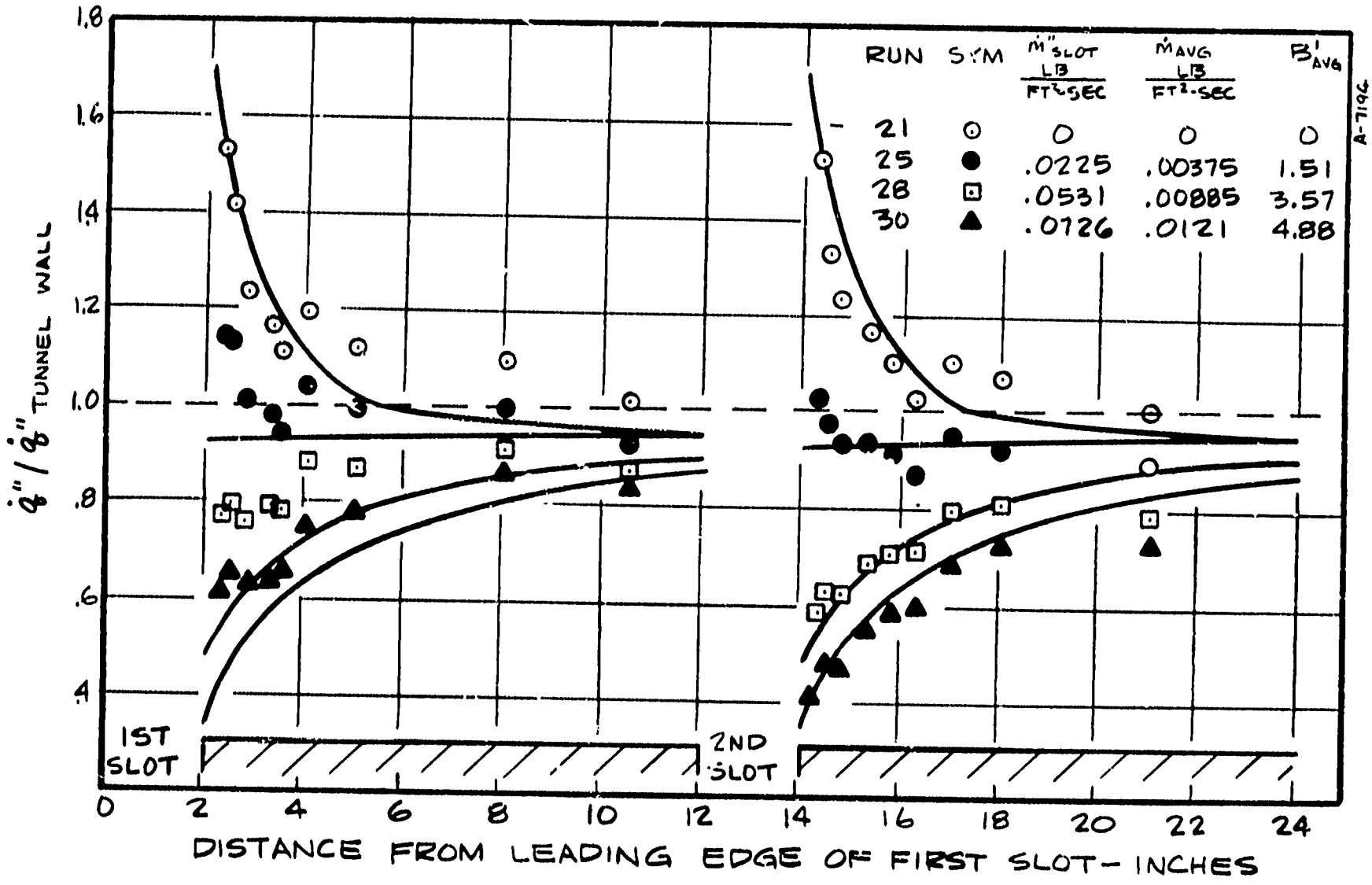

Figure 6-7. Downstream Cooling Effectiveness of External Cooling Experiment, 2.0/10.0

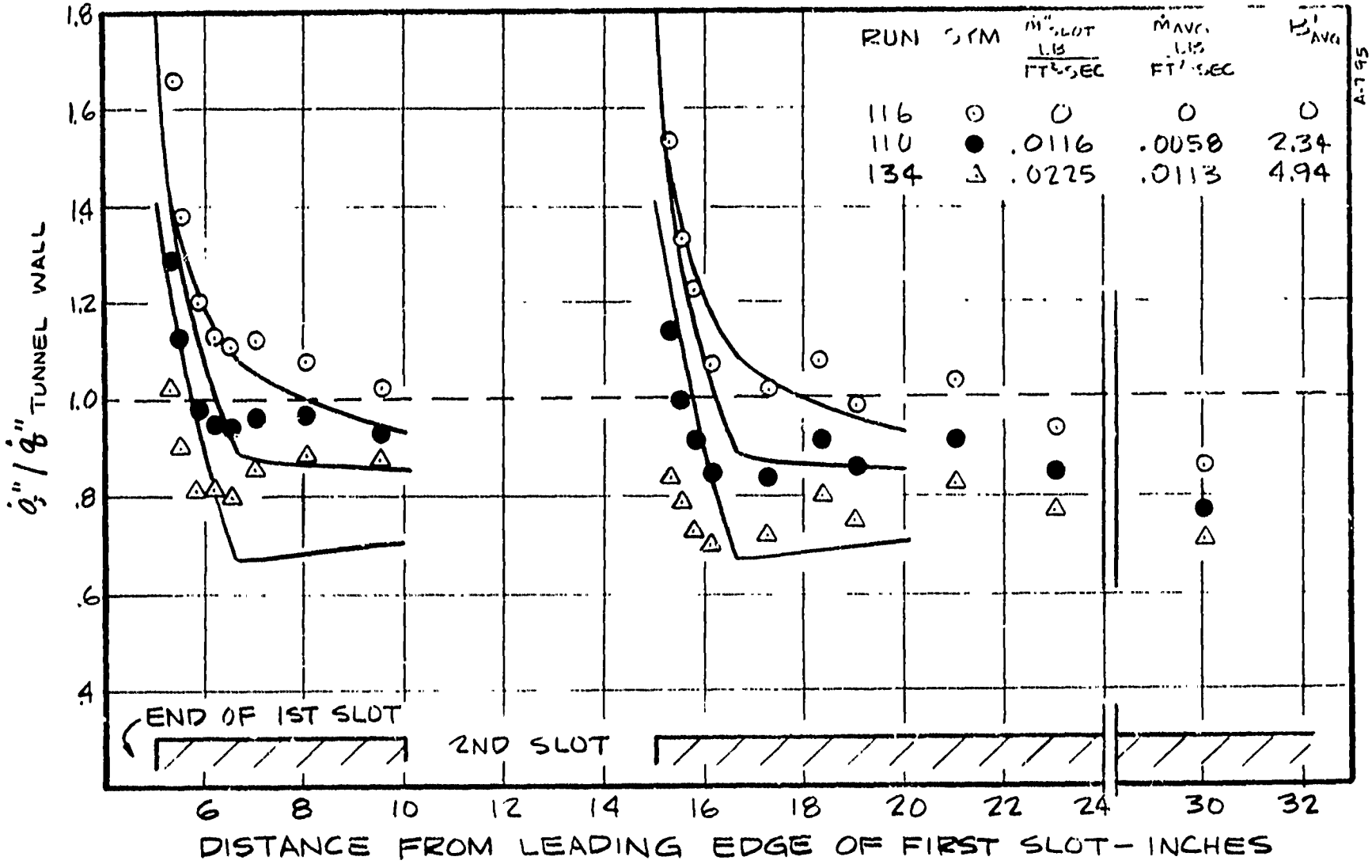

Figure 6-8. Downstream Cooling Effectiveness of External Cooling Experiment, 5.0/5)

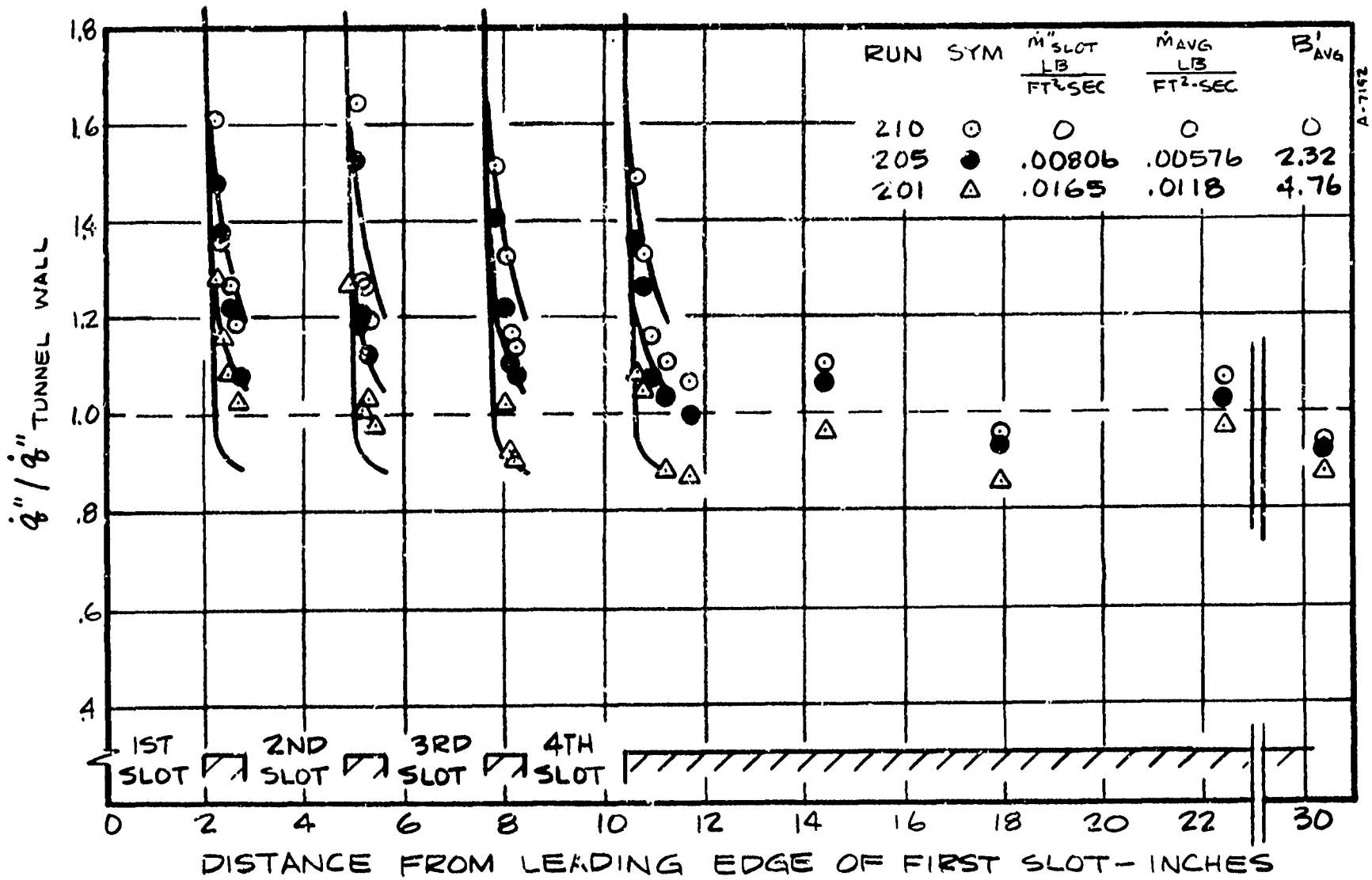

Figure 6-9. Downstream Cooling Effectiveness of External Cooling Experiment, 2.0/0.8

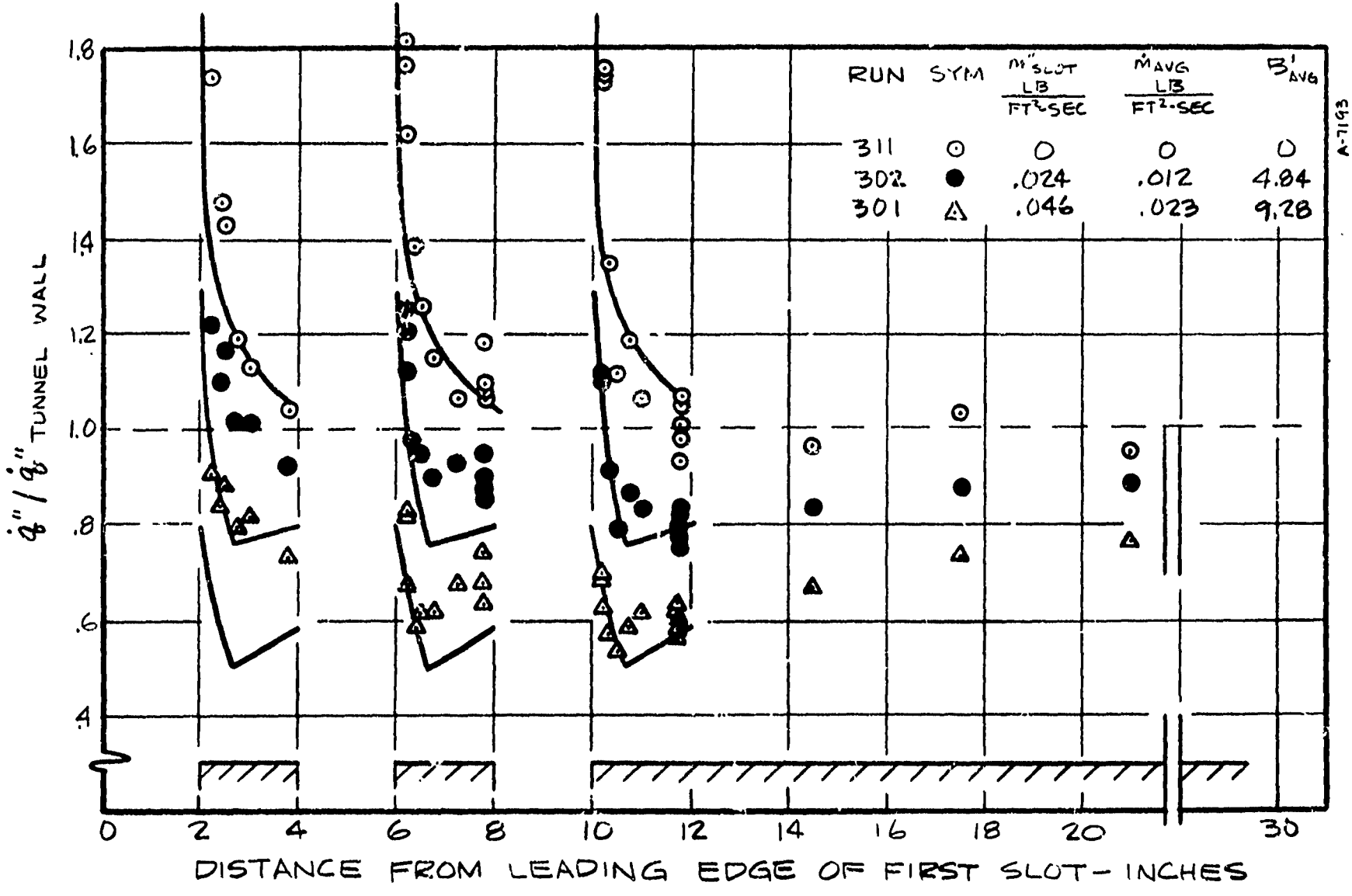

Figure 6-10. Downstream Cooling Effectiveness of External Cooling Experiment, 2.0/2.0

SECTION 7

APPLICATION STUDY

7.1 INTRODUCTION

The three experiments previously described provide information pertinent to the development of a discrete injection heat transfer model.

SPECIFICALLY:

- INTERNAL COOLING - provides information for the evaluation of in-depth heat transfer mechanics
- EXTERNAL COOLING - provides data pertaining to the interrelationship of surface heating, roughness, gaseous (air) blowing and downstream cooling effectiveness
- COMBINED COOLING - provides data pertaining to the interrelationship of injection roughness heating, surface temperature and downstream cooling effectiveness

This information has been assembled into a discrete injection cooling prediction code. In an effort to evaluate the code, an application study has been formulated in which the predictions of the ADICT (Aerotherm Discrete Injection Correlation Technique) code will be compared to those of the current "best" prediction procedure, namely, the Aerospace/GE Q* prediction technique currently being utilized by Aerojet Corporation in their design of flight discrete injection nosetips.

In addition to the predicted heat fluxes encountered at a specific test condition, the ADICT code will provide average slot and land temperatures as well as peak temperatures on lands.

Section 7.2 describes the nosetip geometry and the flow field conditions of interest. Section 7.3 details the specific results of the current "best" prediction technique and the ADICT predictions. Finally, Section 7.4 presents a description of the analysis, a comparison, and specific recommendations on future discrete injection prediction techniques.

7.2 GEOMETRY AND ENVIRONMENT DEFINITION

7.2.1 Nosetip Definition

The nosetip geometry under consideration is a 0.5 inch radius 6°35' sphere cone. The total axial length of the tip is 5.0 inches having a base diameter of 1.95 inches. With the exception of a 0.035 inch thick base plate, the tip is composed entirely of diffusion bonded CRES 347 platelets of 0.001, 0.002 and 0.010 inch thicknesses. Metering of flow is accomplished by through-etched passages of precise width and length in the 0.001 plates. The 0.002 inch platelet serve as separation for the metering platelets in the cap region and in a few instances as regions of additional metering. The 0.010 inch platelets provide flow separation in the sidewall region and also contain 0.0025 inch depth etch pods near the tip boundary for final flow distribution to the surface. These 0.010 platelets also contain the flow collection manifolding which is an integral part of the tip design (Reference 1).

7.2.2 Environment Definition

The ABRES/RPL rocket has been chosen to be used in the application study. This facility is a high temperature rocket equipped with nozzles which can provide Mach numbers of 2.3 and 2.9 with up to 100 atmospheres of nosetip stagnation pressure (P_{t_2}). The rocket has a capability of producing heating rates from 2000 to 5000 Btu/ft^2-sec on full size nosetips. In addition, angle of attack capability can be provided.

Test conditions are held constant through a unique control feedback system which continuously monitors the exhausting gases. Facility instrumentation includes high speed digital acquisition equipment, high frequency FM tape recording, high speed oscillograph data acquisition, television monitoring, high speed motion pictures and still photography. Typical test times are of the order of 10 to 15 seconds.

The specific test environment that has been chosen for this application study are

- M_∞ - 2.87
- P_{t_2} - 50 atms
- H_t - 3000 Btu/lbm

7.2.3 Wall Boundary Condition

The Aerotherm SAANT code, Reference 14, has been utilized in obtaining the wall boundary conditions. Two runs were performed for laminar and turbulent boundary layers, respectively. Input conditions included are:

- free stream
  - M_∞ - 2.87
  - γ - 1.2
  - P_{t_∞} - 2357.43 psia
  - T_{t_∞} - 5690.0°F
  - T_w - 530°
- body geometry
  - R_N - 0.5"
  - θ_c - 6°35'
  - z_{max} - 4.952 inches

Output includes:

- Body geometry parameters
- Shock shape
- Boundary layer wall properties including

  θ, δ, δ^*, Re_θ, $\dot{q}_o^w$

Figure 7-1 presents the results of the two SAANT calcualtions with respect to the cold wall heat flux. Transition is assumed to take place at the turbulent laminar heating cross over, corresponding to $Re_\theta = 175$. This is a conservative transition criterion; however, its effect on total predicted coolant requirement is minimal since the percentage of total area to be protected is not strongly affected by the transition criterion, provided transition is located on the cap region.

7.2.4 Edge Conditions

The Aerotherm SAANT code is also utilized in obtaining the edge boundary layer conditions. Two runs were performed for laminar and turbulent boundary layers respectively. Input conditions remain as in Section 7.2.3. Output includes P_E, T_E, M_E, H_E, T_E, ρ_E, U_E, μ_E, Re_E.

Figure 7-2 presents the calculated edge pressure distribution.

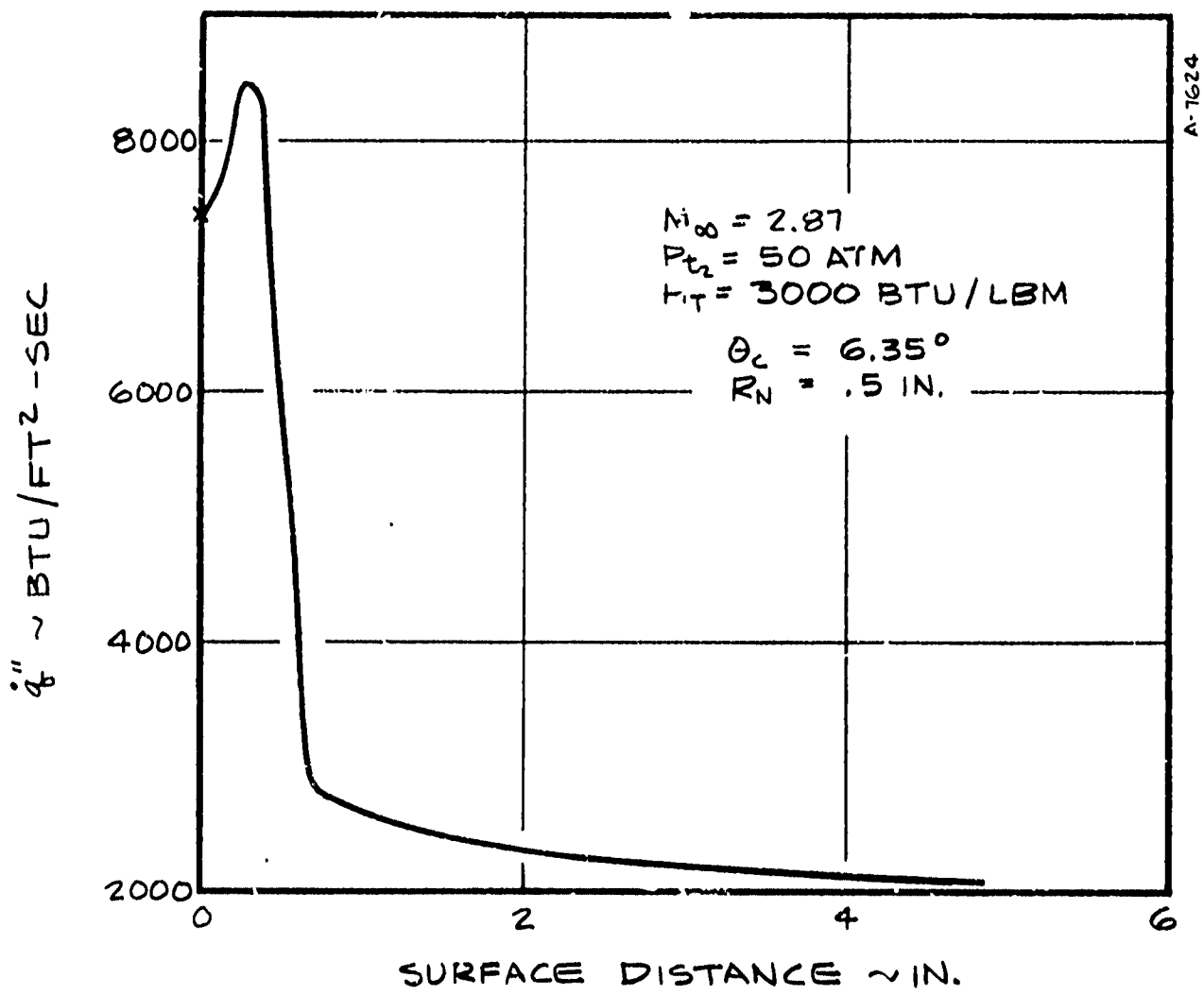

Figure 7-1. Coldwall Heat Flux Distribution

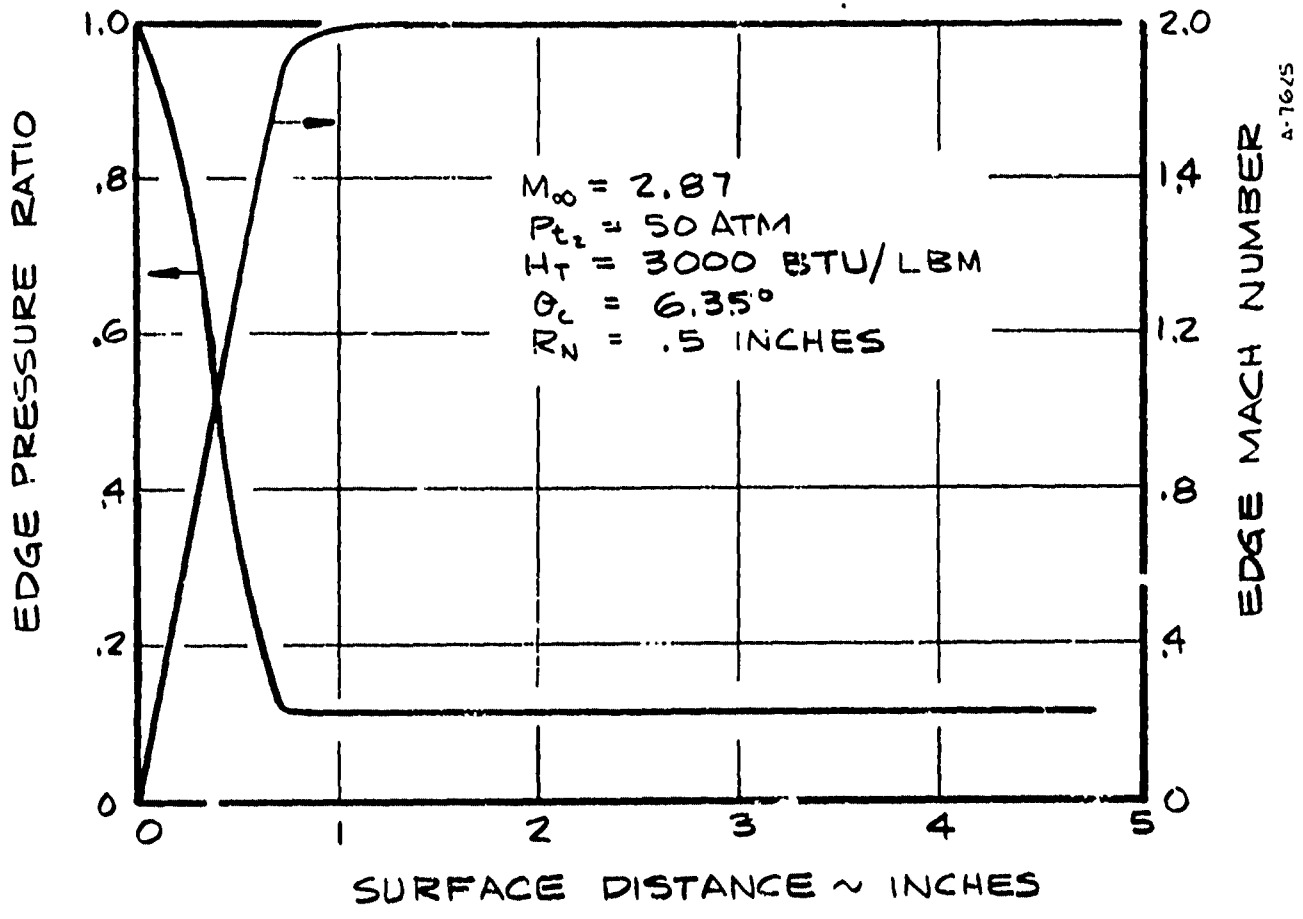

Figure 7-2. SAANT Predictions for Application Study

7.3 RESULTS

7.3.1 Previous and Current Technique

The design criterion in use prior to the ADICT code development has been the Aerospace/GE Q* correlation technique based on the correlation shown in Figure 7-3. This correlation is utilized in the following manner:

- First, the desired operating wall temperature and the free stream stagnation enthalpy are selected. This choice established a Q* ratio where

$$Q^* = \frac{\dot{q}_o''}{\dot{m}_c''} = \frac{\text{cold wall heat flux}}{\text{coolant mass flux}}$$

- From the SAANT solutions of Section 7.2.3, the cold wall heating distribution is known, hence the $\dot{m}_c''$ distribution may be obtained
- Finally, it has been experimentally determined that this $\dot{m}_c''$ distribution should be multipled by a factor of 3 for the cap region ($\theta \leq 30°$) to prevent burnout.

Figure 7-4 presents the combination (laminar - turbulent) SAANT $\dot{q}_o''$ distribution used in this study. The distribution represents the most conservative approach to the nosetip heating problem. Figure 7-5 shows the resulting $\dot{m}_c$ distributions for two wall temperatures, T_w = 1000°F, 1700°F. No multiplication factor has yet been applied. As one would expect, the $\dot{m}_c$ distribution has the overall shape of the heat flux distribution. Knowing the geometry of the vehicle (Section 7.2.1), the overall coolant requirements may be obtained.

T_w	$\dot{m}_c$ ($[S/R_N]_{max}$ = 10.6)
1000°F	0.164 lbm/sec (H_2O)
1700°F	0.148 lbm/sec (H_2O)

Applying the suggested cooling factor (3 x) to the tip region of the configuration ($\theta \leq 30°$) we obtain a new $\dot{m}_c$ distribution. Figure 7-6 shows an example of this modification for T_w = 1700°F. As a result, our coolant requirements are altered accordingly, that is

T_w	$\dot{m}_c$ ($(S/R_N)_{max}$ = 10.6)
1700°F (3x)	.186 lbm/sec (H_2O)

This represents a 25.8 percent increase in required coolant over the uncorrected $\dot{m}_c$ distribution.

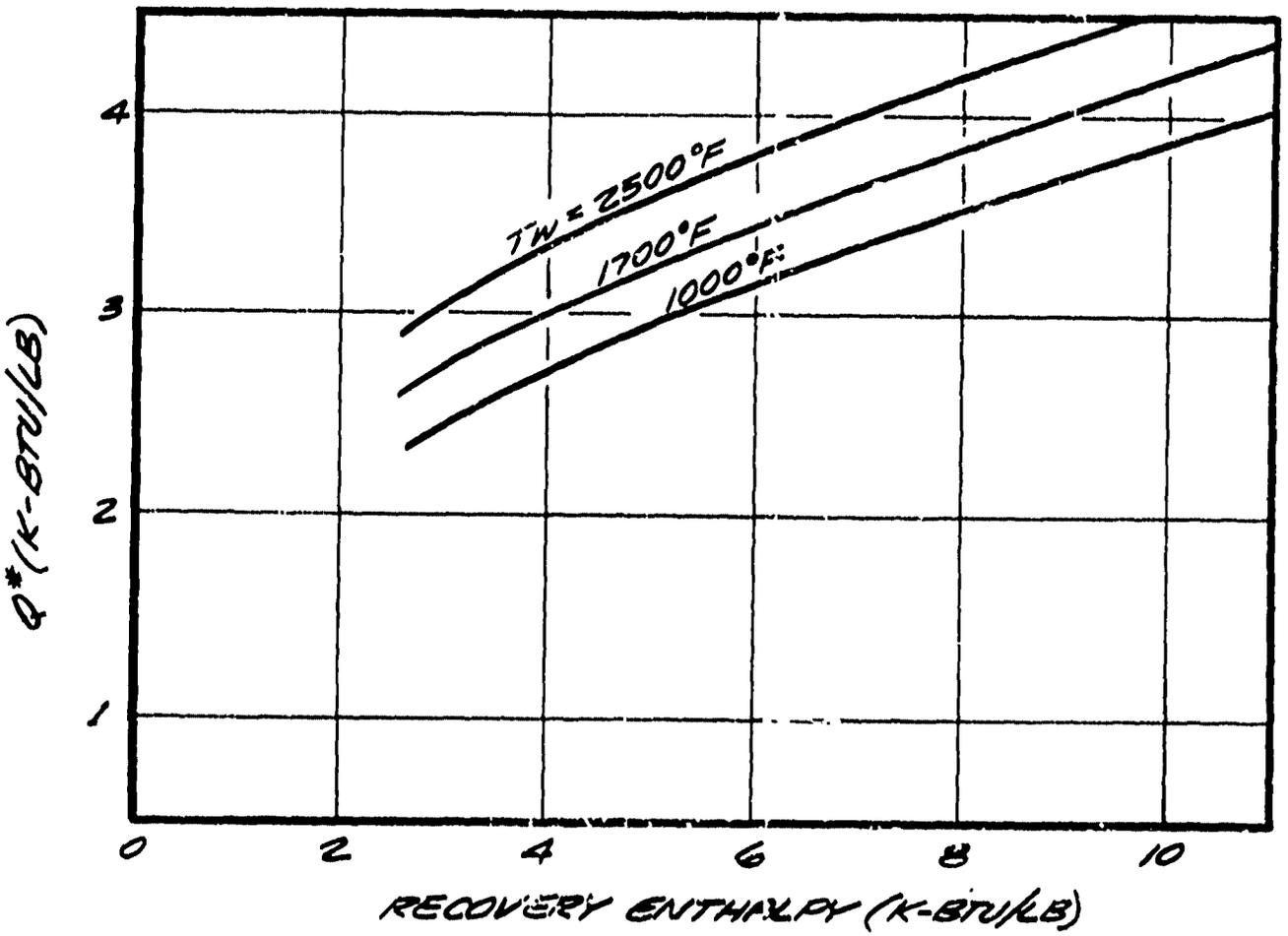

Figure 7-3. Aerospace/GE Q* Correlation

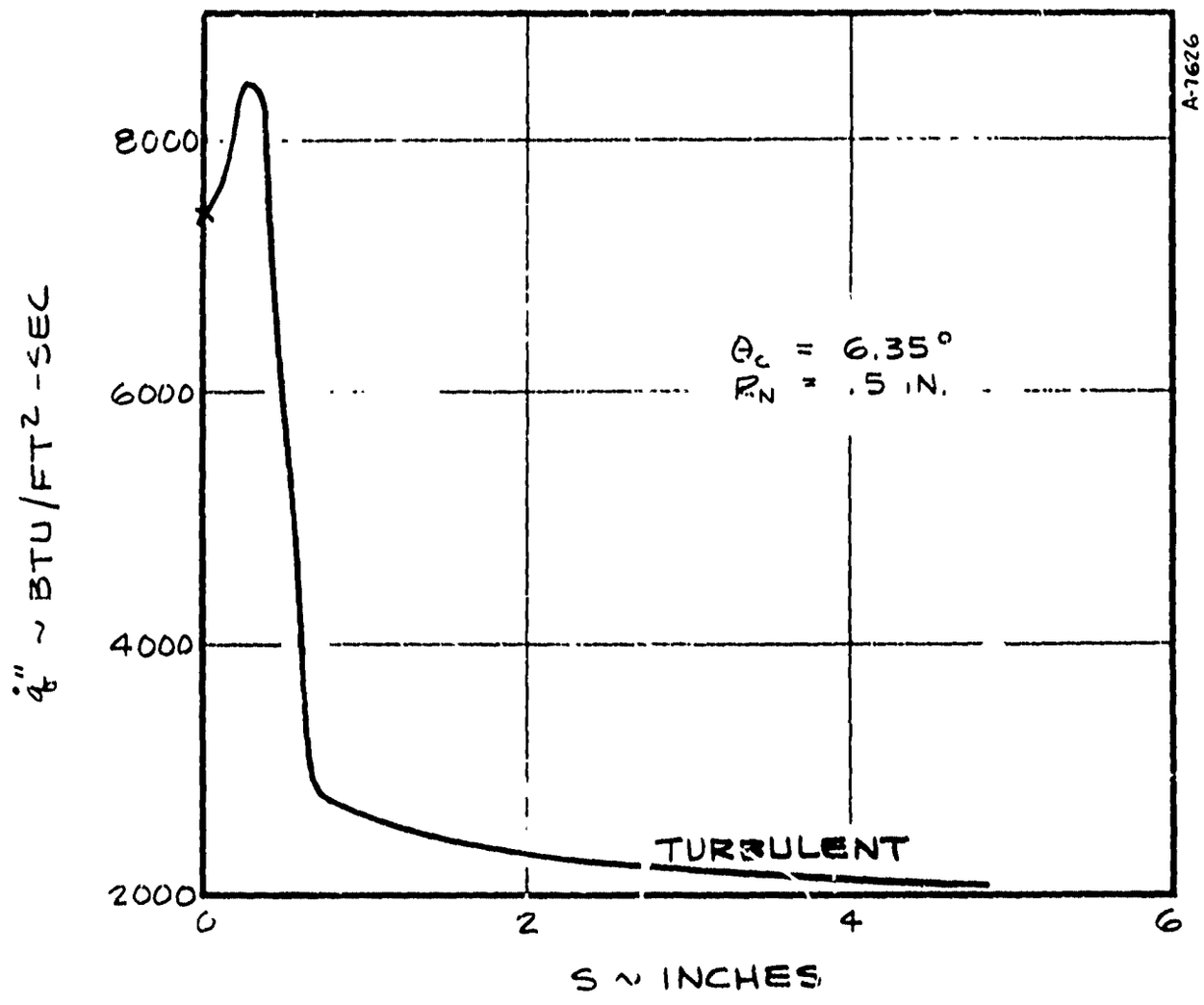

Figure 7-4. Coldwall Heat Transfer Distribution Over Aerojet Nosetip Used In Application Study

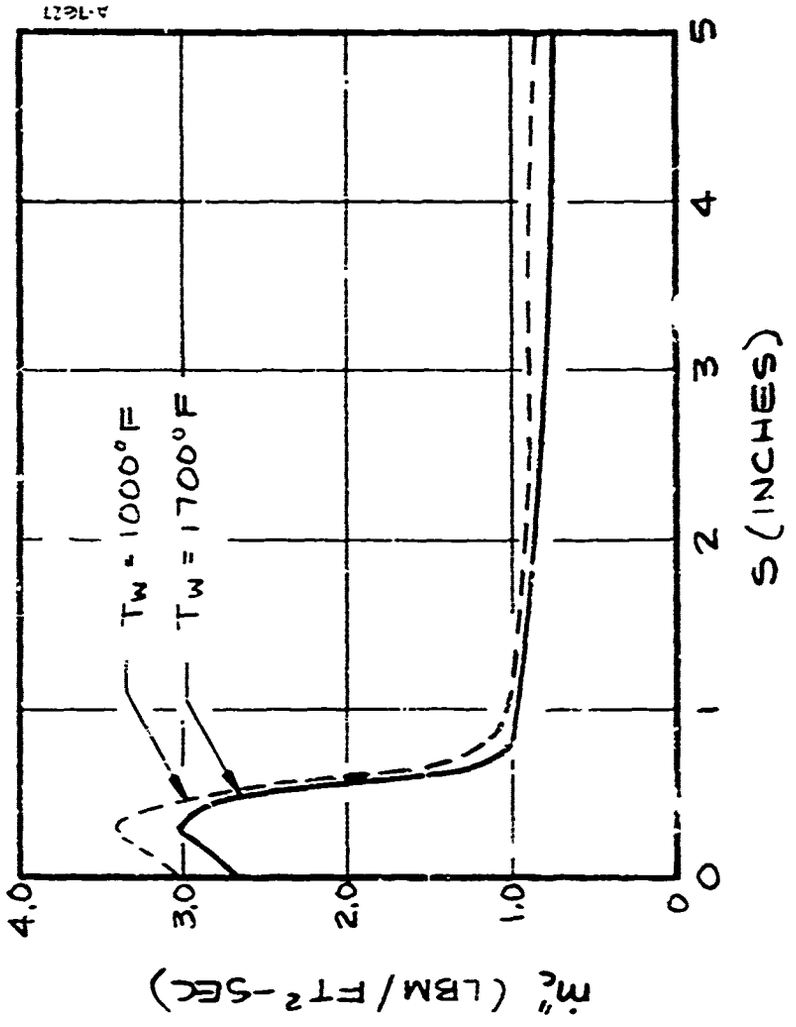

Figure 7-5. Mass Flow Distribution For Aerospace/GE Q* Correlation

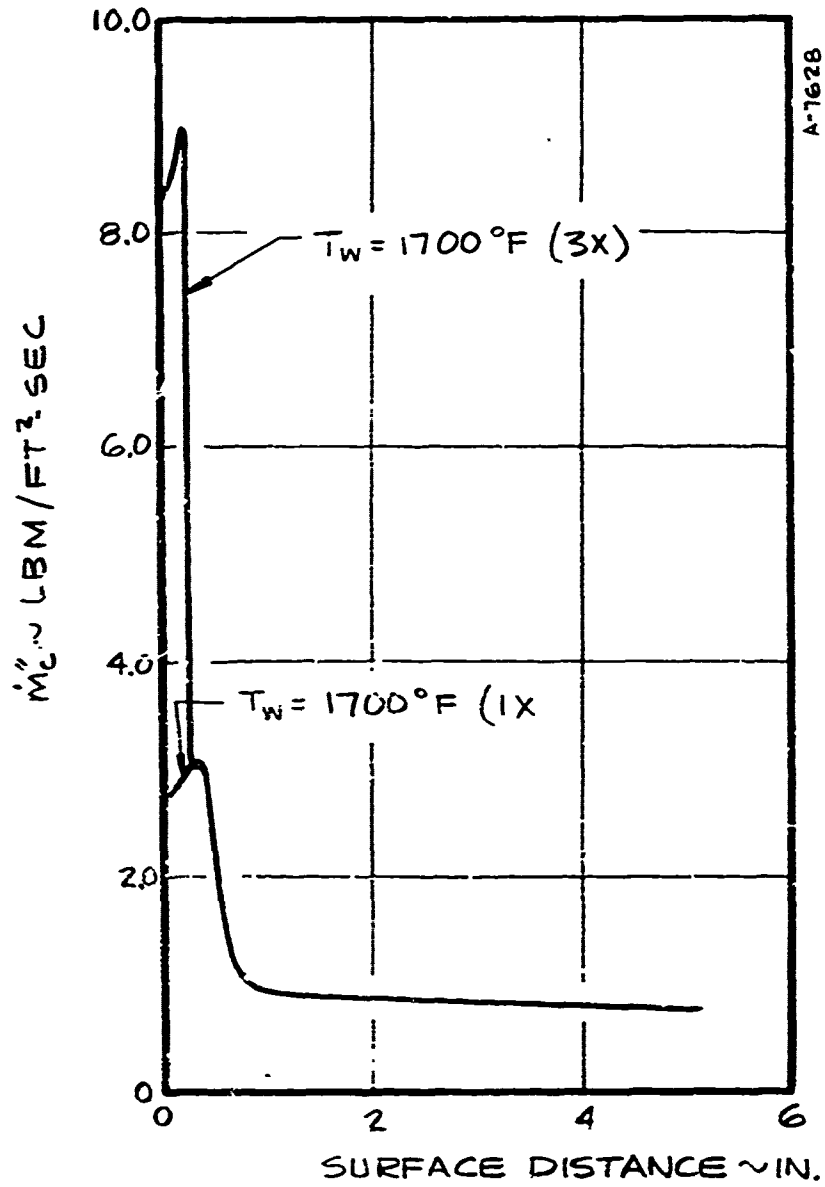

Figure 7-6. Effects of Overcooling In Cap Region of Aerotip

Continuing, therefore, we are now in a position to evaluate the total coolant requirements for a RPL tunnel environment. If we assume a maximum test time in the ABRES facility of 15 seconds, our total coolant requirements become:

T_w	$\dot{m}_c$ (lbm of H_2O)
1000°F (ideal)	2.46
1700°F (ideal)	2.22
1700°F w/3x CAP cooling	2.79

7.3.2 Results of Current Prediction Technique

The environment previously described was input to the ADICT code and the surface temperature distributions were computed. An input requirement is the mass flux distribution; the present technique computes surface temperature for a prescribed mass flux. The GE/Aerospace Q* correlation curves are given only for temperatures of 1000°F and 1700°F. Hence, for the purpose of comparison a set of $\dot{m}$ distributions was input in order to iteratively obtain the mass flux corresponding to one of the aforementioned temperatures. A temperature of 1700°F was chosen as a basis for comparison. Initial runs were made with mass fluxes of 3 x (.75 $\dot{m}_I$, 1.0 $\dot{m}_I$ and 1.25 $\dot{m}_I$ on the skirt region) $\dot{m}_I$ being the ideal mass flux obtained from the GE/Aerospace Q* correlation. The initial runs indicated that a predicted temperature of 1700°F occured for mass fluxes of less than 3 $\dot{m}_I$ in the cap region and mass fluxes in the range (1.00 $\dot{m}_I$ - 1.25 $\dot{m}_I$) on the skirt. Subsequent iterations yielded mass fluxes ranging from 1 $\dot{m}_I$ to 3 $\dot{m}_I$ in the cap region and fluxes of about 1.1 $\dot{m}_I$ on the skirt. Table 7-summarizes the results of the present treatment. Figure 7-7 shows a comparison between the predictions using the present code and the GE/Aerospace Q* correlation. Table 7-2 compares predicted total coolant flow rate requirements based on a fifteen second operating time.

The comparison indicates that the total coolant flow rate requirements predicted by the two methods are in close agreement. The present technique however, predicts slightly larger required mass fluxes on the skirt and considerably lower mass fluxes on the cap than does the GE/Aerospace correlation with a factor of three applied to the cap. The close agreement in total flow rate is due to the fact that the cap area is a small fraction of the total nosetip area.

The surface temperature mass flux relationship will be affected by the computed external heat flux impressed on the system. As was mentioned in Section 6 the external heat transfer correlation combines effects of roughness

TABLE 7-1

SUMMARY OF ADICT PREDICTIONS

	S	B'	$(\dot{q}''/\dot{q}_o'')_S$	$(\dot{q}''/\dot{q}_o'')_L$	$\dot{m}''^*$ (lbm/ft²/sec	T (°R)
CAP	.048	1.020	3767	6230	3.06	2044
	.096	1.030	3848	6478	3.17	2125
	.144	1.036	3908	6646	3.25	2177
	.192	1.040	4048	6933	3.40	2128
SKIRT	.300	1.21	3806	6826	4.25	2200
	.400	1.22	3624	6494	4.00	2190
	.600	1.45	1720	4297	2.54	2096
	.800	1.46	1081	2812	1.55	2140
	1.00	1.45	917	2395	1.25	2110
	2.5	1.45	820	2240	1.1	2100
	5.0	1.45	810	2100	1.0	2150

TABLE 7-2

COMPARISON OF ADICT TOTAL COOLANT FLOW RATE PREDICTION TO AEROSPACE/GE Q* CORRELATION, T_W = 1700°F

ADICT	AEROSPACE/GE Q*
.177 lbm/sec	.186 lbm/sec (3X)
.177 lbm/sec	.148 lbm/sec (1X)

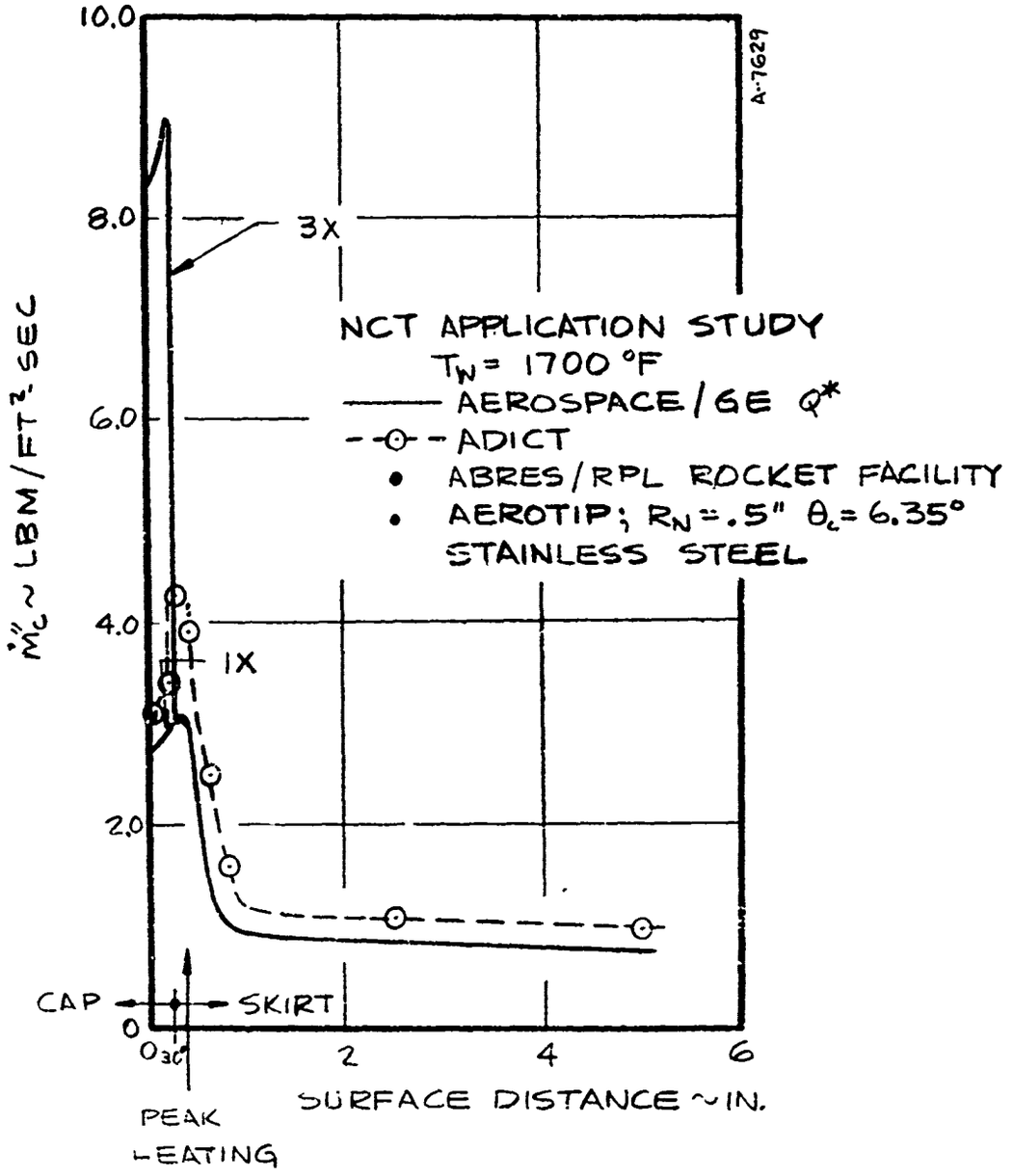

Figure 7-7. ADICT Solution of Application Study

and mass transfer. The data used to validate this correlation is based on measurements taken in supersonic, zero pressure gradient flow, whereas the cap region flow field is predominately subsonic and contains a pressure gradient. The correlation does contain Mach no. effects in that both the effective roughness height and the roughness augmentation heating factor are Mach no. dependent. However these quantities only impact peak heating values and not the decay over a land. The present results indicate that the roughness augmentation effect on the cap region is underpredicted, provided a flow margin of three on the cap is realistic. One possible explanation for the discrepancy if that the present treatment does not properly account for pressure gradient and Mach no. effects in the cap region. A more plausible explanation is given in the following section.

7.4 CONCLUDING REMARKS AND RECOMMENDATIONS

The present technique correlates the combined cooling data and is in reasonably good agreement with the GE/Aerospace Q* correlation for one specific nosetip configuration. The model employed represents a significant advance in that the effects of slot and land dimensions and the effects of nosetip material can each be evaluated independently. Previously all effects were contained within one single parameter, Q*, which had been determined experimentally only as a function of pressure and enthalpy for a single material, stainless steel. Furthermore, the Q* approach to data correlation for DI hardware has been purely empiricaly; that is, no attempt had been made to relate observed values of Q* to nosetip geometry and fundamental heat transfer mechanisms. For this reason it is hard to justify the application of the Q* correlation to configurations and flow field conditions that differ from those upon which the data used to generate Q* is based.

The margin of three recommended for the skirt region is based on Cornel Aeronautical Laboratory data Super-Wave Heater data, Reference 1. Close scrutiny of this data indicates that the average correction factor required is two not three; the factor of three is based on only one out of six data points and is recommended so as to provide a conservative design. Furthermore, the test model for which this data was taken was different than the standard flight type nosetip*. The cap region on the model used in the CAL test series had S/L ratios in the cap region were closer to S/L ratios on the flight nosetip skirt region than the cap region. Hence, a mass flux distribution was computed with the ADICT code for the cap region environment using the skirt region S/L value. This distribution is shown in Figure 7-8. It can be seen that these results

*Private communication, J. Blubaugh, Aerojet Liquid Rocket Company.

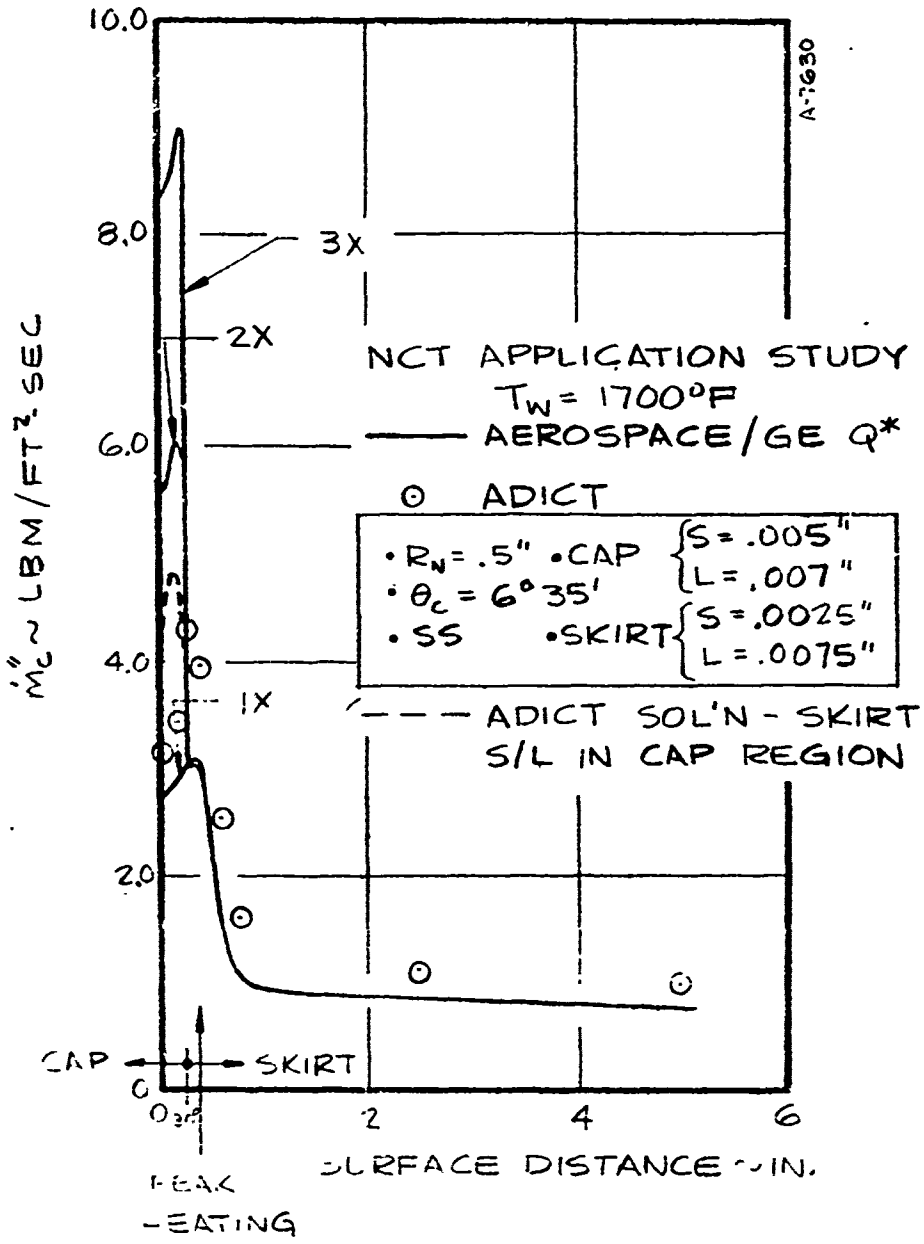

Figure 7-8. ADICT Solution of Application Study

were in somewhat closer agreement with the Q* prediction used with a factor of three correction. The results would be in much closer agreement with the Q* prediction if a factor of two correction had been applied to the cap region as suggested by the data. Thus it can be tentatively concluded that the required correction factor to Q* predictions is geometry dependent. These results clearly point out the advantages of a prediction technique that allows for variable geometry.

Nevertheless, some uncertainty still remains relative to the external heat transfer model for low Mach no. flow with pressure gradient. To remedy this situation it is recommended that further theoretical investigations be directed towards understanding effective roughness for this flow regime and that the data base for this flow regime be expanded.

The present correlation technique is embodied in a code which predicts surface temperature for a specified environment, configuration and mass flux. However, for design purposes it is desirable to be able to generate coolant requirements for a specified operating surface temperature. Hence, it is recommended that the present code be used to generate a set of engineering design charts from which mass flux can readily be obtained for a specified geometry and surface temperature.

SECTION 8

REFERENCES

1. Aerojet Liquid Rocket Company, "Nosetip and Expulsion Subsystem Program, Phase II, Analysis and Study Reports, Nosetip Design and Analysis," June 9, 1970.

2. Brunner, M.: AVCO 10 MW Test Report General Electric Corporation, NCT Log No. 7060.3038, November 1969.

3. Anon.,: "Experimental Recommendation for Nosetip Cooling Technology Program, Task 4.2.1," Aerotherm Corporation, NCT Log No. 7060.76, March 15, 1972.

4. Lane, F.: Liquid-Layer Phenomenology, Report KLD TR-6, KLD Associates, Inc. Huntington, New York, February 1972.

5. Anon.,: "Environmental Test Plan for the NCT External Cooling Experiment," Aerotherm Corporation, NCT Log No. 7060.128, July 18, 1972.

6. Frost, Walter, et al.,: "Internal Cooling Study of Discrete Injector Transpiration Cooled Nosetips Final Report, Aerotherm Corporation and UTSI, August 1973.

7. Anon.," "Environmental Test Plan for the NCT External Cooling Experiment," Aerotherm Corporation, NCT Log No. 7060.170, October 26, 1972.

8. Ferrell, J. E.,: "Nosetip Cooling Technology Program Large Slot External Cooling Tests, Test Report, Aerotherm Corporation, NCT Log No. 7060.230, April 1973.

9. Anon.,: "Experimental Test Plan for the Combined Cooling Experiment," Aerotherm Corporation, April 11, 1973.

10. Clark, K. J. and Mehner, P. O., "Nosetip Cooling Technology Program, Combined Cooling Test, Test Report, Aerotherm Corporation, NCT Log No. 7060.252, September 20, 1973.

11. Aerotherm/ Acurex Corporation, Mountain View, California: Nosetip Cooling Technology (NCT) Program, 3rd TI/TD Meeting, March 1972.

12. Frost, W., Harper, W. L., and Wickman, J. H.: Internal Cooling Study, NCT Experiment Definition Document. The University of Tennessee Space Institute, Tullahoma, Tennessee, March 1972.

13. Aerotherm/Acurex Corporation, Mountain View, California: PANT Program, 3rd TI/TD Meeting, July 1971.

14. Kendall, R. M. and Bartlett, E. P.: Nonsimilar Solution of the Multicomponent Laminar Boundary Layer by an Integral-Matrix Method. AIAA Journal, Vol. 6, 1968, pp. 1089-1097.

15. Grose, R. D. and Kendall, R. M.: Boundary Layer Integral Matrix Procedure - Liquid Layer Version (BLIMPL). Aerotherm Report 70-3, February 1970.

16. Anderson, L. W. and Bartlett, E. P.: Boundary Layer Transition on Reentry Vehicle Nosetips with Consideration of Surface Roughness. Aerotherm Report TM-71-9, July 1971.

17. Powars, C. A.: Surface Roughness Effects on Reentry Heating. Aerotherm Report TM-71-10, July 1971.

18. General Dynamics Convair: Transpiration Techniques Presentation. Convair Report GDC ACW 67-014, July 1967.

19. Nicoll, F. M.: Mass Injection in a Hypersonic Cavity Flow. Aerospace Research Laboratories Report ARL 65-90, May 1965.

20. Welsh, W. E., Jr.: Shape and Surface Roughness Effects on Turbulent Nosetip Ablation. AIAA Paper No. 69-77, June 1969.

21. Gater, R. A. and L'Ecuyer, M. R.: A Fundamental Investigation of the Phenomena that Characterize Liquid-Film Cooling. Int. J. Heat Mass Transfer, Vol. 13, 1970, pp. 1925-1939.

22. Cresci, R. J. and Starkenberg, J.: Liquid Film Cooling on Hypersonic Slender Bodies. Paper presented at XXII Int. Astro. Congress, Brussels, Belgium, September 1971.

23. Gold, H., Otis, J., and Schlier, R.: Surface Liquid Film Characteristics: An Experimental Study. Paper presented at AIAA 4th Fluid and Plasma Dynamics Conference, Palo Alto, California, June 1971.

24. Herman, R. and Melnik, W. L.: Aerodynamic and Heat Transfer Studies with Evaporative Film Cooling at Hypersonic Mach Numbers. Report RR 189, Rosemount Aeronautical Labs., Minneapolis, Minnesota, September 1962.

25. Gold, H., Masola, R. E., and Smith, P. E.: "Flow Characteristics of Porus Media and Surface Liquid Film Interactions." Paper presented at the Eighth Aerospace Sciences Meeting, New York, January 19-21, 1970, AIAA Paper No. 70-152.

26. Widhopf, G. F. and Hall, R.: Transitional and Turbulent Heat Transfer Measurements on a Yawed Blunt Conical Nosetip. AIAA Paper No. 72-212, January 1972.

27. VonReth, Rolf, D.," :An Experimental and Analytical Investigation of One-Dimensional Two-Phase Flow Transpiration Cooling Through Porous Metals," Ph.D. Dissertation, the University of Tennessee, Knoxville, 1971.

28. Knudsen, J. E. and Katz, D. L.: "Fluid Dynamics and Heat Transfer," McGraw-Hill Book Company Inc., New York, 1958.

29. Kreith, F.,: "Principles of Heat Transfer, Second Edition, International Text Book Company, Scrnton, Pennsylvannia, 1965.

30. Anon.: Test Facilities Handbook, Ninth Edition, Arnold Engineering Development Center, July 1971.

31. Matthewd, R. K. and Trimmer, L. L.: "Nozzle Turbulent Boundary Layer Measurements in the VKF 50-Inch Hypersonic Tunnels," AEDC-TR-69-118, June 1969.

REFERENCES (Concluded)

32. Personal Communication, L. L. Trimmer to J. E. Ferrell, July 20, 1972.

33. Anon.: NCT Technical Proposal, Aerotherm Corporation, September 7, 1971.

34. Chir, J. H., Skirvin, S. C., Hayes, L. E. and Burggraf, F.: "Film Cooling with Multiple Slots and Louvers, Part 1, Multiple Continuous Slots," ASME Journal of Heat Transfer, pp. 281-286, August 1961.

35. Baronti, P., Fox, H., and D. Soll,: "A Survey of the Compressible Turbulent Boundary Layer with Mass Transfer," Astronautic Acta. Vol. 13, 1967, pp. 239-249.

36. Covington, M. A. and N. S. Vojvodich, "Turbulent Flow Studies in Two Arc Heated Duct Facilities," J. Spacecraft and Rockets, Vol. 9, No. 6, 1972, pp. 441-447.

37. Jorgensen, L. H. and G. M. Baum," "Charts for Equilbrium Flow Properties of Air in Hypervelocity Nozzles," NASA TND-1333, September, 1962.

38. Moeckel, W. E. and K. C. Weston,: "Composition and Thermodynamic Properties of Air in Chemical Equilibrium," NACA TN-4265, April, 1958.

39. Charwat, A. F., Supersonic Flows with Imbedded Separated Regions, Advances in Heat Transfer, Vol. 6.

40. Nardo, C. T., Heat Transfer Correlation for the NCT Large Slot Tests, Aerotherm Corporation, NCT Log No. 7060.237, May 1973.

41. Powars, C. A., Analysis of PANT Series A Rough Wall Calorimeter Data, Part I: Surface Roughness Effects on Heat Transfer, Aerotherm Corporation, Aerotherm Report 73-80.

42. Laganelli, A. L. and Fogaroli, R. P., Downstream Influence of Film Cooling in a High Speed Boundary Layer, AIAA Paper No. 71-425.

43. Baronti, P. et al., A Survey of the Compressible Turbulent Boundary Layer with Mass Transfer, Astronautica Acta, Vol. 13, 1967.

44. Derbidge, T. C. and Woo_, M. R., "User's Manual: Steady State Analysis of Ablating Nosetips (SAANT)," Aerotherm Corporation, UM-73-88, September 1973.